# Stony Brook University

# The Nature of Optically-Luminous Stellar Clusters in a Large Sample of Luminous Infrared Galaxies

A Dissertation Presented

by

**Tatjana Vavilkin**

to

The Graduate School

in Partial fulfillment of the

Requirements

for the Degree of

**Doctor of Philosophy**

in

**Physics**

Stony Brook University

**August 2011**

**Stony Brook University**

The Graduate School

**Tatjana Vavilkin**

We, the Dissertation committee for the above candidate for the
Doctor of Philosophy degree, hereby recommend
acceptance of this Dissertation.

**Dr. Aaron S. Evans (Dissertation Advisor)**
**Adjunct Professor, Department of Physics and Astronomy**

**Dr. Alan Calder (Chairperson of Defense)**
**Assistant Professor, Department of Physics and Astronomy**

**Dr. Harold J. Metcalf**
**Professor, Department of Physics and Astronomy**

**Dr. Joseph M. Mazzarella**
**Research Scientist, Infrared Processing and Analysis Center, Caltech**

**Dr. Brad Whitmore**
**Astronomer, Space Telescope Science Institute**

This Dissertation is accepted by the Graduate School.

Lawrence Martin
Dean of the Graduate School

Abstract of the Dissertation

# The Nature of Optically-Luminous Stellar Clusters in a Large Sample of Luminous Infrared Galaxies

by

**Tatjana Vavilkin**

**Doctor of Philosophy**

in

**Physics**

Stony Brook University

**2011**

Luminous Star Clusters (SCs) are fundamental building blocks of galaxies, and they provide basic information regarding the mechanisms of star formation and the process of galaxy formation and evolution. In my PhD thesis project I investigate properties of young SCs in a sample of 87 nearby Luminous Infrared Galaxies (LIRGs: $L_{\rm IR} \geq 10^{11.4}$ $\rm L_{\odot}$) imaged with the *Hubble Space Telescope* Advanced Camera for Surveys at 0.4$\mu$m and 0.9$\mu$m. Many LIRGs are observed to be ongoing mergers of gas-rich disk galaxies. They contain extreme starbursts and hence are expected to host particularly rich and luminous populations of SCs. This project represents the largest sample of galaxies with uniformly characterized properties of their SC populations.

A large fraction ($\sim$ 17%) of the cluster population is younger than 10 Myr. There is uncertainty in the determination of the ages of the bulk of the SCs due to an age-extinction degeneracy - the majority of the detected cluster population may have ages of up to a few hundred Myr. The median SC luminosity function index of the LIRG sample is $\alpha \approx -1.8$,

which is in a good agreement with previously published studies in various galaxy types. This sample contains some of the most luminous clusters observed so far, with $M^{max}_{F435W}$ exceeding $-17$ mag. LIRGs follow the "brightest cluster - star formation rate" correlation observed for lower luminosity star-forming galaxies quite closely, although a large degree of scatter possibly due to extinction and over-estimation of Star Formation Rates (SFRs) in galaxies containing an Active Galactic Nucleus (AGN) is present. Thus, the size-of-sample effect and the observed high SFRs are responsible for high luminosity of SCs found in LIRGs. The specific luminosity $T_L$(F435W) – SFR(far-IR + far-UV) relation observed for nearby non-interacting spiral galaxies is not applicable to LIRGs. However, a weak correlation of specific luminosity $T_L$(F435W) – SFR(far-UV) is apparent. No clear trend of SC properties with the merger stage of the LIRG is observed; although in late merger stages the degree of the extended star formation diminishes and the centrally concentrated nuclear starburst or an AGN dominate the energy output of the LIRG. Galaxies with HII-region like (i.e., starburst like) nuclear spectra exhibit higher specific frequency $T_N$, specific luminosity $T_L$ and $M^{max}_{F435W}$ values compared to galaxies where an AGN is present. In a sub-sample of the 15 most cluster-rich LIRG systems, auto-correlation functions reveal a hierarchical spatial distribution of SCs; correlation functions with *GALEX* near-UV and *Spitzer* IRAC 8$\mu$m images show an overlap of near-UV emission and locations of optically visible clusters and no apparent correlation with mid-IR emission (i.e., embedded star formation). Thus, optically visible young SCs and UV emission represent un-obscured star formation which appears to be unassociated with the bulk of the star formation that takes place in dusty central regions of LIRGs.

# Contents

# List of Figures

# List of Tables

# List of Abbreviations

| | |
|---|---|
| ACS | Advanced Camera for Surveys |
| AGN | Active Galactic Nucleus |
| CDF | Cumulative Distribution Function |
| FOC | Faint Object Camera |
| FOV | Field Of View |
| FWHM | Full Width at Half the Maximum |
| GC | Globular Cluster |
| GMC | Giant Molecular Cloud |
| GOALS | Great Observatories All-sky LIRG Survey |
| HST | Hubble Space Telescope |
| IMF | Initial Mass Function |
| IC | Interaction Class |
| IRAS | Infrared All-sky Satellite |
| KS test | Kolmogorov-Smirnov test |
| LIRG | Luminous Infrared Galaxy |
| LF | Luminosity Function |
| MF | Mass Function |
| MWU test | Mann-Whitney U test |
| NED | NASA/IPAC Extragalactic Database |
| PAH | Polycyclic Aromatic Hydrocarbon |
| RBGS | Revised Bright Galaxy Sample |
| SB | Star Burst |
| SC | Star Cluster |
| SF | Star Formation |
| SFE | Star Formation Efficiency |
| SFR | Star Formation Rate |
| SSP | Simple Stellar Population |
| ULIRG | Ultraluminous Infrared Galaxy |
| WFPC | Wide Field Planetary Camera |
| YMC | Young Massive Cluster |

# Acknowledgements

First and foremost, I have to thank my advisor, Prof. Aaron Evans. His excellent "Galaxies" course awakened my interest in the field of galaxy mergers, AGN and star formation. I am grateful to Prof. Evans for hiring me as a Research Assistant when I first came to Stony Brook, for his guidance on this long journey and his persistence to see me through till the end.

I would like to express my gratitude to my co-advisor Dr. Joseph Mazzarella and the members of the GOALS collaboration in Pasadena, Dr. Jason Surace, Dr. Lee Armus, Dr. Justin Howell, Dr. Andreea Petric, Dr. Steve Lord and Dr. Phil Appleton for making my time at IPAC inspiring and productive. I would also like to thank the collaborators elsewhere, Dr. Dong-Chan Kim, Prof. Dave Sanders and Vivian U.

I thank Prof. Alan Calder and Prof. Hal Metcalf for serving on my thesis committee and Dr. Brad Whitmore for his invaluable feedback and advice.

I would like to thank the faculty at the Physics & Astronomy Department in Stony Brook, Prof. Jin Koda, Prof. Fred Walter, Prof. Michal Simon, Prof. Mike Zingale and Prof. Deane Peterson for their help, support and encouragement.

I especially thank my parents who supported me in the decision to take up graduate studies so far away from home. Most importantly I would like to thank my wonderful boyfriend David Franco for believing in me, his love and daily support.

# Chapter 1

# Introduction

Most stars are born embedded within giant molecular clouds as a member of an aggregation of a few hundred to about a million coeval stars. The majority of these "embedded stellar clusters" dissolve after the surrounding gas has been blown way and give rise to the stellar field population. The most dense Star Clusters (SCs) can survive, however, for a prolonged period of time and, once visible at optical wavelengths, can be observed at great distances, providing insights into star formation in a wide variety of galaxy types and environments. In my PhD thesis project I set out to determine the basic properties of luminous star clusters in a large sample of nearby Luminous Infrared Galaxies (LIRGs: $L_{IR} \geq 10^{11.4}$ $L_{\odot}$); many of these systems are ongoing mergers of gas-rich disk galaxies exhibiting high Star Formation Rates (SFRs), and hence are expected to host rich populations of star clusters. In this introductory chapter I provide an overview of the properties of SCs and LIRGs that are relevant to this work and describe the motivation, scientific goals and the extent of this thesis.

## 1.1 Young Massive Star Clusters

### 1.1.1 Scientific Motivation

Young Massive Clusters (YMCs) are dense aggregations of a few hundred to about a million coeval stars; they have ages of few Myr to 1 Gyr and are gravitationally bound at least at the time of their formation. The investigation of star clusters is closely connected to several fundamental research areas in astrophysics, most notably, the mechanisms of star formation and the process of galaxy formation and evolution.

Star clusters are, of course, interesting in their own right as fundamental building blocks of galaxies; physical processes involved in their formation and dynamical evolution are complex and not well understood. A realistic theoretical model has to take into account the effects of stellar evolution, external gravitational fields, and the rapidly varying gravitational potential in the early phases of cluster evolution (Clarke, 2010; Kruijssen et al., 2011). These types of numerical simulations are an active research area and have to be substantiated by observational results. The densest, most massive YMCs have properties (masses and sizes) expected of proto-globular clusters, and it has been suggested that old Globular Clusters (GC) are the end stage of YMC evolution (Schweizer, 1987; Ashman & Zepf, 1992). Thus YMCs provide insights into GC formation that was once thought to have taken place exclusively in the early Universe (Peebles & Dicke, 1968; Fall & Rees, 1985).

The formation of stars is inseparably linked to that of star clusters. Fragmentation of molecular clouds, a key process in star formation, also preferentially results in SC formation. According to estimates of Lada & Lada (2003) the total SFR in embedded clusters in the solar neighborhood ($\sim 3 \times 10^3$ $M_\odot$ $Myr^{-1}$ $kpc^{-2}$) is comparable to the total SFR of field stars in the Milky Way ($3 - 7 \times 10^3$ $M_\odot$ $Myr^{-1}$ $kpc^{-2}$), indicating that 50% – 100% of stars may form in a clustered mode. A large fraction (70% – 90%) of embedded clusters dissolve within a short ($< 10$ Myr) period of time as the removal of the natal gas causes all but the densest clusters to become un-bound; the member stars become part of the general field stellar population. During the subsequent evolution some clusters are destroyed as well by interactions with molecular clouds, tidal stripping by the gravitational field of their host galaxy or several other processes (e.g., Whitmore, 2009).

For relatively nearby, resolved clusters, the stellar population can be studied in detail. Since in most cases SCs can be considered Simple Stellar Populations (SSPs), meaning that the member stars of a cluster formed at the same time and have the same metallicity, SCs are uniquely suited to study stellar luminosity, mass functions and stellar evolution. Relatively high stellar densities in cluster cores facilitate interesting dynamical events, such as stellar collisions, binary formation and disruption, which in turn lead to the formation of exotic objects such as blue stragglers, X-ray binaries, radio pulsars etc. (Portegies Zwart et al., 2010).

Star clusters are useful tracers of the star formation history of their host galaxies. Some of the most massive SCs survive for prolonged periods of time and, being very luminous, can be readily identified and studied at great distances. Because temporal spectral evolution of clusters as SSP can be modeled by evolutionary population synthesis models, SCs are relatively easy to age-date from multi-band photometry or spectroscopy. SCs are especially useful for diagnosing intense episodes of star formation induced by mergers and other dynamical interactions. Cluster age statistics can isolate starburst events in time and trace the propagation of recent star formation across the full extent of galaxies, thus providing constraints to numerical simulations of merging galaxies (Chien et al., 2007; Chien, 2010; Chien & Barnes, 2010).

### 1.1.2 Demographics of Star Clusters

#### The Milky Way Galaxy

Clusters in the Milky Way Galaxy have been traditionally categorized into two distinct groups: globular clusters and open clusters.

The Milky Way Galaxy contains approximately 150 GCs. They have ages comparable to the age of the Universe ($\sim 12-13$ Gyr), are roughly spherical with $10^4-10^6$ member stars and have a mass range of $10^4$ $M_\odot$ to $10^6$ $M_\odot$. The metallicity distribution of GCs in the Galaxy is bimodal, with both peaks at subsolar values. The metal-poor clusters ([Fe/H]$\approx -1.5$) are associated with the Galactic Halo, and the more metal-rich clusters ([Fe/H]$\approx -0.5$) are associated with the bulge of the Galaxy; these two populations are believed to represent two episodes of cluster formation.

Open star clusters are comparably young, typically younger than 1 Gyr, have solar or above solar metallicities and are mainly found in the now metal enriched Galactic spiral

arms. They have almost no central concentration, contain a few tens to thousand of stars and have the mass range of $10^2$ $M_\odot$ – $10^4$ $M_\odot$.

A relatively recent discovery is the presence of YMCs in the Milky Way, star clusters in the mass range of globular clusters but with ages of open clusters. The nearest examples of YMCs in the solar neighborhood are Westerlund 1, Arches and Quintuplet clusters near the Galactic Center (Clark et al., 2005; Figer et al., 1999, 2002).

### The Local Group

The Large and Small Magellanic Clouds, our nearest extragalactic neighbors, contain a large number of SCs, both old GCs and YMCs. One of the most remarkable objects is the giant starburst region 30 Doradus with its central star cluster R136 in the Large Magellanic Cloud. The two other Local Group spirals, M31 and M33, host populations of young and old star clusters that appear to be roughly equivalent to the Milky Way open and globular clusters. Observations of resolved clusters in the Local Group make it possible to assess their stellar content, velocity dispersion and radial profiles (e.g., Goudfrooij et al., 2011b,a).

### Beyond the Local Group

Prior to the launch of the *Hubble Space Telescope* (*HST*), only a handful of barely resolved candidates for YMCs in nearby, star-forming galaxies were known. These observations include the starburst galaxy M82 (van den Bergh, 1971; O'Connell & Mangano, 1978), six unresolved bluish knots in the recent merger remnant NGC 7252 (Schweizer, 1982), interacting galaxy NGC 1569 (Arp & Sandage, 1985), the nuclear clusters of NGC 1705 (Melnick et al., 1985) and NGC 1140 (Gallagher & Hunter, 1987), ten barely resolved knots in merger NGC 3597 (Lutz, 1991) and the starburst NGC 1705 (Meurer et al., 1992).

The launch of the *Hubble Space Telescope* led to a revolution in the field of SC research, increasing greatly the number of detected SCs as well as the number of galaxies accessible to a detailed study of their SC populations. Cluster systems of hundreds to thousands of SCs were detected in merger remnants such as NGC 4038/9 (Whitmore & Schweizer, 1995), NGC 7252 (Whitmore et al., 1993) and NGC 3256 (Zepf et al., 1999), which allowed a statistical approach to the study of SC properties.

Young star clusters have now been observed in a wide variety of environments: normal spiral galaxies, starburst galaxies, dwarf and irregular galaxies, nuclear star bursts, tidal tails and most notably in merging and starburst galaxies, systems where vigorous star formation is occurring. An extensive compilation of SC observations can be found in Whitmore (2003) and Larsen (2006b) reviews, and here I will highlight only a few most interesting examples.

### Mergers / Interacting Galaxies

Interacting galaxies with high SFRs appear to host the richest populations of luminous and massive SCs, possibly due to high gas densities achieved during the merger.

One of the best-studied examples is the ongoing merger of NGC 4038/4039, "the Antennae" system. This pair of disk galaxies is one of the nearest ($z = 0.0055$, $D_{\rm L} = 24.3$ Mpc) and youngest examples in the Toomre Sequence (Toomre, 1977) of merging galaxies. Its rich SC population has been extensively studied in many wavelength regimes and has provided

valuable insights into properties, formation and evolution of SCs, e.g., NGC 4038/9 is one of the few galaxies where the cluster mass function (number of clusters as a function of stellar mass) has been determined (Zhang & Fall, 1999). The typical half-light radius of SCs in NGC 4038/9 is $\sim 4$ pc (Whitmore et al., 1999) and brightest clusters have $M_V \sim -15$ mag (Whitmore & Schweizer, 1995). The Antennae hosts a rich population of YMCs: very young clusters with ages $\leq 5$ Myr, slightly older clusters with ages $5 - 10$ Myr, a SC population of $\sim 100$ Myr, intermediate-age clusters ($\sim 500$ Myr) that probably formed during the initial encounter of the two galaxies, as well as old globular clusters originating from the progenitor galaxies (Whitmore et al., 1999). Zhang et al. (2001) examined the connection between star clusters (broken into three age groups) and properties of the interstellar medium by means of a two-point correlation function between the positions of star clusters and fluxes at various wavelengths (from X-rays to radio). The young embedded clusters (ages $\sim 5$ Myr) appeared to be more associated with long-wavelength radiation (mid-infrared and longer), while clusters with ages $\sim 10$ Myr or older were rather correlated with short-wavelength radiation (far-UV and X-ray). Autocorrelation functions of young star clusters exhibited a power-law behavior with slopes in the range $-0.8$ to $-1.0$ up to a distance of $\sim 1$ kpc, which indicates a "clustered" distribution of young star clusters. In a recent article Whitmore et al. (2010) find the cluster Luminosity Function (LF), down to the observational limit of $M_V \approx -7$ mag, and the mass function for clusters younger than $3 \times 10^8$ yrs to be essentially the same: a single power law with the indices $\alpha = -2.13$ and $\beta = -2.10$, respectively. Also, the LF for intermediate-age clusters ($\sim 100 - 300$ Myr) shows no bend or turn-over down to $M_V \approx -6$ mag.

The SC population in NGC 7252, a somewhat more advanced merger system than the Antennae, has ages between 650 Myr and 750 Myr (Miller et al., 1997) and contains one of the most massive clusters detected so far. Both, photometric and dynamical measurements of the cluster W3 have been used to derive a mass of $\sim 8 \times 10^7$ $M_\odot$ (Maraston et al., 2004). With a halflight radius of $\sim 17.5$ pc, this object is much larger than a normal star cluster, and may be more closely associated with the "Ultra Compact Dwarf Galaxies" (Hilker et al., 1999; Drinkwater et al., 2003).

Surace et al. (1998) examined a sample of nine Ultraluminous Infrared Galaxies (ULIRGs: $L_{IR} \geq 10^{12.0}$ $L_\odot$) imaged with the Wide Field Planetary Camera (WFPC2) onboard of the *HST*. The images revealed between 4 and 31 compact, blue knots of star formation per object. Several knots have $M_B > -15$ mag, corresponding to masses $10^5$ $M_\odot$ – $10^9$ $M_\odot$, and the estimated ages range from few $10^7$ to $1 \times 10^9$ yrs. Given the distance of these systems ($0.042 < z < 0.163$) and an average knot radius of $\sim 65$ pc, most of these star-formation knots are cluster associations, consisting of several unresolved clusters, rather than individual SCs. Despite the high luminosity of these star-formation knots they are not significant contributors to the extremely high bolometric luminosity of these galaxies, providing typically only about 2% of the bolometric luminosity of their host galaxy. Surace et al. (1998) concluded that any ultraluminous starburst should be much more luminous, massive, and dense than the identifed starbursts knots and is therefore likely to be very different from the starburst that is detected optically. As a follow up, near-infrared ground-based imaging of 30 ULIRGs was obtained. Surace & Sanders (1999) and Surace et al. (2000) found no new hidden embedded knots besides these previously observed optically. This led Surace & Sanders to conclude that that either there is no population of moderately embedded star-forming knots in these

galaxies or any additional knots are either extinguished by greater than $A_V = 25$ mag or are intrinsically less luminous than the optical knots.

### (Dwarf) Starburst Galaxies and Irregular Galaxies

Young star clusters are also found in many starburst galaxies, although in somewhat smaller numbers than in merging galaxies. The overall cluster properties are similar to those in mergers, with ages as young as few Myr (e.g., 4 – 6 Myr in NGC 4214, Leitherer et al. (1996); 2.5 Myr in NGC 5253, Calzetti et al. (1997)) and as massive as $10^5$ $M_\odot$ – $10^6$ $M_\odot$ (e.g., in NGC 253, Watson et al. (1996) and in NGC 1569, Hunter et al. (2000)). Meurer et al. (1995) performed an extensive study of nine starburst galaxies obtained with *HST* Faint Object Camera (FOC). All nine of the galaxies contained young SCs and on average, 20% of the total UV flux originates from the clusters. The LFs are approximated by a power law with index $\alpha \sim -2$.

Some of the starburst galaxies show evidence for interactions with other galaxies, e.g., the starburst in M82, a prototypical starburst dwarf galaxy, appears to have been triggered by a tidal interaction with its larger neighbor M81. The galaxy M82 has been long known to harbor several bright knots (van den Bergh, 1971), which were later confirmed by O'Connell et al. (1995) who found about 100 clusters in *HST*/WFPC images concentrated in the inner, relatively dust free 100 pc of the galaxy. Since M82 is viewed nearly edge-on and is heavily extinguished, the total number of young clusters is likely to be much higher. An example of a starburst unlikely to be triggered by an interaction is NGC 5253, which is quite isolated; its nearest neighbor, M83, is located at a distance of $\sim 600$ kpc (Harris et al., 2004).

A peculiar feature of some dwarf starburst galaxy cluster system's is a discontinuity in the luminosity function. For example, in NGC 1569 the two brightest clusters, NGC 1569-A and NGC 1569-B, are more than 2 magnitudes brighter than the next fainter one (O'Connell et al., 1994). This feature is even more prominent in NGC 1705 which has only a single bright cluster, and in NGC 4214 which exhibits a gap of $\sim 1.5$ mag from the brightest two clusters to the next fainter one (Billett et al., 2002).

### Spiral Galaxy Disks

Young SCs have also been found in the disks of quiescent, normal spiral galaxies similar to the Milky Way.

For example, Chandar et al. (1999a,b,c) have used *HST*/WFPC2 observations to study young compact clusters in M33. They found 44 SCs with ages $\sim 100$ Myr and masses in the range $6 \times 10^2$ $M_\odot$ to $2 \times 10^4$ $M_\odot$, which is below the typical masses of GCs. Thus, although young compact clusters appear to currently form in M33, they do not qualify as "super" star clusters seen in mergers / starburst galaxies.

In addition to containing a nuclear starburst, M83 is also known to host a rich population of young star clusters throughout the disk (Bohlin et al., 1990; Larsen & Richtler, 1999; Chandar et al., 2010b), the most massive of which have masses of several times $10^5$ $M_\odot$. An even more extreme cluster is in NGC 6946, with a dynamical mass estimate of about $1.7 \times 10^6$ $M_\odot$ (Larsen & Richtler, 2000).

A detailed ground-based study of young massive clusters in 21 nearby non-interacting

spiral galaxies, carried out by Larsen & Richtler (1999); Larsen (1999); Larsen & Richtler (2000), found rich SC populations in about half of the sample. The age distributions of SCs show no obvious peaks, indicating that massive clusters are formed as an ongoing process in the quiescent environment of these galaxies rather than in bursts. A follow-up study with *HST*/WFPC2 of six spiral galaxies (Larsen, 2002b) found LF power-law slopes of $-2.4 < \alpha < -2.0$.

**Nuclear Regions**

YMCs have been identified in several nuclear and circumnuclear starburst regions, often associated with barred spiral galaxies and arranged in spectacular ring-like structure. Maoz et al. (1996) studied 5 circumnuclear star-forming rings in large nearby galaxies (NGC 1079, NGC 1433, NGC 1512, NGC 2997, NGC 2548) using the *HST*/FOC and found that as much as 15% – 50% of the UV emission originates from compact, young star clusters. They estimated the masses of SCs up to about $10^5$ $M_\odot$ and the luminosity function was consistent with a power-law with slope $\alpha \sim -2$. Other examples of nuclear SCs include: the nuclear ring of NGC 1326, an early-type barred spiral in the Fornax cluster (Buta et al., 2000), NGC 253 with the brightest SC of $M_V \approx -15$ mag and an inferred mass in excess of $1.5 \times 10^6$ $M_\odot$ (Watson et al., 1996), M83 (Harris et al., 2001), NGC 1097 and NGC 6951 (Barth et al., 1995).

**Tidal Tails**

YMCs have been detected in tidal tails of several merging galaxies, although not all tidal tails contain SCs. In a sample of four mergers (NGC 3256, NGC 3921, NGC 4038/4039 and NGC 7252) Knierman et al. (2003) found a large number of SC in only one, the western tail of NGC 3256. The tails of NGC 7252 and NGC 3921 have small populations of SCs, and NGC 4038/9 appears to have essentially no clusters in the tails. A study of 17 tidal tails in 12 interacting galaxies was conducted by Mullan et al. (2011), SC candidates were detected in 10 tails. Other examples of systems containing SCs in tidal tails are NGC 5548 (Tyson et al., 1998) and Stephan's Quintet (NGC 7317, NGC7318A and B, NGC7 319, NGC 7320) (Gallagher et al., 2000).

Young SCs are observed in a variety of different environments where active SF is present. The properties of the YMCs appear to be similar, e.g., the luminosity function is approximated by a power-law with the index $\alpha \sim -2$. The number of clusters and the magnitudes of the brightest clusters seem to scale with the SFR of the host galaxy (Whitmore, 2003; Larsen, 2002a; Bastian, 2008). The finding that all star forming galaxies appear capable of making YMCs suggests that no special conditions are required to produce clusters, the underlying physics of the cluster formation mechanism is largely the same, and the size-of-sample effect is responsible for the large number and high luminosity of SCs in mergers and starburst galaxies.

### 1.1.3 Brief Review of Star Cluster Properties

The amount of recent progress in SC research is extensive, and thus cannot be properly covered in this introduction. The field of SC research encompasses theoretical models and numerical simulation of cluster and star formation, cluster evolution and destruction, observations of resolved clusters in the Local Group and large populations of unresolved clusters in distant galaxies. A recent series of publication in the "Philosophical Transactions of the Royal Society" provides a good overview of the current status of research in the SC field (Larsen, 2010; Lada, 2010; de Grijs, 2010; Portegies Zwart et al., 2010; Bruzual, 2010; Clarke, 2010). Here I review key properties most relevant to this work.

#### Cluster Formation and Evolution

Star cluster formation and evolution are a subject of considerable investigation efforts and significant debate. The underlying physical processes of star and cluster formation in Giant Molecular Clouds (GMCs) are not well understood. Progress in the field of SC dynamical evolution is hampered by absence of large samples with reliable age estimates, in particular in galaxies with high SFRs.

*Cluster Formation*

Star clusters form within giant molecular clouds in massive, dense structures or cores inside GMCs. The massive dense cores are gravitationally unstable; this leads to further fragmentation, then to the collapse and formation of protostellar seeds which grow by accreting surrounding dense gas and become protostars. The exact physical processes that lead to the formation of dense cores, the fragmentation and collapse are not well understood. This scenario is supported by observations at infrared wavelengths of star forming regions and heavily obscured star clusters. For a review of embedded star clusters see Lada & Lada (2003) and Lada (2010).

Since SC formation is closely associated with GMCs, the SC distribution is expected to reflect the spatial distribution of the parent GMCs. The structure of GMCs is self-similar (also referred to as scale-free, hierarchical or fractal) on a wide range of scales. Individual protostellar cores can be grouped into cluster-forming clumps, GMCs are themselves part of a larger hierarchy of structure in the interstellar medium and tend to be organized into giant molecular complexes, which are located along the spiral arms in spiral galaxies. Thus, the spatial distribution of the young SC population is expected to show the same amount of hierarchy as the fractal medium from which they formed (Elmegreen, 2008, 2011), which agrees with findings by Zhang et al. (2001) and Scheepmaker et al. (2009).

Star cluster formation appears to be particularly efficient during violent star-forming episodes triggered by galaxy collisions and close encounters. de Grijs (2004) go as far as naming SC formation "a major or even dominant mode of star formation in violent starburst events". While low-mass clusters trace star formation quite universally, the more long-lived, massive clusters seem to form preferentially in the context of violent star formation. The reason for this is likely related to the higher gas densities and pressures achieved during a merger. In addition to the increased frequency of molecular cloud collisions in interacting galaxies, molecular clouds get shock-compressed by external pressure allowing them to grow

denser and more massive; both factors considerably enhance star formation (e.g., Jog & Solomon, 1992; Barnes, 2004; Ashman & Zepf, 2001).

Current numerical merger simulations rely on two different star formation mechanisms: the "density-dependent" (e.g., Schmidt, 1959; Kennicutt, 1998) and the "shock-induced" (e.g., Scoville et al., 1986; Jog & Solomon, 1992). The two star formation prescriptions differ in their predictions of the timing of the onset of SF during the merger and of the spatial distribution of star-forming regions.

The "density-dependent" numerical simulations (e.g., Mihos & Hernquist, 1994, 1996), that parametrize the SFR as a function of the local gas density (Schmidt law), predict that most SF is strongly concentrated toward the central region of the merger remnant since the process of rapid gas funneling to the central region reduces the supply of gas needed to produce SF elsewhere. These simulations can explain the central starburst observed in the (Ultra-) Luminous Infrared Galaxies, however, they underestimate large-scale SF that is observed in many galaxy mergers. For example, according to Barnes (2004), the density-dependent models for NGC 4676 ("The Mice") predict a moderate increase in SF delayed until after the 1st apocenter as galaxies fall towards each other, followed by a strong nuclear SB when the galaxies finally merge.

The "shock-induced" SF models (Barnes, 2004), that consider SF triggered by shocks, predict a wider spread, spatially-extended bursts of star formation. Shock-induced SF models respond promptly to external disturbances, while in density-dependent models the SF activity is delayed until sufficient gas density has build up. The larger spatial extent of SF in shock-induced models is, in part, a consequence of the earlier onset of activity in such models, since the gas is more widely distributed at earlier times. For example, in the shock-induced model of NGC 4676 (Barnes, 2004) a first sharp burst of star formation occurs at the 1st pericenter as the disks interpenetrate. A second rise in the SFR follows during the apocenter when galaxies are flying apart, but the amplitude of this SB depends on the geometry of the encounter (Chien, 2010, Figure 1). The 2nd pericenter produces another SB, and the final SB occurs as galaxies merge, this last SB is concentrated within the nuclear region.

In both merger simulation models the timing and strength of SB episodes during the merger process are strongly depend on the properties of progenitor galaxies (mass ratio, amount of gas, bulge/disk ratio (Mihos & Hernquist, 1996)) and the geometry of the encounter (inclination, prograde vrs retrograde collisions).

The "density-dependent" and "shock-induced" models predict significantly different star formation histories and distributions in merging galaxies, thus a study of the spatial distribution of SCs with known ages should be able to discern between these two models.

*Cluster Disruption*

The evolution of a SC is divided into two main phases (*i*) "infant mortality" followed by (*ii*) secular evolution.

Upon formation, new stars will immediately begin to disrupt their surrounding gaseous environments, terminating SF and initiating the first phase of cluster's dynamical evolution. Gas is expelled from the cluster through outflows, ionizing radiation and winds from massive stars, with radiation pressure from massive stars as the dominant gas-evacuation mechanism (Krumholz & Matzner, 2009) and later (after several Myr) supernovae explosions. As the cluster loses mass, stars in the cluster find themselves in a gravitational potential well that

suddenly becomes shallower. The important point is that the removal of mass happens on a timescale shorter than the crossing timescale of stars in the cluster (Goodwin, 1997). Therefore, stars cannot immediately adapt to the lower potential (they need a few crossing times to do this) and many stars will have a velocity higher than the one dictated by virial equilibrium. As a result the cluster will expand, a certain fraction of stars will leave the cluster and, if enough mass is lost, the cluster will become unbound. The embedded phase with high dust extinction lasts only a few Myr (e.g., Larsen, 2010) and ends with the cluster emerging from the enshrouding gas cloud, becoming optically visible but possibly an unbound system. The "infant mortality" phase duration is about 10 – 30 Myr. The main factor that determines the survival of a cluster is the Star Formation Efficiency (SFE). SFE is defined as the mass fraction of the giant molecular cloud that is turned into stars; a comparison of the stellar content of embedded clusters with the mass of their surrounding cores yields star-formation efficiencies of typically between 10% and 30% (Lada & Lada, 2003). If a cluster's SFE is less than about 30%, independent of the mass of the cluster, the cluster is likely to become unbound (de Grijs & Parmentier, 2007).

If the SC survives the first phase of "infant mortality", the gas-free star-depleted cluster is back into viral equilibrium within about 50 Myr and enters the "secular evolution" phase. The combined internal effects (mass loss through stellar evolution, internal 2-body relaxation) and external effects (interactions with the tidal field associated with the underlying galactic gravitational potential, external shocks such as encounters with spiral arms, GMC or GC on eccentric orbits, passages through the galactic disk or near the bulge) lead to tidal stripping and evaporation of a fraction of the low-mass stars, thus resulting in the gradual dissolution of the star cluster.

Two different schools of thought concerning the SC evolution after the first $\sim 10$ Myr currently exist: the mass-dependent approach from the "Utrecht group" and mass-independent from the "Baltimore group" (Lamers, 2009). The scenario of the "Baltimore group" or the "Universal" model is largely based on observations of cluster masses and age distributions in NGC 4038/9 (Fall et al., 2005, 2009; Whitmore et al., 2007, 2010), SMC and LMC (Chandar et al., 2006, 2010a) and M83 (Chandar et al., 2010b). According to this model, internal processes (e.g., infant mortality, 2-body relaxation) dominate the cluster disruption and hence are relatively universal. The disruption rate does not depend on cluster mass and roughly 80% – 90% of all remaining clusters are destroyed during each decade in age. The resulting (mass-limited) age distribution is observed to decline inversely with time as $dN/dt \propto t^{-1}$. The "Utrecht group" or "Environment Dependent" model (Boutloukos & Lamers, 2003; Gieles et al., 2006c; Lamers et al., 2005b,a; Larsen, 2006a; Bastian et al., 2011), based on age and mass distributions of luminosity-limited cluster samples in different galaxies (SMC, M51, M33, M83), proposes that the dominant processes are environmental (e.g., tidal shear, GMC interactions), and hence vary dramatically for each galaxy. In this model, the disruption is mass-dependent and the dissolution time follows a simple scaling relation with cluster mass and environment. It appears that in some galaxies, e.g., LMC, the disruption is less efficient and clusters live longer, and in other galaxies, e.g., M51, the disruption time scale is shorter. Observations can be interpreted following both models, taking into account factors such as incompleteness, evolutionary fading and variation in SFR.

**Deriving Cluster Ages: Evolutionary Population Synthesis Models**

Ages of star clusters can be estimated using a variety of different techniques.

The most accurate method of determing ages is to obtain high resolution high S/N spectroscopy of individual SCs in order to compare the age- and metallicity-sensitive spectral features with the appropriate modeled spectra. However, this approach is very time-consuming, and can be applied only to a limited number of bright clusters in a small number of galaxies. Another shortcoming of this method is a strong bias towards the youngest and most massive objects in spectroscopic cluster samples.

For a young cluster population, imaging H$\alpha$ emission in a narrow-band filter can be used to provide an age constraint. The presence of H$\alpha$ emission itself indicates that a cluster is younger than 10 Myr, since the O and B stars required to ionize the gas only live for this long and the size of the H$\alpha$ ring around a cluster can give an age estimate.

The most widely used method is photometric: it involves obtaining photometry of clusters in several filters and comparing the observed magnitudes and colors with those predicted by evolutionary population synthesis models. A clear advantage of this method is the efficient age-dating of large samples of SCs.

The underlying assumption of evolutionary population synthesis models is to regard star clusters as simple stellar populations: a SC is composed of stars which formed within a short time ($< 10^5$ yrs), and individual stars have the same initial chemical composition. SSPs can be modeled theoretically relatively easily, and their temporal evolution can be calculated accurately. Three basic ingredients are necessary for evolutionary population synthesis models: stellar evolutionary tracks, stellar atmosphere models or observed spectral libraries and the Initial Mass Function (IMF) that specifies the original distribution of stellar masses (e.g., Salpeter, 1955; Miller & Scalo, 1979; Kroupa et al., 1993; Chabrier, 2003). A set of stellar evolutionary tracks describes the evolution in time on the Hertzsprung – Russell diagram of stars of different mass and metal content. At each time step isochrones in the theoretical Hertzsprung – Russell diagram are computed using isochrone synthesis. The number of stars at each position along the isochrone is obtained from the assumed stellar IMF. Spectra of individual stars (from stellar atmosphere models or observed spectral libraries) are summed up to give a model grid of integrated spectra as a function of the age of the stellar population and its metallicity. By convolving the integrated spectra with filter response functions, artificial magnitudes and colors are synthesized, which can be compared with observed magnitudes and colors.

Many evolutionary population synthesis models are available today, (e.g., Leitherer et al., 1999; Bruzual & Charlot, 2003; Anders et al., 2003; Maraston, 2005). Most of these models have a different treatment of the Red Giant Branch (RGB) and Asymptotic Giant Branch (AGB) phases, resulting in large differences in the model output (such as intrinsic color) at certain ages where these phases become important (e.g., between 200 Myr and 1 Gyr for the AGB phase and between 1 – 2 Gyr when the RGB develops). SC ages in this thesis were estimated using Bruzual – Charlot evolutionary population synthesis models (Bruzual & Charlot, 2003) under the assumption of an instantaneous starburst with solar metallicity and a Salpeter IMF. The isochrone synthesis code of Bruzual & Charlot (2003) computes the spectral evolution of a stellar population based on Padova 1994 stellar evolution prescription and STELIB, a library of observed stellar spectra. The output of the model

(spectral energy distribution) was convolved with the ACS F435W and F814W filter response functions in order to obtain magnitudes and colors in these filters, and scaled with the mass of a cluster. Since photometric measurements in only two filters are available, the color-magnitude diagrams suffer from color-age and extinction-age degeneracies. A more detailed discussion of my approach to SC age-dating can be found in Chapter 3.3.5.

Photometric measurement in several filters make the age estimates more precise and provide independent means of solving for the age and the reddening caused by dust extinction. For example, Whitmore et al. (1999) use UBVI photometry to derive reddening-free Q parameters and to determine ages for the clusters in NGC 4038/9. According to Alvensleben (2004), in order to recover ages, metallicities and extinctions for YMCs, a long wavelength basis from U band through NIR is necessary and the availability of U band photometry is crucial, whereas one NIR-band J, H, or K is important for determination of cluster metallicities.

**Luminosity Function**

The Luminosity Function (LF) is a relatively easy to determine and thus widely used parameter to describe SC populations. The luminosity function is defined as the number of clusters per unit luminosity ($dN/dL$). Essentially all studies of the LFs of young clusters have found them to be well approximated by a power-law distribution:

$$N(L)dL \propto L^{\alpha}dL$$

with values of the exponent $\alpha$ in the range of $-1.7$ to $-2.4$ (Larsen, 2002b; Whitmore, 2003) and $\alpha \sim -2$ index as general consensus (Portegies Zwart et al., 2010). There is a hint that the LF tends to be slightly steeper at the bright end (Whitmore et al., 1999; Larsen, 2002b; Gieles et al., 2006a), although the evidence is not conclusive and a recent Whitmore et al. (2010) article finds no steepening in the LF in NGC 4038/9, contrary to Whitmore et al. (1999). The measurements of LF indices are complicated by incompleteness and contamination effects that can be difficult to fully control.

The LF indirectly provides information about the underlying cluster Mass Function (MF), the number of clusters per mass interval, although practical implementation is not straightforward since the LF of a cluster population consists of clusters with different ages, masses and metallicities. Since the mass-to-light ratios are strongly age-dependent, an accurate determination of cluster masses requires reliable age information for each individual cluster. In order to construct a cluster MF, it is necessary to accurately age-date large numbers of clusters.

So far, MFs have only been constrained for a few well-studied systems. In general, the cluster MF can be approximated by a power-law relation:

$$N(M)dM \propto M^{\beta}dM$$

In NGC 4038/9, Zhang & Fall (1999) found the power-law exponent $\beta \sim -2$ over the mass range $10^4$ $M_{\odot}$ to $10^6$ $M_{\odot}$, similar to the MF of young LMC clusters. Bik et al. (2003) find $\beta = -2.1$ over the range $10^3$ $M_{\odot}$ to $10^5$ $M_{\odot}$ for M51, and de Grijs et al. (2003) find $\beta = -2.04$ and $\beta = -1.96$ in NGC 3310 and NGC 6745. Other studies have found possible evidence

for a truncation of this power law at the high-mass end (Gieles et al., 2006b; Bastian, 2008; Larsen, 2009). Even if LF and MF appear similar, it is important to recognize that they are not the same and their similarity leads to important conclusions about cluster formation and evolution. According to Fall (2006), LF is a power law with the same exponent as MF because the MF is a power law and is statistically independent of the age distribution of SCs, i.e. clusters form with $dN(M)/dM \propto M^{-2}$ and are then disrupted during the "infant mortality" phase at a rate independent of the mass of the cluster.

The LF of old GCs is remarkably different from the LF of YMCs. The GC LF is a Gaussian distribution with a peak (or "turn-over") at a magnitude of $M_V = -7.4$ mag, and a standard deviation $\sigma_V$ of 1.2 – 1.4 mag (e.g., Harris, 1991; Harris et al., 2001). The shape and the turn-over magnitude of GC LF is universal among galaxies and shows only a weak dependence on the size, the morphological type, the metallicity and the environment of the host galaxy (Harris, 1999; Whitmore et al., 2002).

The key issue of the proposed evolutionary connection between the old GCs and YMCs is whether the power-law cluster LF of YMCs will evolve into a bell shape similar to the LF of old GCs. Fall & Zhang (2001) suggest that the dynamical evolution of the cluster system, which makes the fainter, less massive clusters disrupt more quickly, will transform an initial power-law mass distribution into the bell-shaped MF seen in old GC systems.

Since the power-law LF and MF have no characteristic scale, there is no meaningful physical division between low-mass open clusters and higher-mass "super" clusters. Thus it appears that there is no fundamental difference between the physical processes behind formation of clusters of various masses. Another property following from the $\alpha = -2$ power law LF is that the luminosity of the most luminous cluster, $L_{max}$, increases linearly with the total number of clusters, $N_{cl}$, and is determined by sampling statistics (Whitmore, 2003; Larsen, 2002b). A similar scaling between $L_{max}$ and the SFR was found by Weidner et al. (2004) and Bastian (2008). With the brightest clusters simply forming the tail of a continuous distribution, no special physical conditions are needed to form "super" clusters.

### Specific Frequency and Specific Luminosity

Specific frequency and specific luminosity are two relatively easily measured quantities that are correlated with the richness of a cluster population within a galaxy. They were first defined for old GC populations by Harris & van den Bergh (1981) and Harris (1991).

Specific frequency $S_N$ is a function of the number of clusters and the luminosity of the galaxy

$$S_N = N_{cl} \times 10^{0.4(M_V+15)}$$

(Harris & van den Bergh, 1981), where $N_{cl}$ is the total number of globular clusters and $M_V$ is the absolute visual magnitude of the galaxy. Because the shape of the GC LF is well approximated by a Gaussian distribution, $N_{cl}$ may be estimated with reasonable accuracy even if the faintest clusters cannot be directly observed.

Specific luminosity $S_L$ is a measure of the percentage of flux contributed by clusters

$$S_L = 100 \times \frac{L_{\rm clusters}}{L_{\rm galaxy}}$$

(Harris, 1991), where $L_{\rm clusters}$ is the total luminosity of GCs in a galaxy and $L_{\rm galaxy}$ the total luminosity of the galaxy itself. The effects of incompleteness at the faint end of the luminosity distribution are minimal; for a Gaussian shaped LF, 90% of the light originates from clusters brighter than the peak of the LF. The advantage of specific luminosity over specific frequency is that specific luminosity is independent of the distance modulus and reddening effects.

Elliptical galaxies have much higher specific frequency values ($S_N \sim 2-6$) (Harris, 1991; Elmegreen, 1999) of old GCs than spiral galaxies ($S_N < 1$). Schweizer (1987) and Ashman & Zepf (1992) suggest that a large number of SCs form during a merger of two gas-rich disk galaxies that will produce high $S_N$ values in the resultant elliptical merger remnant.

Unlike old GCs that have a Gaussian luminosity distribution and therefore a well defined total number of clusters, young clusters have an exponential distribution, and the number of clusters counted in a galaxy depends on the detection limit of the data. Larsen & Richtler (1999) define $T_N$, a quantity equivalent to specific frequency $S_N$, for young clusters

$$T_N = N_{cl} \times 10^{0.4(M_B+15)}$$

where $M_B$ is the B-band absolute magnitude and $N_{cl}$ is the number of young clusters above a certain limiting magnitude.

The specific luminosity $T_L$ is defined accordingly

$$T_L = 100 \times \frac{L_{\rm clusters}}{L_{\rm galaxy}}$$

(Larsen & Richtler, 2000), where $L_{\rm clusters}$ is the total luminosity of young clusters and $L_{\rm galaxy}$ the total luminosity of the galaxy.

As in the case of GCs, the specific luminosity of YMCs is independent of the distance modulus and is also relatively insensitive to incompleteness at the faint end of cluster luminosity distribution.

Larsen & Richtler (2000) found a relation between specific luminosity $T_L$(U) and the SFR per unit area, $\Sigma_{SFR}$, for YMCs in a sample of 21 nearby non-interacting spiral galaxies. $T_L$(U), which is a proxy for cluster formation efficiency, increases steadily with $\Sigma_{SFR}$ and led Larsen & Richtler (2000) to conclude that "The cluster formation efficiency seems to depend on the SFR in a continuous way, rather than being related to any particularly violent mode of star formation".

## 1.2 Luminous Infrared Galaxies

A large population of "infrared galaxies", in which the infrared emission dominates the optical emission, was discovered in the 1980s after an all-sky survey was conducted by the *Infrared All-sky Satellite* (*IRAS*; Neugebauer et al., 1984). Luminous Infrared Galaxies were defined to be infrared galaxies with $L_{\rm IR}[8-1000\mu{\rm m}] \geq 10^{11}$ L$_\odot$, with Ultraluminous Infrared Galaxies ($L_{\rm IR}[8-1000\mu{\rm m}] \geq 10^{12}$ L$_\odot$) constituting the high luminosity end of the LIRG population. The bulk of the objects discussed in this dissertation are LIRGs, and I will refer to both LIRGs and ULIRGs, collectively as LIRGs.

Luminous Infrared Galaxies play an important role in the star formation history of the Universe. The space density of LIRGs was much higher in the past and exceeded the density of optically selected galaxies (Sanders et al., 2004). LIRGs are major contributors to the Cosmic Infrared Background and a large fraction of present-day stars were formed in LIRGs (Elbaz et al., 2005; Le Floc'h et al., 2005).

Luminous Infrared Galaxies emit most of their bolometric luminosity (up to 90%) in the far-infrared. The origin of the strong IR emission is dust heated by intense star formation and / or an Active Galactic Nucleus (AGN), although the relative fraction of SF/AGN contribution is difficult to disentangle. Studies of LIRGs in the local universe have found that a large fraction are merging and interacting systems (e.g., Kim et al., 2002). Numerical simulations have shown that the merger process is responsible for tidal dissipation that drives material from gas-rich progenitor galaxy disks towards the nucleus, fueling an intense burst of star formation and/or an AGN (Mihos & Hernquist, 1994, 1996; Barnes & Hernquist, 1996; Barnes, 2004).

IR galaxies show systematic trends as a function of total far-infrared luminosity; more luminous systems are more likely to appear to be merger remnants or interacting pairs, and the percentage of LIRGs with AGN-like nuclear spectra increases systematically with increasing infrared luminosity (Kim et al., 1995, 2002). ULIRGs, at the high luminosity end of the LIRG population, exhibit many features such as emission line diagnostics and dominant unresolved nuclear power sources that suggest an AGN is the dominant contributor to their total energy output. On the other hand, the majority of LIRGs show signatures of ongoing star formation such as enormous molecular disks, reddened blue continua, strong absorption features of young stars in near-IR spectra and mid-IR emission lines diagnostic diagrams consistent with SF, and appear to be predominantly powered by a starburst (Genzel et al., 1998; Petric et al., 2011). AGN activity and starburst activity often occur at the same time since nuclear concentrations of molecular gas can feed a starburst as well as a massive central black hole, thus explaining a connection between AGN activity and co-evolution of black holes and stellar bulges (Magorrian et al., 1998; Ferrarese & Merritt, 2000; Gebhardt et al., 2000).

Local LIRGs are unique laboratories for studying intense SF, offering insights into its physical properties as well as processes that trigger star formation and its link to galaxy mergers. Additionally, LIRGs are thought to be local counterparts of high-redshift sub-millimeter galaxies observed with SCUBA (Smail et al., 1999; Barger et al., 1999), which are regarded to be major contributors to high-redshift star formation. Thus, LIRGs may provide insight into high-redshift star formation and serve as a test-bed for the viability of various star formation tracers (i.e., PAH, UV and radio luminosities); these correlations, if successful, can be applied to dusty star-forming galaxies at cosmological distances.

### 1.2.1 GOALS

Luminous Infrared Galaxies contain large quantities of dust that is responsible for re-processing the UV radiation from SB and/or AGN and conceals the true nature of the power source. Hence, a multi-wavelength approach to studying these galaxies is the best manner in which to gain insight into the physical processes in these highly dust enshrouded systems.

The Great Observatories All-sky LIRG Survey (GOALS; Armus et al., 2009) probes local

LIRGS at multiple wavelengths, combining data from *Chandra*, *GALEX*, *HST*, *Spitzer*, the VLA and ground-based optical imaging and spectroscopy.

The GOALS sample was drawn from the *IRAS* Revised Bright Galaxy Sample (RBGS; Sanders et al., 2003). The RBGS is a complete sample of extragalactic objects with 60$\mu$m flux densities above 5.24 Jy, covering the entire sky surveyed by *IRAS* at Galactic latitudes $|b| > 5°$. RBGS contains 629 objects out to a maximum redshift of $z = 0.088$ (median $z = 0.008$), among them 181 LIRGs and 21 ULIRGs. These 202 objects with $L_{\rm IR} \geq 10^{11}$ L$_\odot$ constitute the GOALS sample. The galaxies in the GOALS sample span the full range of nuclear spectral types (Type-1 and Type-2 Seyfert, LINERs, and starbursts) and interaction stages (major mergers, minor mergers, and isolated galaxies). The size of the sample and the proximity of the objects, combined with the broad wavelength coverage, allow a study of their physical processes in great detail. In particular, the GOALS survey is intended to assess the nature of star formation and AGN activity as a function of merger stage, luminosity and optical depth.

## 1.3 Thesis Objectives

As outlined in Chapter 1.2, Luminous Infrared Galaxies are natural laboratories for studying intense star formation and related processes. Due to the high SFRs of LIRGs, they are expected to host particularly rich and luminous populations of star clusters.

Eighty-seven LIRGs with $L_{\rm IR} \geq 10^{11.4}$ L$_\odot$ in the GOALS sample were imaged with the *Hubble Space Telescope* Advanced Camera for Surveys (ACS) Wide Field Channel (WPC) at 0.4$\mu$m (F435W) and 0.9$\mu$m (F814W). The completeness of the survey, combined with the high resolution ($\sim$ 0.1") and large field of view (3.4' $\times$ 3.4') of the *HST*/ACS images makes the HST GOALS data set the best sample for studying optically-visible luminous star clusters in luminous starburst galaxies.

At the distance of these systems ($0.009 < z < 0.088$), SCs are unresolved and are visible as point-like luminous sources within their underlying host galaxies. Accordingly, the focus of this PhD thesis is the determination of the collective properties of unresolved SC populations such as young cluster specific frequency, specific luminosity, the cluster luminosity function and cluster ages.

The current work represents the largest sample of galaxies for which the properties of SC populations have been determined in a uniform fashion, and it significantly enlarges the number of galaxies, in particular in the high SFR range, studied in this manner. The size of the sample allows an identification of possible trends of SC properties with merger stage, SFR and nuclear activity type.

The availability of GOALS multi-wavelength data makes it possible, for a limited number of most cluster-rich and near-by galaxies, to assess the connection of optically visible young SCs with star formation indicators across the spectrum. Tracing the spatial distribution of star-forming regions at different wavelengths sheds light on the issue of whether the optical star formation as traced by clusters is just the optically visible components of embedded star-forming regions.

A comparison of SC properties in LIRGs with SC systems found in nearby lower luminosity galaxies permits an assessment whether star and cluster formation in the violent

environments of luminous galaxy mergers is fundamentally different than in quiescent galaxies.
To summarize, the objectives of this PhD thesis are to:

*(i)* determine collective properties of star clusters such as young cluster specific frequency $T_N$, specific luminosity $T_L$, the cluster luminosity function, ages and spatial distribution

*(ii)* investigate how the derived cluster properties relate to host galaxy properties such as the merger stage, SFR and nuclear activity type

*(iii)* correlate the spatial distribution of star clusters and star formation tracers such as UV and mid-IR emission

*(iv)* compare properties of star clusters found in LIRGs with studies in other systems.

This dissertation is organized as follows: Chapter 1 is the Introduction, Chapter 2 describes the data reduction and the cluster detection algorithm, Chapter 3 presents the analysis of the cluster-rich sample of 15 LIRGs, Chapter 4 extends the analysis to the complete 87 HST-GOALS LIRGs and Chapter 5 provides a summary.

# Chapter 2

# Observations, Data Reduction and Cluster Detection Procedure

## 2.1 Observations

*Hubble Space Telescope* observations of a complete sample of 87 GOALS LIRGs with $L_{\rm IR} > 10^{11.4}$ $L_{\odot}$ (PID #10592, "An ACS Survey of a Complete Sample of Luminous Infrared Galaxies in the Local Universe", PI A. Evans) were obtained during a 2005 – 2006 (HST Cycle 14) campaign. The galaxies were imaged with the Advanced Camera for Surveys (ACS) Wide Field Channel (WFC). The large field of view of the WFC ($202''\times 202''$) allows the extended tidal features and galaxy pairs to be imaged at high resolution of $\sim 0.1''$. One galaxy was observed per orbit in the ACCUM mode with three 420 sec integrations in F435W filter and two 360 sec integrations in F814W filter using the LINE dither pattern. The observations are summarized in Table 2.1.

## 2.2 Data Reduction

The data products available from the Multimission Archive at STScI (MAST) were initially reduced using the standard STScI calibration pipeline that removes instrumental signatures, subtracts a dark image, performs flat-fielding, removes cosmic rays when combining associated images, removes geometric distortion and calibrates the images. Due to the small number of exposures, the cosmic ray removal in the standard STScI pipeline was ineffective; a significant number of cosmic ray-affected pixels remained. The visible bias level offsets between the four quadrants of the images presented an additional concern.
In order to address these issues following steps were taken:
1) The reprocessing began with the FLT files downloaded from the *HST* archive. The FLT files are the dark image subtracted, flat-fielded, calibrated individual exposures that are the end product of the CALACS package of the STScI pipeline.
2) As a first step to removing cosmic rays, the routine lacos_im (van Dokkum, 2001) was executed on the FLT files. This algorithm uses the Laplacian edge detection method to identify cosmic rays due to the sharpness of their edges. The routine is more effective on non-drizzled images, since drizzling smooths the edges. Pixels adjacent to cosmic rays were also flagged in order to remove residual halos. All the flagged pixels were replaced with a median value calculated in a $10 \times 10$ pixel box surrounding the flagged pixel.

3) In order to remove bias level offsets between the four quadrants of an image, the sky was estimated and subtracted separately for each quadrant.
4) The reprocessed individual exposure files were then passed on to the MULTIDRIZZLE task (Koekemoer et al., 2002; Fruchter & Hook, 2002) in the PyRAF/STSDAS package that removes geometric distortion and combines the dithered individual exposures into a final calibrated image. The same set of parameters as in the STScI pipeline was used, except no sky subtraction was performed (see step 3).
5) Further cosmic ray removal was performed with the jcrrej2.cl task for IRAF as described in Rhoads (2000). This routine convolves the image with a spatial filter consisting of a Gaussian (approximating the point spread function) minus a delta function. Strongly negative pixels in the convolved image are flagged as cosmic ray hits. The few remaining cosmic rays were removed by eye using imedit in IRAF.
6) As the final step, the *HST* images were rotated such that North is up and East left, F435W and F814W images aligned, and the 2MASS catalogue positions of several bright stars in each LIRG field were used to apply WCS corrections to each image. The typical WCS correction was about $1''$ and the resultant average astrometric precision is $0.1''$.

## 2.3 Cluster Detection Procedure

### 2.3.1 Detection

The detection of star clusters was performed on images prior to rotation (before step 6 in Chapter 2.2) in order to eliminate possible effects of rotation on counts in pixels and thus on photometry.

Due to the large FOV of the ACS, the images cover not only the entire galaxy and its extended features, but also contain a good deal of foreground stars and background galaxies. The foreground stars are used to create a PSF model, make precise WCS corrections and to determine the expected percentage of contamination of foreground stars to the number of detected clusters.

The large FOV makes it also a necessary first step to mask the portion of the image over which the galaxy subtends and the cluster detection will be performed. Masks were created to outline the galaxy to $\sim 24.5$ mag/arcsec$^2$ surface brightness in the F814W images. This is approximately the surface brightness level that can be traced "by eye" and encloses essentially all of the visible galaxy features.

Masks were created by first median smoothing the F814W image using a $40 \times 40$ pixel box (in order to remove small-scale features), and then by boxcar smoothing with a $50 \times 50$ pixel box. The IRAF routine IMREPLACE was used to set pixel values below the chosen cut-off to 0 (i.e., the sky portion of the image) and above to 1 (the galaxy). The few remaining bright stars outside of the galaxy were removed by hand with IRAF IMEDIT. The mask image was then multiplied by the science image, leaving only the galaxy area above 0. For each galaxy, the F814W mask was applied to both the F435W and F814W science images.

Once the masks were applied, the routine Source Extractor (Bertin & Arnouts, 1996) was executed to identify potential clusters in each image. The parameters for SExtractor were set rather generously in order to find as many candidate sources as possible. Source Extractor

was also used to fit and subtract the non-uniform background, i.e. the underlying galaxy, for SC photometry. Weight maps created by MultiDrizzle were also used for detection purposes.

All sources detected with SExtractor were passed on to IDL routines to apply a set of selection criteria. To be deemed viable, a cluster candidate had to *(i)* be detected in both F435W and F814W filters *(ii)* have full width at half the maximum intensity, FWHM, in the range of $1.7 - 4$ pixels and *(iii)* have a signal-to-noise, S/N, greater than 5.

Centroids of the SExtractor positions were computed with the IDL procedure CNTRD. The FWHM of each candidate was calculated with the procedure RADPROF that fits a Gaussian in a $5 \times 5$ pixel box. While the objects with high S/N have FWHM of about $2 - 3$ pixels, the FWHM of low S/N objects exhibit a lot of scatter. The range of FWHM between 1.7 and 4 includes also faint sources that appear point-like while excluding fuzzy extended sources.

An example of the detected clusters is shown in Figure 2.1. The left panel shows the original F435W image. In the right panel, the underlying galaxy is subtracted and clusters are marked with circles. The images were inspected by eye to ensure that the detected sources were indeed point-like and located within the galaxy. Obvious stars and galaxy nuclei were removed.

### 2.3.2 Cluster and Galaxy Photometry

Accurate cluster photometry is complicated by the non-uniform light distribution of the underlying galaxy. Source Extractor was used to map and subtract the background (i.e., the underlying galaxy) by computing a bi-cubic-spline interpolation over background values estimated in a $9 \times 9$ pixel grid. The mesh size was chosen to be large enough not to be affected by clusters but small enough to reproduce the small scale variations of the underlying galaxy. Such a mesh size did an efficient job of removing the galaxy and minimizing the creation of holes surrounding clusters during the extraction. In order to minimize the flux contribution from clusters to the galaxy map, detected clusters were masked out before fitting the background with SExtractor.

Cluster photometry was performed with the IDL routine APER in a $0.3''$ (6 pixels) diameter aperture after the underlying galaxy was subtracted by Source Extractor. The sky uncertainty was measured in an annulus $0.25'' - 0.5''$ ($5 - 10$ pixels) and used to calculate signal-to-noise and photometric uncertainty for clusters. Aperture corrections, applied to each cluster, were determined for each image by following the procedure outlined in Sirianni et al. (2005). Bright stars in each image were used to create a PSF and to calculate the fraction of encircled flux in a $0.15''$ radius aperture as compared to $0.5''$ aperture. After that the correction values from $0.5''$ aperture to infinity (Table 5 of Sirianni et al. (2005)) were added. The derived aperture corrections are in good agreement with the measured values listed in Table 3 of Sirianni et al. (2005). Since the FHWM of high S/N clusters are comparable or only marginally larger than the ACS PSF ($\sim 2$ pixels, depending on the filter), all clusters were treated as unresolved and PSF aperture corrections were uniformly applied. Even in two of the nearest galaxies (NGC 3256 and NGC 3690), clusters are only very slightly resolved and the above procedure for aperture corrections produces less than a 0.1 mag difference.

All magnitudes are in the VEGAMAG magnitude system – ACS/WFC zero points are

25.793 mag for F435W and 25.536 mag for the F814W filter[1]. Absolute magnitudes and colors of SCs were calculated taking into account the effect of foreground Galactic extinction (see Table 2.1) using the values calculated following Schlegel et al. (1998) and provided by the NASA/IPAC Extragalactic Database (NED).

The cosmology adopted throughout this dissertation is consistent with Armus et al. (2009). The systemic heliocentric recession velocities were corrected according to the flow model of Mould et al. (2000) that accounts for the three major attractors in the local universe (Virgo Supercluster, Great Attractor, Shapley Supercluster) and adopting $H_0 = 70$ km s$^{-1}$ Mpc$^{-1}$, $\Omega_M = 0.28$, and $\Omega_\Lambda = 0.72$ based on the five-year WMAP results (Hinshaw et al., 2009), as provided by NED.

The accuracy of our photometric measurements was tested while assessing the efficiency of the detection algorithm (see Chapter 2.3.4). Artificial stars of known magnitudes were added to the image, and the detection procedure and photometry measurements were performed and compared to the original values. For clusters brighter than an apparent magnitude of 25, the average photometric error was determined to be less than 0.10 mag.

To measure total fluxes of each galaxy, the masks described in Chapter 2.3.1 were used. The flux inside the mask was calculated. The background level was measured outside of the masked galaxy and its contribution was subtracted. The flux of foreground stars, present inside the masked region in several galaxies, was also measured and subtracted. Photometric uncertainties were calculated taking into account the error from the count rate and sky variance.

### 2.3.3 Contamination by Foreground Stars

Foreground Galactic stars and distant galaxies are present throughout the ACS images. In order to account for the level of contamination, the assumption was made that foreground stars in each magnitude range are evenly distributed throughout each ACS/WFC image. Thus, one can account for the contamination along the line-of-sight to the galaxy by measuring the magnitudes of objects in the "sky portion" of each image. To this end, the cluster detection procedure (Chapter 2.3.1) was applied to the sky portion of each image. The number of detected sources per magnitude bin was then normalized by the ratio of the image area covered by the galaxy and the sky. The degree of contamination varies widely between 3% and 90%, depending on Galactic latitude of the galaxy, the with a median of $\sim$10%

### 2.3.4 Completeness

The efficiency of the detection algorithm was tested using the IRAF ADDSTAR routine. This routine adds artificial stars to the image with a uniform distribution in positions and magnitudes. The apparent magnitude range was chosen between 18 and 27 mag, and a PSF created from bright stars in the image was used. In order to avoid overcrowding, the number of artificial stars added to the image did not exceed 10% of the detected clusters

[1]For revised ACS zero-points posted on 2009 May 19 see `http://www.stsci.edu/hst/acs/analysis/zeropoints`

(i.e., only 10% of the number of detected objects was added to the image). The detection procedure described in Chapter 2.3.1 and photometry (Chapter 2.3.2) were then performed on the images with added stars, and the number and magnitudes of recovered objects were recorded. This procedure was repeated 100 times per galaxy in order to build up good statistics. A completeness function, i.e. the fraction of recovered objects as a function of apparent magnitude, was calculated for each galaxy; an example of the completeness function is shown in Figure 2.2. The cluster detection for the F435W and F814W images is found to be complete at the 50% level at apparent magnitudes of $\sim$25.5 and $\sim$25.0, respectively.

The images were not subdivided into areas with different surface brightness / background levels, as is sometimes done for nearby, large galaxies like NGC 4038/4039 (e.g., Whitmore et al., 1999). Since artificial stars were distributed randomly, and the detection of artificial stars was performed over the same area of the image as cluster detection, the completeness function reflects the overall cluster detection efficiency in a given galaxy, and will therefore be appropriate for all but the relatively small regions of very high background.

Due to the time consuming nature of this procedure, it was performed only in 16 LIRGs: the 15 members of the cluster-rich sample described in Chapter 3 and Mrk 266 (Mazzarella et al, 2011). For the rest of the LIRGs the average of the 16 completeness functions was calculated; this "average" completeness function is shown in Figure 2.2 panel b).

Table 2.1. *HST*/ACS Observations of the HST-GOALS Sample

| Name | Dataset[a] | Observation Date | Exposure Time (sec) F435W | F814W | Extinction $A_B$ (mag) | $A_I$ (mag) |
|---|---|---|---|---|---|---|
| NGC 0034 | J9CV010*0 | 2006 Jul 05 | 1260 | 720 | 0.116 | 0.052 |
| Arp 256 | J9CV020*0 | 2006 May 23 | 1260 | 720 | 0.156 | 0.070 |
| MCG+12-02-001 | J9CV030*0 | 2005 Sep 04 | 1500 | 880 | 2.681 | 1.205 |
| IC 1623 | J9CV040*0 | 2006 Jul 12 | 1260 | 720 | 0.069 | 0.031 |
| MCG-03-04-014 | J9CV050*0 | 2006 Jul 10 | 1260 | 720 | 0.094 | 0.042 |
| CGCG 436-030 | J9CV060*0 | 2005 Aug 26 | 840 | 720 | 0.157 | 0.071 |
| IRAS F01364-1042 | J9CV070*0 | 2005 Dec 05 | 1260 | 720 | 0.093 | 0.042 |
| III Zw 035 | J9CV080*0 | 2005 Aug 26 | 1260 | 720 | 0.269 | 0.121 |
| NGC 0695 | J9CV090*0 | 2005 Aug 23 | 1260 | 720 | 0.388 | 0.174 |
| MCG+05-06-036 | J9CV100*0 | 2006 Jul 22 | 1275 | 730 | 0.339 | 0.153 |
| UGC 02369 | J9CV110*0 | 2006 Jul 22 | 1260 | 720 | 0.442 | 0.199 |
| IRAS F03359+1523 | J9CV120*0 | 2005 Oct 14 | 1260 | 720 | 1.128 | 0.507 |
| ESO 550-IG 025 | J9CV130*0 | 2006 Aug 31 | 1260 | 720 | 0.178 | 0.080 |
| NGC 1614 | J9CV140*0 | 2006 Aug 14 | 1260 | 720 | 0.663 | 0.298 |
| ESO 203-IG001 | J9CV150*0 | 2006 Apr 28 | 1350 | 780 | 0.044 | 0.020 |
| VII Zw 031 | J9CV160*0 | 2005 Sep 03 | 1500 | 880 | 0.425 | 0.191 |
| IRAS F05189-2524 | J9CV170*0 | 2006 Aug 13 | 1275 | 730 | 0.126 | 0.057 |
| IRAS 05223+1908 | J9CV180*0 | 2005 Nov 01 | 1260 | 720 | 2.781 | 1.250 |
| MCG+08-11-002 | J9CV190*0 | 2005 Sep 05 | 1350 | 780 | 1.301 | 0.585 |
| IRAS F06076-2139 | J9CV200*0 | 2005 Nov 14 | 1260 | 720 | 0.301 | 0.135 |
| ESO 255-IG007 | J9CV210*0 | 2006 Apr 19 | 1350 | 780 | 0.162 | 0.073 |
| AM 0702-601 | J9CV220*0 | 2005 Sep 19 | 1425 | 830 | 0.487 | 0.219 |
| IRAS 07251-0248 | J9CV230*0 | 2005 Nov 05 | 1260 | 720 | 0.487 | 0.219 |
| IRAS 08355-4944 | J9CV240*0 | 2005 Sep 08 | 1350 | 780 | 3.589 | 1.614 |
| NGC 2623 | J9CV250*0 | 2005 Nov 29 | 1275 | 730 | 0.177 | 0.080 |
| ESO 060-IG 016 | J9CV260*0 | 2006 Apr 15 | 1485 | 870 | 0.467 | 0.210 |
| IRAS F08572+3915 | J9CV270*0 | 2005 Dec 09 | 1305 | 750 | 0.115 | 0.051 |
| IRAS 09022-3615 | J9CV280*0 | 2006 Jun 07 | 1305 | 750 | 1.742 | 0.783 |
| IRAS F09111-1007 | J9CV290*0 | 2005 Nov 01 | 1260 | 720 | 0.287 | 0.129 |
| UGC 04881 | J9CV300*0 | 2005 Dec 05 | 1320 | 760 | 0.075 | 0.034 |
| UGC 05101 | J9CV310*0 | 2006 Jan 29 | 1440 | 840 | 0.144 | 0.065 |
| ESO 374-IG 032 | J9CV320*0 | 2005 Nov 06 | 1290 | 740 | 0.381 | 0.171 |
| IRAS F10173+0828 | J9CV330*0 | 2005 Dec 01 | 1260 | 720 | 0.112 | 0.051 |
| NGC 3256 | J9CV340*0 | 2005 Nov 06 | 1320 | 760 | 0.524 | 0.236 |

Table 2.1. – Continued

| Name | Dataset[a] | Observation Date | Exposure Time (sec) F435W | F814W | Extinction $A_B$ (mag) | $A_I$ (mag) |
|---|---|---|---|---|---|---|
| IRAS F10565+2448 | J9CV350*0 | 2005 Nov 15 | 1260 | 720 | 0.066 | 0.030 |
| MCG+07-23-019 | J9CV360*0 | 2005 Nov 20 | 1320 | 760 | 0.038 | 0.017 |
| IRAS F11231+1456 | J9CV370*0 | 2005 Nov 20 | 1260 | 720 | 0.127 | 0.057 |
| NGC 3690 | J9CV380*0 | 2006 Mar 19 | 1425 | 830 | 0.072 | 0.032 |
| IRAS F12112+0305 | J9CV390*0 | 2006 Feb 20 | 1260 | 720 | 0.092 | 0.042 |
| IRAS 12116-5615 | J9CV400*0 | 2005 Sep 07 | 1425 | 830 | 1.984 | 0.892 |
| UGC 08058 | J9CV410*0 | 2006 May 11 | 1425 | 830 | 0.041 | 0.018 |
| CGCG 043-099 | J9CV420*0 | 2005 Dec 23 | 1260 | 720 | 0.126 | 0.057 |
| ESO 507-G070 | J9CV430*0 | 2006 Feb 26 | 1260 | 720 | 0.592 | 0.266 |
| NGC 5010 | J9CV440*0 | 2006 Feb 26 | 1260 | 720 | 0.282 | 0.127 |
| IRAS 13120-5453 | J9CV450*0 | 2006 Jun 04 | 1425 | 830 | 1.702 | 0.765 |
| VV 250a | J9CV460*0 | 2006 May 11 | 1440 | 840 | 0.097 | 0.043 |
| UGC 08387 | J9CV470*0 | 2006 Jan 11 | 1290 | 740 | 0.054 | 0.024 |
| NGC 5256 | J9CV480*0 | 2005 Nov 17 | 1350 | 780 | 0.056 | 0.025 |
| Arp 240 | J9CV490*0 | 2005 Dec 21 | 1260 | 720 | 0.119 | 0.054 |
| UGC 08696 | J9CV500*0 | 2005 Nov 17 | 1425 | 820 | 0.036 | 0.016 |
| NGC 5331 | J9CV510*0 | 2005 Dec 23 | 1260 | 720 | 0.129 | 0.058 |
| IRAS F14348-1447 | J9CV520*0 | 2007 Jan 03 | 1260 | 720 | 0.525 | 0.236 |
| IRAS F14378-3651 | J9CV530*0 | 2006 Feb 17 | 1305 | 750 | 0.311 | 0.140 |
| VV 340a | J9CV540*0 | 2006 Jan 07 | 1260 | 720 | 0.183 | 0.082 |
| VV 705 | J9CV550*0 | 2005 Nov 14 | 1320 | 760 | 0.113 | 0.051 |
| ESO 099-G004 | J9CV560*0 | 2006 Apr 14 | 1440 | 840 | 2.496 | 1.122 |
| IRAS F15250+3608 | J9CV570*0 | 2006 Jan 25 | 1305 | 750 | 0.082 | 0.037 |
| UGC 09913 | J9CV580*0 | 2006 Jan 06 | 1260 | 720 | 0.219 | 0.098 |
| NGC 6090 | J9CV590*0 | 2005 Sep 18 | 1380 | 800 | 0.085 | 0.038 |
| IRAS F16164-0746 | J9CV600*0 | 2006 Feb 14 | 1260 | 720 | 1.155 | 0.519 |
| ESO 069-IG006 | J9CV610*0 | 2006 Apr 09 | 1485 | 870 | 0.381 | 0.172 |
| IRAS F16399-0937 | J9CV620*0 | 2006 Feb 04 | 1260 | 720 | 1.879 | 0.845 |
| NGC 6240 | J9CV630*0 | 2006 Feb 11 | 1260 | 720 | 0.330 | 0.148 |
| IRAS F17132+5313 | J9CV640*0 | 2005 Sep 18 | 1380 | 800 | 0.090 | 0.040 |

Table 2.1. – Continued

| Name | Dataset[a] | Observation Date | Exposure Time (sec) F435W | F814W | Extinction $A_B$ (mag) | $A_I$ (mag) |
|---|---|---|---|---|---|---|
| IRAS F17138-1017 | J9CV650*0 | 2006 Mar 31 | 1260 | 720 | 2.978 | 1.339 |
| IRAS F17207-0014 | J9CV660*0 | 2006 Apr 04 | 1260 | 720 | 1.485 | 0.668 |
| IRAS 18090+0130 | J9CV670*0 | 2006 Mar 30 | 1260 | 720 | 2.296 | 1.032 |
| IC 4687 | J9CV680*0 | 2006 Apr 08 | 1425 | 830 | 0.433 | 0.195 |
| IRAS F18293-3413 | J9CV690*0 | 2006 Apr 01 | 1290 | 740 | 0.613 | 0.276 |
| NGC 6670 | J9CV700*0 | 2005 Oct 31 | 1425 | 830 | 0.206 | 0.093 |
| VV 414 | J9CV710*0 | 2006 Mar 11 | 1515 | 890 | 0.609 | 0.274 |
| ESO 593-IG008 | J9CV720*0 | 2006 Mar 20 | 1260 | 720 | 0.550 | 0.247 |
| IRAS F19297-0406 | J9CV730*0 | 2006 Jul 22 | 1260 | 720 | 2.396 | 1.077 |
| IRAS 19542+1110 | J9CV740*0 | 2006 Apr 18 | 1260 | 720 | 0.969 | 0.436 |
| IRAS 20351+2521 | J9CV750*0 | 2006 Apr 15 | 1275 | 730 | 0.846 | 0.380 |
| CGCG 448-020 | J9CV760*0 | 2006 Apr 15 | 1260 | 720 | 0.360 | 0.162 |
| ESO 286-IG019 | J9CV770*0 | 2006 Mar 28 | 1320 | 760 | 0.186 | 0.084 |
| IRAS 21101+5810 | J9CV780*0 | 2005 Nov 03 | 1425 | 830 | 2.471 | 1.111 |
| ESO 239-IG002 | J9CV790*0 | 2006 Jul 16 | 1350 | 780 | 0.042 | 0.019 |
| IRAS F22491-1808 | J9CV800*0 | 2006 May 04 | 1260 | 720 | 0.154 | 0.069 |
| NGC 7469 | J9CV810*0 | 2006 Jun 12 | 1260 | 720 | 0.297 | 0.134 |
| ESO 148-IG002 | J9CV820*0 | 2006 Mar 22 | 1425 | 830 | 0.078 | 0.035 |
| IC 5298 | J9CV830*0 | 2006 Aug 16 | 1275 | 730 | 0.372 | 0.167 |
| ESO 077-IG014 | J9CV840*0 | 2005 Aug 18 | 1485 | 860 | 0.165 | 0.074 |
| NGC 7674 | J9CV850*0 | 2006 Jun 10 | 1260 | 720 | 0.254 | 0.114 |
| IRAS F23365+3604 | J9CV860*0 | 2006 Jun 12 | 1305 | 750 | 0.468 | 0.210 |
| IRAS 23436+5257 | J9CV870*0 | 2005 Nov 02 | 1380 | 800 | 1.178 | 0.529 |
| MRK 0331 | J9CV880*0 | 2006 May 30 | 1260 | 720 | 0.337 | 0.152 |

[a]'*' is replace by 1 for F435W, 2 for F814W filter

Note. — Column 1: Name of the optical source. Column 2: Name of the dataset in MAST archives. Column 3: Observation date. Columns 4 and 5: Exposure times in F435W and F814W filters. Columns 6 and 7: Foreground Galactic Extinction following Schlegel et al. (1998), available from NED. B band corresponds closely to F435W filter and I band to F814W filter.

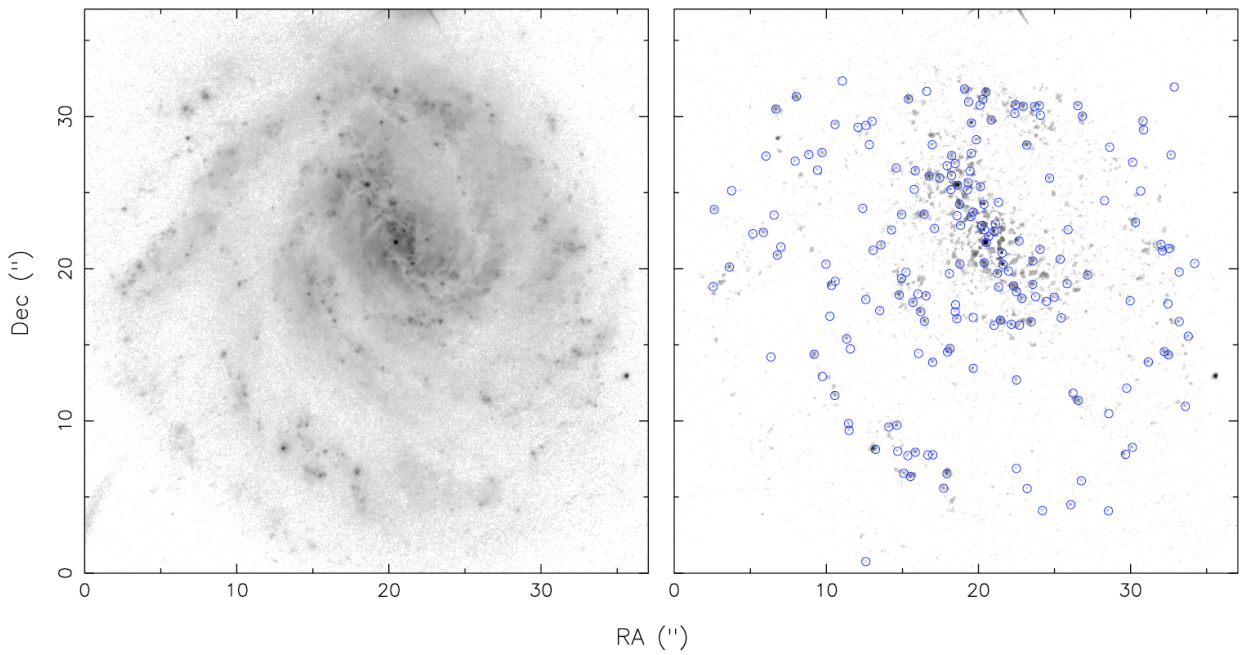


Figure 2.1: *HST*/ACS F435W images of VV 340b. (a) The original image of the galaxy. (b) The image of the galaxy after the underlying galaxy has been subrated by SExtractor; identified clusters are designated with blue circles.

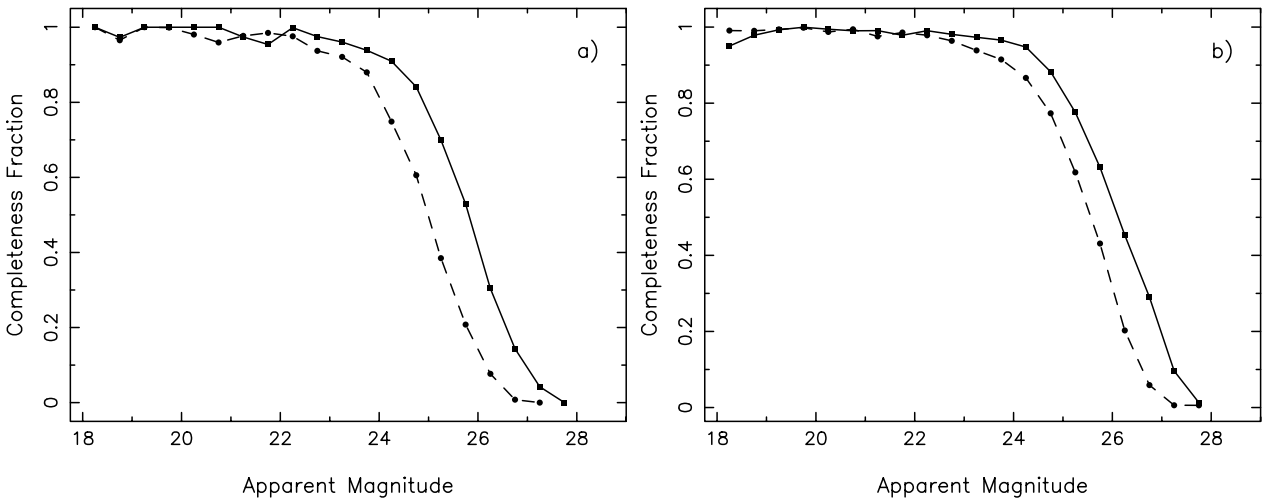


Figure 2.2: Star cluster detections completeness functions for the F435W filter (solid line) and the F814W filter (dashed line). (a) NGC 0034 (b) Average of 16 galaxies.

# Chapter 3

# Properties and Distribution of Optically-Luminous Stellar Clusters in Nearby Cluster-Rich Luminous Infrared Galaxies

This chapter examines properties of star clusters in a sample of 15 cluster-rich nearby LIRGs. Each galaxy contains $> 140$ clusters, and in total over 7000 luminous star clusters were detected in this sample. First, basic properties of SCs (number of SC, median (F435W−F814W) color of the cluster population, specific frequency, specific luminosity, luminosity function, the magnitude of the brightest cluster and the fraction of age-dated young clusters) are determined. Then I examine the connection of specific luminosity and the magnitude of the brightest cluster with the SFR; these correlations were established for normal spiral galaxies (in case of specific luminosity) and for various galaxies in a wide SFR range. Finally, I inspect the spatial distribution of SCs and correlate SC locations (i.e. optically visible star formation) with mid-IR and near-UV emission.

## 3.1 Sample Selection

The sample of LIRGs discussed in this chapter is selected from the *HST* optical survey (Evans et al., in prep.) of a complete sample of 87 $L_{\rm IR} > 10^{11.4}$ $L_\odot$ LIRGs in the Great Observatories All-Sky LIRG Survey (GOALS; Armus et al., 2009). GOALS consists of all LIRGs in the flux limited (i.e., $f_{60\mu{\rm m}} > 5.24$ Jy) *IRAS* Revised Bright Galaxy Sample (RBGS; Sanders et al., 2003), and contains 202 objects with $L_{\rm IR} \geq 10^{11}$ $L_\odot$ out to a maximum redshift of $z = 0.088$ (median $z = 0.008$). The LIRGs imaged at F435W and F814W with *HST* exhibit a wealth of point-like luminous sources superimposed on the underlying galaxy – these are all candidate luminous star clusters and cluster associations, although some are inevitably foreground Galactic stars. Using the detection procedure described in Chapter 2.3.1, SCs were extracted in the complete sample of all 87 galaxies imaged with *HST*.

The primary goal of the this chapter is a detailed study of the nature of luminous star clusters in a substantial sample of LIRGs. To achieve this, the following are required: *(i)* the LIRGs in the sample must contain a sufficient number of clusters visible per galaxy to build up robust statistics and *(ii)* the LIRGs must be at a low enough redshift to allow for comparisons to be made between the spatial distribution of the detected clusters and the lower resolution *GALEX* UV and *Spitzer* mid-IR emission. As a result, the selection criteria

are naturally biased towards relative nearby, "face-on" LIRGs.

The sample selection was chosen as follows: The distribution of the number of clusters per system (i.e., galaxy pairs were counted as one system) is shown in the histogram in Figure 3.1. Three LIRGs (NGC 3256, NGC 3690 and NGC 5257) are absent from this histogram due to a very large (>800) number of clusters. The first and highest bin of the histogram contains 19 galaxies ($\approx 22\%$ of the HST-GOALS sample) with less than 20 clusters. The distribution falls off gradually until the $120 - 140$ bin and rises slightly again in consequent bins. This second "peak", comprised of systems with $140-220$ detected clusters, and a tail with systems containing $> 220$ clusters constitute the cluster-rich LIRGs sample that is the focus of this chapter (20 systems $\approx 23\%$ of the HST-GOALS sample).

In Figure 3.2, the number of clusters per system is plotted versus redshift for the HST-GOALS sample. The systems in the cluster-rich sample are designated with triangle symbols and are located in the upper left corner ($> 150$ and $z < 0.033$). There is a moderate correlation (Spearman rank correlation coefficient $r_s = -0.60$ with significance $7.2 \times 10^{-10}$) between the number of SCs and the redshift of the galaxy. This is expected due to the decreasing metric resolution and the decreasing sensitivity to faint cluster detection as a function of increasing redshift.

The presence of a "break" at $\sim 140$ clusters in both figures reflects a transition in appearance of galaxies; i.e., from large, well resolved galaxies to smaller and mostly more distant galaxies with less details. For this reason, a limit of 140 clusters as the main selection criterion for the current sample was chosen. While this criterion only selects a small fraction of the total HST-GOALS sample, it allows for a more robust statistical analysis of the optically-visible cluster population in each galaxy. This criterion also naturally limits the redshift range of the systems in a manner that allows detailed morphological analysis and multi-wavelength comparisons. Specifically, the redshift range of this sample is $0.009 \leq z \leq 0.034$ (NGC 3256 being the closest and VV 340 the most distant), corresponding to a luminosity distance range of $D_{\rm L} \sim 38.9$ Mpc – 157 Mpc and a median redshift of $z = 0.02$ (85.5 Mpc). Analysis of SCs in the complete HST-GOALS sample is presented in Chapter 4.

For LIRGs comprised of two or more galaxies, at least one of the galaxies has to fulfill the selection criterion of more than 140 clusters. Two systems, NGC 5331 and CGCG 448-020, have more than 140 clusters in total, but the individual galaxies contain less than 100 clusters. Three LIRGs, NGC 6240, IC 4686/7/9 and IRAS 20351+2521 that also fulfill the selection criterion (175, 243 and 174 clusters, respectively) are located in crowded star fields (i.e., $\sim 20\%$ of detected clusters could be foreground Galactic stars, see Chapter 2.3.3), and therefore are not included in this analysis.

The resultant sample of 15 LIRGs analyzed in the this chapter is presented in Table 3.1. For LIRGs containing two or more distinct galaxies, the galaxies have been individually tabulated. Of the present sample, six LIRGs are galaxy pairs, resulting in a total of 21 individual galaxies. Two galaxies within a galaxy pair, VV 340a and NGC 7674A, contain too few clusters, 14 and 0, respectively, therefore cluster analysis is performed only on 19 galaxies. Note that a cluster analysis of NGC 2623 and IC 0883 have been presented in previous publications, i.e., Evans et al. (2008) and Modica et al. (2011), respectively.

## 3.2 Results

### 3.2.1 Host Galaxy Optical Morphology and Photometry

Host galaxy photometry in F435W and F814W filters was measured following the procedure outlined in Chapter 2.3.2, and the results are listed in Table 3.2. The absolute magnitudes range between −19.62 mag to −21.79 mag in the F435W filter and −21.56 mag to −23.40 mag in F814W, with median values of −21.20 mag and −22.76 mag, respectively. The optically brightest galaxy in this sample is NGC 0695.

Figure 3.3 shows the ACS/WFC F435W images of the sample; LIRGs are arranged in an approximate merger stage sequence. It should be noted that an exact order is difficult to establish. The sample encompasses objects in different interaction stages: from an apparently undisturbed disk of NGC 0695, through widely separated galaxy pairs with either intact disks (VV 340, NGC 7674, NGC 6786 / UGC 11415) or asymmetric disks and tidal tails (NGC 7469, NGC 5257/8, Arp 256), to systems with two distinguishable bodies in a common envelope (NGC 3690, IC 1623) and advanced mergers with disturbed morphology and long prominent tails (IC 0883, NGC 1614, NGC 2623, NGC 3256, NGC 0034, Arp 220). In this chapter, VV 340, NGC 7674, NGC 6786, NGC 7469, NGC 5257, Arp 256 are referred to as early merger stage systems; NGC 3690, IC 1623, IC 0883, NGC 1614, NGC 2623 are mid-merger stage systems; and NGC 3256, NGC 0034, Arp 220 are late merger stage systems. The early merger stage systems in this sample are dominated by face-on spirals, the mid-merger stage systems have irregular amorphous bodies and long tails, while the late merger stage systems have somewhat more regular and symmetrical appearance but still display clear signs of a merger event.

The infrared luminosity of LIRGs in this sample is $L_{\rm IR} = 10^{11.48-12.28}$ $L_\odot$, with Arp 256 being the least luminous LIRG and Arp 220 being the most luminous. The median luminousity of the sample is $L_{\rm IR} = 10^{11.65}$ $L_\odot$. The sample includes only one ULIRG, Arp 220; other ULIRGs in the GOALS sample have fewer detected clusters due to their large distances. In four galaxy pairs (VV 340, NGC 7674, NGC 7469, Arp 256), most of the IR flux is attributed to only one galaxy. In the case of VV 340 and Arp 256, the IR-bright galaxy contains less detected clusters than the companion. In NGC 6786 and NGC 5257, the IR fluxes are approximately equally divided between both galaxies (see also Mazzarella et al., in prep.).

### 3.2.2 Cluster Properties

#### Number of Clusters

The number of detected clusters per galaxy shows a variation of an order of magnitude, between $\sim 150$ and $\sim 1700$, with the median of 296 (see Table 3.3, Column 2). In NGC 3256 and NGC 3690, the closest galaxies in the sample, the number of clusters exceeds by far the rest of the sample.

The number of detected clusters may not reflect the intrinsic cluster population of a galaxy. Several observational factors such as distance, angular size of the galaxy, orientation and possibly the amount of dust obscuration affect our ability to detect SCs. For obvious reasons, the number of detected clusters strongly depends on the distance of a galaxy (see also

Chapter 3.1, Figure 3.2). The lower limit on the cluster number as selection criterion favors nearby well-resolved galaxies with large angular size. The median angular size (measured in masks described in Chapter 2.3.1) of LIRG systems in this sample is about double the size of the other systems in the HST-GOALS sample: $\sim 1$ arcmin$^2$ versus $\sim 0.4$ arcmin$^2$ (median of the complete HST-GOALS sample, excluding the 15 cluster-rich systems). Orientation affects angular size and extinction, with face-on galaxies having larger sizes and also less dust obscuration, therefore most galaxies in the sample are viewed face-on. The amount of dust obscuration seems also important, for example in the highly reddened ULIRG Arp 220 relatively few clusters are detected.

There is no straight-forward correlation between the number of clusters and the merger stage, $L_{\rm IR}$ or optical magnitude of the galaxy.

**Luminosity Distribution**

Figures 3.4 and 3.5 show the distribution of absolute F435W and F814W magnitudes of clusters in each LIRG. The absolute magnitudes of detected clusters range typically between about $-8$ mag and $-16$ mag in both, the F435W and F814W, filters.

The faint end of the brightness distribution is a consequence of the detection limit and the distance of the sample. Given the redshift range $0.009 \leq z \leq 0.034$, the distance modulus is 32.95 mag $\leq (m - M) \leq$ 35.98 mag with a median $(m - M)_{\rm med} = 35.07$ mag. At the detection limit of $\sim 26$ apparent magnitude, the absolute magnitudes of clusters are expected to be limited to about $-7$ mag and $-9$ mag for most of the galaxies in the sample, which is in good agreement with the measurements. The decrease in the number of clusters at the faint end of the brightness distribution is caused by the decreased detection efficiency; when corrected for completeness the distribution keeps rising (Chapter 3.3.4).

The most luminous clusters are found in NGC 7469 ($M_{\rm F435W} = -17.0$ mag) in a circumnuclear ring, and in a spiral arm close to the nucleus of NGC 6786 ($M_{\rm F435W} = -16.7$ mag). The least luminous clusters are found in Arp 220; the brightest cluster member in Arp 220 has an absolute magnitude of $M_{\rm F435W} = -12.2$ mag. The magnitudes of the brightest cluster in each galaxy is listed in Table 3.4. Particular care was taken to remove galactic nuclei and obvious Galactic stars. Although stars posing as bright clusters cannot be completely excluded, all bright clusters have colors $(m_{\rm F435W} - m_{\rm F814W}) < 1.5$, consistent with them being young clusters. The largest number of bright ($M_{\rm F435W} < -12$ mag) clusters is found in NGC 0695, and they constitute 35% of the complete cluster population in this galaxy. Arp 220 has the least number of bright clusters, only 0.5% of its cluster population have $M_{\rm F435W} < -12$ magnitude.

In galaxies in early merger stages (i.e., the face-on spirals NGC 0695, NGC 5257, Arp 256, NGC 7674) bright clusters are located in spiral arms in high surface brightness regions and are often grouped in star cluster complexes. In mid-merger stages (NGC 3690, IC 1623) SCs are also located in high surface brightness regions. In late mergers stages (NGC 0034, IC 0883, NGC 2623) bright clusters are found dispersed through-out the main body of the galaxy.

**Cluster Colors**

Figure 3.6 shows histograms of the number of clusters versus the (F435W – F814W) colors of clusters. The cluster colors are in the range $-0.5 < (\mathrm{F435W} - \mathrm{F814W}) < 3$ with the highest bin between 0.5 to 1. Clusters with $(\mathrm{F435W} - \mathrm{F814W}) > 2.0$ are either heavily extinguished or foreground stars (see Chapter 3.3.5).

A median (F435W – F814W) color of all clusters in each galaxy was calculated; the color range is between 0.43 and 1.13; the values are listed in Table 3.3. The galaxies with the reddest median cluster color are Arp 220 and IC 5283 , while Arp 256 and IC 1623 have the most blue median cluster colors. The median cluster color for the entire sample is $0.72 \pm 0.19$.

## 3.3 Analysis and Discussion

### 3.3.1 Specific Frequency

Specific frequency of young clusters $T_N$ was introduced in Chapter 1.1.3. Following Larsen & Richtler (1999) definition

$$T_N = N_{cl} \times 10^{0.4(M_B+15)}$$

where $M_B$ is the B-band absolute magnitude of the galaxy and $N_{cl}$ is the number of young clusters above a certain limiting magnitude, I calculate the specific frequency of SCs in the cluster-rich LIRGs sample, limiting to clusters brighter than $-9$ mag in F435W. The F435W filter matches closely the Johnson B-band; an absolute magnitude of $\mathrm{M}_{F435W} = -9$ mag corresponds roughly to the 50% completeness and is also a brightness threshold for individual stars. The completeness correction is applied to the number of clusters (see Chapter 2.3.4), and the resultant corrected $T_N$ values are as listed in Table 3.3. The errors were calculated using the Poisson statistics of the cluster counts and photometric errors in the galaxy magnitudes.

The distribution of $T_N$ values is shown in Figure 3.7. The $T_N$ values range between 0.67 in NGC 0034 and 1.73 in NGC 3690 with a median of $1.14 \pm 0.30$. While the number of clusters in NGC 3256 ($\sim 1700$) exceeds the other galaxies in the sample by almost a factor of 10, the $T_N$ of 1.30 is just slightly above the median of the sample.

Table 1 of Larsen & Richtler (2000) lists $T_N$ values for a sample of 21 nearby spiral galaxies. While the limiting magnitude is somewhat comparable to ours ($M_V < -8.5$ mag and $M_V < -9.5$ mag for "red" and "blue" population of clusters), Larsen & Richtler (2000) used ground based observations that cover only the central parts of the galaxies and the number of clusters was not corrected for completeness. The highest $T_N$ value in the Larsen & Richtler (2000) sample is 1.77 (NGC 5236) and is consistent with the highest value of 1.73 (NGC 3690) in the present sample. The median $T_N$ value in Larsen & Richtler (2000) is $0.45 \pm 0.53$ and is smaller than in the cluster-rich LIRGs sample ($1.14 \pm 0.30$). While 60% of galaxies in Larsen & Richtler (2000) sample have $T_N$ values less than 0.5, all galaxies in the cluster-rich LIRGs sample have values above 0.5. Even keeping in mind the shortcomings of the comparison, it appears that the specific frequency $T_N$ is enhanced in this sample of LIRGs as compared to local spirals.

Elliptical galaxies have much higher values of the specific frequency $S_N$ for their population of old globular clusters; i.e., in the range of $S_N \sim 2-6$ (Harris, 1991; Elmegreen, 1999) as compared to spiral galaxies ($T_N$ <1). Schweizer (1987) and Ashman & Zepf (1992) suggest that a large number of SCs form during a merger process of two gas-rich disk galaxies leading to a high $S_N$ for elliptical galaxies. The $T_N$ values for young clusters discussed in this section cannot be compared directly to values of $S_N$ for old globular clusters for various reasons. For example, the majority of young clusters may disperse with time, and additional clusters may be continuously forming during the merger process. Further, the $M_V$ of the galaxy will change with time due to fading of the underlying stellar population with age. Although merging LIRGs show higher $T_N$ values as compared to local spirals, the infant mortality of young clusters is very high; roughly 80 - 90% are expected to dissolve in each logarithmic decade of time, meaning that only about 1 in 1,000 clusters with mass greater than $10^4$ $M_\odot$ will survive to become an old globular cluster (Whitmore, 2004). As $T_N$ values at the present stage suggest, more clusters need to be formed in order to account for the high $S_N$ of an elliptical galaxy .

### 3.3.2 Specific Luminosity

Specific luminosity $T_L$, a measure of the percentage of flux contributed by clusters, is written in the form

$$T_L = 100 \times \frac{L_{\rm clusters}}{L_{\rm galaxy}},$$

(Harris, 1991; Larsen & Richtler, 2000), where $L_{\rm clusters}$ is the total luminosity of clusters and $L_{\rm galaxy}$ the total luminosity of the galaxy.

The specific luminosity is independent of the distance modulus. It is also relatively insensitive to incompleteness at the faint end of cluster luminosity distribution because most of the cluster flux originates from a handful of the brightest clusters. On average, only the brightest 12% of SCs in the entire SC population are responsible for 80% of F435W flux from clusters, with the two extremes being observed in NGC 7469 (the brightest 1.7% of SCs) and Arp 220 (the brightest 52% of SCs).

The specific luminosities are listed in Table 3.3. Errors were calculated by taking into account uncertainties in both cluster and galaxy photometry. The contribution of visible clusters to the total flux in F435W filter varies between 0.5% (Arp 220) and 7.3% (NGC 7469), with a median of $3.4 \pm 2.0$%. For the F814W images these numbers are 0.3% (Arp 220) to 3.5% (IC 1623), with a median of $1.9 \pm 0.9$%. Arp 220 has the least contribution of flux from clusters, possibly due to a very high amount of dust extinction. The specific luminosity distribution in F435W and F814W images is plotted in Figure 3.8. The histogram of $T_L$(F435W), the specific luminosity $T_L$ in F435W images, shows a rather uniform distribution with a small peak in the $3-4$% bin, while the $T_L$(F814W) values have a smaller range and peak in the $1-2$% bin.

Table 1 of Larsen & Richtler (2000) lists $T_L$ values in the U and V filters for nearby spiral galaxies and starburst/mergers. Our $T_L$ values are significantly higher than Larsen & Richtler (2000) values for spiral galaxies (median for U is 0.5 and for V is 0.3) and are in the starburst/merger galaxies range.

Larsen & Richtler (2000) find an upward trend of specific luminosity $T_L$(U) with SFR calculated using FIR *IRAS* fluxes and a correlation between $T_L$(U) and $\Sigma_{SFR}$ (SFR per unit area) for nearby spiral galaxies. Figure 3.9 shows a plot of the specific luminosity $T_L$(F435W) versus SFRs calculated in Howell et al. (2010) using *IRAS* FIR and *GALEX* FUV fluxes (SFR total, panel a)) and *GALEX* FUV fluxes only (SFR UV, panel b)). The $T_L$(F435W) versus $\Sigma_{SFR}$ (SFR per unit area) for respective SFRs is plotted in Figure 3.10. Panel a) in both figures shows no clear trends, the Spearman rank correlation coefficients are $r_s = 0.18$ with significance 0.5 and $r_s = -0.19$ with significance 0.4 for SFR total and $\Sigma_{SFR}$ total, respectively. Panel b) exhibits an upward trend in $T_L$(F435W) with increasing SFR UV (Spearman rank correlation coefficient $r_s = 0.70$ with significance $8.1 \times 10^{-4}$) and $\Sigma_{SFR}$ UV (Spearman rank correlation coefficient $r_s = 0.56$ with significance $1.2 \times 10^{-2}$). Unlike in Larsen & Richtler (2000), the scatter in the plotted data does not decrease when using $\Sigma_{SFR}$ instead of SFR. A possible source of scatter in $T_L$(F435W) versus SFR or $\Sigma_{SFR}$ plots are uncertainties in the estimation of SFRs due to the AGN contribution.

Larsen & Richtler (2000) list $T_L$(U) and $T_L$(V) values, thus in order to compare Larsen & Richtler (2000) $T_L$ values with $T_L$(F435W) values of the cluster-rich LIRGs sample, an extrapolation to $T_L$(B) values is needed. The galaxy magnitudes were calculated using B−V galaxy colors listed in Table 2 of Larsen & Richtler (2000) and the SC magnitudes were extrapolated assuming a mean cluster color of B−V= 0.2. Although this estimate is somewhat crude, it nevertheless allows a direct comparison presented in Figure 3.11. The $T_L$(B) data points for nearby normal spiral galaxies from Larsen & Richtler (2000) are designated with triangles, and the $T_L$(F435W) values of the cluster-rich sample are points. The two populations are disconnected; the Larsen & Richtler (2000) sample has lower SFRs and shows an upward trend, while the cluster-rich LIRGs sample has higher SFR values but no trend emerges.

In the present LIRGs sample, unlike in the Larsen & Richtler (2000) nearby spiral galaxies sample, no correlation between $T_L$(F435W) and SFR or $\Sigma_{SFR}$ derived from FIR fluxes is found. In LIRGs, the IR luminosity that is used to derive SFR originates for the most part in the nuclear region and not in the extended main body of the galaxy where SCs are located. Instead, a trend of $T_L$(F435W) with SFR or $\Sigma_{SFR}$ derived using FUV fluxes emerges. FUV emission arises from young, massive, un-obscured stars, the same type of SF that is traced by young SCs (see Chapter 3.3.7 and Chapter 3.3.8).

### 3.3.3 Brightest Clusters

Table 3.4 lists the absolute F435W magnitudes, the (F435W−F814W) colors, ages and masses of the most luminous cluster found in each galaxy. The age and the mass of the cluster were derived following the method described in Chapter 3.3.5. Eleven clusters have (F435W−F814W) $< 0.5$ resulting in ages younger that 7.6 Myr. Seven clusters have $0.5 <$ (F435W−F814W) $< 1.0$ and one cluster (F435W−F814W)= 1.36, they suffer from a color-age degeneracy, and the smallest masses and consequently youngest ages were assumed in this analysis. No correction for extinction was performed due to difficulties in determining the extinction to each SC, as described in Chapter 3.3.5. The brightest clusters are young, with ages varying between 4.8 Myr and 8.3 Myr with a median of 7.6 Myr. The masses of brightest clusters vary between $1.1{\times}10^5$ $M_\odot$ and $5.8{\times}10^6$ $M_\odot$, with a median of

$1.5\times10^6$ $M_\odot$. The ages are upper limits and the masses are lower limit estimates due to unknown extinction.

The present LIRGs sample contains some of the most luminous clusters observed so far. As described in Chapter 3.2.2, NGC 7469 ($M_{F435W}$=−17.1 mag) and NGC 6786 ($M_{F435W}$=−16.7 mag) harbor the brightest clusters in our sample; the median of the sample is $M_{F435W}$=−15.4 mag. For comparison, the brightest individual cluster in the Local Group, 30 Dor/R136 in the Large Magellanic Cloud, has $M_V = -11.1$ mag (Hunter et al., 1995), and W3 in NGC 7252 (Schweizer & Seitzer, 1998) has $M_V = -16.2$ mag. The luminosities of clusters in the present LIRGs sample are comparable to those found in a sample of warm ULIRGs (Surace et al., 1998).

Surace et al. (1998) speculate that the brightest clusters in their ULIRG sample could be in fact cluster associations. Although the bright clusters in the present sample appear as unresolved, point-like and symmetric sources, the resolution of the *HST* observations corresponds to size scales of 19 – 71 pc. Given that cluster associations can have sizes as small as 20 pc, the possibility that some of the brightest clusters are indeed cluster associations cannot be ruled out. Alternatively, since the majority of bright clusters are located in areas with high surface brightness (e.g., nuclear regions) there may be flux contributions from the underlying galaxy.

Several authors (Whitmore, 2003; Larsen, 2002b; Weidner et al., 2004; Bastian, 2008) have investigated the correlation between the brightest young cluster and the SFR of its host galaxy. Figure 1 in Bastian (2008) shows a plot of V-band luminosity of the brightest cluster versus log(SFR) with an apparent linear relation over several magnitudes of SFRs, from individual star-forming regions to ULIRGs. An analogous plot including the present sample is shown in Figure 3.12. The F435W magnitude values are used since, according to Bruzual & Charlot (2003) evolutionary models, $B-V \approx 0$ for clusters in this age range. The SFRs were derived using *IRAS* FIR and *GALEX* FUV fluxes (Howell et al., 2010). The galaxies from the Larsen (2002b) sample are designated with triangles, the squares mark data from Bastian (2008) Table 1. Four LIRGs (NGC 2623, NGC 3256, NGC 6240 and IRAF 19155−2124) in Bastian (2008) Table 1 are also present in the GOALS sample and are excluded or replaced with our values. The cluster-rich LIRGs are indicated with star symbols. The straight line is the fit derived by Weidner et al. (2004) using the sample of spiral and dwarf galaxies observed by Larsen (2002a,b), i.e.,

$$M_V = -1.87(\pm0.06) \times log(\mathrm{SFR}) - 12.14(\pm0.07)$$

(i.e., Equation 2 of Weidner et al. (2004)). The brightest clusters in the cluster-rich LIRGs sample follow the correlation and are located at the high end of luminosities and SFRs. The amount of scatter is within the range of previous datasets and the outliers may be due to extinction (points below the line) and/or uncertainties in SFR estimation (e.g. as a result of AGN contribution). The outlier IC 5283 illustrates the effects of extinction - the brightest cluster in IC 5283 has an estimated age of 807 Myr, which is significantly higher than the estimated ages of less than 10 Myr for the brightest SC in the rest of the sample. If an extinction of $A_V = 1$ mag is adopted for this SC, the age estimate would change to 7.6 Myr (median age of the sample), $M_{F435W} = -13.7$ mag ($\Delta$B=1.4 mag) and shift the location in the V-band luminosity versus SFR very close to the best-fit line. In the case of

Arp 220, the cluster with the brightest measured F435W magnitude is the one plotted in the Figure. However, the forth brightest F435W cluster is the brightest in F814W filter and is estimated to have the extinction of E(B-V)=1.48 (Wilson et al., 2006); this corresponds to an $A_V = 4.4$ mag. If this magnitude is extinction corrected, the resulting $M_V = -16.48$ mag, making it the brightest cluster overall. It should also be noted that although the $M_V$ are similar to Wilson et al. (2006), our SFR is larger by $\sim 90$ $M_\odot$ $yr^{-1}$ and Arp 220 still falls below the line.

The brightest cluster – SFR correlation can be explained by the size-of-sample effect (Whitmore, 2003; Bastian, 2008). A galaxy with higher SFR forms more young clusters and consequently is able to sample the cluster mass function to higher masses. Given the high SFRs of LIRGs in the present sample, it is not surprising to find that they harbor some of the most luminous clusters. Another important requirement for a brightest cluster – SFR correlation is that the brightest cluster has to be young in order to correlate with the present SFR. Bastian (2008) concludes that the youngest clusters ($< 10$ Myr) are predominantly the brightest, which is consistent with our findings.

### 3.3.4 Luminosity Function

Figures 3.13 and 3.14 show histograms of the cluster luminosity distribution as measured in the F435W and F814W images; luminosity functions have been fitted to each histogram. The data are presented in 0.5 mag bins, the width of the bin is large enough that photometric uncertainties should have little effect on the form of the distribution. The red histograms represent the raw, uncorrected luminosity distribution, the black histograms are corrected for foreground stars contamination and for the efficiency of the detection algorithm. The number of foreground Galactic stars expected in each luminosity bin was estimated using the procedure described in Chapter 2.3.3 and subtracted from the number of clusters in each respective magnitude bin. A correction for the efficiency of the detection algorithm was made by dividing the histograms by the completeness functions determined in Chapter 2.3.4. The histograms were not reddening corrected due to difficulties in determining the extinction (see Chapter 3.3.5).

The cluster luminosity function is a power law of the form

$$dN(L_i)/dL_i = \beta L_i^{\alpha}$$

where $L_i$ is the luminosity of the cluster in a filter $i$. In $\log - \log$ space, the power law becomes a liner relation

$$logN(L_i) = aM_i + b$$

with the variable $a$ being related to the luminosity function index $\alpha$ as

$$\alpha = -(2.5a + 1)$$

(Larsen, 2002b).

The linear relation was fitted to each histogram using the least squares fit weighted by the square root of the number of clusters in the bin. The range of the fit was limited to the magnitude bins in which at least half of the artificial stars were identified (Chapter 2.3.4); this limit is indicated in Figures 3.13 and 3.14 by an arrow.

Values of the LF indices $\alpha$ are listed in Table 3.5. They range from $-1.5$ to $-2.3$ with a median of $-1.91 \pm 0.21$ and $-1.88 \pm 0.20$ in the F435W and F814W images, respectively. Corrections for foreground stars and completeness have only a minor effect on LF indices; on average the slope becomes $\sim 0.09$ steeper. A fit to the raw luminosity histograms performed to the 80% completeness level (the highest uncorrected bin), results in median values of $-1.81 \pm 0.21$ in F435W and $-1.71 \pm 0.26$ in the F435W and F814W images, respectively.

The corrected luminosity histograms show no turn-over seen in the distribution of old globular clusters, although only NGC 3256 and NGC 3690 probe the LF beyond the peak magnitude of $M_I = -8.5$ mag (see e.g., Kundu & Whitmore (2001) for a discussion of globular cluster luminosity functions).

The LF for young clusters has been studied in numerous galaxies and galaxy types, and the index $\alpha \sim -2$ (Portegies Zwart et al. (2010) and references therein) is a representative value. Schweizer & Seitzer (2007) derive the LF index of $-1.75 \pm 0.10$ for NGC 0034 in V band, which is in excellent agreement with our values of $-1.70 \pm 0.3$. Zepf et al. (1999) find a LF index of $\sim -1.8$ in NGC 3256, which is again in good agreement with our values of $-1.84 \pm 0.17$ (F435W) and $-1.91 \pm 0.15$ (F814W). LF index values for the present sample are somewhat lower than the generally accepted LF index $\alpha \approx -2$. Possible sources of uncertainties in our LF index estimates are extinction and blending of individual clusters into cluster associations due to limited resolution; both make the slope of the LF shallower. It is also possible that the completeness corrections have been underestimated since a single completeness function was calculated for the entire galaxy, without a sub-division into several surface brightness areas (Chapter 2.3.4). Therefore, our derived LF index values are lower limits.

### 3.3.5 Cluster Ages

#### Color-Magnitude Diagrams

Figures 3.15 and 3.16 show color-magnitude diagrams of absolute F435W magnitudes plotted versus (F435W − F814W) color of SCs. Evolutionary tracks computed using Bruzual-Charlot population synthesis models (Bruzual & Charlot, 2003) for an instantaneous starburst with solar metallicity are plotted for cluster masses of $10^5$ $M_\odot$ and $10^6$ $M_\odot$. In the lower right panel, an evolutionary track for a cluster of mass $10^4$ $M_\odot$ is also shown; the arrow in the right upper corner represents 1 magnitude of visual extinction.

The evolutionary tracks in Figures 3.15 and 3.16 originate from GALAXEV (version 2003), a library of evolutionary stellar population synthesis models that were computed using the isochrone synthesis code of Bruzual & Charlot (2003). This code computes the spectral evolution of a stellar population based on a stellar evolution prescription (Padova 1994) and a library of observed stellar spectra (STELIB). The tracks in Figures 3.15 and 3.16 are for the case of an instantaneous starburst, solar metallicity and Salpeter IMF. The output of the model (spectral energy distribution) was convolved with the ACS F435W and F814W filter response functions in order to obtain magnitudes and colors in these filters and scaled with the mass of a cluster. The age and mass estimation using color-magnitude diagrams together with evolutionary tracks suffers from two major shortcomings *(i)* color–age degeneracy and *(ii)* unknown extinction that varies from cluster to cluster.

*(i)* Color–age degeneracy. Figure 3.17 shows the evolution of (F435W−F814W) color of a cluster as the cluster ages. The shape of the evolutionary track exhibits a color–age degeneracy for ages between 7.6 Myr to 500 Myr and colors $0.51 <$ (F435W−F814W) $< 0.98$. A color value in this range can be attributed to at least three different ages. This degeneracy persists in color-magnitude diagrams; without a knowledge of cluster mass, the proper evolutionary track cannot be assigned to individual clusters and the absolute magnitude cannot break the degeneracy. A combination of younger age and smaller mass produces the same color and absolute magnitude as an older and more massive cluster. A $10^5$ $M_\odot$ cluster with an age of $10^7$ years has the same $M_{\rm F435W}$ and (F435W–F814W) as a $10^6$ $M_\odot$ cluster with an age of few$\times 10^8$ years (see bottom right panel in Figure 3.15).

*(ii)* Extinction–age degeneracy. The extinction vector for $M_{F435W}$ magnitude and (F435W − F814W) color is parallel to evolutionary tracks, therefore the effects of reddening by dust cannot be distinguished from aging. Unfortunately, imaging in only two bands makes it impossible to get a good estimate of extinction. Certainly, all clusters suffer some amount of extinction, which also varies from cluster to cluster. In particular, extinction has a strong effect on age estimates of clusters with (F435W − F814W) $> 1.0$, located to the right of the evolutionary tracks. Even a moderate amount of extinction of $A_V$=1 can make a cluster appear $\sim$ 800 Myr older, as in the case of the brightest cluster in IC 5283 (Chapter 3.3.3). Given these shortcomings, ages and masses were determinated only for clusters with (F435W − F814W) $< 0.51$, corresponding to the age of 7.6 Myr. The ages are upper limits and masses are lower limits since I do not attempt to correct for extinction.

**Extinction**

The extinction affecting SCs, once corrected for foreground reddening as discussed in Chapter 2.3.2, can be either due to dust associated with the local star-forming region where a cluster formed, or due to the wider dust distribution within the host galaxy. The dust surrounding the birthplace of a cluster is cleared within a few Myr (see review by Larsen (2010)). Therefore the dust in the galactic environment is likely responsible for the majority of extinction. In the case of LIRGs it is of particular concern, since these galaxies contain large amounts of dust obscuring their nuclear regions, resulting in their high IR luminosities.

Figure 3.19 shows the location of star clusters overlaid on (F435W−F814W) images. The grey-scale displays the (F435W−F814W) color of the galaxy with darker shades corresponding to larger (F435W−F814W) values and redder color and lighter shades to smaller (F435W−F814W) values and bluer color. Cluster symbols are color-coded indicating the color and hence a combination of the ages and reddening of clusters. SCs designated with blue dots have (F435W−F814W) $< 0.51$. These SCs can be reliably age-dated as being younger than 7.6 Myr. SCs designated with green triangles have (F435W−F814W) $= 0.51 - 1.0$ and have a wide range of possible ages from $7.6 - 500$ Myr. This color bin covers the widest range of cluster ages and therefore contains the largest number of SCs; the peak of the cluster color histograms is within this bin (see Chapter 3.2.2). SCs designated with yellow squares have (F435W−F814W) $= 1.0 - 1.5$ and ages between 500 Myr and 1 Gyr. SCs designated with red stars have (F435W−F814W) $> 1.5$ and ages older than 1 Gyr. These could be either globular clusters, highly reddened young clusters or foreground Galactic stars.

The inspection of Figure 3.19 shows that clusters are found predominantly in galaxy

regions with relatively blue (F435W−F814W) colors. In early merger stages SCs are located predominantly in spiral arms, in what appears to be high surface brightness high cluster density regions. The spiral arms are accompanied by dark dust lanes containing relatively few SCs. In general, it appears that the colors of clusters found in red dusty regions are redder than other clusters. Figure 3.18 supports the assumption that the red cluster colors are due to extinction rather than age-related. This figure shows the ratio (percentage) of clusters found in "red" regions of the galaxy (i.e., redder than the median galaxy color) to all detected clusters as a function of cluster color. For (F435W−F814W) > 2, 80% of the clusters are found in red, highly extinguished galaxy regions.

**Age–Dating**

While the unknown extinction and masses of clusters prevent an accurate determination of the ages of the majority of SCs, clusters with (F435W − F814W)< 0.51 are not subjected to color-age degeneracy and are sufficiently blue that they cannot suffer a significant amount of extinction, and thus limits can be placed on their ages and masses. Clusters can be as young as 1.5 Myr (NGC 3690, NGC 5257, NGC 6786, NGC 7674), and the median age for the young clusters in this LIRGs sample is $\sim$ 6.9 Myr. It should be emphasized that ages are upper limits, while the masses are lower limits, since no attempt was made to correct for extinction. Clearly, some amount of extinction is present. In particular, young SCs are assumed to be embedded in dust that is present in the star-forming region. Although the dust might clear in as little as a few Myr (Larsen, 2010), $0.5 < A_V < 2.5$ mag extinction is found for 0−4 Myr old clusters (Whitmore & Zhang, 2002; Reines et al., 2008). On the other hand, given the blueness of clusters with (F435W−F814W) < 0.51, the extinction cannot be larger than $A_{\rm V} = 1$ mag.

Table 3.5 lists the percentage of SCs with (F435W−F814W) < 0.51. The percentage of these young clusters is highest in Arp 256 NED02 (57%) and lowest in Arp 220 (7%) with a median of $\sim$ 30%. The available data make it difficult to determine if a larger percentage of young clusters in a galaxy is due to a younger cluster population or due to less extinction.

For clusters with 0.51 < (F435W−F814W) < 0.98 the color-age degeneracy and unknown masses make an age estimate difficult. It would be reasonable to assume that some distribution of masses and ages is present; in which case the age range could span from a few Myrs to a few hundred Myrs. For example, Whitmore et al. (2010) find in the Antennae a similar range of cluster ages.

Clusters with (F435W−F814W)> 1.0 have either ages above 500 Myr or are much younger clusters affected by a moderate amount of extinction. Several clusters have very red colors indicating possible ages above 1 Gyr and hence could be old globular clusters. However, objects with (F435W−F814W) > 1.5 and $\rm M_{F435W} < -9.5$ mag cannot be old globular clusters (assuming the upper mass limit of globular clusters of $10^6$ $\rm M_\odot$) and have be to either foreground Galactic stars or highly extinguished clusters. The same argument applies to objects that lie outside of the color range of the evolutionary models. Most galaxies in the present sample have several clusters in this region of the color-magnitude diagram, but only NGC 3256 and NGC 3690 have a significant percentage of cluster population in this range. The observed extremely red colors can be produced even by a moderate amount of extinction of $\rm A_V$=2.

It is certain that young massive un-extinguished clusters with ages less than 7.6 Myr are present and make up a large fraction of cluster population ($\sim 30\%$) in this sample of LIRGs. A population of heavily extinguished clusters is present as well. An age distribution with a range of a few Myr to a few hundred Myr as seen in the Antennae is likely. Imaging with additional filters or spectroscopy are needed to further constrain the cluster ages.

### 3.3.6 Spatial Distribution of Star Clusters

#### Surface Density Profiles

Figure 3.20 shows the cluster surface density profiles as a function of distance from the 8$\mu$m core. The 8$\mu$m core is used as the location of the nucleus of each merger component, since it suffers from less dust extinction than the optical *HST* images. The cluster surface density was calculated in circular annuli of 1 kpc width, and only the area within the masks outlining the galaxy (Chapter 2.3.1) was taken into account. The cluster surface density is generally highest near the nucleus of a galaxy and it gradually decreases with distance. Most clusters are found in the main body of a galaxy within 10 kpc. The shape of the cluster surface density profiles can be interpreted by comparing them to optical images (Figure 3.23) and to grey-scale maps in Figure 3.25. The surface density profiles of galaxies in early merger stages (NGC 0695 to Arp 256) appear jagged and have several peaks that correspond to locations of spiral arms; clusters are predominantly located in spiral arms where the cluster surface density is increased. Galaxies in late merger stages (NGC 3256 - Arp 220) have smooth surface density profiles; clusters are distributed more uniformly through-out the body of the galaxy. Mid-merger stages (NGC 3690 - NGC 2623) have profiles with several peaks that reflect an irregular distribution of large star-forming regions in the galaxy.

For roughly half of the galaxies in the sample (11 out of 19), the maximum cluster surface density coincides with the nucleus. In the remaining 8 galaxies, the maximum cluster surface density is displaced at about $1-3$ kpc from the nucleus. Four galaxies (VV 340b, NGC 7469, Arp 256 NED02, IC 5283), all of them early stage mergers, have narrow central peaks; in the rest of the sample the central peaks are broader and the cluster surface density values drop to half of their maximum values at $\sim 5$ kpc. The highest cluster surface density value (20 clusters/kpc$^2$) is found in NGC 3256, which is easily explained by its large number of clusters and proximity. The lowest cluster surface density value is in NGC 7674, which is due to the large linear size of the galaxy and more widespread distribution of clusters.

Six galaxies in this sample have extended tails: NGC 3690, IC 0883, NGC 1614, NGC 2623, NGC 3256 and NGC 0034. The LIRGs NGC 1614 and NGC 2623 have $\sim 20\%$ of their optically-visible cluster population in tails, NGC 3690 and IC 0883 have around $\sim 10\%$ and NGC 0034 and NGC 3256 have less than 1%. NGC 3256 tails are not covered completely by the ACS/WFC images.

#### Autocorrelation Functions

A more quantitative approach to the characterization of SC distribution was taken by Zhang et al. (2001). They introduced the two-point correlation function in order to investigate the spatial distribution of star clusters and compare them to flux maps in other

wavelength bands in NGC 4038/4039, the Antennae galaxies. The two-point correlation function is a well-known technique that has been extensively used to study the large scale galaxy distribution (Peebles, 1973, 1980) and can be easily adopted for the two-dimensional discrete distribution of star clusters. The three-dimensional two-point correlation function $\xi$ is defined such that $\bar{n}[1+\xi(r)]dr^3$ is the probability of finding a neighbor in a volume $dr^3$ within a distance $r$ from a random object in the sample with the average density of objects $\bar{n}$. With this, the autocorrelation function for clusters can be defined as

$$1+\xi(r) = \frac{1}{\bar{n}N}\sum_{i=1}^{N} n_i(r)$$

where $n_i(r)$ is the number density of clusters found in an aperture of radius $r$ centered on, but excluding cluster $i$, $N$ is the total number of clusters and $\bar{n}$ is the average number density of clusters. On the right hand side of the equation the mean surface density within radius $r$ from a cluster is divided by the mean surface density of the total sample; therefore $1+\xi(r)$ is effectively the surface density enhancement within radius $r$ as compared to the average over the whole galaxy. For a random distribution of clusters the auto-correlation function will be flat with $1+\xi(r) = 1$. For a clustered distribution, $1+\xi(r) > 1$ and the auto-correlation function will be peaked at small radii. The width of the central peak represents the characteristic spatial scale of association between the clusters. The statistical uncertainty is estimated as $N_p^{-1/2}$ with $N_p$ the number of pairs formed with the central clusters $i$ of the aperture (Peebles, 1980; Zhang et al., 2001). In order to estimate the number density $n_i(r)$ of clusters in an aperture centered at cluster $i$, the area of each aperture was calculated explicitly. Only the area within the masks outlining the galaxy was taken into account.

Figure 3.21 shows plots of the auto-correlation functions of SCs on a logarithmic scale. The auto-correlation functions peak sharply on small scales with a median FWHM of 0.53 pc. FWHM values show strong correlations with galaxy distance and therefore are largely artifacts of resolution rather than being representative of the true spatial scale of clustering.

The maximum $\xi+1$ values are between 25 and 13. The $\xi+1$ axis scaling is somewhat arbitrary. As already mentioned, $\xi+1$ values are a measure of overdensity within the aperture of radius $r$ as compared to the average density over the whole galaxy $\bar{n}$. The area of a galaxy is not well-defined and consequently the average density over the galaxy $\bar{n}$ is not well-defined either. In general, an aperture of 10 kpc radius centered on the 8$\mu$m core was used (except for NGC 7674), since most clusters are found within 10 kpc from the nucleus. There is no correlation with maximum values of Figure 3.20, e.g. NGC 3256 has the highest peak cluster surface density while the maximum of its auto-correlation function is one of the lowest in the sample. The reason for this is the following: the peak values of cluster surface density reflect the highest density found in a region of a galaxy, while the maximum of the auto-correlation function in Figure 3.21 reflects the local overdensity measured for all clusters in a galaxy.

Autocorrelation functions have their maxima at small radii and decrease at larger radii. Up to a distance of 1 kpc, the autocorrelation functions in a log-log plot are linear and can be approximated with a power law. Slopes are fit out to a radius of 1 kpc; the resulting power law indices are provided in Table 3.5. The median of the sample is $-0.77 \pm 0.13$ with minimum and maximum values of $-0.52$ and $-0.95$, respectively. These values are in

good agreement with values found by Zhang et al. (2001) in the Antennae ($-0.83$ to $-1.06$ for cluster populations of different ages ) and Scheepmaker et al. (2009) in M51 ($-0.8$ and $-0.7$).

In Figure 3.22, indices of the power law, fitted to the auto-correlation functions, are plotted versus the merger order of the galaxy (as seen in Figure 3.3). Merger orders $4-7$ are galaxy pairs and therefore have two data points. The steepest slopes are found in UGC 11415, IC 5283 and Arp 256 NED02 and the shallowest slopes are in NGC 3256 and NGC 3690. A possible trend emerges: early merger stage LIRGs (merger orders $1-7$) appear to have steeper slopes and late merger stages (merger orders $8-15$) shallower slopes. The median auto-correlation function index of galaxies in early merger stages is $-0.84 \pm 0.07$ and the median index of galaxies in late merger stages is $-0.62 \pm 0.09$. The Mann-Whitney U test shows a statistically significant difference of both means ($p = 5.2 \times 10^{-5}$), and the Kolmogorov-Smirnov test ($p = 2.7 \times 10^{-4}$) confirms that the auto-correlation function indices of galaxies in early and late merger stages were drawn from different populations. A higher power-law index of galaxies in early merger stages indicates a larger degree of "clustering", while in late merger stages individual clusters are distributed through-out the galaxy. This finding is confirmed also by a visual inspection of the ACS images and cluster surface density profiles. Clusters in early merger stages are found in spiral arms and giant star-forming regions with a large degree of "clustering", while in late merger stages clusters are spread out through-out the galaxy.

The two-point auto-correlation function provides some insights into the physical processes of cluster formation. Since SCs form in molecular could complexes, the spatial distribution of young star clusters is likely to reflect the structure of the ISM. Zhang et al. (2001) note that the scale of 1 kpc is comparable to the size of giant molecular cloud complexes in the Antennae. The power-law dependency of $\xi + 1$ with radius $r$ is a sign of a hierarchical, self-similar or fractal distribution. The index of a power-law $n$ is related to the fractal dimension $D2$ as $D2 = n + 2$ (Scheepmaker et al., 2009; Mandelbrot, 1983). Elmegreen & Elmegreen (2001) showed that the ISM has a fractal dimension of 1.3. The mean power-law index of our sample ($-0.77$) is in a good agreement. Late merger stages have smaller indexes, possibly indicating that the ISM has a different fractal dimension in late-stage mergers than in spirals, or that clusters have dispersed from their original formation locations.

### 3.3.7 Distribution of Flux in near-UV and mid-IR

One of the main benefits of the GOALS data set is the availability of observations at multiple wavelengths (Armus et al., 2009), which makes it possible to compare the properties of star formation traced by the optically visible SCs to star formation traced by *GALEX* near-UV and *Spitzer* mid-IR images. The *GALEX* and *Spitzer* IRAC resolutions ($5.3''$ and $2''$, respectively), although significantly lower than the resolution of *HST*/ACS ($0.1''$), still permit an assessment of the distribution of large-scale star-forming regions as traced at these wavelengths. The details of *GALEX* near-UV and *Spitzer* mid-IR imaging are presented in Howell et al. (2010) and Mazzarella (2011).

Continuum fluxes in the ultraviolet and infrared spectral regions are among the main indicators of star-formation activity and are widely used to estimate star formation rates of galaxies (e.g., Kennicutt, 1998). The far- and near-UV trace directly the emission from

photospheres of young massive stars. Dust attenuation poses a serious problem since even a moderate amount of dust extinction reduces the UV flux significantly. In the particular case of LIRGs, UV traces on average only $\sim 2.8\%$ of the total SFR (Howell et al., 2010). The IRAC 8$\mu$m channel is dominated by emission from Polycyclic Aromatic Hydrocarbons (PAH) which are heated by UV photons. In certain cases, the PAH emission can be regarded as a measure of the amount of UV radiation, e.g. in actively star-forming regions with uniform metallicity and little contribution from the general radiation field of the galaxy, the 8$\mu$m emission correlates almost linearly with the SFR (e.g., Figure 3 of Calzetti et al., 2007). The application of PAHs as a star formation tracer on galactic scales is problematic since the PAH abundance is dependent on metallicity and PAHs are excited by the general radiation field originating from older stars as well. Besides, PAHs are destroyed by harsh UV photon fields in star-forming regions and the emission rather originates in the rims of HII regions (Helou et al., 2004; Bendo, 2006). MIPS 24$\mu$m channel is a good tracer of star formation as well (Calzetti et al., 2005, 2007), but it is not used for this morphology analysis because the 24$\mu$m images are have low resolution and show signatures of the instrumental PSF.

Figure 3.23 shows the appearance of LIRGs in the cluster-rich sample in four different filters: *GALEX* near-UV (0.23$\mu$m), *HST*/ACS F435W (0.4$\mu$m) and F814W (0.8$\mu$m) and *Spitzer* IRAC 8$\mu$m. The images are in the same merger sequence as Figure 3.3. The 3.6$\mu$m, 4.5$\mu$m and 5.8$\mu$m IRAC images are omitted since their morphology is very similar to the 8$\mu$m images. The *Spitzer* MIPS 24$\mu$m emission is not resolved and is omitted as well.

Optical F435W and F814W *HST*/ACS images of our sample show a wide variety of morphologies. These high resolution images reveal an abundance of structures – spiral arms, dust lanes, star-forming regions/complexes and tails. The F435W and F814W images are similar in appearance. The F435W images highlight star-forming regions; dust lanes are prominent as dark patches. The F814W images are less affected by dust and trace light from the older stellar population and the nucleus.

The morphology of *GALEX* near-UV images can be roughly divided into 2 classes: (i) bright nuclear region with knots distributed throughout the lower surface brightness spiral arm emission and (ii) diffuse UV emission similar in extent to optical images with a lack of prominent UV emission from the nucleus. Class (i) encompasses early merger stages VV 340b, NGC 7674, NGC 6786 / UGC 11415, NGC 7469, as well NGC 3690, IC 1623 and NGC 3256. Class (ii) is represented by NGC 0695, NGC 5257/8, Arp 256, IC 0883, NGC 2623 and NGC 0034. In NGC 1614 most UV emission originates from a bright star-forming region, and the nucleus is less prominent. Arp 220 shows very little UV emission.

The IRAC 8$\mu$m images can be divided into three classes. The first two classes are identical to the UV classes; and class (iii) are systems with an unresolved bright nucleus and almost no extended emission. Class (i), similar to UV images, encompasses early merger stages VV 340b, NGC 7674, NGC 6786 / UGC 11415, Arp 256 NED01 as well as NGC 3690, IC 1623, NGC 1614 and NGC 3256. Class (ii) includes NGC 0695, NGC 5257/8 and Arp 256 NED02. Finally, class (iii) contains predominantly late merger stages NGC 7469, IC 0883, NGC 2623, NGC 0034 and Arp 220.

In general, two clearly different trends as a function of merger stage are observed:
(1) In the early merger stages, the near-UV and 8$\mu$m morphology appear similar. The nuclear regions are bright, and emission from spiral arms is clearly visible.
(2) In the late merger stages, the near-UV and 8$\mu$m morphologies are very different. The

near-UV appears more diffuse and extented, whereas the 8$\mu$m morphology is more concentrated and originates primarily from the nucleus.

Figure 3.24 shows (F435W−F814W) images in grey-scale with near-UV and 8$\mu$m contours overlaid. The (F435W−F814W) images, already used in Figure 3.19, give a better view of the structure of galaxies such as dust lanes, obscured nuclei (dark shading) and blue star-forming regions (light shading). In early merger stages (mostly face-on spiral galaxies), blue star-forming regions in spiral arms run along dark red dust lanes. In late merger stages the nuclear region is obscured by dust and appears red, and giant star-forming regions stand out in light shading. As expected, in general the near-UV and 8$\mu$m emission originate in different regions: the UV flux coincides with blue galaxy regions while 8$\mu$m flux correlates with red, dusty regions. In early merger stages (NGC 0695, VV 340b, NGC 7674 and NGC 6786 / UGC 11415) 8$\mu$m and UV contours overlap somewhat since both follow the spiral arms. Starting with NGC 7469 the overlap disappears: the maxima of emission are offset, an in some cases are opposite: e.g., in IC 1623 the western galaxy is bright in UV and the eastern nucleus is bright in 8$\mu$m.

These multi-wavelength figures clearly illustrate a scenario in which the star formation within LIRGs occurs throughout the spiral arms and nuclear region of the progenitors in the early stages, with dust playing a smaller role in obscuration. As the merger progresses and gas flows inward as the spiral structure is disrupted, the star formation in the nuclear regions is enhanced, and dust has a much stronger affect on obscuring the nuclear starburst at optical and UV wavelengths.

### 3.3.8 Distribution of Star Clusters Relative to near-UV and mid-IR Emission

Figure 3.25 shows in grey-scale the surface density of clusters. The grey-scale maps were created by smoothing an image containing the positions of clusters with a Gaussian filter to match the resolution of the IRAC 8$\mu$m images. Overlaid on the grey-scale SC surface density are contours of near-UV and 8$\mu$m emission. In general, the distribution of near-UV emission appears to correlate better with the cluster distribution than the 8$\mu$m emission. As described in the previous section, the 8$\mu$m emission in early stage mergers follows roughly the spiral arms tracing the dark dust lanes that run along these spiral arms (e.g., in NGC 7674, NGC 6786 / UGC 11415, NGC 5257/8 and Arp 256). In these cases, there is some degree of overlap between cluster locations and 8$\mu$m emission contours. For example, in NGC 7674 knots of 8$\mu$m emission coincide with high cluster density areas as well as spiral arms. With progressing merger stage the images no longer show a clear association between 8$\mu$m emission and cluster locations. In particular, 8$\mu$m emission emanates from the nucleus while the SC distribution is extended. In these late merger stage systems, the near-UV emission appears to trace the clusters more effectively than the 8$\mu$m emission. In some cases the peaks (NGC 3690, IC 1623, IC 0883, NGC 1614) or higher contours (NGC 2623, NGC 3256) of near-UV emission are directly associated with cluster-dense regions.

To test the above visual impression, cross-correlation functions between SC locations and the 8$\mu$m and near-UV fluxes were calculated. Zhang et al. (2001) define the cross-correlation

function between SC locations and flux maps as

$$1 + \xi(r) = \frac{1}{\bar{f}N} \sum_{i=1}^{N} f_i(r)$$

where $f_i(r)$ is the intensity (i.e. flux per pixel) in an aperture with radius $r$ centered on cluster $i$, and $\bar{f}$ is the mean intensity over the galaxy. Only the statistical uncertainty due to a finite number of clusters $N$ is taken into account; the uncertainty in flux estimates is neglected, leading to uncertainties of $N^{-1/2}$.

Figure 3.26 shows the results of the cross-correlation of SC locations with 8$\mu$m and near-UV fluxes. Some degree of correlation is expected simply due to the fact that both, SCs and flux, are located within the galaxy. As mentioned in Chapter 3.3.6, the $\xi + 1$ axis scaling is somewhat arbitrary. In case of cross-correlation functions, $\xi + 1$ values are a measure of flux excess within the aperture of radius $r$ as compared to the average flux $\bar{f}$ over the whole galaxy. In order to compare near-UV and 8$\mu$m fluxes, the correlation functions were calculated using the same area in both the UV and 8$\mu$m images, usually 48″ was sufficient to cover the entire flux of a galaxy.

Correlation functions with near-UV emission (red line) have Gaussian shapes, with a maximum at small radii and decreasing smoothly. The FWHM has a median value of 6.9 kpc; i.e., the near-UV emission traces clusters rather diffusely. The FWHM of the correlation functions show a strong dependence on the distance of the galaxy, which is clearly an effect of resolution.

The 8$\mu$m correlation functions (black line) have peaks with approximately half the amplitude of the near-UV functions. Further, the profiles are flatter and peak either at small radii or have a maximum at 5−8 kpc. This latter feature is due to the fact that, in many LIRGs, the mid-infrared emission is concentrated in the nuclear region, which is offset from the main location of clusters (e.g., NGC 2623). These offsets primarily occur at late merger stages, a slightly better correlation for early merger stages can be inferred, as seen also in Figure 3.25.

The correlation functions confirm the visual impression: near-UV emission is clearly better associated with young SCs than 8$\mu$m emission. This finding is not surprising: as already mentioned in Chapter 3.3.2 the UV emission arises from young massive un-obscured stars and traces the same type of star formation as the young SCs.

## 3.4 Conclusions

The cluster populations of 15 cluster-rich ($> 140$), nearby ($z < 0.034$) LIRGs from the GOALS sample were investigated. *Hubble Space Telescope* ACS/WFPC images obtained with the F435W and F814W filters were used for cluster detection and photometry. The following conclusions have been reached:

- The overall appearance of host galaxies in optical images shows clear signs of an interaction process. The cluster-rich LIRGs sample contains systems at different interaction stages, from widely separated galaxy pairs to apparent single-nucleus late-stage mergers.

- The number of detected SCs ranges between 150 and 1700 per galaxy, with a median of $\sim 300$ clusters. The number of detected SCs is affected by the distance to the galaxy, galaxy orientation, and the amount of dust obscuration, and thus may not reflect the intrinsic cluster population of a LIRG.

- The apparent magnitudes of detected SCs in F435W and F814W filters range from 21 to 27 mag, corresponding to the absolute magnitude range of $-13$ to $-9$ mag.

- The (F435W$-$F814W) colors of clusters vary between $-0.5 <$ (F435W$-$F814W) $< 3$; median (F435W$-$F814W) colors of a SC population in a galaxy range between 0.43 and 1.13.

- The specific frequency, $T_N$, (i.e., a measure of the number of clusters per unit host galaxy luminosity) for young clusters, limited to $M_{F435W} < -9$ mag and corrected for completeness, ranges from 0.67 to 1.73 with a median of $1.14 \pm 0.30$. The specific frequency is enhanced in this sample of LIRGs as compared to local spirals, which have values in the range of 0.18 to 1.75 with a median of $0.45 \pm 0.53$ (Larsen & Richtler, 2000).

- The specific luminosity, $T_L$, (i.e. the percentage of flux contributed by clusters to the total flux of the host galaxy) varies between 0.3 and 7.3 with a median $3.4 \pm 2.0$ in F435W and $1.9 \pm 0.9$ in F814W images. The relation of $T_L$ with total SFR, found in normal spiral galaxies (Larsen & Richtler, 2000) is not valid for LIRGs, but instead a trend of $T_L$ with SFR derived from FUV fluxes is observed.

- The present LIRGs sample contains some of the most luminous clusters observed so far, with brightest clusters having $M_{F435W} \sim -17$ mag. The cluster-rich LIRGs follow well the brightest cluster – SFR correlation observed for lower luminosity star-forming galaxies.

- Power-law indices of completeness-corrected luminosity functions have median values of $-1.91 \pm 0.21$ and $-1.88 \pm 0.20$ for F435W and F814W images, respectively. These values are in good agreement with previously published results for other galaxy samples (e.g., Portegies Zwart et al. (2010) and references therein).

- In order to constrain cluster ages, color-magnitude diagrams ((F435W$-$F814W) versus $M_{F435W}$) were constructed and Bruzual-Charlot population synthesis models were plotted for various cluster masses. A significant population of very young un-extinguished SCs that can be reliably age-dated as being younger than 7.6 Myr is present. These clusters comprise $\sim 9\% - 60\%$ of the cluster population, with a median value of $\sim 30\%$. Given the unknown extinction and cluster masses, the ages of cluster population can vary from $5 \times 10^6$ years to few $10^8$ years. Approximately 80% of the clusters with colors $> 2.0$ are associated with dust lanes, and thus their colors are likely red primarily due to extinction rather than age.

- Autocorrelation functions of SC locations were calculated and a power-law fit to the inner 1 kpc. The power-law indices vary between $-0.52$ and $-0.95$ with a median of

$-0.77 \pm 0.13$. Early merger stage LIRGs have the median auto-correlation function index of $-0.84 \pm 0.07$ and late merger stages have the median index of $-0.62 \pm 0.09$, indicating a larger degree of "clustering" in early merger stages. SCs in LIRGs in early merger stages are found in spiral arms and giant star-forming regions with a large degree of clustering, while in late merger stages SCs are dispersed throughout the galaxy.

- A comparison of galaxy morphology in near-UV and mid-IR ($8\mu$m) shows that early stage mergers have similar near-UV and $8\mu$m morphologies, with bright nuclear regions and emission from spiral arms. In contrast, late stage mergers have extended and diffuse near-UV emission and compact $8\mu$m emission primarily concentrated in the nuclear regions. This is consistent with a scenario in which the star formation within LIRGs occurs throughout the spiral arms and nuclear regions of the progenitors in the early stages, with dust playing a smaller role in obscuration. As the merger progresses and gas flows inward as the spiral structure is disrupted, the star formation in the nuclear regions is enhanced, and dust has a much stronger effect on obscuring the nuclear starburst.

- Cluster density maps were constructed in order to compare the distribution of optically visible clusters with IR and UV imaging data. The cluster-overdense regions do not coincide well with $8\mu$m/PAH emission as traced by *Spitzer* IRAC images but are rather associated with high surface brightness regions in *GALEX* near-UV images. Cross-correlation functions of SC locations with near-UV and $8\mu$m fluxes were computed. The correlation coefficients (amplitudes) of the near-UV are about twice as large as $8\mu$m coefficients. It is concluded that, in general, the optical star formation is not associated with regions of strong PAH emission and imbedded star formation. This finding is not surprising since un-obscured young SCs are expected to produce a significant amount of UV emission and $8\mu$m/PAH emission originates primarily in obscured central regions.

- Optically visible young clusters and UV emission represent un-obscured star formation which appears to be unassociated with the bulk of the star formation that takes place in the dusty central regions of LIRGs.

Table 3.1. Cluster–Rich LIRGs Sample

| Name IRAS | Name Optical ID | R.A. (J2000) | Dec. (J2000) | $V_{Helio}$ ($kms^{-1}$) | $D_L$ (Mpc) | scale (kpc/") | log $L_{IR}$ ($L_\odot$) |
|---|---|---|---|---|---|---|---|
| 00085-1223 | NGC 0034 | 00h11m06.5s | -12d06m26s | 5881 | 84.1 | 0.392 | 11.49 |
| 00163-1039 | Arp 256 | | | | | | 11.48 |
| | Arp 256 NED02 | 00h18m50.1s | -10d21m42s | 8193 | 118.0 | 0.540 | |
| | Arp 256 NED01 | 00h18m50.9s | -10d22m37s | 8125 | 117.0 | 0.536 | |
| 01053-1746 | IC 1623 | 01h07m47.2s | -17d30m25s | 6016 | 85.5 | 0.399 | 11.71 |
| 01484+2220 | NGC 0695 | 01h51m14.2s | +22d34m57s | 9735 | 139.0 | 0.634 | 11.68 |
| 04315-0840 | NGC 1614 | 04h33m59.8s | -08d34m44s | 4778 | 67.8 | 0.319 | 11.65 |
| 08354+2555 | NGC 2623 | 08h38m24.1s | +25d45m17s | 5549 | 84.1 | 0.393 | 11.60 |
| 10257-4338 | NGC 3256 | 10h27m51.3s | -43d54m14s | 2804 | 38.9 | 0.185 | 11.64 |
| 11257+5850 | NGC 3690 | 11h28m32.2s | +58d33m44s | 3093 | 50.7 | 0.242 | 11.93 |
| 13183+3423 | IC 0883 | 13h20m35.3s | +34d08m22s | 6985 | 110.0 | 0.507 | 11.73 |
| 13373+0105 | Arp 240 | | | | | | 11.62 |
| | NGC 5258 | 13h39m57.7s | +00d49m51s | 6757 | 108.0 | 0.500 | |
| | NGC 5257 | 13h39m52.9s | +00d50m24s | 6798 | 109.0 | 0.503 | |
| 14547+2449 | VV340 | | | | | | 11.74 |
| | VV340a | 14h54m48.3s | +24d49m03s | 10094 | 157.0 | 0.710 | |
| | VV340b | 14h54m47.9s | +24d48m25s | 10029 | 156.0 | 0.706 | |
| 15327+2340 | Arp 220 | 15h34m57.1s | +23d30m11s | 5434 | 87.9 | 0.410 | 12.28 |
| 19120+7320 | VV 414 | | | | | | 11.49 |
| | NGC 6786 | 19h10m53.9s | +73d24m37s | 7500 | 113.0 | 0.519 | |
| | UGC 11415 | 19h11m04.5s | +73d25m36s | 7555 | 113.0 | 0.522 | |
| 23007+0836 | Arp 298 | | | | | | 11.65 |
| | NGC 7469 | 23h03m15.6s | +08d52m26s | 4892 | 70.8 | 0.332 | |
| | IC 5283 | 23h03m18.0s | +08d53m37s | 4804 | 69.6 | 0.327 | |
| 23254+0830 | Arp 182 | | | | | | 11.56 |
| | NGC 7674 | 23h27m56.7s | +08d46m45s | 8671 | 125.0 | 0.574 | |
| | NGC 7674A | 23h27m58.8s | +08d46m58s | 8852 | 128.0 | 0.585 | |

Note. — Column 1: Name of the IRAS source. Column 2: Name of the optical source. The systems are separated into individual galaxies/components. Columns 3 and 4: Right Ascension and Declination from NED. Column 5: Heliocentric velocity. Column 6: The luminosity distance in Megaparsecs. Column 7: The total infrared luminosity in log10 Solar units. The redshift dependent values were derived by correcting the heliocentric velocity for the 3-attractor flow model of Mould et al. 2000 and adopting cosmological parameters $H_0 = 70 kms^{-1}Mpc^{-1}, \Omega_M = 0.28$, and $\Omega_V = 0.72$ based on the five-year WMAP results (Hinshaw et al., 2009), as provided by NED. Values are consistent with Armus et al., 2009.

Table 3.2. Host Galaxy Photometry in the Cluster–Rich LIRGs Sample

| Name | $m_{F435W}$ | $M_{F435W}$ | $m_{F814W}$ | $M_{F814W}$ | merger stage |
|---|---|---|---|---|---|
| NGC 0034 | 13.91 ± 0.005 | -20.83 | 12.32 ± 0.002 | -22.36 | late |
| Arp 256 | 13.99 ± 0.005 | -21.52 | 12.61 ± 0.003 | -22.81 | early |
| Arp 256 NED02 | 14.73 ± 0.007 | -20.77 | 13.34 ± 0.004 | -22.17 | |
| Arp 256 NED01 | 14.75 ± 0.007 | -20.75 | 13.39 ± 0.004 | -22.12 | |
| IC 1623 | 13.31 ± 0.003 | -21.42 | 12.06 ± 0.002 | -22.63 | mid |
| NGC 0695 | 14.32 ± 0.006 | -21.79 | 12.49 ± 0.003 | -23.40 | early |
| NGC 1614 | 13.69 ± 0.004 | -21.13 | 11.87 ± 0.002 | -22.59 | mid |
| NGC 2623 | 14.29 ± 0.005 | -20.51 | 12.61 ± 0.003 | -22.10 | mid |
| NGC 3256 | 12.22 ± 0.002 | -21.25 | 10.42 ± 0.001 | -22.76 | late |
| NGC 3690 | 12.34 ± 0.002 | -21.25 | 10.77 ± 0.001 | -22.79 | mid |
| IC 0883 | 14.54 ± 0.006 | -20.72 | 12.92 ± 0.003 | -22.31 | mid |
| Arp 240 | 12.86 ± 0.003 | -22.44 | 11.28 ± 0.002 | -23.95 | early |
| NGC 5258 | 13.64 ± 0.004 | -21.65 | 11.97 ± 0.002 | -23.27 | |
| NGC 5257 | 13.58 ± 0.004 | -21.71 | 12.10 ± 0.002 | -23.13 | |
| VV340 | 14.35 ± 0.006 | -21.81 | 12.43 ± 0.003 | -23.63 | early |
| VV340a | 15.33 ± 0.009 | -20.83 | 13.09 ± 0.004 | -22.98 | |
| VV340b | 14.96 ± 0.007 | -21.21 | 13.37 ± 0.004 | -22.69 | |
| Arp 220 | 14.08 ± 0.005 | -20.86 | 12.07 ± 0.002 | -22.75 | late |
| VV 414 | 13.72 ± 0.004 | -22.15 | 11.79 ± 0.002 | -23.75 | early |
| NGC 6786 | 14.30 ± 0.005 | -21.57 | 12.47 ± 0.003 | -23.07 | |
| UGC 11415 | 14.67 ± 0.006 | -21.20 | 12.63 ± 0.003 | -22.91 | |
| Arp 298 | 13.09 ± 0.003 | -21.46 | 11.15 ± 0.001 | -23.23 | early |
| NGC 7469 | 13.30 ± 0.003 | -21.24 | 11.41 ± 0.002 | -22.98 | |
| IC 5283 | 14.92 ± 0.007 | -19.62 | 12.82 ± 0.003 | -21.56 | |
| Arp 182 | 13.78 ± 0.004 | -21.95 | 11.99 ± 0.002 | -23.61 | early |
| NGC 7674 | 14.10 ± 0.005 | -21.64 | 12.35 ± 0.003 | -23.25 | |
| NGC 7674A | 16.05 ± 0.012 | -19.69 | 13.96 ± 0.005 | -21.64 | |

Note. — Column 1: Name of the optical source. Column 2: Apparent F435W magnitude. Column 3: Absolute F435W magnitude calculated using luminosity distance in Table 1. Column 4: Apparent F814W magnitude. Column 5: Absolute F814W magnitude calculated using luminosity distance in Table 1. Column 6: Merger stage

Table 3.3. Star Cluster Properties in the Cluster–Rich LIRGs Sample I

| Name | $N_{cl}$ | (F435W−F814W) | $T_N$ | $T_L$(F435W) | $T_L$(F814W) |
|---|---|---|---|---|---|
| NGC 0034 | 182 | 0.84 ± 0.48 | 0.674 ± 0.03 | 2.43 ± 0.04 | 1.52 ± 0.03 |
| Arp 256 | 274 | | | | |
| Arp 256 NED02 | 169 | 0.43 ± 0.45 | 1.442 ± 0.10 | 4.64 ± 0.09 | 1.86 ± 0.05 |
| Arp 256 NED01 | 105 | 0.52 ± 0.46 | 0.971 ± 0.06 | 2.72 ± 0.07 | 1.37 ± 0.05 |
| IC 1623 | 313 | 0.57 ± 0.72 | 0.990 ± 0.04 | 7.01 ± 0.12 | 3.54 ± 0.07 |
| NGC 0695 | 200 | 1.01 ± 0.57 | 1.003 ± 0.08 | 3.80 ± 0.15 | 2.18 ± 0.09 |
| NGC 1614 | 374 | 0.69 ± 0.55 | 1.191 ± 0.06 | 3.37 ± 0.09 | 1.82 ± 0.04 |
| NGC 2623 | 211 | 0.72 ± 0.61 | 0.946 ± 0.04 | 1.24 ± 0.04 | 0.69 ± 0.02 |
| NGC 3256 | 1729 | 0.90 ± 0.62 | 1.298 ± 0.03 | 4.83 ± 0.11 | 2.80 ± 0.06 |
| NGC 3690 | 1321 | 0.66 ± 0.62 | 1.729 ± 0.05 | 5.42 ± 0.10 | 3.17 ± 0.06 |
| IC 0883 | 164 | 0.83 ± 0.61 | 1.187 ± 0.07 | 3.07 ± 0.04 | 1.90 ± 0.02 |
| Arp 240 | 860 | | | | |
| NGC 5258 | 385 | 0.88 ± 0.59 | 1.208 ± 0.07 | 3.81 ± 0.07 | 1.95 ± 0.05 |
| NGC 5257 | 475 | 0.73 ± 0.56 | 1.529 ± 0.09 | 3.88 ± 0.13 | 1.89 ± 0.07 |
| VV340 | 202 | | | | |
| VV340a | 14 | | | | |
| VV340b | 188 | 0.56 ± 0.50 | 0.870 ± 0.07 | 2.53 ± 0.10 | 1.09 ± 0.06 |
| Arp 220 | 204 | 1.13 ± 0.65 | 0.709 ± 0.03 | 0.50 ± 0.03 | 0.33 ± 0.01 |
| VV 414 | 421 | | | | |
| NGC 6786 | 293 | 0.63 ± 0.56 | 1.137 ± 0.09 | 6.28 ± 0.12 | 2.04 ± 0.06 |
| UGC 11415 | 128 | 0.73 ± 0.53 | 0.721 ± 0.05 | 0.89 ± 0.04 | 0.37 ± 0.02 |
| Arp 298 | 414 | | | | |
| NGC 7469 | 332 | 0.71 ± 0.64 | 0.690 ± 0.02 | 7.31 ± 0.11 | 2.66 ± 0.07 |
| IC 5283 | 82 | 1.12 ± 0.87 | 1.194 ± 0.05 | 0.96 ± 0.05 | 0.66 ± 0.03 |
| Arp 182 | 299 | | | | |
| NGC 7674 | 299 | 0.68 ± 0.50 | 1.315 ± 0.11 | 1.70 ± 0.06 | 0.60 ± 0.03 |
| NGC 7674A | 0 | | | | |

Note. — Column 1 : Name of the optical source. Column 2: Number of detected star clusters. Column 3: Median (F435W−F814W) color of clusters in a galaxy. Column 4: Corrected specific frequency $T_N$, limited to $M_{F435W} < -9$ and corrected for completeness. Column 5: Specific luminosity $T_L$ in the F435W images. Column 6: Specific luminosity $T_L$ in the F814W images. No analysis was performed for VV 340a and NGC 7674A.

Table 3.4. Most Luminous Star Clusters in the Cluster–Rich LIRGs Sample

| Name | $M_{F435W}$ (mag) | (F435W−F814W) (mag) | Age (Myr) | Mass $\times 10^6(M_\odot)$ | SFR total ($M_\odot yr^{-1}$) |
|---|---|---|---|---|---|
| NGC 0034 | -15.15 | 0.78 | 7.94 | 1.33 | 46.9 |
| Arp 256 | | | | | |
| Arp 256 NED02 | -15.75 | -0.08 | 5.01 | 1.74 | 3.9 |
| Arp 256 NED01 | -14.62 | 0.28 | 6.61 | 0.67 | 48.6 |
| IC 1623 | -16.16 | -0.17 | 4.79 | 2.54 | 94.1 |
| NGC 0695 | -15.18 | 0.60 | 7.59 | 1.26 | 84.6 |
| NGC 1614 | -15.52 | 0.66 | 7.94 | 1.84 | 78.7 |
| NGC 2623 | -14.06 | 0.91 | 8.32 | 0.58 | 69.2 |
| NGC 3256 | -15.85 | 0.26 | 6.61 | 1.96 | 76.5 |
| NGC 3690 | -15.85 | 0.45 | 7.24 | 2.12 | 150.5 |
| IC 0883 | -16.27 | 0.75 | 7.94 | 3.53 | 94.2 |
| Arp 240 | | | | | |
| NGC 5258 | -16.22 | 0.92 | 8.32 | 3.77 | 36.0 |
| NGC 5257 | -15.35 | 0.50 | 7.59 | 1.46 | 35.7 |
| VV340 | | | | | |
| VV340a | | | | | |
| VV340b | -14.78 | 0.15 | 5.75 | 0.70 | 17.6 |
| Arp 220 | -12.24 | 0.73 | 7.94 | 0.11 | 327.7 |
| VV 414 | | | | | |
| NGC 6786 | -16.67 | -0.14 | 5.01 | 3.94 | 143.2 |
| UGC 11415 | -14.75 | 0.50 | 7.59 | 0.86 | 54.5 |
| Arp 298 | | | | | |
| NGC 7469 | -17.09 | 0.27 | 6.61 | 5.83 | 66.7 |
| IC 5283 | -12.30 | 1.36 | 807.24 | 0.24 | 10.7 |
| Arp 182 | | | | | |
| NGC 7674 | -14.41 | 0.05 | 5.25 | 0.52 | 61.3 |
| NGC 7674A | | | | | |

Note. — Column 1: Name of the optical source. Column 2: Absolute F435W magnitude of the most luminous cluster. Columns 3: (F435W−F814W) color of the most luminous cluster. Columns 4 and 5: Age and mass for the respective age according to Bruzual & Charlot 2003 evolutionary models. Column 6: SFR derived from *IRAS* FIR and *GALEX* FUV fluxes (Howell et al., 2010).

Table 3.5. Star Cluster Properties in the Cluster–Rich LIRGs Sample II

| Name | Luminosity Function Index $\alpha$F435W | $\alpha$F814W | Percentage SCs younger 7.6 Myr | Autocorrelation index |
|---|---|---|---|---|
| NGC 0034 | -1.70 ± 0.28 | -1.70 ± 0.26 | 9.9 | -0.69 ± 0.18 |
| Arp 256 | | | | |
| Arp 256 NED02 | -1.81 ± 0.21 | -1.78 ± 0.34 | 56.8 | -0.92 ± 0.25 |
| Arp 256 NED01 | -1.76 ± 0.22 | -1.72 ± 0.24 | 48.6 | -0.84 ± 0.33 |
| IC 1623 | -1.54 ± 0.20 | -1.50 ± 0.20 | 44.7 | -0.77 ± 0.10 |
| NGC 0695 | -1.65 ± 0.20 | -1.72 ± 0.23 | 18.0 | -0.77 ± 0.18 |
| NGC 1614 | -1.82 ± 0.27 | -1.75 ± 0.25 | 30.7 | -0.65 ± 0.07 |
| NGC 2623 | -2.12 ± 0.27 | -2.16 ± 0.24 | 25.1 | -0.77 ± 0.15 |
| NGC 3256 | -1.84 ± 0.17 | -1.91 ± 0.15 | 17.1 | -0.52 ± 0.03 |
| NGC 3690 | -1.80 ± 0.16 | -1.76 ± 0.15 | 38.3 | -0.54 ± 0.03 |
| IC 0883 | -2.17 ± 0.22 | -2.01 ± 0.21 | 17.1 | -0.59 ± 0.29 |
| Arp 240 | | | | |
| NGC 5258 | -1.91 ± 0.30 | -1.88 ± 0.29 | 16.6 | -0.84 ± 0.15 |
| NGC 5257 | -1.96 ± 0.29 | -1.97 ± 0.28 | 29.5 | -0.77 ± 0.12 |
| VV340 | | | | |
| VV340a | | | | |
| VV340b | -1.93 ± 0.26 | -1.97 ± 0.21 | 44.1 | -0.89 ± 0.38 |
| Arp 220 | -2.27 ± 0.30 | -2.15 ± 0.27 | 6.9 | -0.56 ± 0.24 |
| VV 414 | | | | |
| NGC 6786 | -1.81 ± 0.29 | -1.78 ± 0.30 | 37.9 | -0.75 ± 0.15 |
| UGC 11415 | -2.27 ± 0.30 | -1.94 ± 0.36 | 27.3 | -0.94 ± 0.26 |
| Arp 298 | | | | |
| NGC 7469 | -1.98 ± 0.39 | -2.02 ± 0.33 | 31.9 | -0.77 ± 0.11 |
| IC 5283 | -2.16 ± 0.29 | -1.54 ± 0.27 | 15.9 | -0.95 ± 0.15 |
| Arp 182 | | | | |
| NGC 7674 | -2.20 ± 0.30 | -2.22 ± 0.20 | 37.8 | -0.84 ± 0.20 |
| NGC 7674A | | | | |

Note. — Column 1: Name of the optical source. Columns 2 and 3: Luminosity function index $\alpha$ for F435W and F814W images. Column 4: Percentage of cluster population that can be reliably age-dated as younger than 7.6 Myr with no extinction correction. Column 5: Autocorrelation function index.

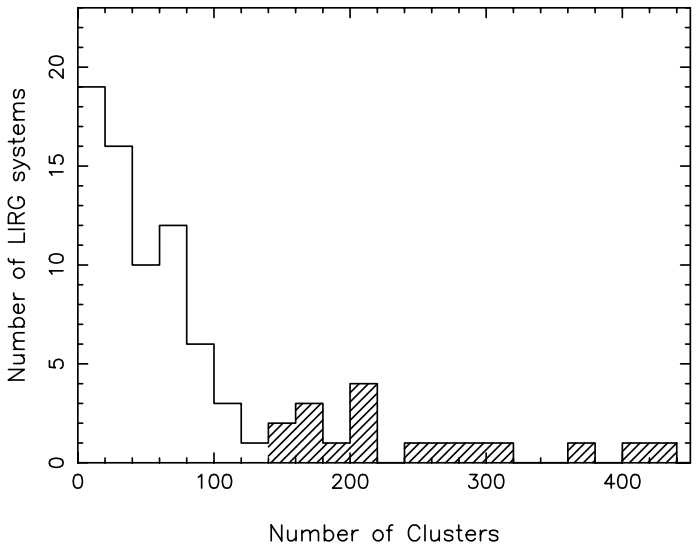


Figure 3.1: The distribution of the number of SCs per LIRG system (i.e. galaxy pairs count as one system). Three LIRGs (NGC 3256, NGC 3690 and NGC 5257) are absent from this histogram due to a very large (>800) number of SCs. The shaded portion of the histogram constitutes the cluster-rich LIRGs sample.

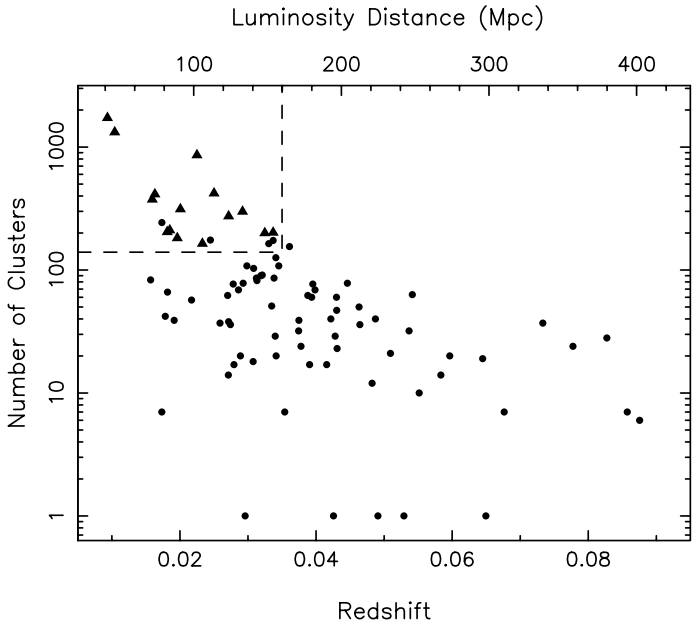


Figure 3.2: Number of detected SCs versus luminosity distance. The system in the cluster-rich LIRGs sample are denoted with triangles. The horizontal dashed lines indicates the number of clusters selection criterion, the vertical dashed line indicates the resulting luminosity distance range.

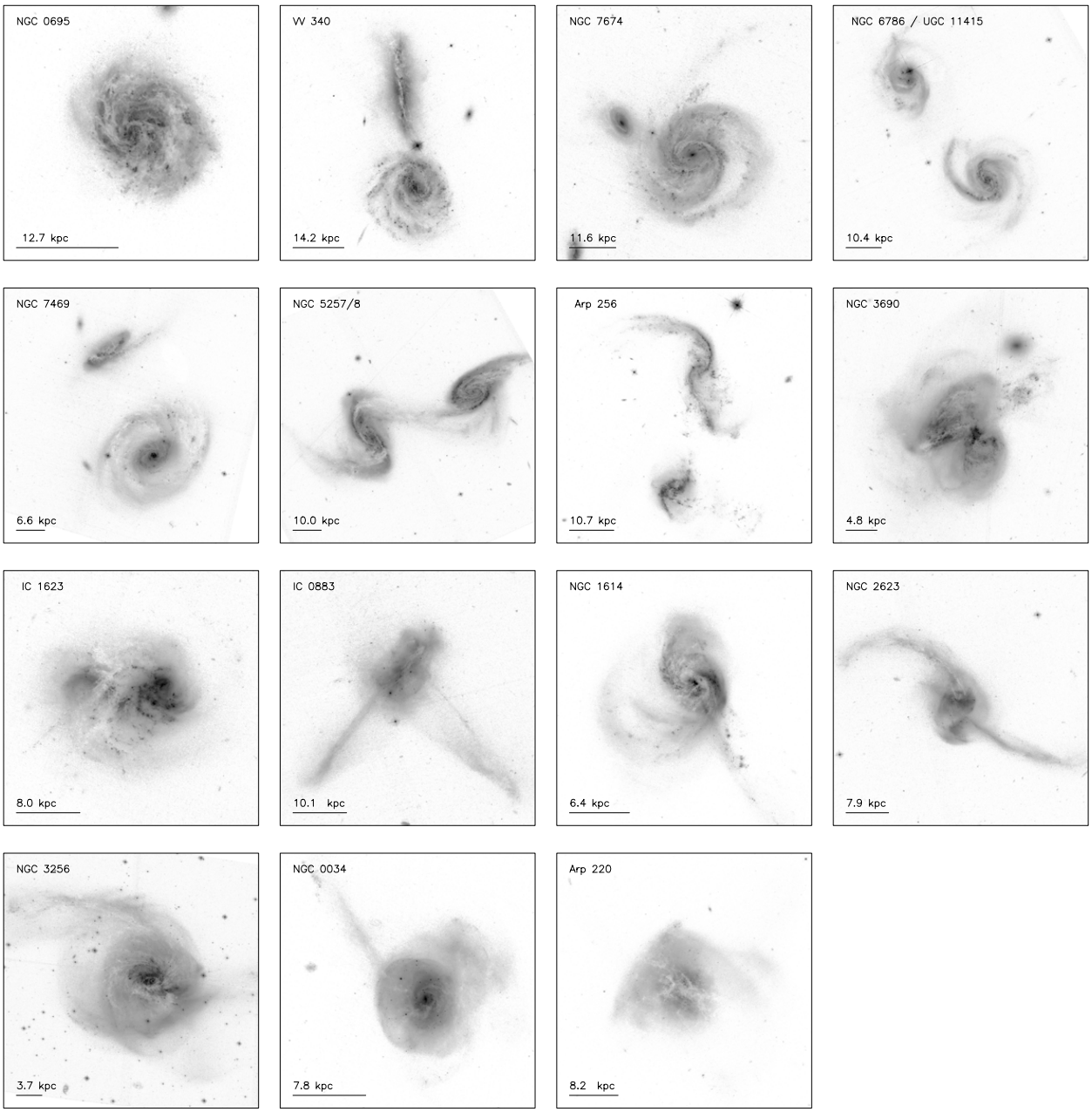


Figure 3.3: F435W images of the cluster-rich LIRGs sample in merger sequence order from the earliest stage in the upper left to latest stage in the lower right. This order is retained in subsequent figures. The scale bar in the lower left corner corresponds to 20" and the number above indicates the scale in kpc at the distance of the system.

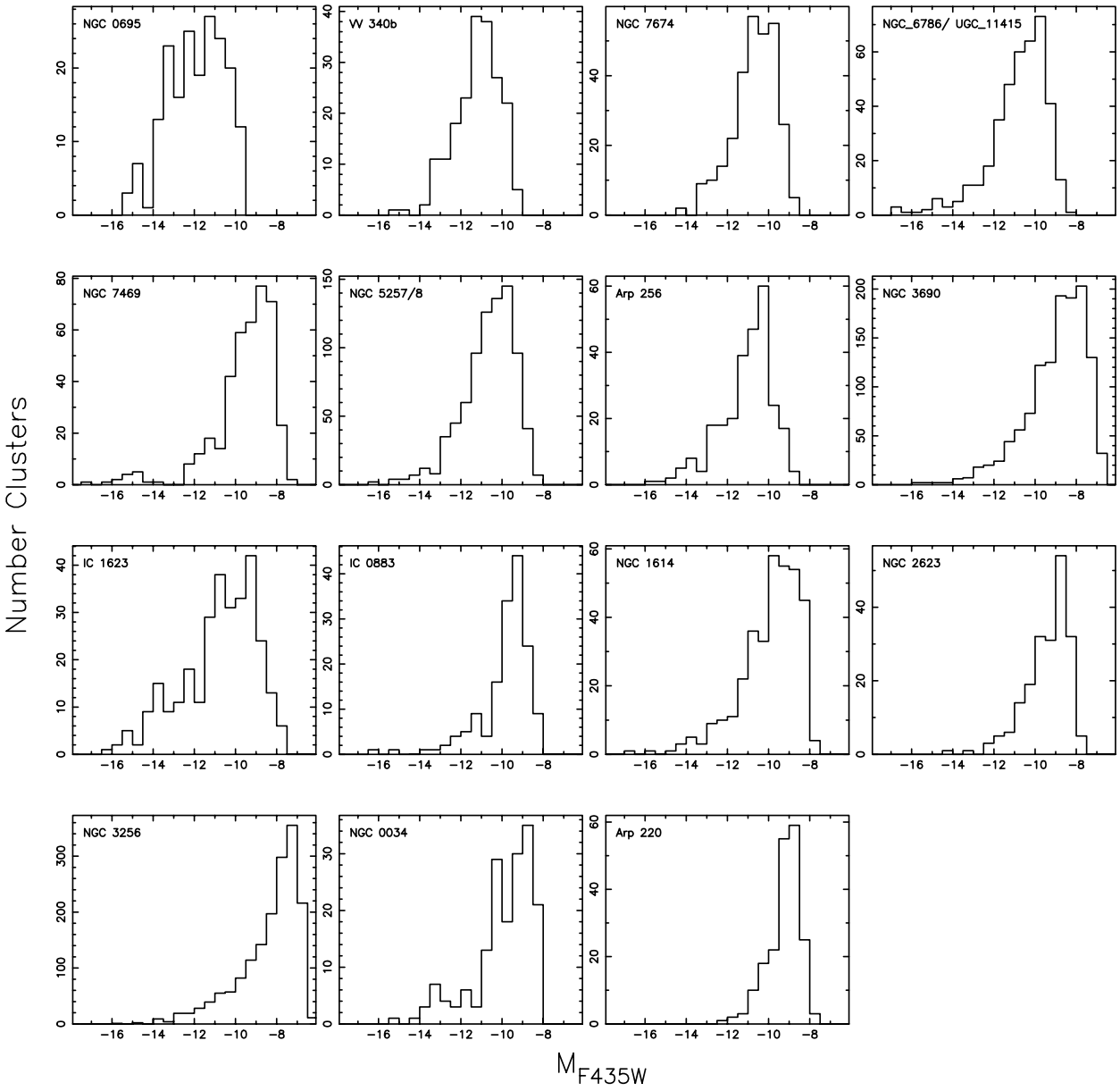


Figure 3.4: Distribution of absolute F435W magnitudes.

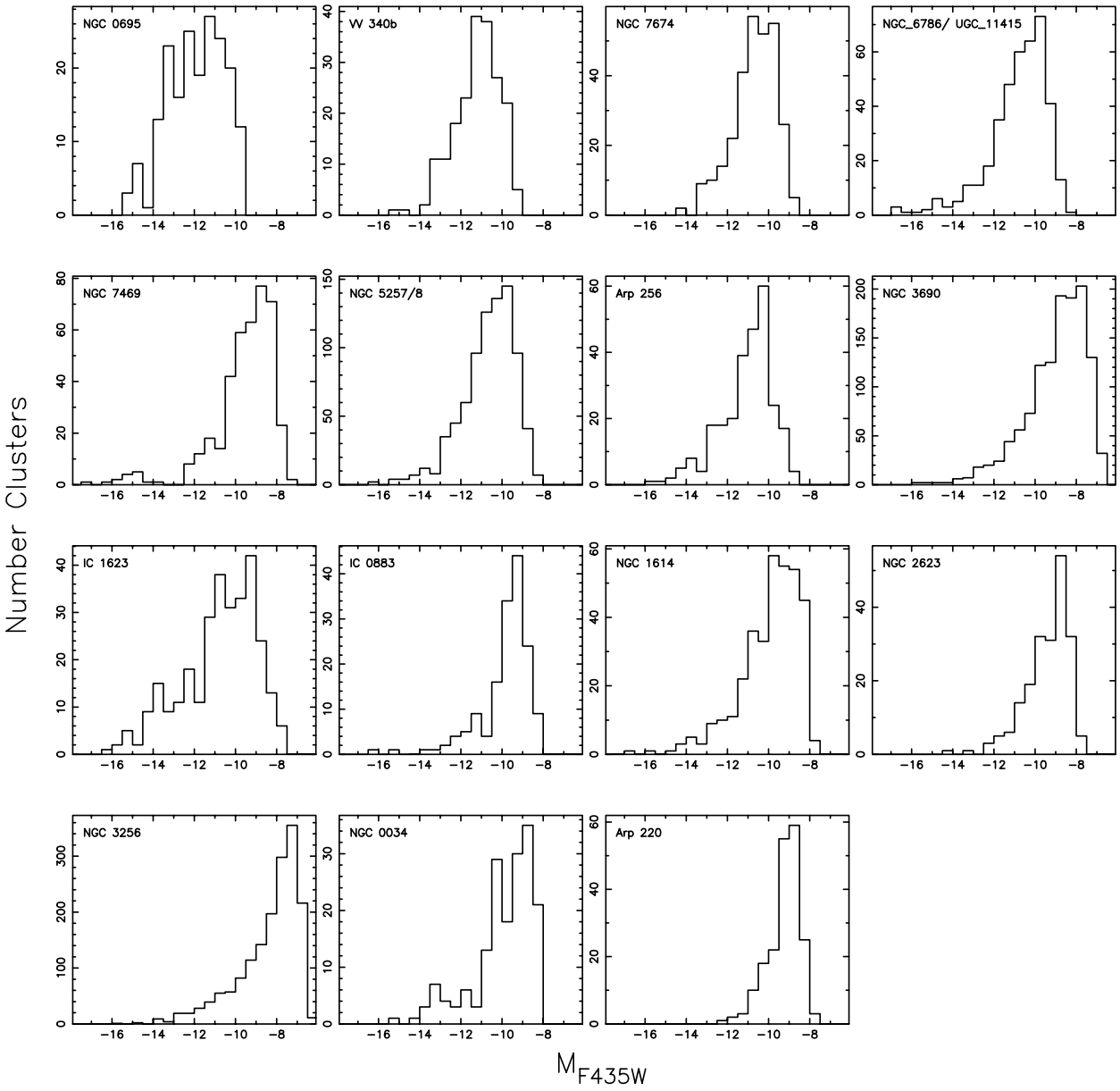


Figure 3.5: Distribution of absolute F814W magnitudes.

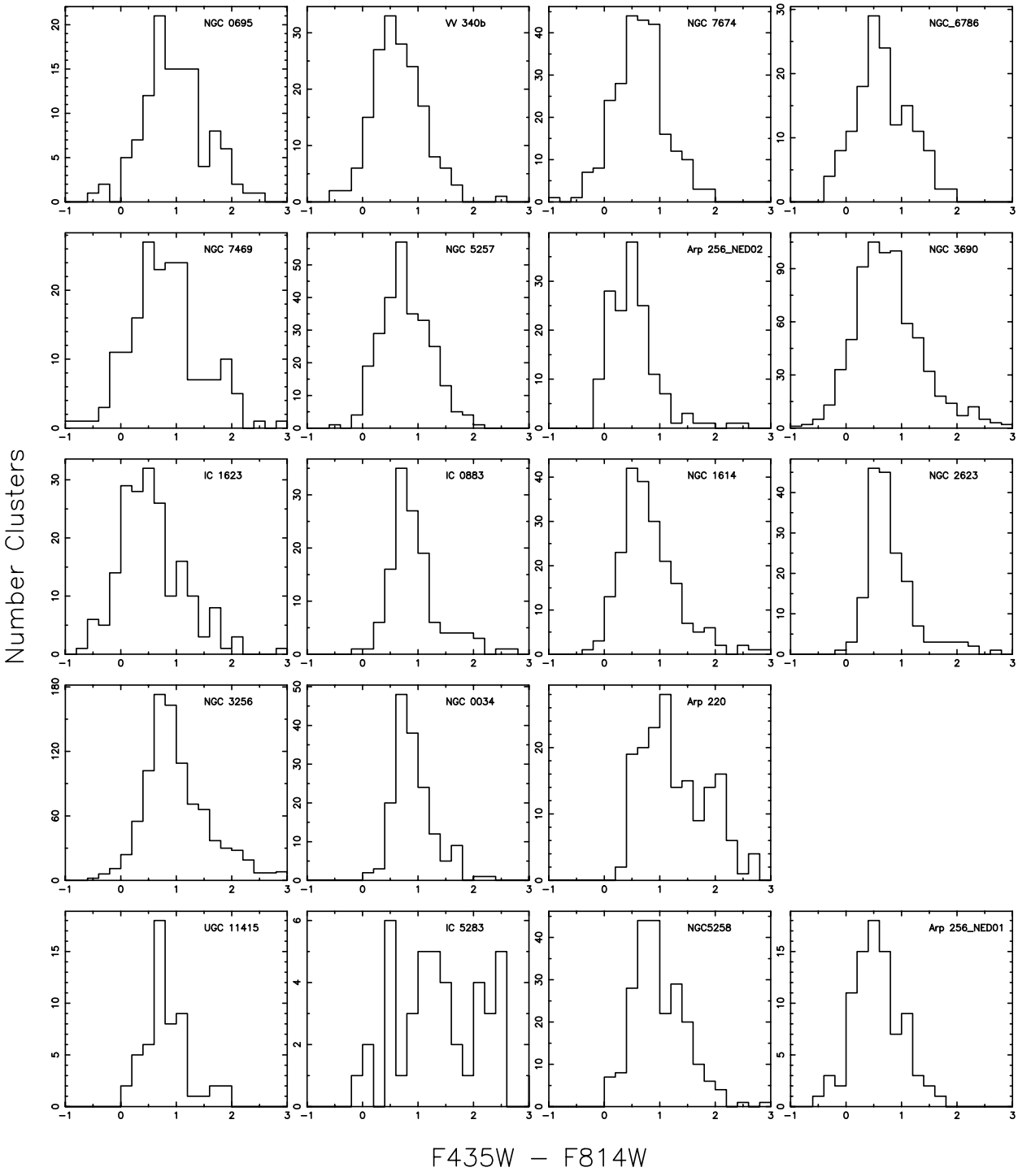


Figure 3.6: Distribution of (F435W−F814W) colors of clusters. The bottom row shows the four galaxies that are members of galaxy pairs and have fewer detected clusters.

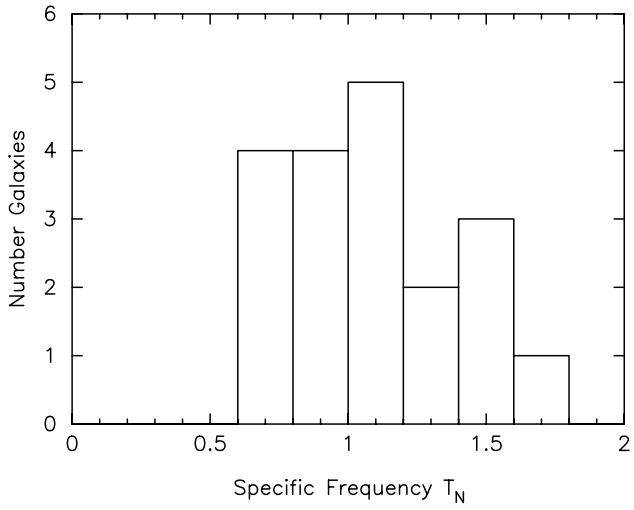


Figure 3.7: Distribution of corrected specific frequency $T_N$ values in the cluster-rich LIRGs sample.

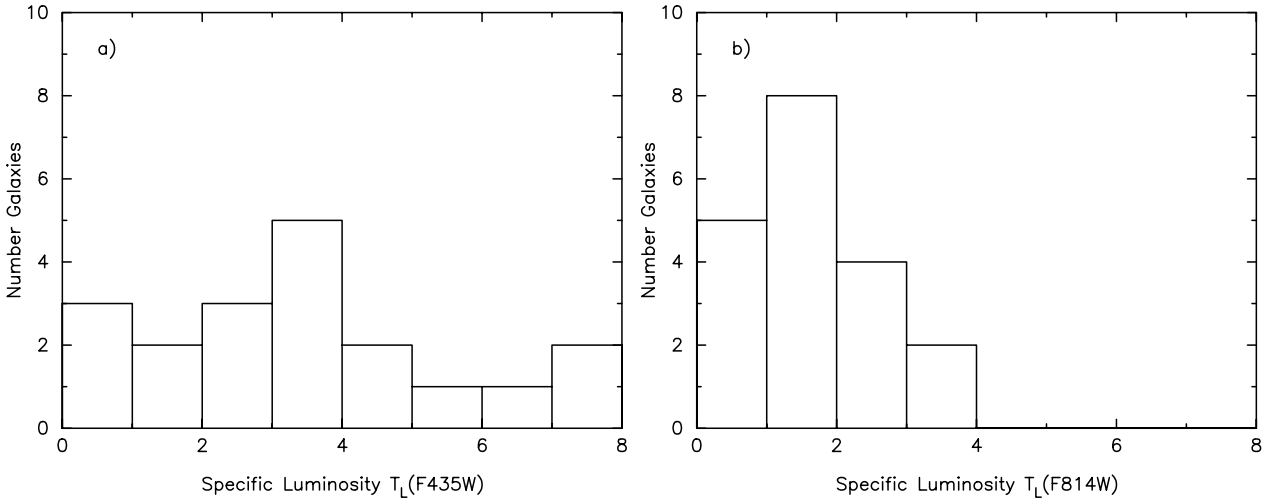


Figure 3.8: Distribution of specific luminosity $T_L$ values in the cluster-rich LIRGs sample in the F435W (panel a)) and F814W (panel b)) images.

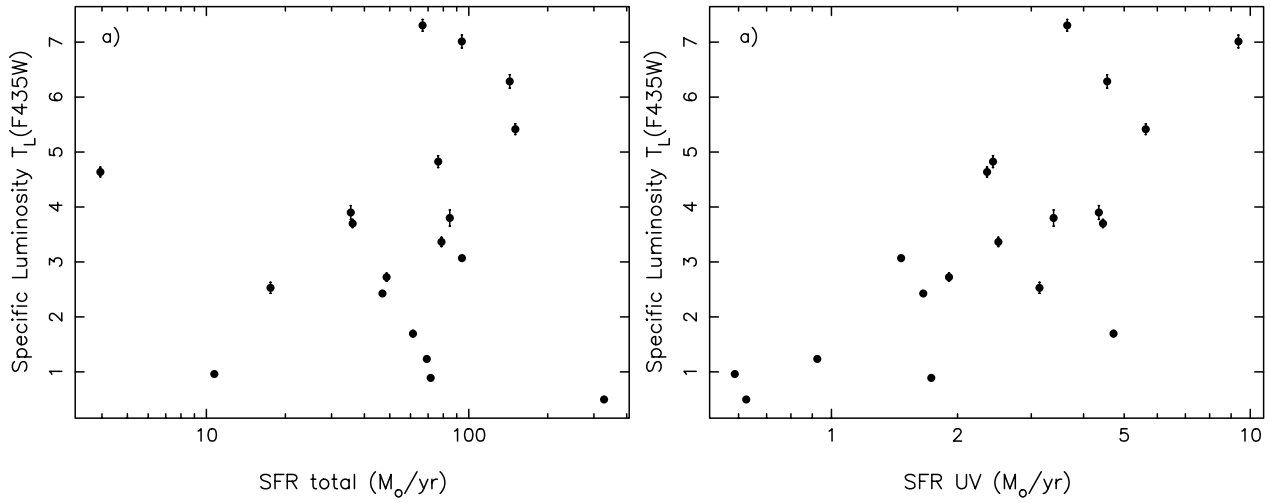


Figure 3.9: Specific luminosity $T_L$ in the F435W image versus SFR derived from FIR and FUV fluxes (panel a)) and FUV fluxes only (panel b)).

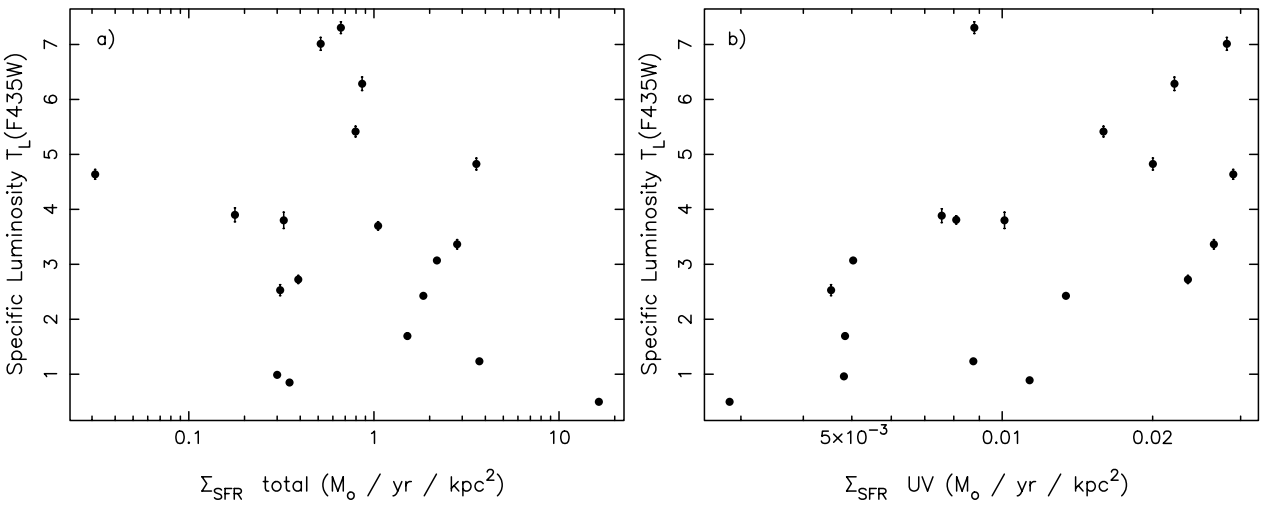


Figure 3.10: Specific luminosity in the F435W image versus $\Sigma_{SFR}$ (SFR per unit area) derived from FIR and FUV fluxes (panel a)) and $\Sigma_{SFR}$ derived from FUV fluxes only (panel b)).

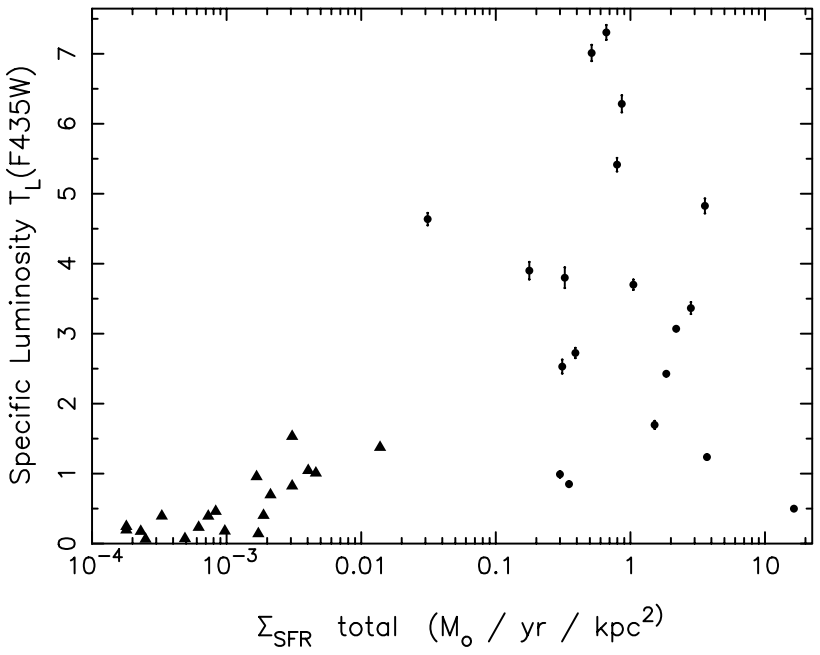


Figure 3.11: Specific luminosity $T_L$(B) versus SFR derived from FIR fluxes. The $T_L$(B) data points for nearby normal spiral galaxies from Larsen & Richtler (2000) are designated with triangles; the $T_L$(F435W) values of the cluster-rich sample are designated with points.

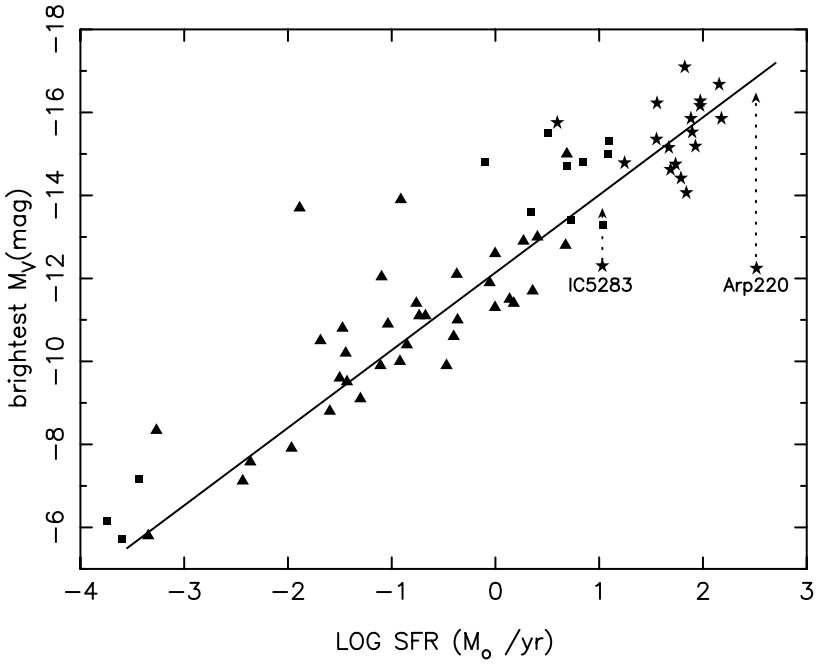


Figure 3.12: $M_V$ of the most luminous cluster within the galaxy versus SFR. The galaxies from the Larsen (2002b) sample are designated with triangles, the squares mark data from Bastian (2008) Table 1. The cluster-rich LIRGs are indicated with star symbols. The diagonal line is the fit from Weidner et al. (2004). The dashed arrows show the location of two outliers, IC 5283 and Arp 220, after correction for extinction.

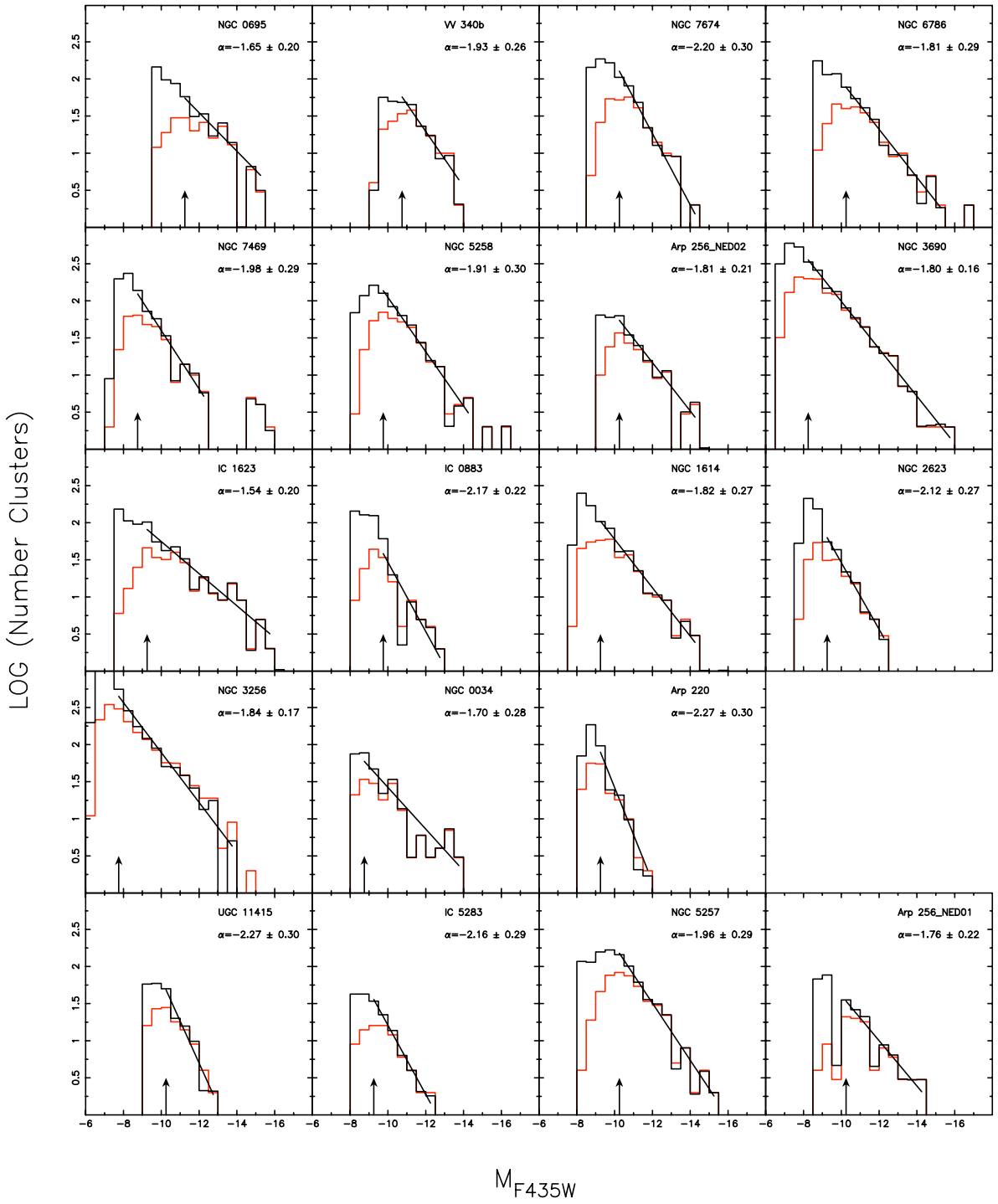


Figure 3.13: Cluster luminosity function for F435W images. The red histograms represent the raw, uncorrected luminosity distribution. The black histograms have been corrected for foreground stars contamination and for the efficiency of the detection algorithm. The black line is the $\chi^2$ fit to the corrected histograms and the derived power-law index $\alpha$ of the luminosity function is quoted in the upper right corner. The arrow indicates the 50% detection completeness limit.

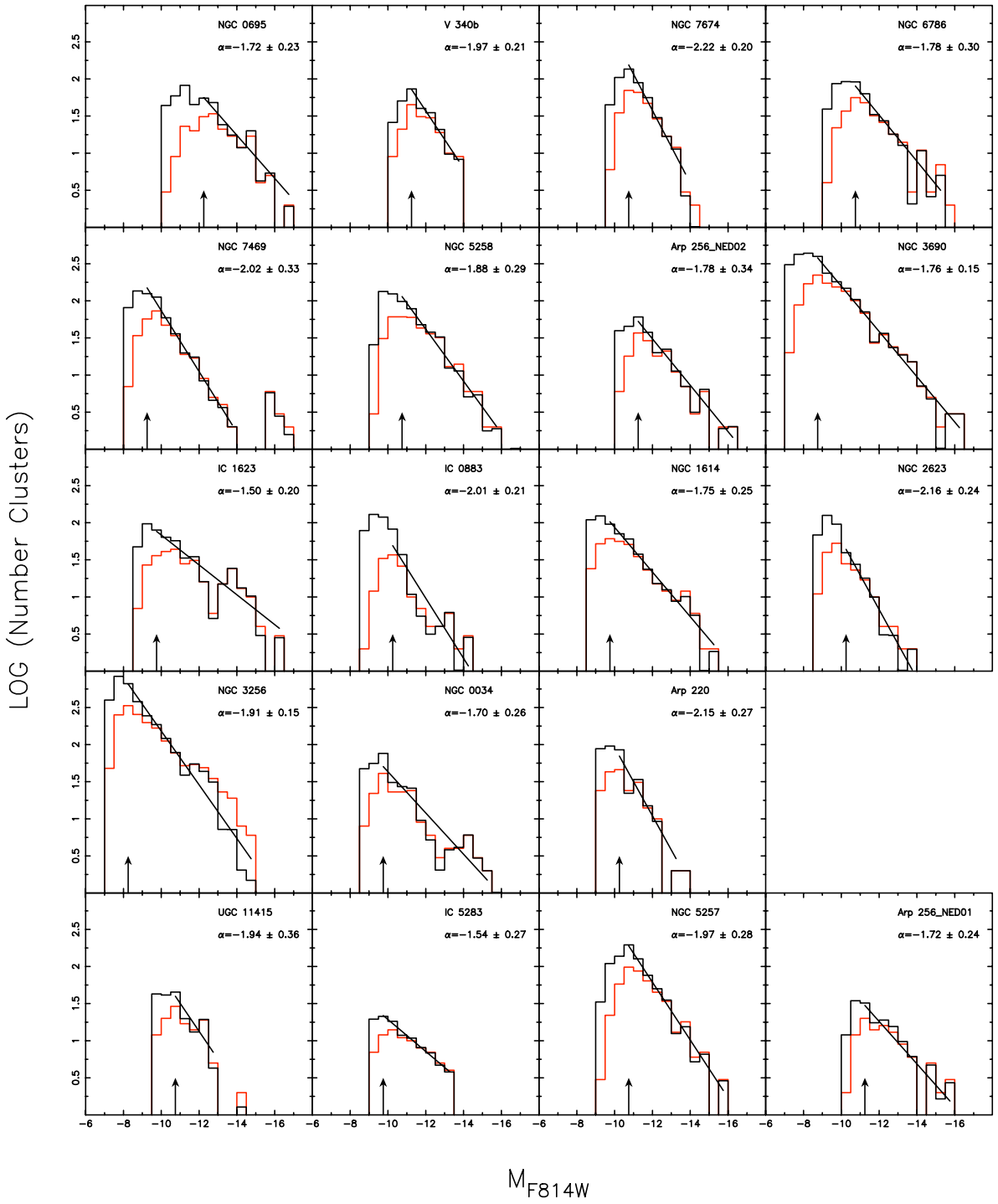


Figure 3.14: Cluster luminosity function for F814W. The red histograms represent the raw, uncorrected luminosity distribution. The black histograms have been corrected for foreground stars contamination and for the efficiency of the detection algorithm. The black line is the $\chi^2$ fit to the corrected histograms and the derived power-law index $\alpha$ of the luminosity function is quoted in the upper right corner. The arrow indicates the 50% detection completeness limit.

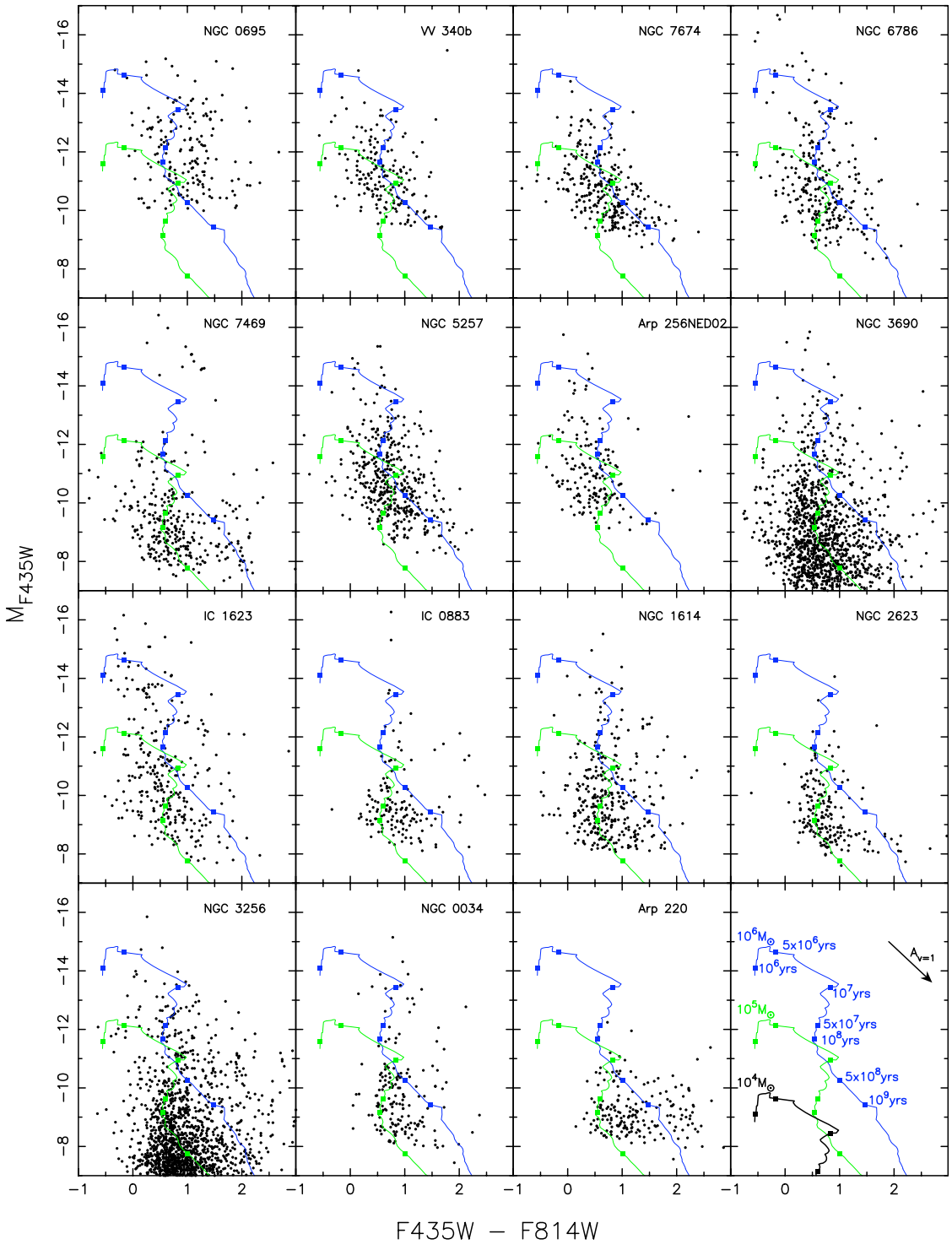


Figure 3.15: The $M_{F435W}$ versus (F435W−F814W) color-magnitude diagrams. Evolutionary tracks from Bruzual-Charlot population synthesis models for an instantaneous starburst are plotted for cluster masses with $10^5$ $M_\odot$ (green) and $10^6$ $M_\odot$ (blue). The lower right panel contains also the $10^4$ $M_\odot$ track in black. The blue $10^6$ $M_\odot$ track is labeled with ages. The arrow represents 1 magnitude visual extinction. Only SC with (F435W−F814W) error $< 0.25$ mag are plotted.

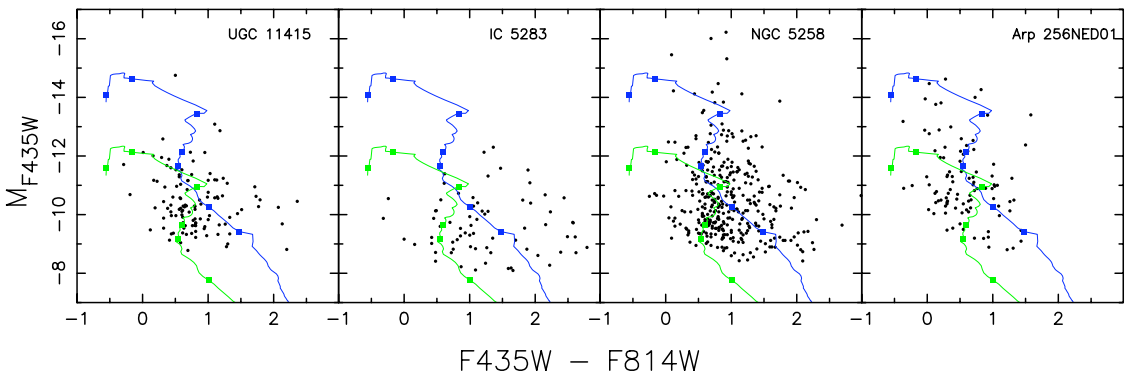


Figure 3.16: The $M_{F435W}$ versus (F435W−F814W) color-magnitude diagram for the four galaxies that are members of galaxy pairs and have fewer detected clusters.

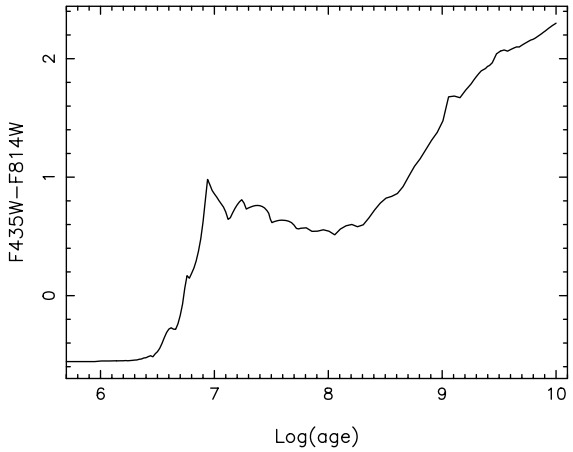


Figure 3.17: (F435W−F814W) color evolutionary track according to Bruzual-Charlot population synthesis models.

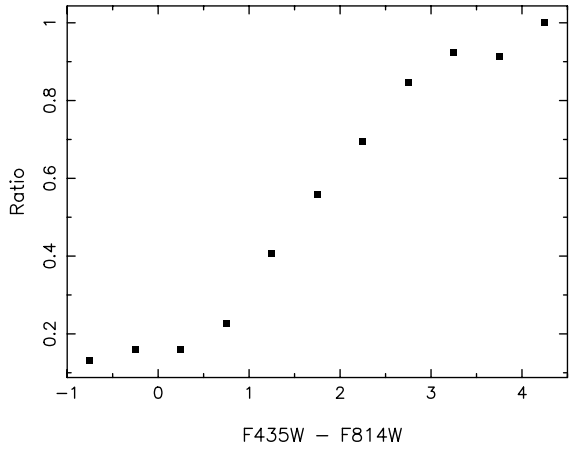


Figure 3.18: Ratio of clusters located in red galaxy regions (i.e., redder than the median galaxy color) to all detected clusters as a function of cluster color.

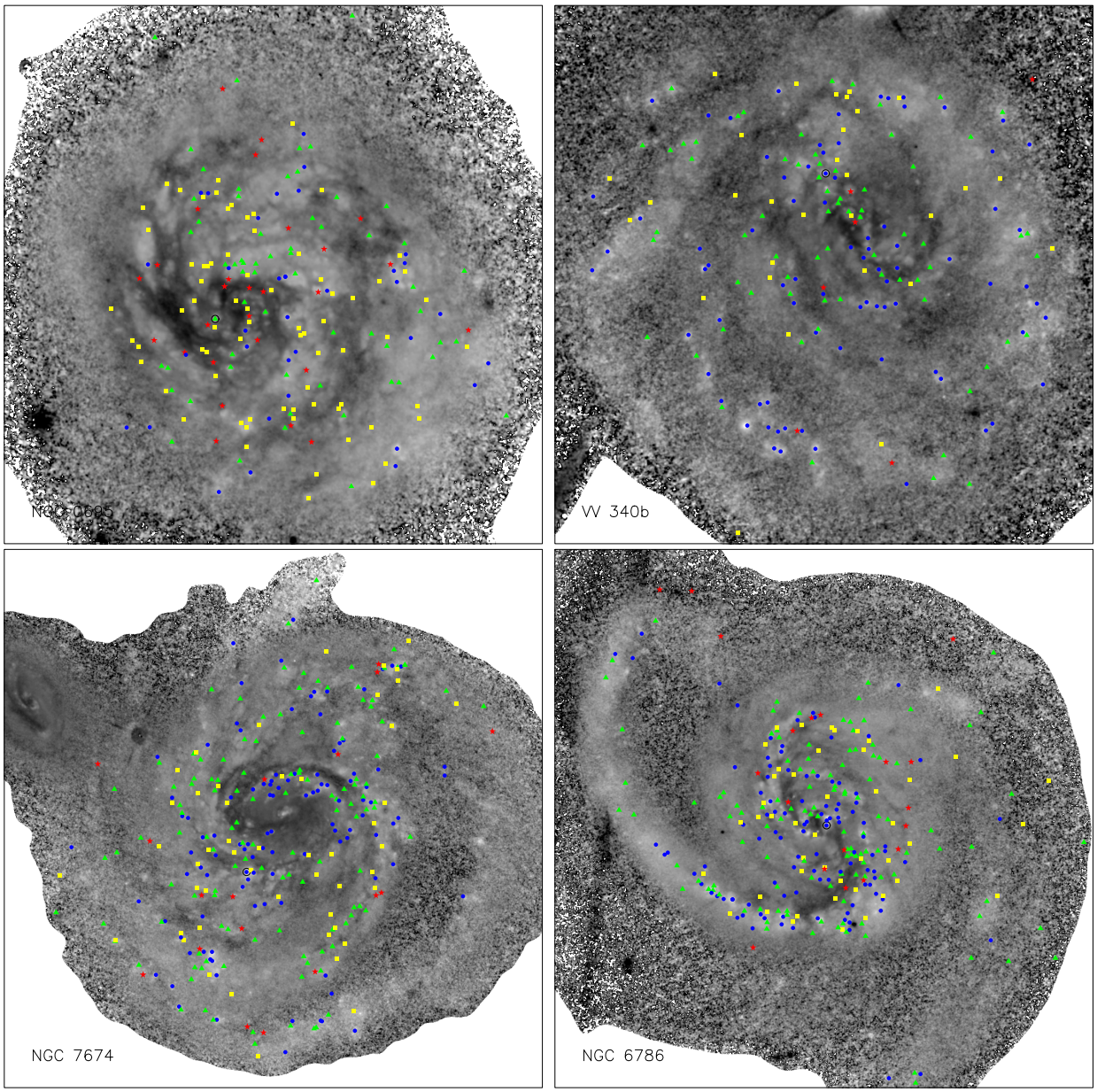


Figure 3.19: Grey-scale (F435W−F814W) host galaxy images with superposed positions of clusters I. Darker shades correspond to larger (F435W−F814W) values and redder color and lighter shades to smaller (F435W−F814W) values and bluer color. The color value of the cluster represents the (F435W−F814W) bin the cluster is in. (F435W−F814W) $< 0.51$ bin clusters are designated with blue dots, $0.51 <$(F435W−F814W) $< 1.0$ with green triangles, $1.0 <$(F435W−F814W) $< 1.5$ with yellow squares, (F435W−F814W)$> 1.5$ with red stars. Black circle indicates the most luminous cluster. LIRGs are arranged in the merger sequence order.

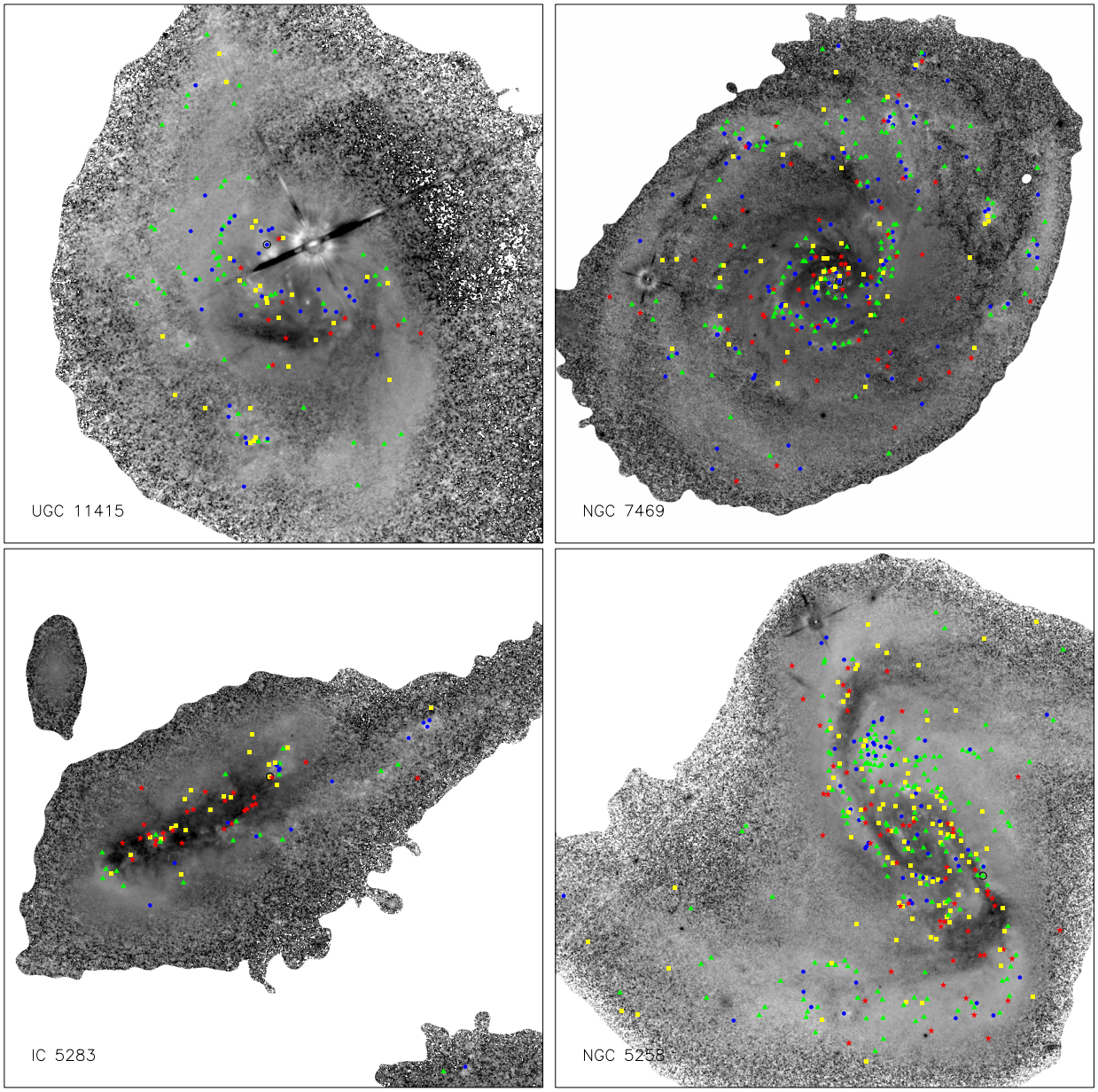


Figure 3.19: (F435W−F814W) images with superposed positions of clusters II. The color value of the cluster represents the (F435W−F814W) bin the cluster is in. (F435W−F814W) $<$ 0.51 bin clusters are designated with blue dots, 0.51 $<$(F435W−F814W) $<$ 1.0 with green triangles, 1.0 $<$(F435W−F814W) $<$ 1.5 with yellow squares, (F435W−F814W)$>$ 1.5 with red stars. Black circle indicates the most luminous cluster.

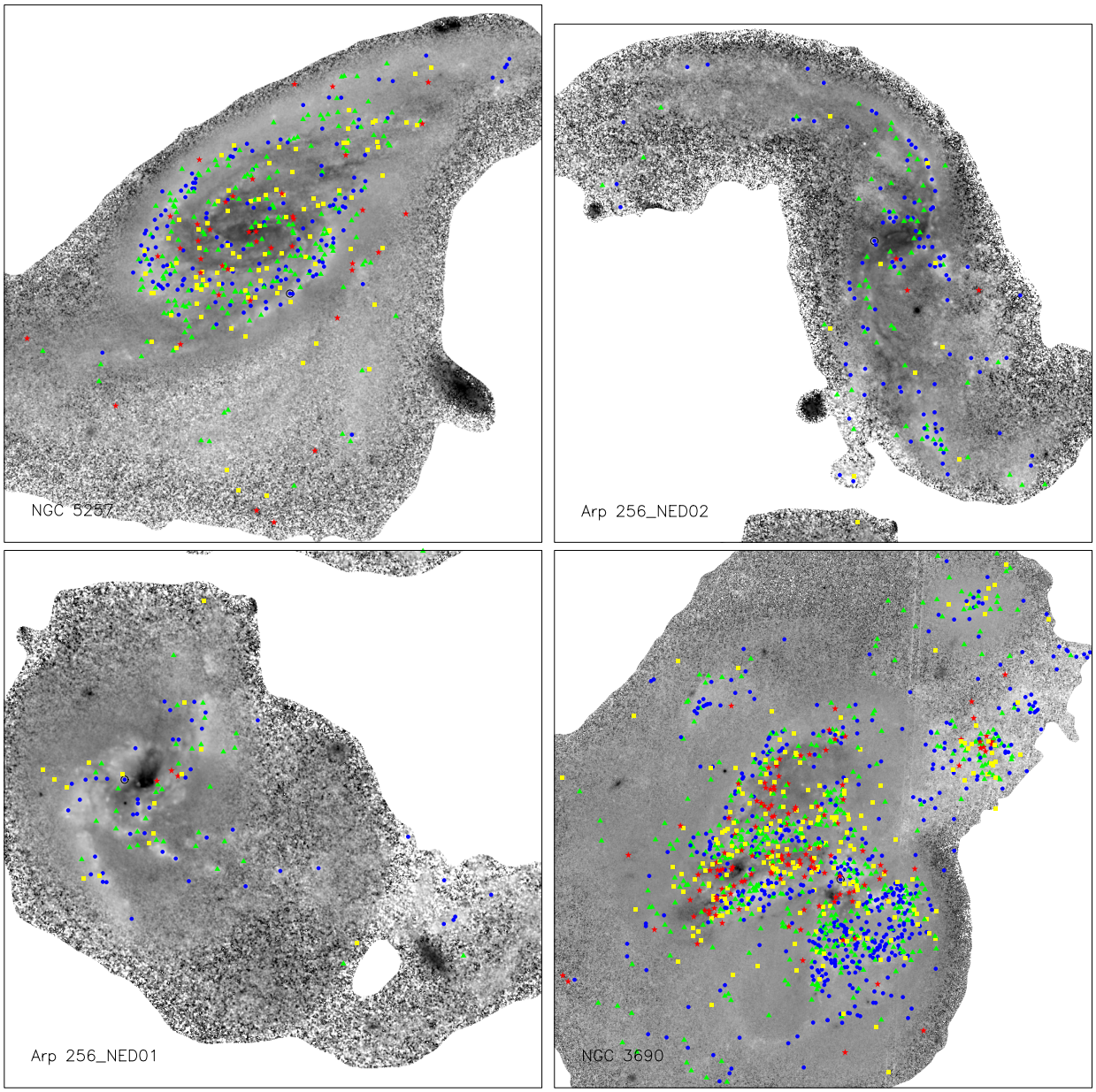


Figure 3.19: (F435W−F814W) images with superposed positions of clusters III. The color value of the cluster represents the (F435W−F814W) bin the cluster is in. (F435W−F814W) $< 0.51$ bin clusters are designated with blue dots, $0.51 <$(F435W−F814W) $< 1.0$ with green triangles, $1.0 <$(F435W−F814W) $< 1.5$ with yellow squares, (F435W−F814W)$> 1.5$ with red stars. Black circle indicates the most luminous cluster.

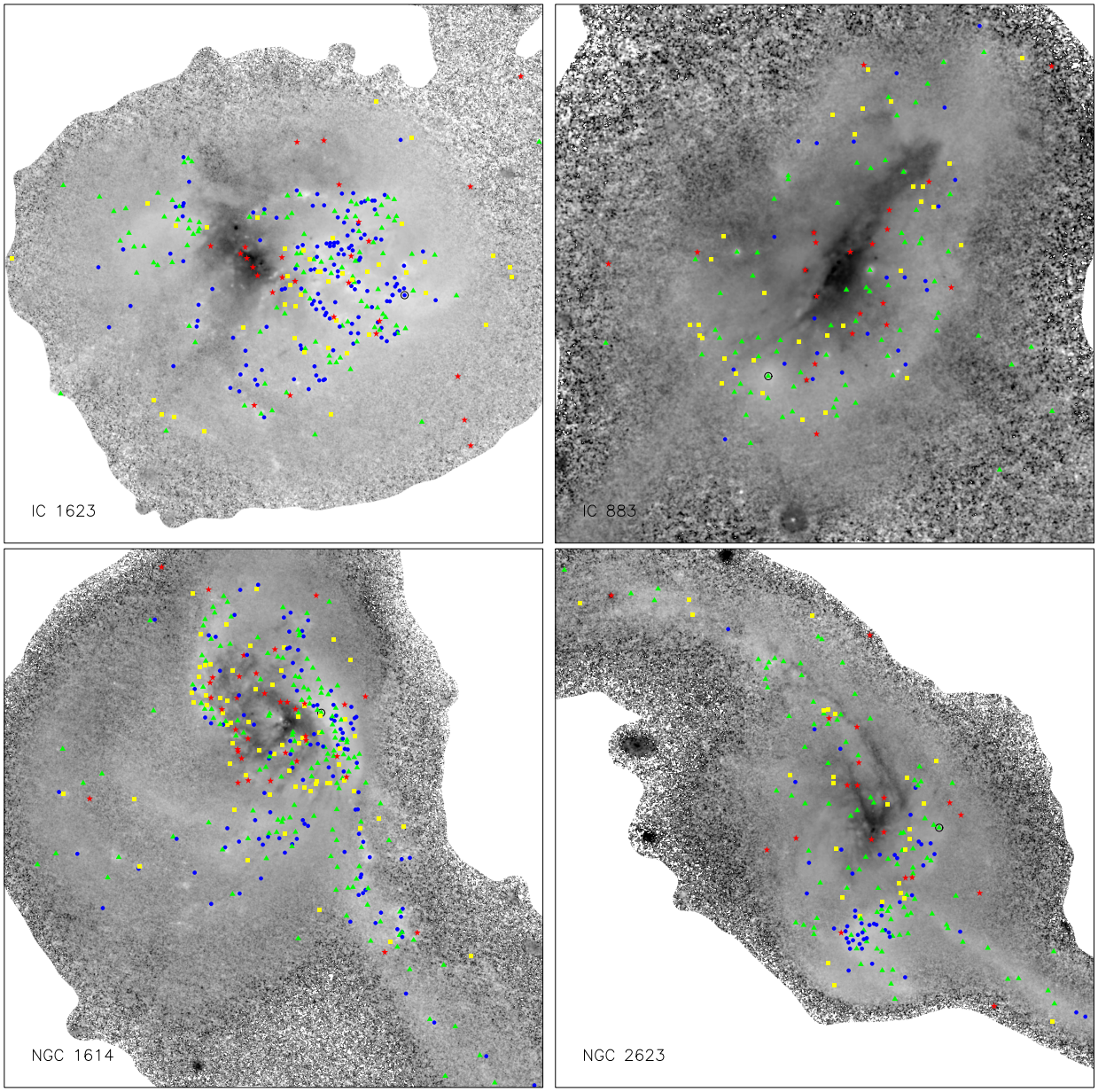


Figure 3.19: (F435W−F814W) images with superposed positions of clusters IV. The color value of the cluster represents the (F435W−F814W) bin the cluster is in. (F435W−F814W) $< 0.51$ bin clusters are designated with blue dots, $0.51 <$(F435W−F814W) $< 1.0$ with green triangles, $1.0 <$(F435W−F814W) $< 1.5$ with yellow squares, (F435W−F814W)$> 1.5$ with red stars. Black circle indicates the most luminous cluster.

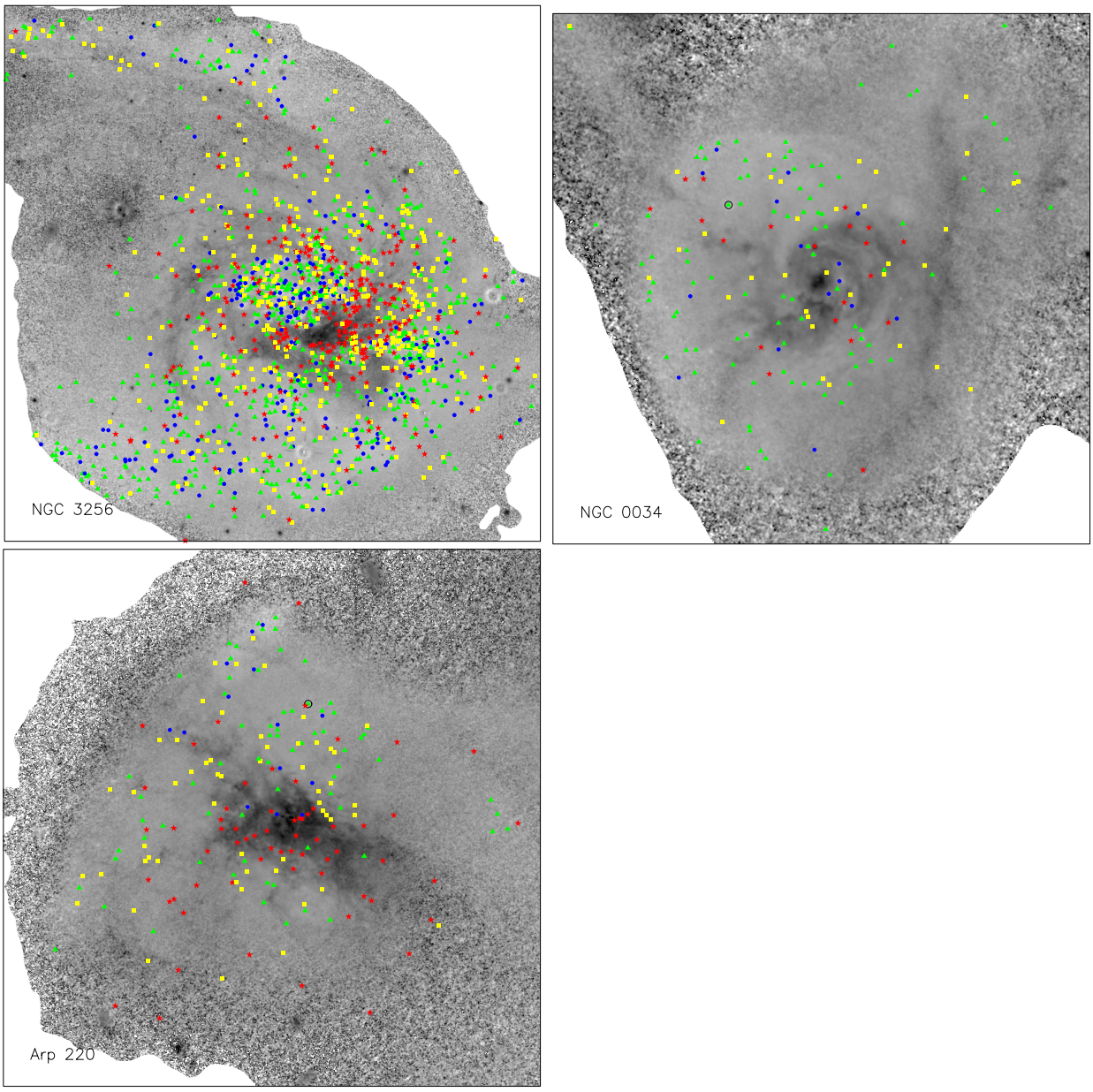


Figure 3.19: (F435W−F814W) images with superposed positions of clusters V. The color value of the cluster represents the (F435W−F814W) bin the cluster is in. (F435W−F814W) $< 0.51$ bin clusters are designated with blue dots, $0.51 <$(F435W−F814W) $< 1.0$ with green triangles, $1.0 <$(F435W−F814W) $< 1.5$ with yellow squares, (F435W−F814W)$> 1.5$ with red stars. Black circle indicates the most luminous cluster.

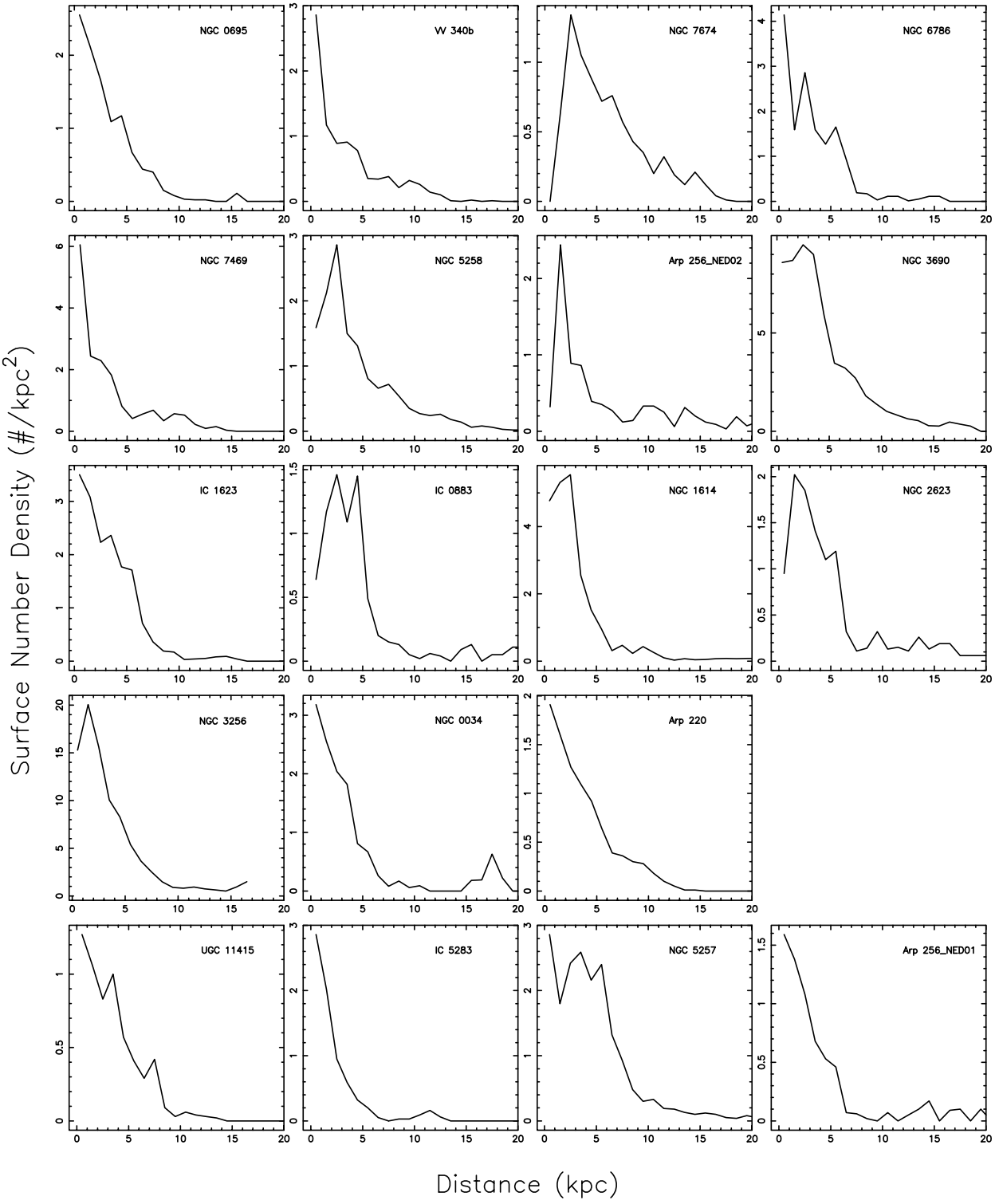


Figure 3.20: Cluster surface density as a function of distance from the 8$\mu$m centroid. The bottom row shows the four galaxies that are members of galaxy pairs and have fewer detected clusters.

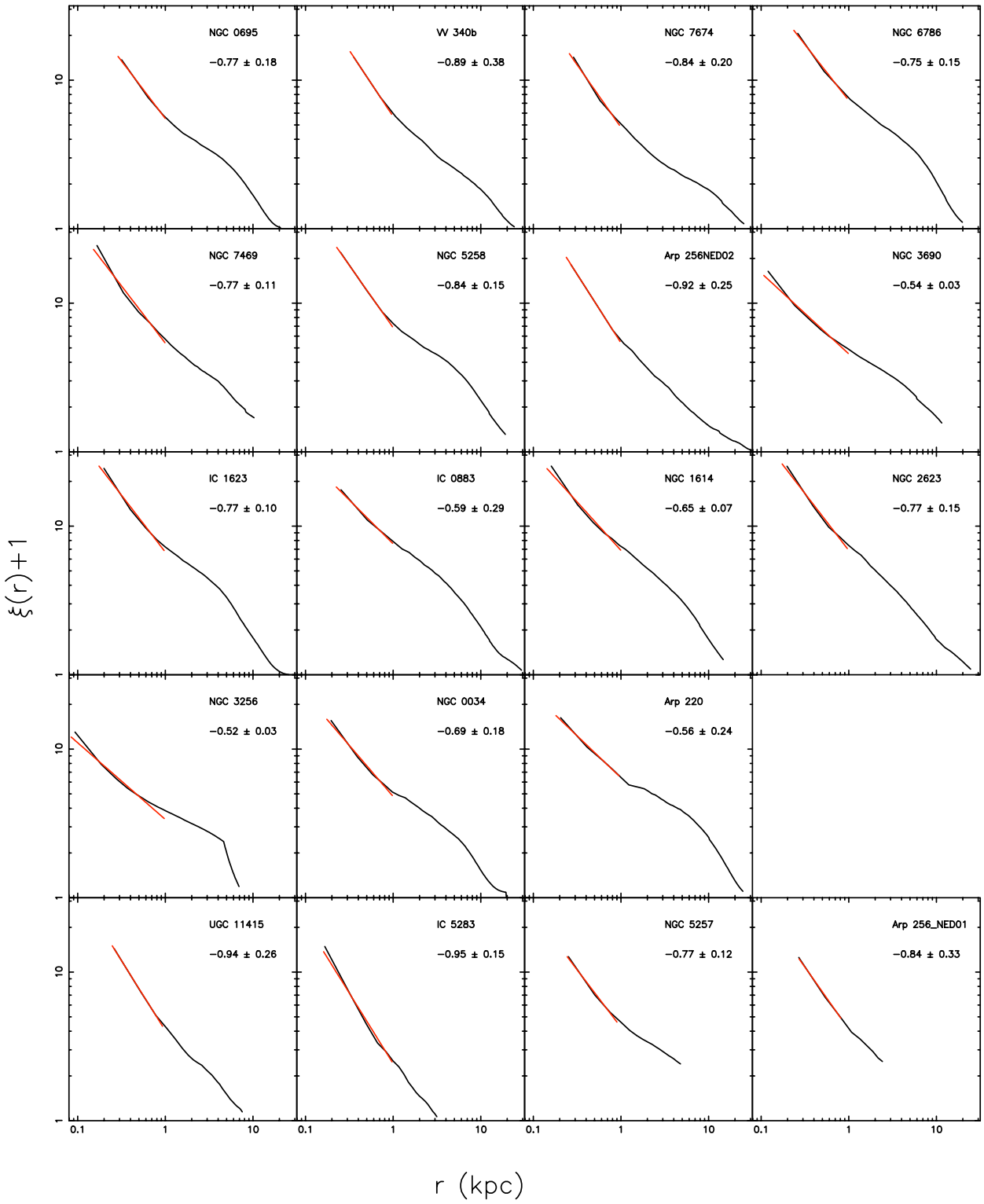


Figure 3.21: Autocorrelation functions of SCs. Both axis are shown on a logarithmic scale. The red line is a linear fit to the autocorrelation function up to a distance of 1 kpc. The index of the power-law is indicated in the upper right corner. The bottom row shows the four galaxies that are members of galaxy pairs and have fewer detected clusters.

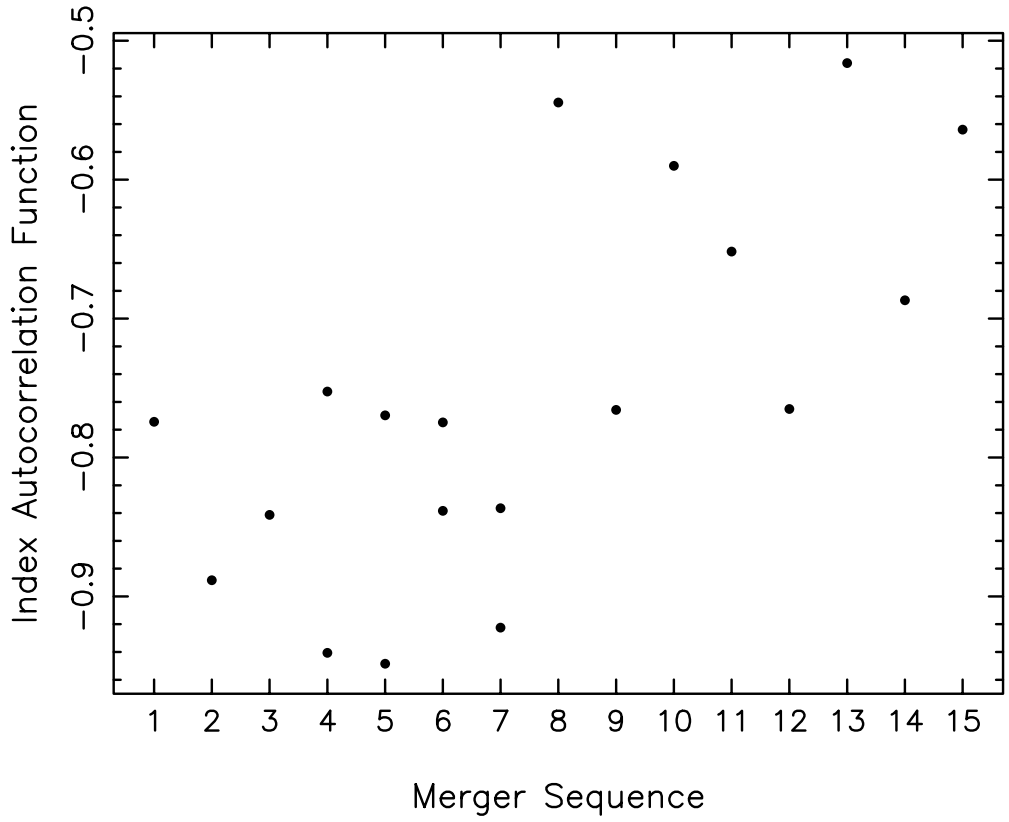


Figure 3.22: Indices of the power law fit to autocorrelation functions versus merger sequence in the same order as in Figure 3.3.

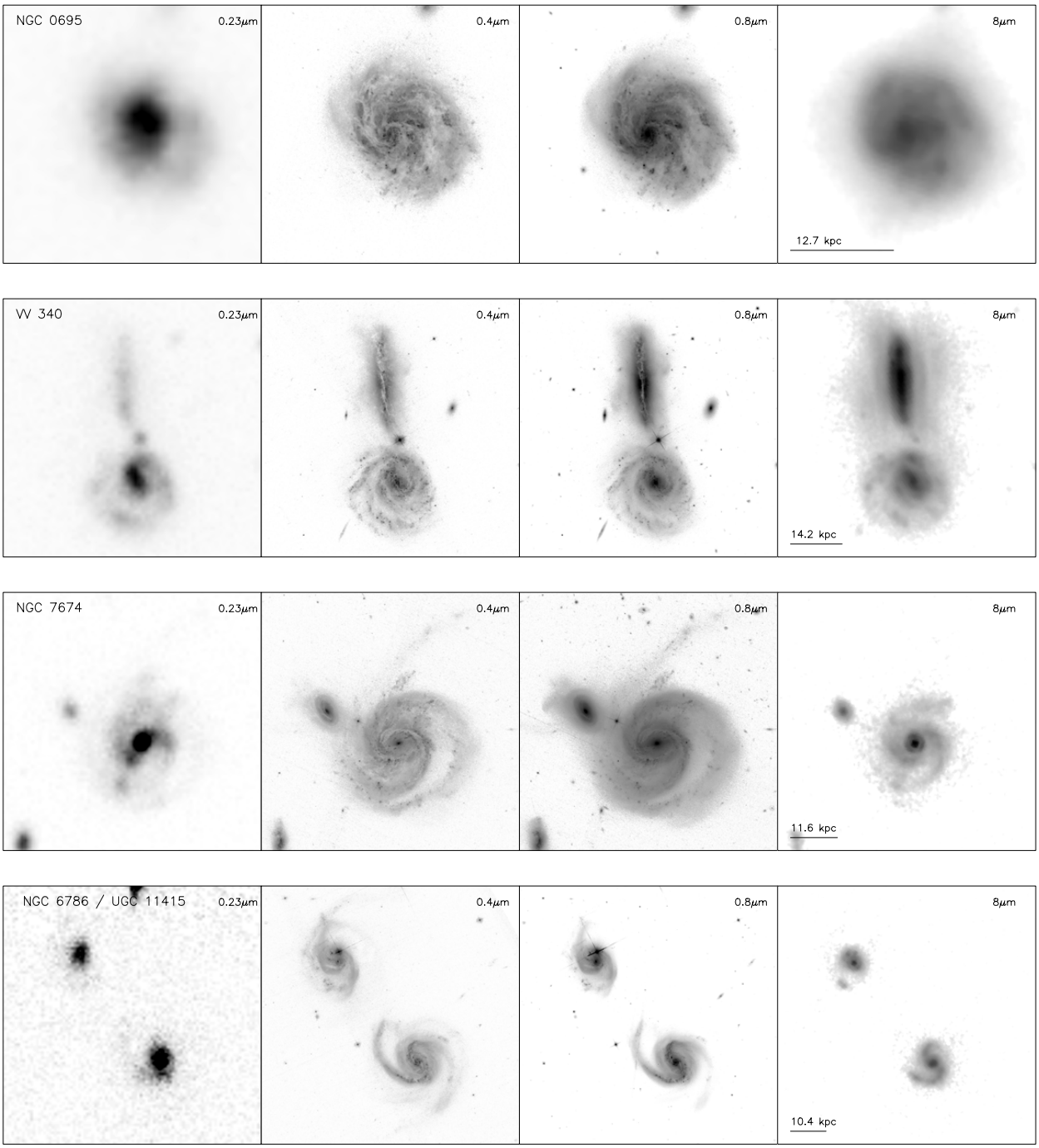


Figure 3.23: Multi-wavelength view of the cluster-rich LIRGs sample I. Each row shows *GALEX* near-UV, *HST*/ACS F435W, *HST*/ACS F814W and *Spitzer* IRAC 8$\mu$m images. The scale bar in the lower left corner corresponds to 20" and the number above indicates the scale in kpc at the distance of the system. LIRGs are arranged in the merger sequence order.

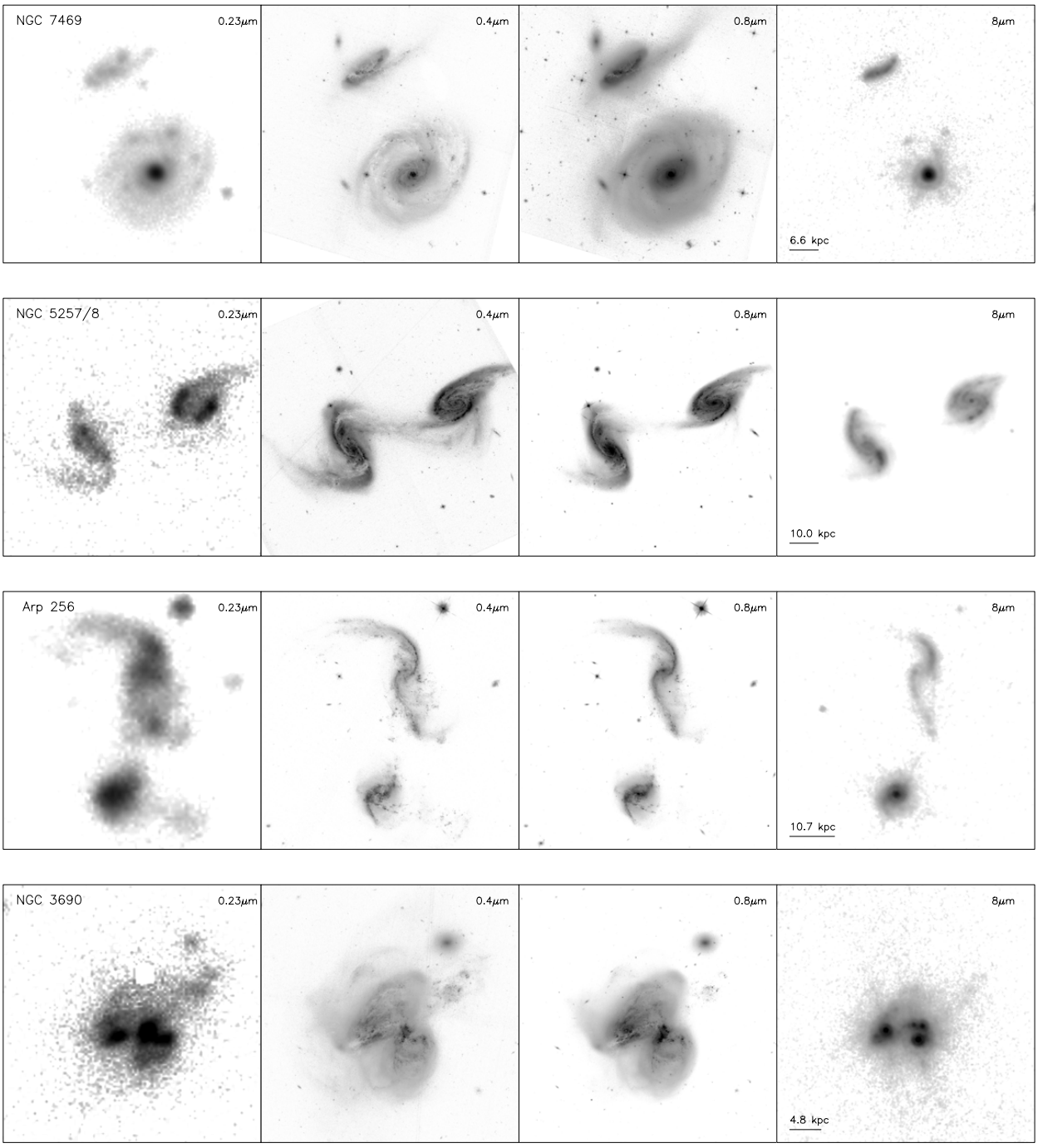


Figure 3.23: Multi-wavelength view of the cluster-rich LIRGs sample II. Each row shows *GALEX* near-UV, *HST*/ACS F435W, *HST*/ACS F814W and *Spitzer* IRAC 8$\mu$m images. The scale bar in the lower left corner corresponds to 20" and the number above indicates the scale in kpc at the distance of the system. LIRGs are arranged in the merger sequence order.

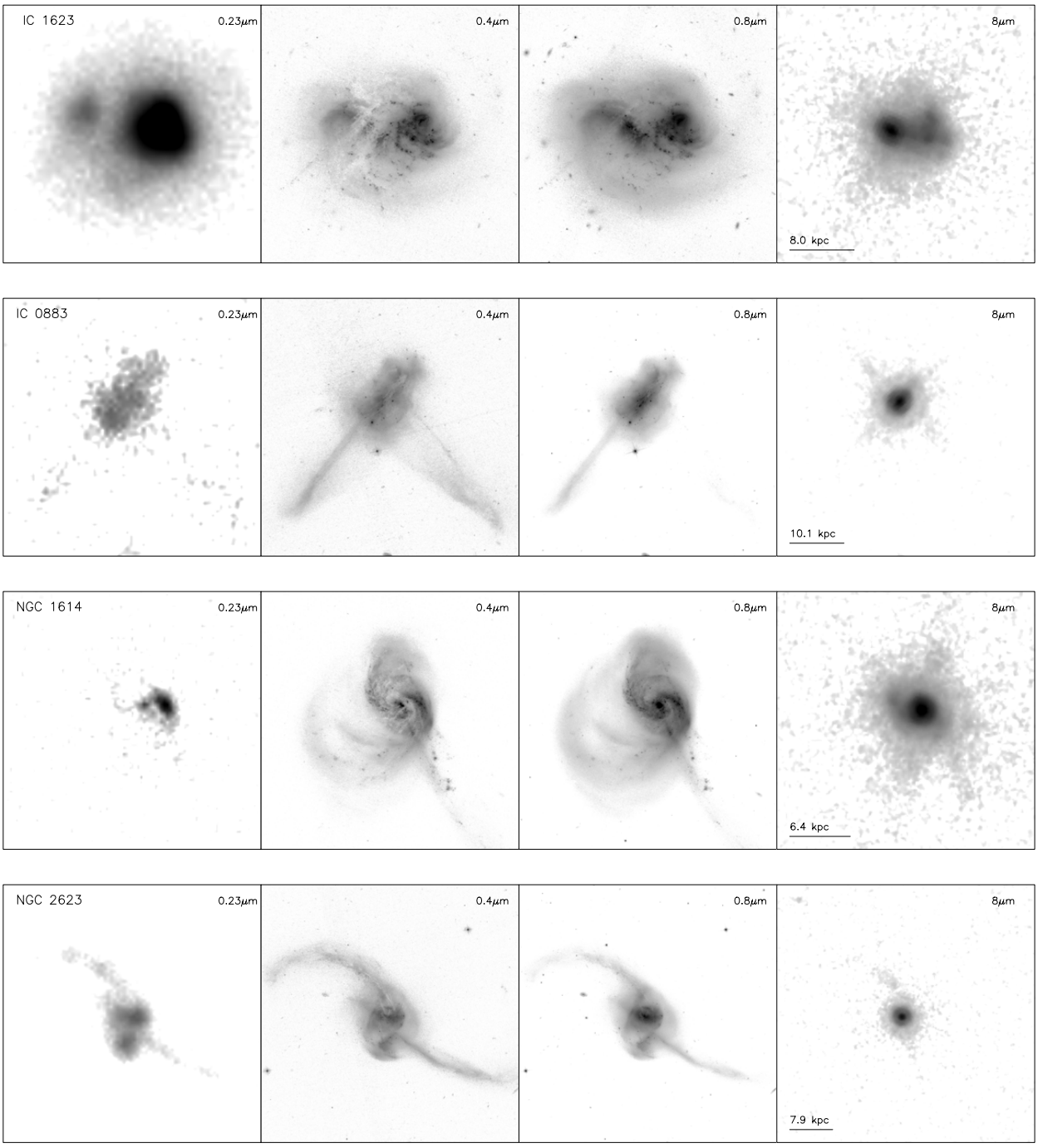


Figure 3.23: Multi-wavelength view of the cluster-rich LIRGs sample III. Each row shows *GALEX* near-UV, *HST*/ACS F435W, *HST*/ACS F814W and *Spitzer* IRAC 8$\mu$m images. The scale bar in the lower left corner corresponds to 20" and the number above indicates the scale in kpc at the distance of the system. LIRGs are arranged in the merger sequence order.

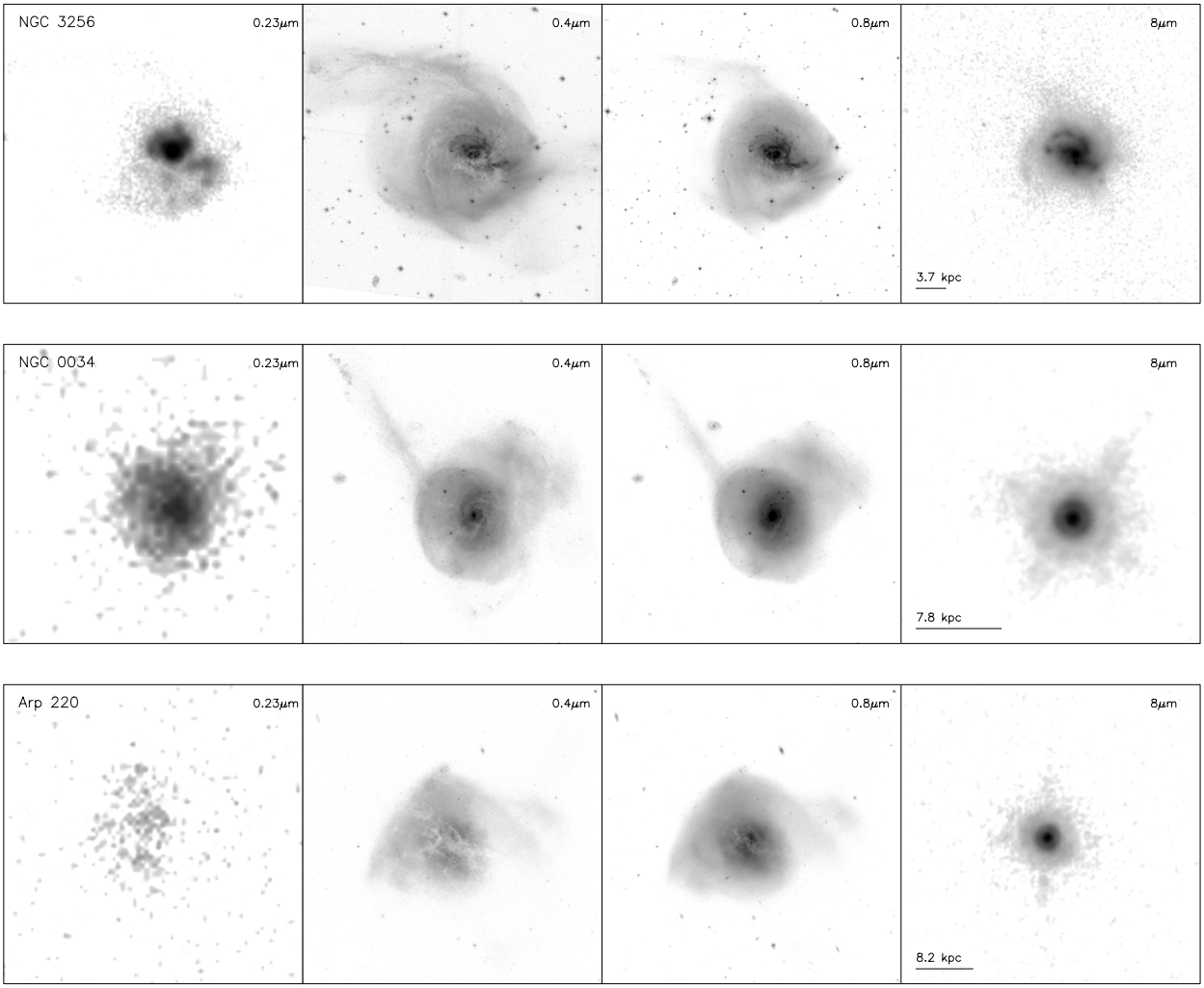


Figure 3.23: Multi-wavelength view of the cluster-rich LIRGs sample IV. Each row shows *GALEX* near-UV, *HST*/ACS F435W, *HST*/ACS F814W and *Spitzer* IRAC 8$\mu$m images. The scale bar in the lower left corner corresponds to 20" and the number above indicates the scale in kpc at the distance of the system. LIRGs are arranged in the merger sequence order.

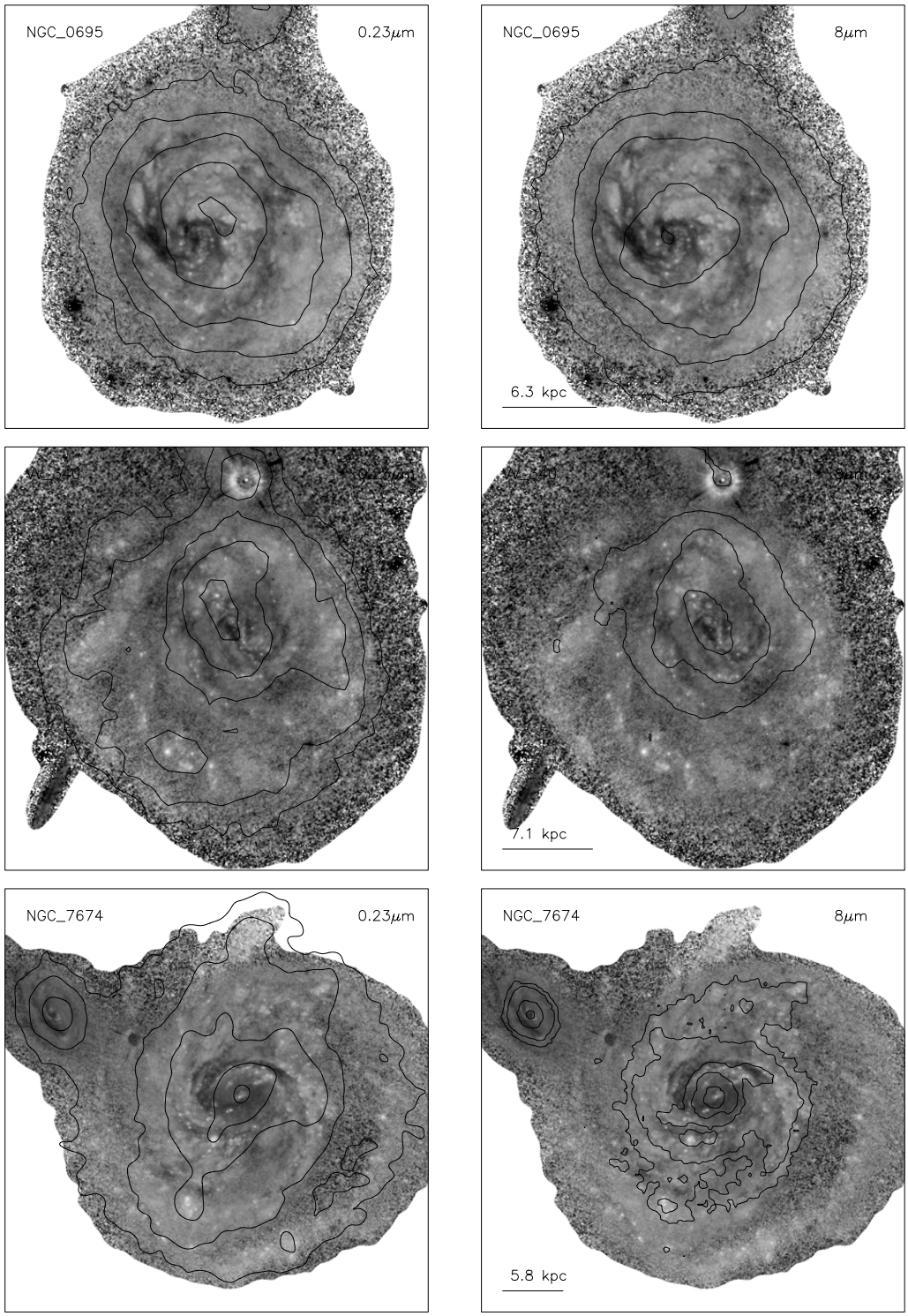


Figure 3.24: *GALEX* NUV 0.23$\mu$m contours (left column) and *Spitzer* IRAC 8$\mu$m contours superposed on grey-scale (F435W−F814W) host galaxy images I. Darker shades correspond to larger (F435W−F814W) values and redder color and lighter shades to smaller (F435W−F814W) values and bluer color. The scale bar in the lower left corner corresponds to 10" and the number above indicates the scale in kpc at the distance of the system. LIRGs are arranged in the merger sequence order.

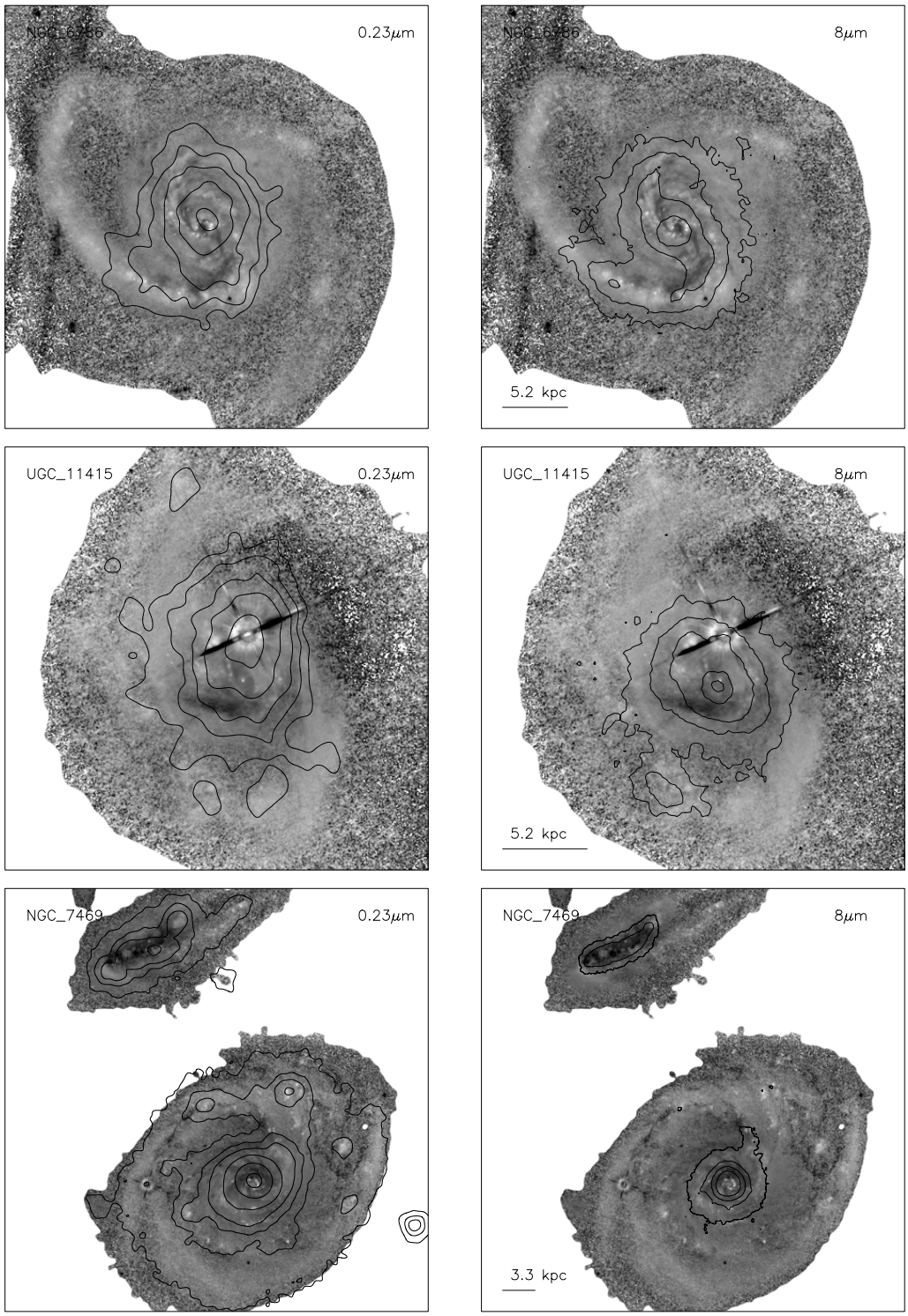


Figure 3.24: *GALEX* NUV 0.23$\mu$m contours (left column) and *Spitzer* IRAC 8$\mu$m contours superposed on grey-scale (F435W−F814W) host galaxy images II.

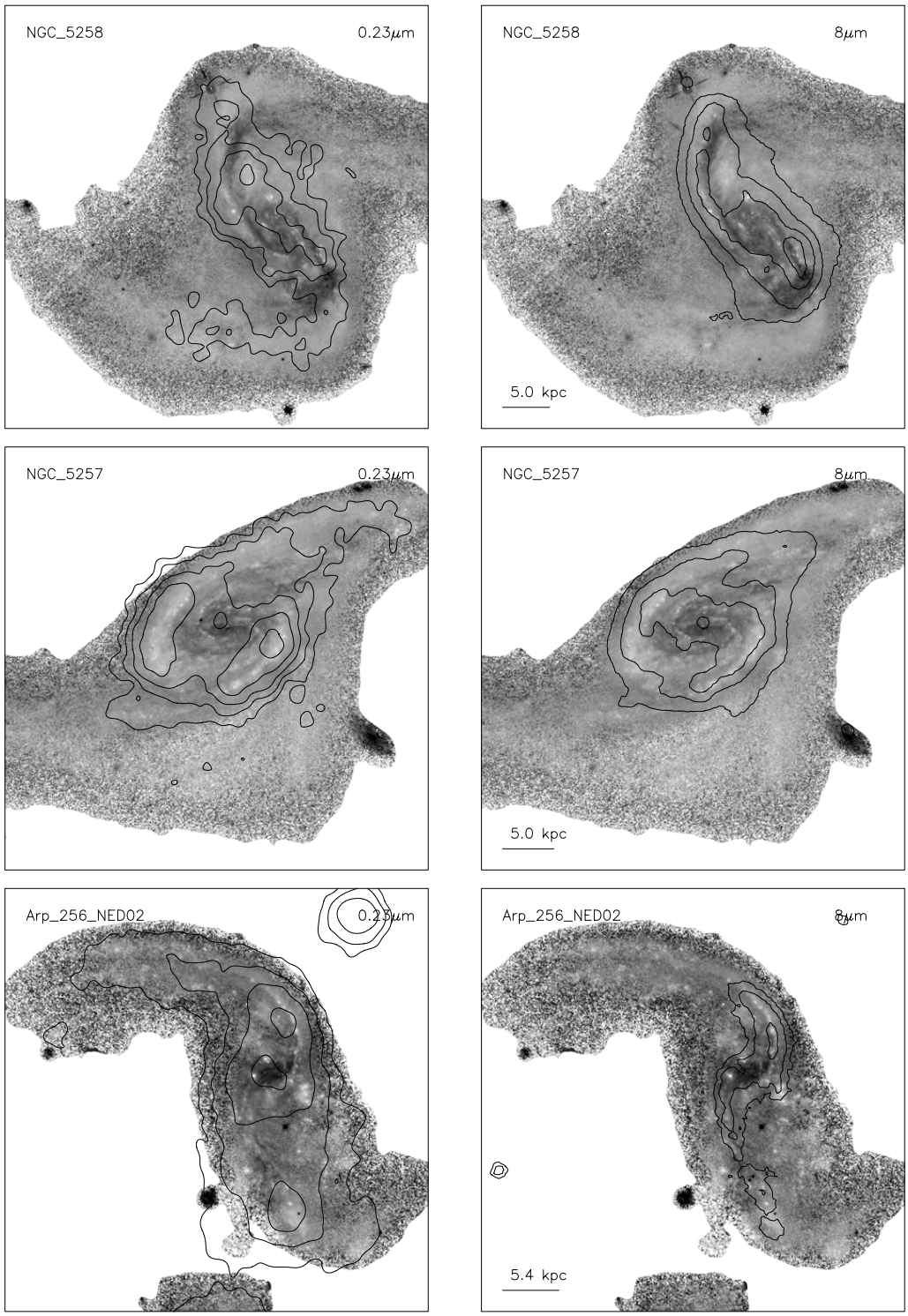


Figure 3.24: *GALEX* NUV 0.23$\mu$m contours (left column) and *Spitzer* IRAC 8$\mu$m contours superposed on grey-scale (F435W−F814W) host galaxy images III.

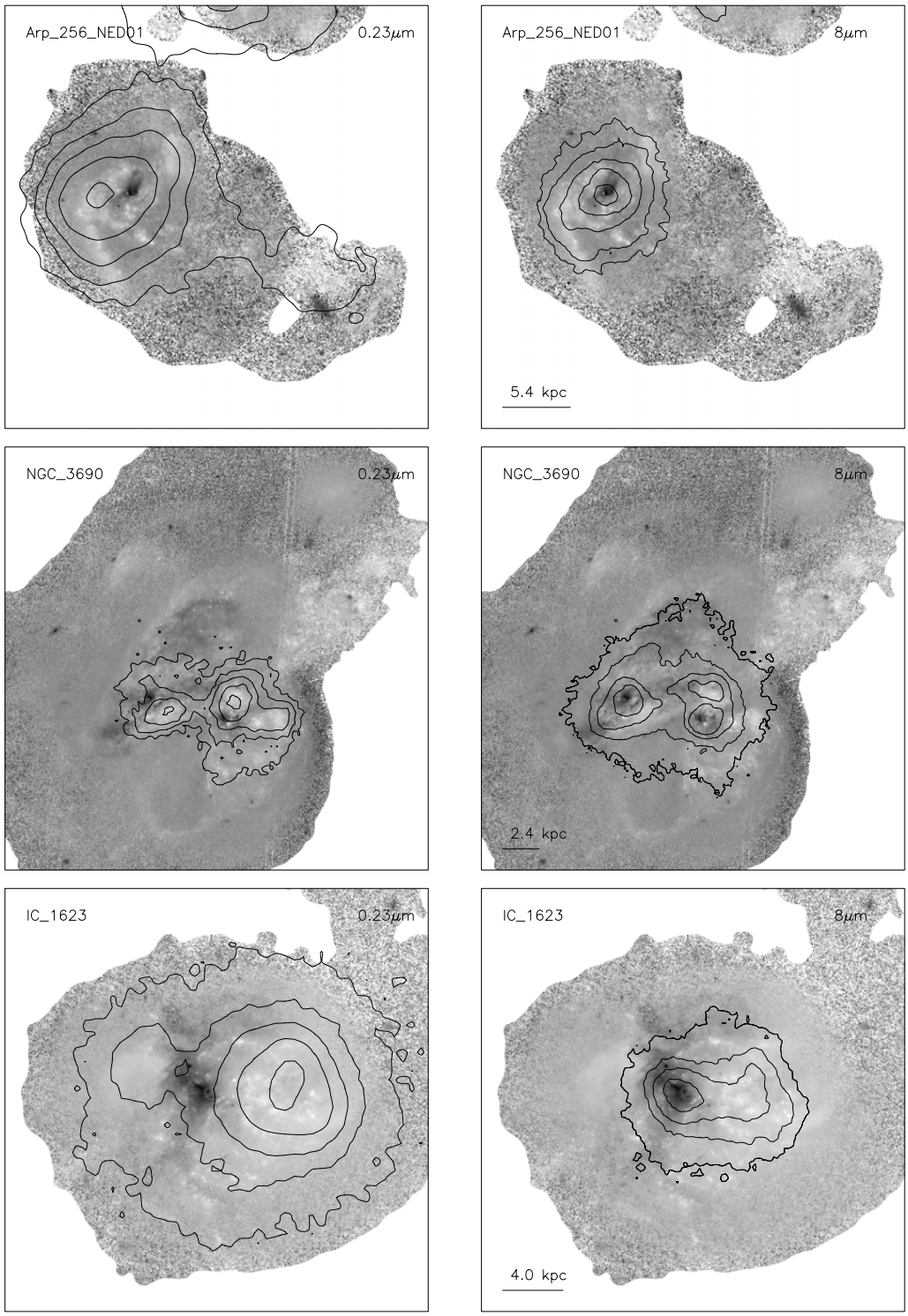


Figure 3.24: *GALEX* NUV 0.23$\mu$m contours (left column) and *Spitzer* IRAC 8$\mu$m contours superposed on grey-scale (F435W−F814W) host galaxy images IV.

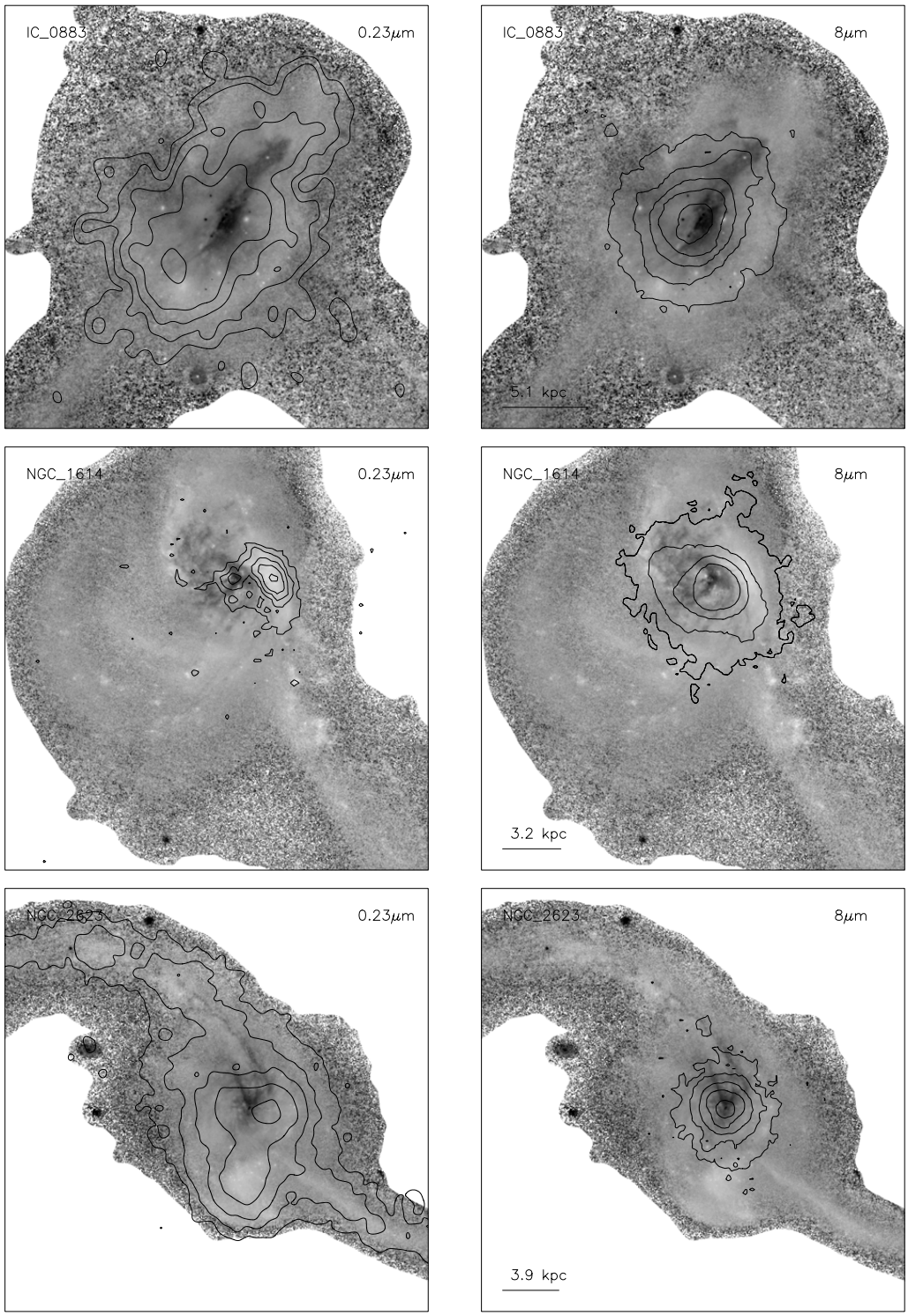


Figure 3.24: *GALEX* NUV 0.23$\mu$m contours (left column) and *Spitzer* IRAC 8$\mu$m contours superposed on grey-scale (F435W−F814W) host galaxy images V.

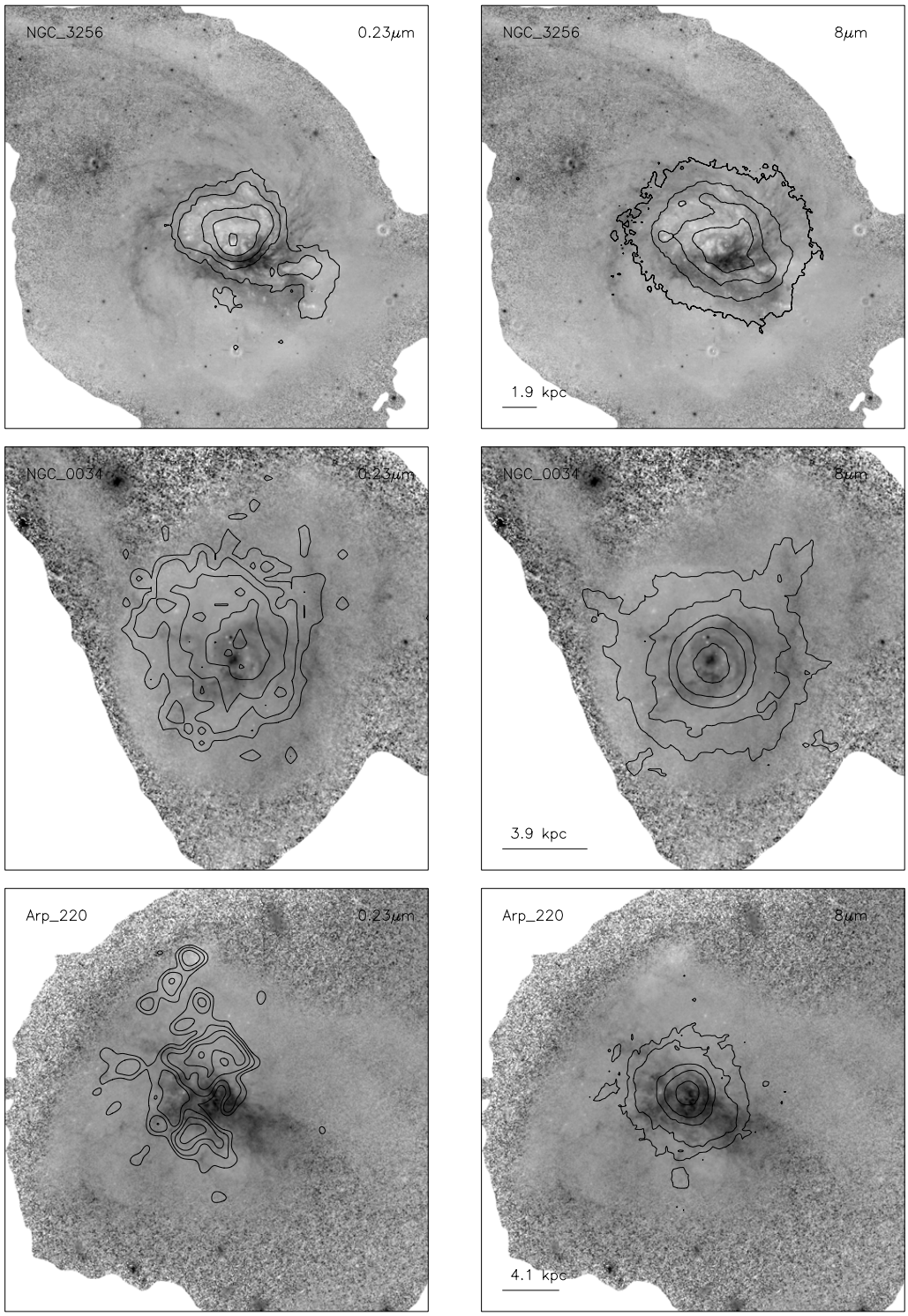


Figure 3.24: *GALEX* NUV 0.23$\mu$m contours (left column) and *Spitzer* IRAC 8$\mu$m contours superposed on grey-scale (F435W−F814W) host galaxy images VI.

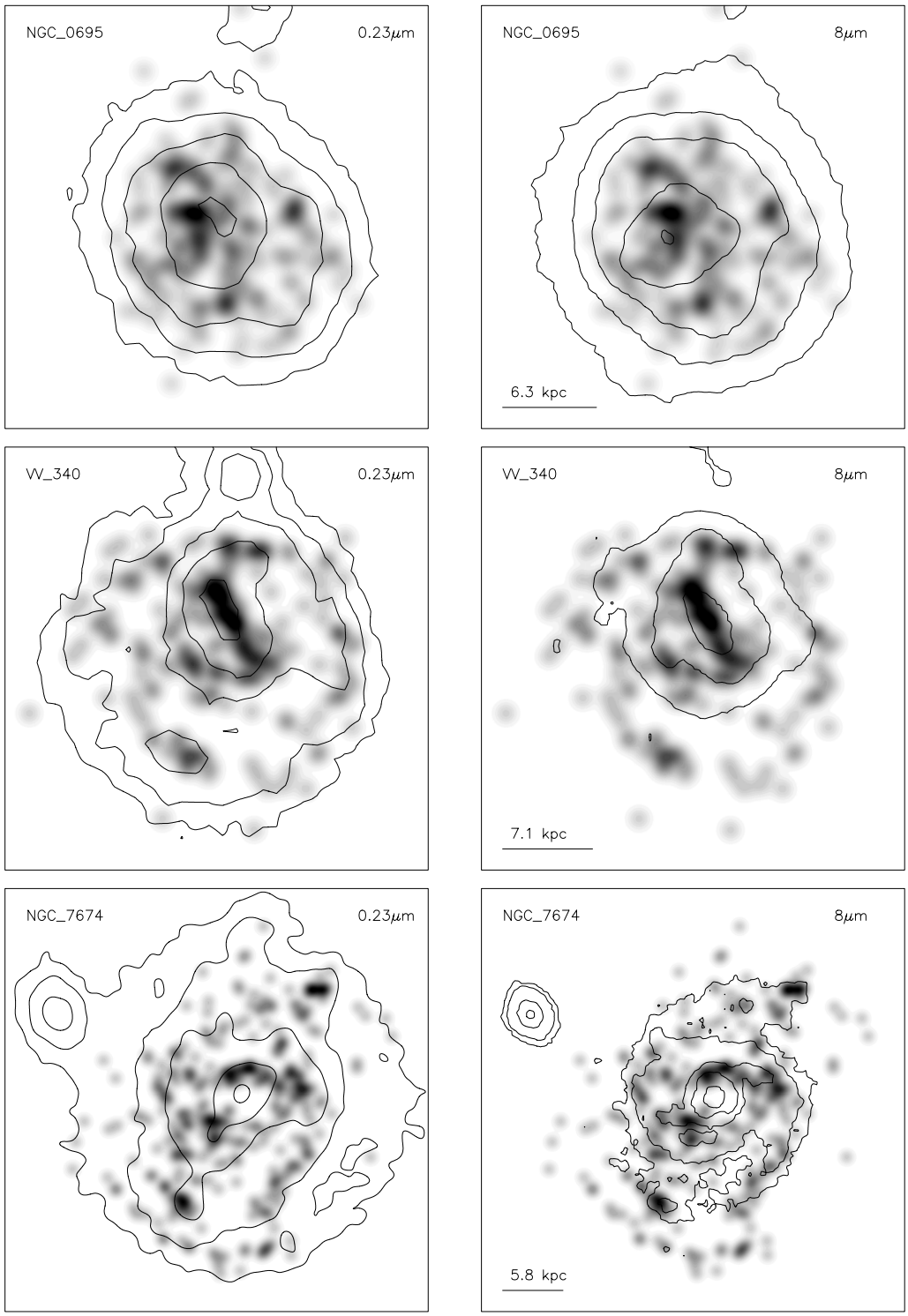


Figure 3.25: *GALEX* NUV 0.23$\mu$m contours (left column) and *Spitzer* IRAC 8$\mu$m contours superposed on grey-scale SC density maps I. Darker shades correspond to larger SC density values and lighter shades to smaller SC density values. The scale bar in the lower left corner corresponds to 10" and the number above indicates the scale in kpc at the distance of the system. LIRGs are arranged in the merger sequence order.

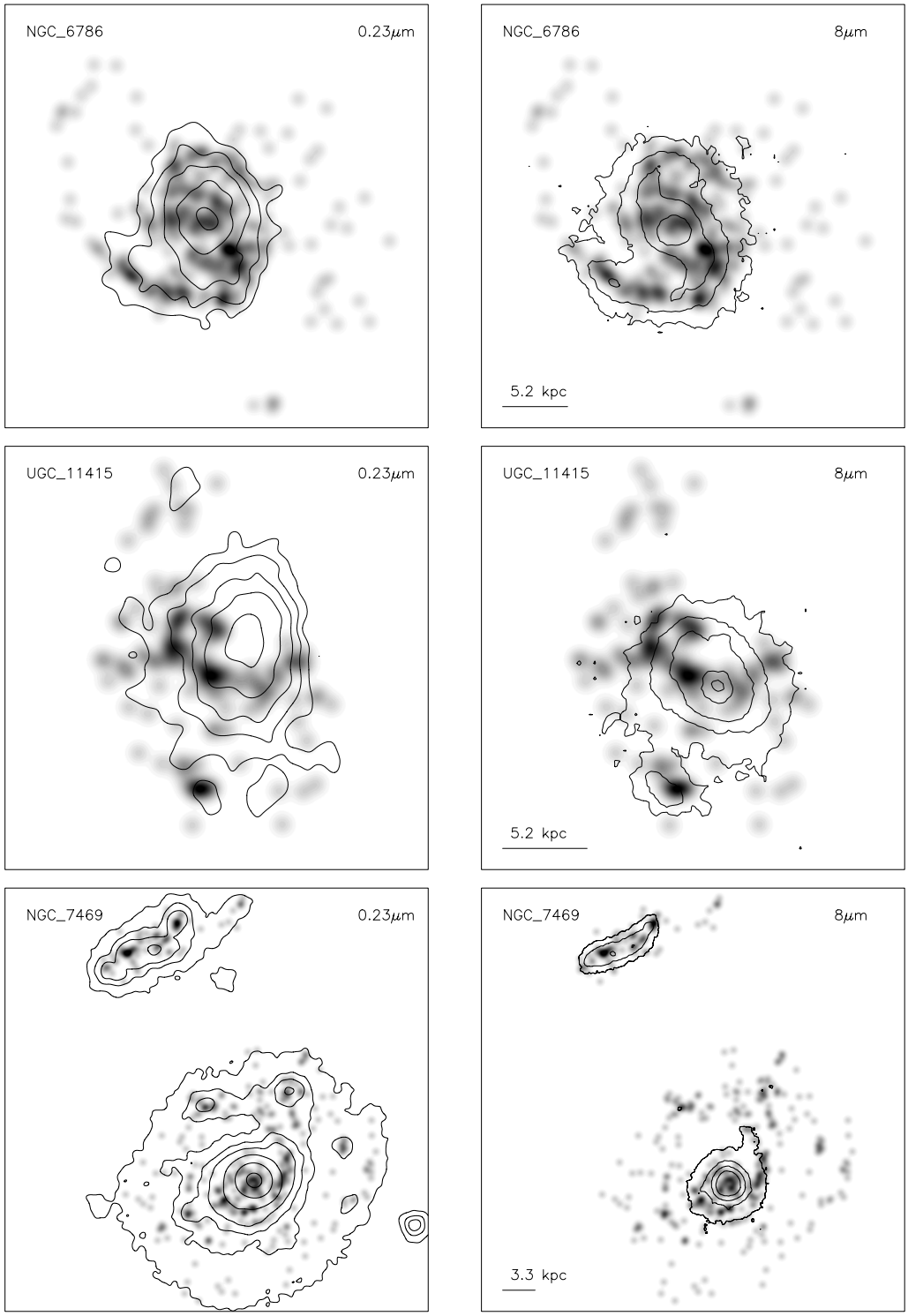


Figure 3.25: *GALEX* NUV 0.23$\mu$m contours (left column) and *Spitzer* IRAC 8$\mu$m contours superposed on grey-scale SC density maps II.

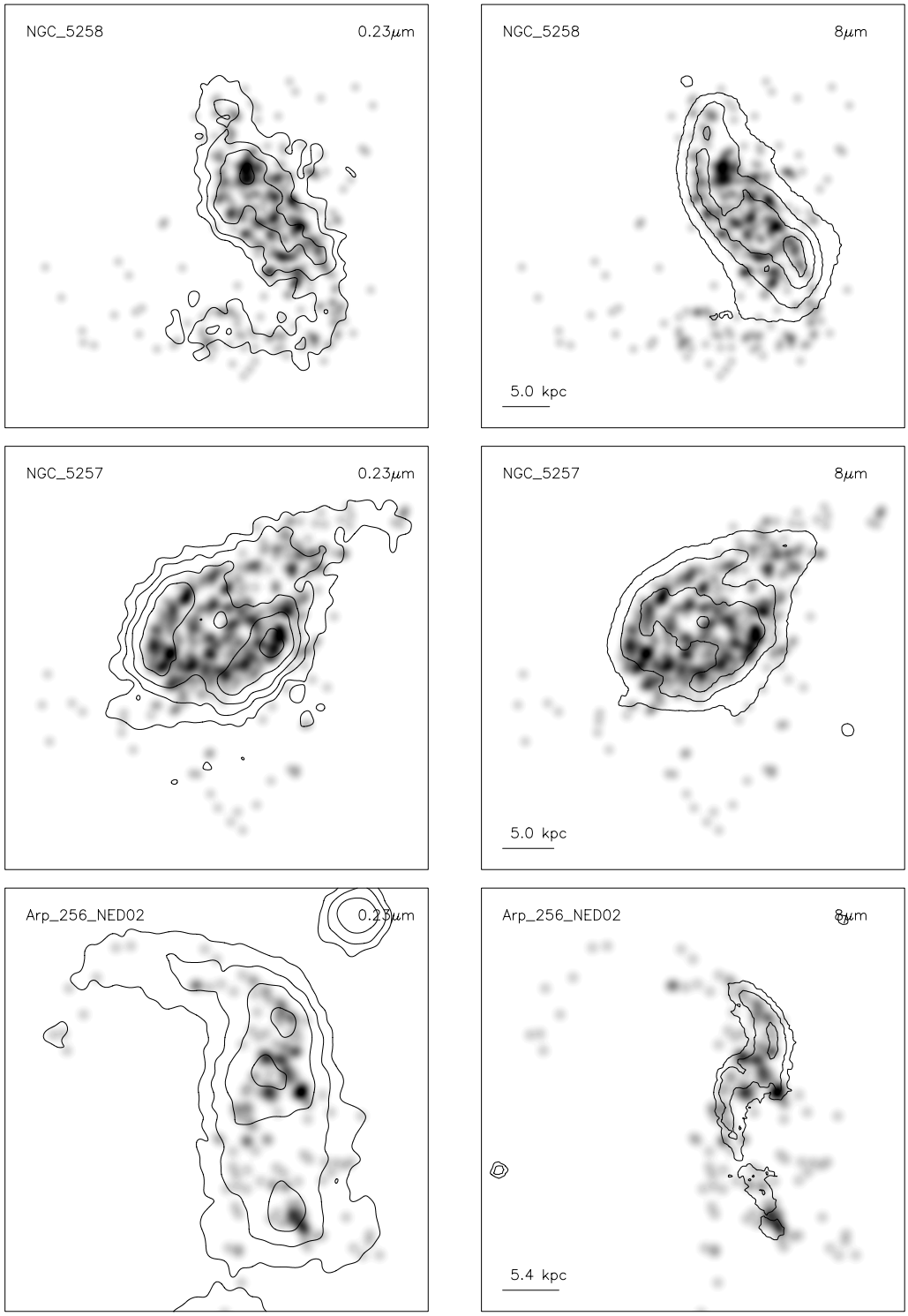


Figure 3.25: *GALEX* NUV 0.23$\mu$m contours (left column) and *Spitzer* IRAC 8$\mu$m contours superposed on grey-scale SC density maps III.

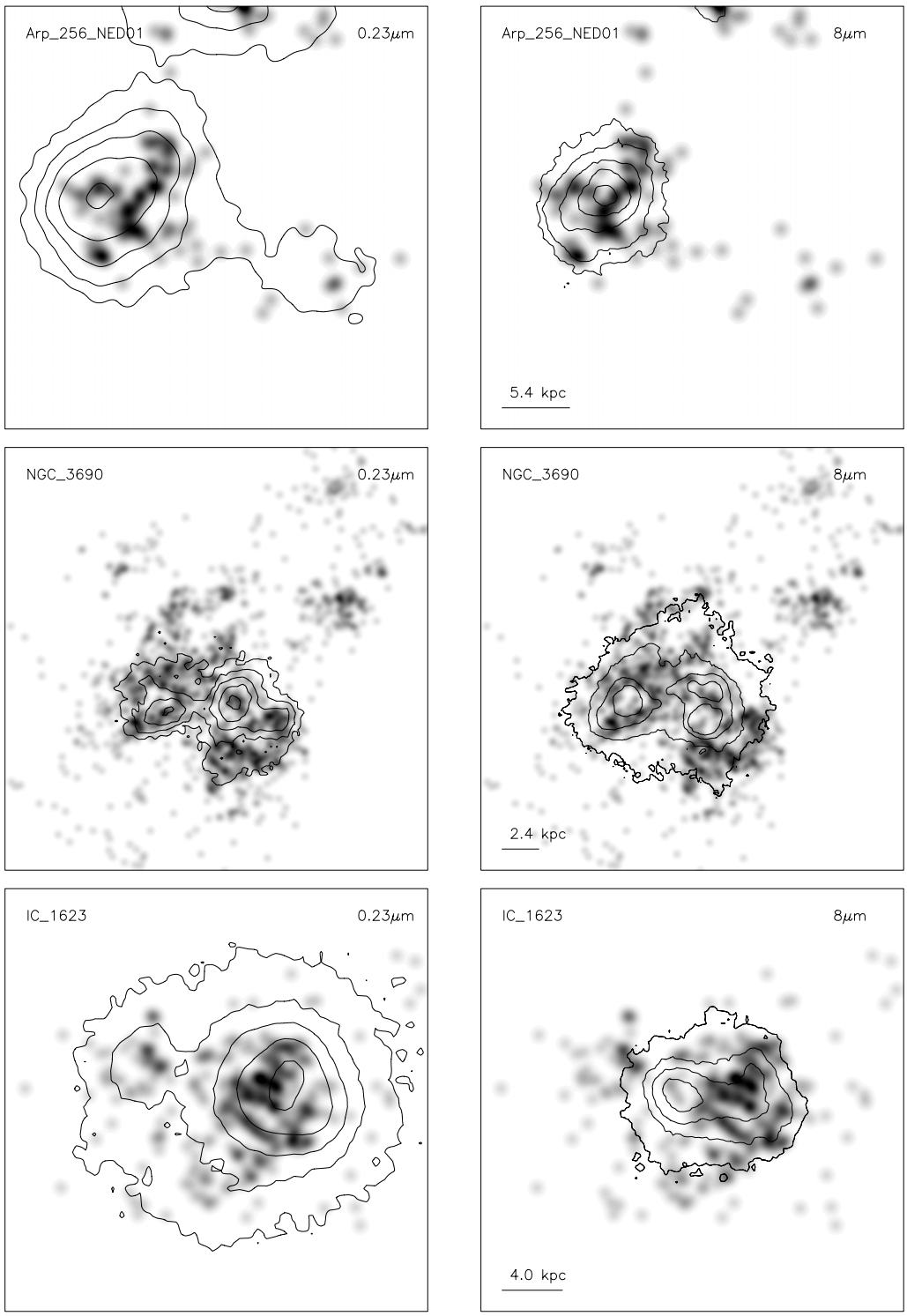


Figure 3.25: *GALEX* NUV 0.23$\mu$m contours (left column) and *Spitzer* IRAC 8$\mu$m contours superposed on grey-scale SC density maps IV.

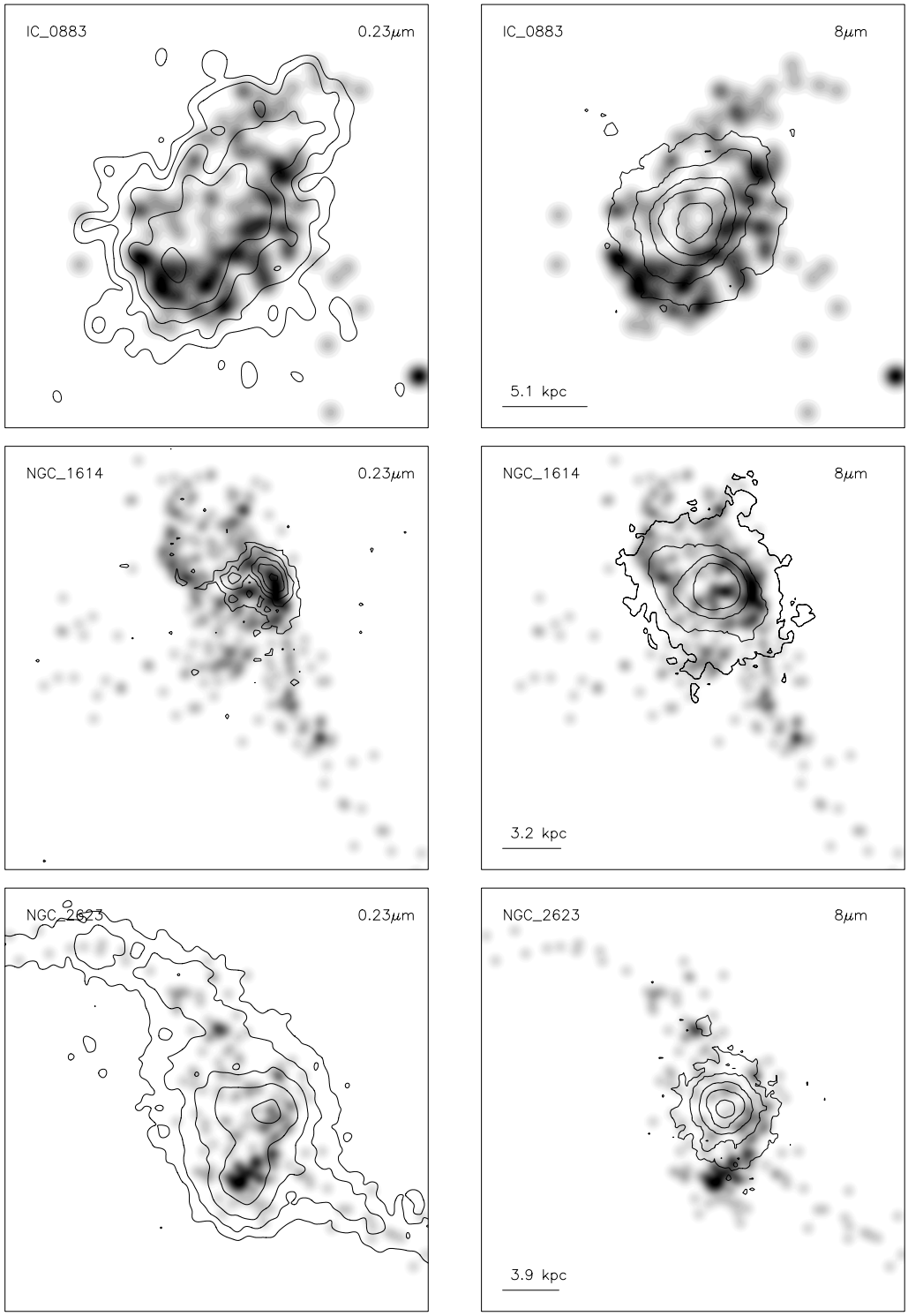


Figure 3.25: *GALEX* NUV 0.23$\mu$m contours (left column) and *Spitzer* IRAC 8$\mu$m contours superposed on grey-scale SC density maps V.

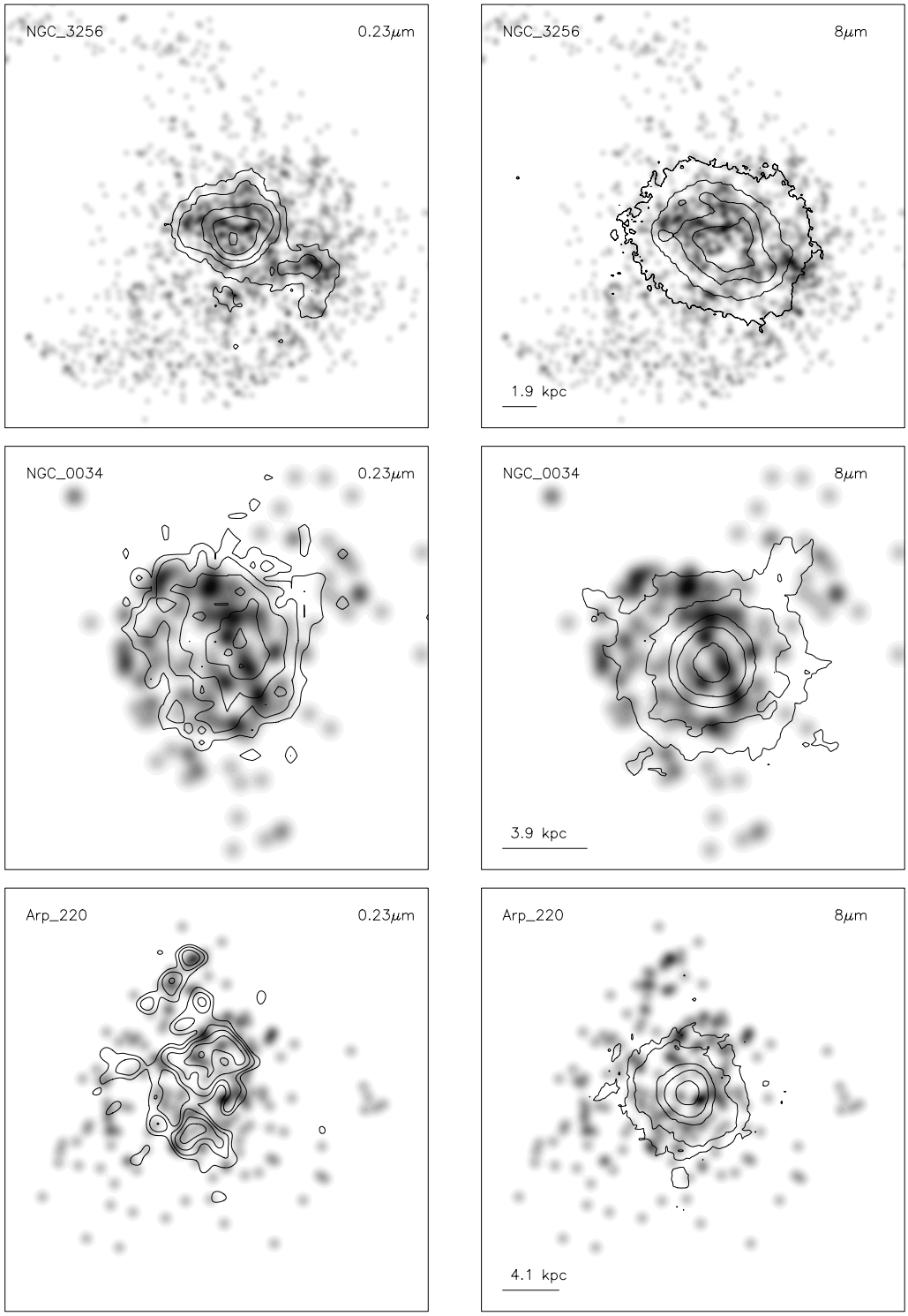


Figure 3.25: *GALEX* NUV 0.23$\mu$m contours (left column) and *Spitzer* IRAC 8$\mu$m contours superposed on grey-scale SC density maps VI.

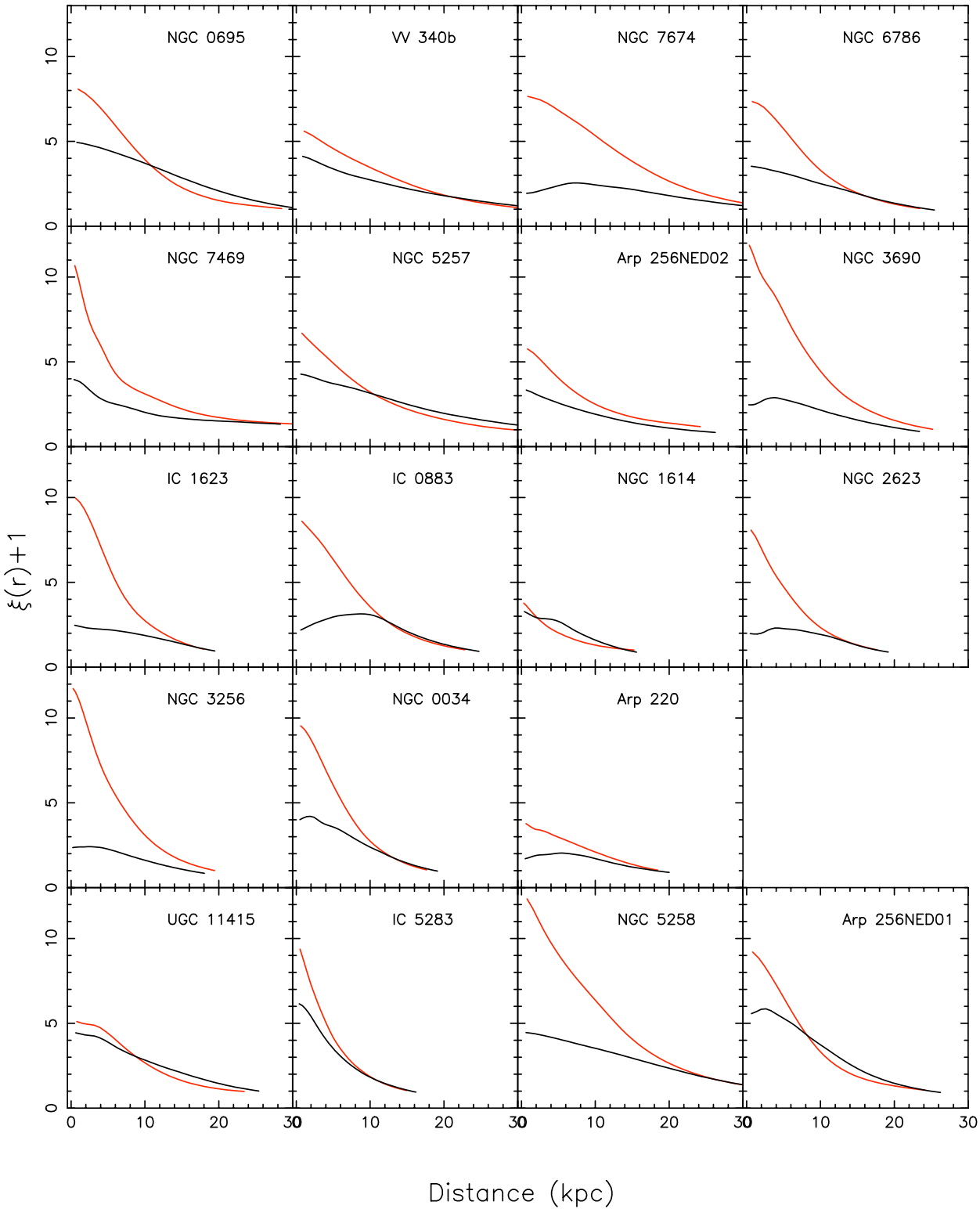


Figure 3.26: Cross-correlation functions of SC locations with *Spitzer* IRAC 8$\mu$m (black) and *GALEX* 0.23$\mu$m (red) fluxes. The bottom row shows the four galaxies that are members of galaxy pairs and have fewer detected clusters.

# Chapter 4

# Properties of Optically Luminous Stellar Clusters in a Complete Sample of Luminous Infrared Galaxies

In this chapter the analysis of SC populations in the complete sample of 87 LIRGs imaged with *HST*/ACS as part of the Great Observatories All-Sky LIRG Survey (GOALS) is presented. The focus of this chapter is to quantify collective SC properties discussed in the previous chapter (number of SCs, specific frequency, specific luminosity, luminosity function, the magnitude of the brightest cluster, median (F435W−F814W) color of the cluster population and fraction of age-dated young clusters) in a large number of galaxies and to unveil possible trends with host galaxy properties such as optical and infrared luminosities, (F435W−F814W) color, merger stage, SFR and nuclear activity type.

## 4.1 Sample

The sample of galaxies discussed in this chapter is the complete HST-GOALS sample. It consists of 87 LIRGs with $L_{\rm IR} \geq 10^{11.4}$ L$_\odot$ drawn from the flux limited (i.e., $f_{60\mu{\rm m}} > 5.24$ Jy) *IRAS* Revised Bright Galaxy Sample (RBGS; Sanders et al., 2003). The HST-GOALS sample represents the most luminous IR sources in the GOALS sample (Armus et al., 2009). The luminosity cutoff of the HST-GOALS sample reflects the fact that at luminosities above $L_{\rm IR} \geq 10^{11.4}$ L$_\odot$ the space density of far-infrared selected galaxies exceeds that of optically selected galaxies (Sanders et al., 2004). The infrared luminosity of the HST-GOALS sample covers the range $L_{\rm IR}$=$10^{11.46-12.57}$ L$_\odot$ with a median of $L_{\rm IR}$=$10^{11.72}$ L$_\odot$ and contains 66 LIRGs and 21 ULIRGs. The redshifts range between $0.009 \leq z \leq 0.088$ with the median $z = 0.034$, corresponding to luminosity distances of 38.9 Mpc to 400 Mpc with a median of 150 Mpc.

The galaxies in the HST-GOALS sample span the full range of nuclear spectral types (Type-1 and Type-2 Seyferts, LINERs and starbursts) and interaction stages (isolated galaxies, galaxy pairs, coalesced galaxies and late stage mergers). The size of the sample and the relative proximity of the objects combined with the high resolution ($\sim 0.1$") and large field of view (3.4' × 3.4') of the *HST*/ACS images make the HST-GOALS data set the best sample for studying optically-visible star clusters in luminous starburst galaxies. The HST-GOALS sample is presented in Table 4.1. In LIRG systems composed of two or more distinct galaxies, the galaxies have been individually tabulated.

In six LIRGs (ESO 203-IG001, IRAS F05189-2524, IRAS 05223+1908, IRAS F10173+0828, IRAS F14378-3651, IRAS 19542+1110) no star clusters have been detected and these systems

are excluded from the cluster analysis. These galaxies are relatively distant with a median $z \approx 0.05$ and are characterized by small angular sizes and smooth light distributions. Four LIRGs (ESO 099-G004, ESO 069-IG006, IRAS F17138-1017, IRAS F18293-3413) are located in crowded stellar fields and have a high percentage (median $\sim 60\%$) of foreground Galactic stars contamination (Chapter 2.3.3) making a reliable star cluster analysis impossible. Hence, out of 87 HST-GOALS LIRGs, 10 are excluded from cluster analysis resulting in 77 LIRG systems. In 13 LIRG systems (12 galaxy pairs and 1 triple) SC population analysis for each component was performed separately; these LIRG systems possess a sufficient number of clusters ($\gtrsim 60$) and individual galaxies have a sufficiently wide separation to clearly recognize with which galaxy SCs are affiliated. In total, the SC analysis was performed on 91 individual galaxies.

## 4.2 Results and Analysis

Observations of 87 HST-GOALS LIRGs with *HST*/ASC in the F435W and F814W filters, standard STScI calibration pipeline data reduction and consecutive cosmic ray removal as well as cluster detection and photometric measurement procedures for the clusters and the total galaxy fluxes are described in Chapter 2.

The basic host galaxy properties are summarized in Table 4.2, the SC properties are presented in Tables 4.3 and 4.4. For each interaction class and nuclear activity type, a mean, median, and the standard deviation of SC properties are tabulated in Tables 4.5 and 4.6.

In order to assess the statistical significance of the differences of SC properties between different merger stages and nuclear activity types, Mann-Whitney U (MWU) and Kolmogorov-Smirnov (KS) tests were performed. Mann-Whitney U-Test tests the hypothesis that two sample populations have the same mean of distribution against the hypothesis that they differ, with low p-values ($< 0.05$) indicating that the means are different. Kolmogorov-Smirnov statistics is based on the Cumulative Distribution Functions (CDFs) and low KS p-values ($< 0.15$) indicate that the null hypothesis that the two CDFs are drawn from the same parent set can be rejected. While the Mann-Whitney U-Test tests for differences in the location of two samples (locations of the ranks), the Kolmogorov-Smirnov test is also sensitive to differences in the general shapes of the distributions in the two samples. The results of MWU and KS tests are presented in Tables 4.7 and 4.8.

### 4.2.1 Host Galaxy Properties

#### Optical Photometry

Optical photometry of 87 HST-GOALS LIRGs in the ACS F435W and F814W filters is presented in Table 4.2. When possible, LIRG systems are separated in individual components and values for each galaxy are tabulated. In cases when the LIRG is located in a crowded stellar filed, the photometry is somewhat uncertain, since the flux contribution of foreground Galactic stars in the line of sight of the LIRG is difficult to subtract.

The absolute magnitudes of individual galaxies range from $-18.5$ mag to $-22.4$ mag in F435W and from $-20.2$ mag to $-23.8$ mag in F814W, with median values of $-20.9 \pm 0.7$ mag

and $-22.6\pm0.7$ mag, respectively. The F814W fluxes are consistently higher than the F435W fluxes. The optically brightest galaxy in this sample is the ULIRG IRAS 09022-3615.

(F435W−F814W) galaxy colors are listed in Table 4.2. The range of galaxy colors is between 1.0 mag and 2.4 mag with a median of $1.8 \pm 0.3$ mag.

**Merger/ Interaction Stage**

The merger/interaction stage for each LIRG was assigned based on optical appearance according to a classification scheme first described in Surace (1998) and Evans et al. (in preparation) and is listed in Table 4.2.

The six Interaction Classes (ICs) are:

- Class 0: A single galaxy or a galaxy with a minor companion
- Class 1: Separate galaxies with undisturbed/intact symmetric disks and no tails
- Class 2: Separate galaxies with asymmetric or amorphous disks and tidal tails
- Class 3 : Two nuclei in common envelope
- Class 4: Double nuclei and tidal tails, but separate galaxy disks not distinguishable
- Class 5 : Single or obscured nucleus, disturbed morphology, long prominent tails
- Class 6 : Single or obscured nucleus, disturbed central morphology, short faint tails or tails absent, shells

The interaction classes follow the progressing stages of the merger of two disk galaxies. IC 0 contains isolated galaxies that do not appear to be involved in an interaction process. IC 1 is comprised of widely separated galaxy pairs during the first approach stage, prior to the first close passage (or 1st pericenter). At this stage, the galaxy disks appear yet relatively unperturbed and do not show signs of the interaction process. IC 2 consists of galaxies after the first contact (1st pericenter); although without kinematic information available, it is impossible to determine whether the galaxies are flying away or toward each other (before or after 1st apocenter). Galaxies during this merger stage have perturbed disks and develop tidal tails and ridges. IC 3 encompasses galaxies during the second contact (2nd pericenter), although, as in the IC 2, it is impossible to distinguish if the closest passage already took place (before or after 2nd pericenter). The individual bodies of progenitor galaxies are still distinguishable at this merger stage. Tidal tails that developed after the 1st passage are also visible. It is possible that the IC 3 also contains systems experiencing the 1st pericenter, since a clear classification is difficult. Systems classified as IC 4 are closer together than the ones comprising IC 3; the two galactic bodies can no longer be distinguished, although two nuclei are present. These are presumably systems at the time of third close passage (or 3rd pericenter). ICs 5 and 6 are final merger stages; the galactic bodies and the nuclei have merged. IC 5 features prominent signs of the merger process, such as disturbed morphology and tidal tails. These signs are less visible in IC 6, although it still displays disturbed central morphology and possibly short faint tails or shells.

In Chapter 3, Figure 3.3 illustrates the different interaction classes: NGC 0695 belongs to the IC 0; VV 340, NGC 7674, NGC 6786 / UGC 11415 and NGC 7469 / IC 5283 are classified as IC 1; NGC 5257/8 and Arp 256 are members of IC 2; NGC 3690 and IC 1623 are IC 3; IC 0883 is IC 4; NGC 1614, NGC 2623 and NGC 3256 are IC 5; NGC 0034 and Arp 220 are IC 6. Throughout Chapter 3 classes 1 and 2 are referred to as the early merger stages, classes 3 and 4 are the mid-merger stages, and classes 5 and 6 are late mergers.

Figure 4.1 depicts the histogram distribution of the number of LIRG systems in each interaction class. LIRG systems in ICs 1 and 2 contain two or more galaxies; all other merger stages are single galaxies. Most LIRGs in the HST-GOALS sample belong to IC 2.

It should be noted that the affiliation with a particular interaction class is difficult to establish and in some cases is ambiguous; the classification scheme cannot account for orientation effects which can cause degeneracy between classes. It is possible that some LIRGs will be assigned a different merger class in the future, as more data (e.g., multiple nuclei hidden in optical) and theoretical merger stimulations become available

**Nuclear Activity Type**

Kim et al. (1995) and Veilleux et al. (1995) carried out an extensive survey of optical nuclear spectra of 200 luminous IRAS galaxies in order to identify the main source of ionization based on optical emission line diagnostics. The nuclear emission line spectra were classified, using a large number of line-ratio diagnostics, as "HII region-like", i.e. the nucleus powered by a starburst, or "AGN-like" where the spectrum showed a presence of an active galactic nucleus. "AGN-like" galaxies include Seyfert galaxies as well as LINERs (Low Ionization Nuclear Emission Regions). However, most "AGN-like" galaxies also display a high level of circumnuclear starburst activity; in fact, the contribution of AGN luminosity to the total energy output in the majority of GOALS LIRGs is only $\sim 12\%$ (Petric et al., 2011).

The optical spectroscopic sample of Kim et al. (1995) and Veilleux et al. (1995) provides classification of 53 HST-GOALS LIRGs. Petric et al. (2011) performed an analysis of *Spitzer* Infrared Spectrograph (IRS) spectra of 202 GOALS systems. In 19 HST-GOALS LIRGs the high ionization [NeV] 14.3$\mu$m line in their mid-IR spectra has been detected, confirming the presence of an AGN. Iwasawa et al. (2011) present Chandra X-ray observations of 44 GOALS LIRGs (C-GOALS sample). Applying either hard X-ray color (HR$> -0.3$) as a selection criterion or detection of the 6.4 keV Fe K line, AGN presence was found in 17 HST-GOALS LIRGs.

Table 4.2 contains the classification of nuclear activity of HST-GOALS LIRGs. 35 (=34% of the sample) LIRGs posses no known nuclear spectral classification; this sub-sample presumably contains both, "HII region-like" and "AGN-like" galaxies. HII region-like nuclei powered by a starburst are found in 31 (= 30%) galaxies, and an AGN is present in 38 (= 36%) (Seyfert and LINERs) galaxies.

The fractional contribution of AGN luminosity to total luminosity varies significantly among the HST-GOALS sample. [NeV/NeII] ratios and X-ray/IR luminosity ratios indicate an AGN contribution of less than 10% in 19 systems, 10% - 50% in 8 systems, and only two LIRGs have an AGN contribution above 50%. While it would be useful to compare star cluster properties as a function of AGN strength, it is not currently possible due to the small size of the sub-sample with established AGN / starburst luminosity fractions.

**Star Formation Rate**

Star formation rates for the HST-GOALS sample are listed in Table 4.2 and range from 4 $M_{\odot}yr^{-1}$ to a prodigious 650 $M_{\odot}yr^{-1}$ in ULIRG UGC 08058 with a median of $78 \pm 125$ $M_{\odot}yr^{-1}$. The majority of SFR values are originally found in Tables 3 and 4 in Howell et al. (2010); these are estimates of the total (obscured plus unobscured) SFRs using combined *IRAS* FIR and *GALEX* FUV fluxes. In a few cases where data are not available in Howell et al. (2010), SFRs were calculated using *IRAS* fluxes and Equation 4 in Kennicutt (1998). The contribution of FUV-estimated SFRs in GOALS LIRGs accounts only for an average of 2.8% of the total SFR (Howell et al., 2010) and, for the purpose of this work, can be safely neglected if no *GALEX* FUV data are available. SFRs in galaxies containing an AGN are upper limits due to the contribution of AGN to the dust heating.

### 4.2.2 Number of Clusters and Specific Frequency

The number of clusters in each LIRG is listed in Table 4.3. The distribution of the number of clusters per system and the dependence of the number of clusters on the redshift are shown in Figures 3.1 and 3.2, and a description of these figures is given in Chapter 3.1. The main conclusion reached was that the number of detected clusters may not reflect the intrinsic cluster population of a galaxy since several observational factors such as distance, angular size of the galaxy, orientation and possibly the amount of dust obscuration affect the ability to detect SCs. The last point is confirmed by a weak anti-correlation (Spearman rank correlation coefficient $r_s = -0.40$, with significance $9.2 \times 10^{-5}$) found between the (F435W−F814W) host galaxy color (which, in part, is due to the amount of extinction present in a galaxy) and the number of detected clusters (Figure 4.2).

The young clusters specific frequency $T_N$ has been introduced in Chapter 1.1.3 and the details of the calculation of $T_N$ values are outlined in Chapter 3.3.1. Table 4.3 lists $T_N$ values that were corrected for the efficiency of the cluster detection procedure using the average completeness function (see Chapter 2.3.4). The completeness correction has only a minor effect on $T_N$: raw $T_N$ values range from 0.02 to 1.55 with a median of $0.21 \pm 0.28$ and the range of corrected $T_N$ values extends from 0.02 to 1.67 with a median of $0.32 \pm 0.40$. The distribution of corrected $T_N$ values is shown in Figure 4.3. Corrected specific frequency $T_N$ values for galaxies in the cluster-rich sample listed in Table 3.3 differ from the ones in Table 4.3 since a different completeness function, individually calculated for each galaxy, was applied in Chapter 3.

The median specific frequency $T_N$ value of the cluster-rich sample ($1.14 \pm 0.30$) is significantly higher than the median $T_N$ of the complete HST-GOALS sample ($0.32 \pm 0.40$), which is not surprising given that the number of SCs was the primary selection criterion for the cluster-rich LIRGs sample.

Figure 4.4 shows the distribution of specific frequency $T_N$ values with the merger stage. The highest median $T_N$ values are found in ICs 1, 2 and 3, the lowest values are associated with ICs 0, 4 and 5. According to the KS and MWU tests, the $T_N$ values of galaxies in ICs 4 and 5 were drawn from a different population distribution than the rest of the ICs. The relatively low specific frequency $T_N$ values in ICs 4 and 5 are probably due to the fact that the median luminosity distance is the largest for these merger stages ($> 160$ Mpc) and thus

the number of detected SCs is the lowest (see Table 4.5). A plot of specific frequency $T_N$ versus luminosity distance (Figure 4.5) shows a sharp drop in $T_N$ values for galaxies beyond $\sim$ 160 Mpc, which is the result of the anti-correlation of the number of clusters with the galaxy distance (see Figure 3.2).

Galaxies with "HII region-like" nuclei have a higher median specific frequency $T_N$ (0.40) than "AGN-like" galaxies (0.30) and the "unknown" nuclear activity sample (0.24). According to the KS and MWU tests the specific frequencies of the "HII region-like" and "AGN-like" galaxies are indeed different.

### 4.2.3 Specific Luminosity

The specific luminosity $T_L$ (i.e., the percentage of flux contributed by clusters to the total luminosity of a galaxy in a given filter) has been described in Chapter 1.1.3 and in Chapter 3.3.2.

The specific luminosity $T_L$ values for F435W and F814W images are listed in Table 4.3 and histogram distributions are plotted in Figure 4.6. Both histograms are skewed towards low $T_L$ values; the first and highest bin (0-1) contains 26 (= 29% of the sample) and 36 (= 39% of the sample) galaxies for F435W and F814W, respectively. The specific luminosity $T_L$ in F435W images varies between 0.1% and 10.8%, with a median of $1.8 \pm 2.3\%$, in F814W images $T_L$ values range from 0.03% to 5.3%, with a median of $1.2 \pm 1.2\%$. It appears that the optically visible SCs contribute rather little to the optical luminosity of LIRGs and certainly play a minor role in the total energy output of these IR luminous systems. No correlation was found between specific luminosity $T_L$(F435W) and F435W absolute magnitude of the host galaxy (Figure 4.7), refuting the idea that in more luminous galaxies SCs contribute a larger percentage of flux.

The median specific luminosity $T_L$ values of the HST-GOALS sample are lower in both filters compared to the cluster-rich LIRGs sample ($3.4 \pm 2.0\%$ in F435W and $1.9 \pm 0.9\%$ in F814W), although the range of specific luminosity $T_L$ values in the HST-GOALS sample is larger than the $T_L$ range of the cluster-rich sample, extending to lower as well as higher values.

The highest median specific luminosity $T_L$ values are found in ICs 0, 2 and 4, followed by ICs 1, 3 and 5, and the lowest median $T_L$ value is associated with IC 6 (Figure 4.8). The range of $T_L$ values in each interaction class is large; the KS and MWU tests do not support a significant change of $T_L$ values along the merger sequence, except in IC 6.

Galaxies with "HII region-like" nuclei have a higher median specific luminosity $T_L$ value (2.63 in F435W and 1.85 in F814W) than "AGN-like" galaxies (1.40 in F435W and 0.77 in F814W) and the "unknown" nuclear activity sample (1.60 in F435W and 1.18 in F814W), this difference is also confirmed by the KS and MWU tests.

### 4.2.4 Luminosity Function

The luminosity function indices $\alpha$ were calculated following the procedure outlined in Chapter 3.3.4. The luminosity distribution of each galaxy was corrected using an average completeness function derived from 16 individually calculated completeness functions

(Chapter 2.3.4). The LF indices for 15 cluster-rich galaxies derived in Chapter 3.3.4 using individually calculated completeness functions for each galaxy show only an average difference of 0.05 in the LF indices derived using the average completeness function; this demonstrates that the use of the average completeness function is justified in most galaxies.

In order to obtain a good fit to the cluster luminosity distribution, a SC population of more than 40 clusters is required; thus the LF index could be determined only for $\sim 60$ galaxies. Values of the corrected LF indices for F435W and F814W images are listed in Table 4.4. The distribution of the LF indices is shown in Figure 4.9. LF indices range from $-1.4$ to $-2.7$ with a median of $-1.86 \pm 0.27$ in F435W and $-1.77 \pm 0.24$ in F814W for corrected values. Corrections for foreground stars and completeness have only a minor effect on LF indices, on average the slope becomes $\sim 0.11$ steeper. A fit to raw luminosity histograms performed up to 80% completeness (the highest uncorrected bin) results in median values of $-1.74 \pm 0.23$ in F435W and $-1.67 \pm 0.23$ in F814W.

The median LF indices of the HST-GOALS sample are consistent with the median LF indices of the cluster-rich sample ($-1.91 \pm 0.21$ and $-1.88 \pm 0.20$ in the F435W and F814W, respectively). Median LF indices of both samples are somewhat lower than the generally accepted LF index $\alpha \approx -2$. A shallower LF slope could be caused by blending of individual clusters into cluster associations due to limited resolution. In this case the LF index should show a dependence on the luminosity distance of the galaxy; this is ruled out by Figure 4.10 which exhibits no such trend. Other possible sources of uncertainties in LF index determination are extinction and an underestimation of the completeness corrections. Both effects are possible and are hard to rule out. In particular, a single completeness function was calculated for the entire galaxy, without a sub-division into several surface brightness regions (Chapter 2.3.4) resulting in lower limits of the LF indices.

The plot of the median LF indexes for each interaction class versus the merger stage (Figure 4.11) shows no significant trend, which is also confirmed by the KS and MWU tests.

Galaxies with "HII region-like" nuclei have slightly smaller median LF indexes value ($-1.75 \pm 0.20$ in F435W and $-1.75 \pm 0.21$ in F814W) than "AGN-like" galaxies ($-1.94 \pm 0.30$ in F435W and $-1.93 \pm 0.23$ in F814W) and the "unknown" nuclear activity sample ($-1.93 \pm 0.29$ in F435W and $-1.71 \pm 0.29$ in F814W) (see Table 4.6), but this finding is not supported as statistically significant by the KS and MWU tests.

### 4.2.5 Cluster Colors and Ages

Median (F435W−F814W) cluster colors for each galaxy are listed in Table 4.3 and the distribution of cluster colors is shown in Figure 4.12. Median cluster colors range from 0.43 mag to 2.25 mag with the median cluster color for the entire sample of $0.91 \pm 0.36$ mag.

Cluster ages and masses were estimated using color-magnitude diagrams and Bruzual-Charlot population synthesis models (Chapter 3.3.5). Due to difficulties associated with age-dating of SCs using only two filters, the analysis is limited to determination of the lower limit of the SC population fraction younger than 7.6 Myr, i.e., (F435W−F814W) $< 0.51$ (see Chapter 3.3.5) in each galaxy. This percentage of age-dated young clusters in each galaxy is listed in Table 4.4 and ranges between 0% and 70% with a median of $17.1 \pm 14.9$%. The distribution is shown in Figure 4.13. The fraction of young SCs is lower in the complete HST-GOALS sample than in the cluster-rich LIRGs sample (median $\sim 30$%).

Figure 4.14 shows a plot of median cluster colors versus the host galaxy color. A clear correlation between both properties is observed (Spearman rank correlation coefficient $r_s = 0.65$, with significance $2.4 \times 10^{-12}$). Also, a correlation between the median fractions of young clusters and host galaxy color exists (Spearman rank correlation coefficient $r_s = 0.59$, with significance $6.8 \times 10^{-10}$). Since SCs contribute rather little to the total optical luminosity of their host galaxy, the colors of SCs do not have a strong influence on the galaxy color. The stellar field population and the amount of dust are presumably the major factors determining galaxy color. It is apparent that galaxies with young stellar field population and small amount of extinction would have larger fractions of young clusters.

Since cluster ages are determined based on (F435W−F814W) cluster color, median cluster colors and median fractions of young clusters show similar trends with merger stage (Figure 4.15). The fraction of young clusters in ICs 0 – 5 varies between 17% – 29%; the KS and MWU tests show no statistically significant difference between these merger stages. The fraction of young clusters in IC 6 is considerably lower ($\sim 10\%$), and the significance is confirmed by both tests.

The fraction of young clusters remains unchanged in different nuclear activity types, all three values are around 17%.

### 4.2.6 Brightest Clusters

Table 4.4 includes, besides the F435W absolute magnitudes, the (F435W−F814W) colors, ages and masses of the most luminous cluster in each galaxy. The absolute magnitudes of the brightest clusters cover the range of $-11.8$ mag $> M^{max}_{F435W} > -18.0$ mag with the median of $-15.18 \pm 1.44$ mag. The distribution is shown in Figure 4.16. In 8 galaxies (UGC 02369 NED01, AM 0702-601 NED02, IRAS 07251-0248, IRAS 09022-3615, NGC 6090, ESO 286-IG019, IRAS F22491-1808 and NGC 7469) the F435W absolute magnitude of the most luminous cluster exceeds $-17$ mag. The (F435W−F814W) color of these very luminous clusters is $< 0.8$, excluding the possibility of these objects being foreground stars or the galactic nuclei (additionally, near-IR and mid-IR centroids were checked), although it is still possible that these are SC complexes rather than individual SCs.

Reliable age-estimates are available only for 37 (= 41%) of the brightest clusters in the HST-GOALS sample with (F435W−F814W) $< 0.51$. The brightest clusters in 30 (= 33%) galaxies have colors $0.51 <$(F435W−F814W) $< 1.0$ and an age-range between 10 to 500 Myr. The age-estimates in this color range are subject to an age-color degeneracy (see Chapter 3.3.5) and the youngest possible ages are listed in Table 4.4. The last 24 (= 26%) of the brightest clusters have (F435W−F814W) $> 1.0$ and ages from 500 Myr to few Gyr, assuming no extinction.

The plot of the median $M^{max}_{F435W}$ for each interaction class versus the merger stage (Figure 4.17) has the appearance of the median $M^{max}_{F435W}$ rising from IC 1 to IC 4 and falling again in ICs 5 and 6. However, the KS and MWU tests do not support this trend as statistically significant.

Galaxies with HII region-like nuclei have higher median $M^{max}_{F435W}$ values ($-15.7 \pm 1.4$ mag) than "AGN-like" galaxies ($-14.9 \pm 1.5$ mag) and the "unknown" nuclear activity sample ($-14.8 \pm 1.4$ mag). The difference between HII and AGN-like galaxies is confirmed by KS and MWU tests

## 4.3 Discussion

### 4.3.1 Specific Luminosity – SFR Relation

In order to assess the validity of the specific luminosity – SFR relation found by Larsen & Richtler (2000) in a sample of nearby spiral galaxies with respect to Luminous IR Galaxies, the analysis performed in Chapter 3.3.2 is extended to include all HST-GOALS LIRGs. Figure 4.18, panel a) shows the F435W specific luminosity $T_L$(F435W) plotted versus SFRs derived from combined FIR and FUV fluxes. No correlation is apparent, and the visual impression is confirmed by the Spearman rank correlation coefficient $r_s = 0.06$, with significance 0.59. In Figure 4.18, panel b) $T_L$(F435W) plotted versus SFRs derived from FUV fluxes only, displays a weak trend, with the Spearman rank correlation coefficient $r_s = 0.41$, with significance $6.5 \times 10^{-4}$. The same argument as in Chapter 3.3.2 applies here: optically visible SCs and FUV fluxes both trace unobscured star formation, while the total SFRs trace mostly star formation that is hidden at shorter wavelengths.

### 4.3.2 Brightest Cluster – SFR Relation

Chapter 3.3.3 contains a discussion of the $M^{max}_{F435W}$ – SFR correlation observed for lower luminosity star-forming galaxies in Whitmore (2003) and Bastian (2008). Figure 4.19 shows a plot of F435W (or V band as in Bastian (2008)) absolute magnitude of the most luminous cluster versus the SFR of the host galaxy with the data for the complete HST-GOALS sample included; it is analogous to Figure 3.12 for the cluster-rich sample. While the LIRGs in the cluster-rich sample were in good agreement with previously published observations (Bastian, 2008) and followed the best fit to the data from Weidner et al. (2004) quite closely, the HST-GOALS sample exhibits considerable scatter.

The brightest clusters located above the Weidner et al. (2004) fit line are brighter relative to the SFRs of their host galaxies; it is possible that that these points do not represent individual SCs, but are instead unresolved SC complexes.

The degree of scatter is more severe below the Weidner et al. (2004) fit to the data; data points located below the fit line indicate SCs that are fainter relative to the SFRs of their host galaxies. So, using the median value of SFR of the HST-GOALS sample (78 $M_\odot$ $yr^{-1}$) in Equation 2 of Weidner et al. (2004) predicts $M^{max}_V = -15.68$ mag, which is 0.5 mag brighter than the median F435W absolute magnitude of the brightest cluster (-15.18 mag) observed in the HST-GOALS sample.

Possible explanations of the significant population of brightest clusters in the $M^{max}_{F435W}$ – SFR plot below the fit line include: *(i)* extinction; *(ii)* the large range of cluster colors resulting in a large range of cluster ages (Bastian (2008) states that the brightest cluster – SFR relation is valid only for relatively young clusters i.e., $< 10$ Myr); *(iii)* the color & age dependency of the transformation of F435W to V band magnitudes (the assumed B−V $\approx 0$ is valid only for clusters younger than $\sim 125$ Myr); and finally *(iv)* the overestimation of the SFR due to AGN contributions to the dust heating and $L_{\rm IR}$.

In order to address *(i)* and *(ii)*, the symbols in the $M^{max}_{F435W}$ – SFR plot in Figure 4.20 were color-coded according to the (F435W−F814W) color of the cluster they represent. Red ((F435W−F814W) $> 1.0$) clusters are absent above the fit line, all clusters located in this plot

region have blue ((F435W−F814W) < 0.51) or intermediate (0.5 < (F435W−F814W) < 1.0) colors, indicating that these SCs are relatively young and unaffected by extinction. All three groups of color-coded points, blue ((F435W−F814W) < 0.51), intermediate (0.5 < (F435W−F814W) < 1.0) and red ((F435W−F814W) > 1) are found below the fit line. While the presence of red clusters can be easily explained with extinction, the presence of blue clusters is somewhat surprising, and other factors besides extinction must be responsible for blue clusters being fainter than expected from the SFR of their host galaxies. Additionally, no dependence of the F435W magnitude of the brightest cluster on the cluster color is apparent in Figure 4.21, contrary to an expectation that blue clusters would be more luminous, and red (i.e. extinguished or old) clusters would be faint. Extinction and the large range of cluster colors alone cannot explain the scatter in $M^{max}_{F435W}$ - SFR plot.

The transformation from F435W to V band magnitudes (point *(iii)*) affects clusters older than 125 Myr; for clusters younger than $\sim$ 125 Myr the (F435W−V) < 0.1 and for clusters above this age 0.1 mag < (F435W−V) < 1 mag. Thus some of the intermediate and red color clusters should be brighter, although this effect alone is insufficient to significantly reduce the scatter.

In order to address point *(iv)*, the symbols in the $M^{max}_{F435W}$ - SFR plot in Figure 4.22 were color-coded according to the nuclear activity type of their host galaxy: galaxies with "HII region-like" nuclei are designated with blue dots, galaxies with "AGN-like" nuclei are designated with red stars, and the "unknown nuclear activity sample is omitted. Most "HII region-like" galaxies follow the fit line reasonably well. Galaxies with "AGN-like" nuclei either follow the fit line or are located below the fit line. This hints at an overestimation of the SFR in galaxies with AGN presence. The median SFR for "AGN-like" galaxies ($\sim$ 149 $M_\odot$ $yr^{-1}$) is higher than for "HII region-like" galaxies ($\sim$ 94 $M_\odot$ $yr^{-1}$). Additionally, the median brightest cluster $M^{max}_{F435W}$ in "AGN-like" galaxies (-14.9 mag) is lower than in "HII region-like" galaxies (-15.7 mag).

The scatter below the fit line, which mostly includes galaxies with "AGN-like" nuclei, may be due to an overestimation of SFRs (i.e., contribution of the AGN to $L_{\rm IR}$) combined with extinction.

### 4.3.3 Trends with Merger Stage

In the "Results and Analysis" section various SC properties were calculated for each merger stage in an attempt to determine the time and the strength of the merger-induced starburst. However, the range of values associated with each merger stage is large, the mean and median values of different interaction classes are located well within the 1-sigma uncertainties of each other. Furthermore, the KS test is consistent, for the most part, with the distribution of values in each interaction class being drawn from the same population, and the differences in mean and median values along the merger stage sequence are not significant according to the MWU test.

As described in Chapter 1.1.3, the numerical simulation models with shock-induced SF prescription predict strong SBs during the 1st and 2nd pericenter, when galactic disk are interpenetrating (Barnes, 2004). In our merger classification scheme the IC 3 contains systems during the 2nd and possibly also 1st pericenter. Another SB, predicted by both SF prescriptions, shock-induced as well as density-dependent, occurs when the galaxies finally

merge, corresponding to ICs 4 or 5. Therefore, one would expect the most young SCs to be detected in merger stages 3, 4 and 5. Unfortunately, the analysis of SC properties as a function of merger stage does not provide a clear indication to support this assumption. Specific frequency $T_N$ values are high in IC 3 and low in ICs 4 and 5. Specific luminosity $T_L$ values are low in IC 3 and high in IC 4. The median magnitudes of the brightest cluster, $M^{max}_{F435W}$, are highest in ICs 3, 4 and 5. The fraction of age-dated young clusters is high in IC 3 but declines in ICs 4 and 5. Ultimately, the KS and MWU tests do not confirm the uniqueness of any of these values. The difference is due to statistical effects, the values in each interaction class are consistent with being drawn from the same distribution.

The late merger stages 5 and 6 show a consistent decline in specific luminosity, fraction of young clusters and median magnitude of the brightest cluster. These trends indicate that optically visible, extended (i.e. spread out throughout the body of the galaxy as opposed to concentrated in the nucleus) SF becomes less prominent in late merger stages. On the other hand, $L_{\rm IR}$ and thus SFRs are increased in late merger stages. Chapter 3.3.7 describes the finding that the mid-IR flux becomes more centrally concentrated in late merger stages. The above facts suggest that a nuclear obscured SB or AGN are responsible for high SFRs which are not reflected in the optically visible extended star formation.

IC 5 represents a transition between extended SF to strongly nuclear concentrated SB in IC 6, dominated by a compact nuclear power-sources as seen in mid-IR morphology in Chapter 3.3.7. Post-merger stage 6 is the only interaction class where specific luminosity, fraction of young clusters and magnitudes of the brightest clusters stand out from other merger stages according to KS and MWU tests. This finding is consistent with the numerical simulation models predicting a nuclear SB when the galaxies finally merge and the gas has had time to accumulate in the nucleus to fuel nuclear SB and/or an AGN.

Properties of SC populations in pre-merger and early merger stage LIRGs (ICs 0, 1 and 2) do not differ significantly from other merger stages according to KS and MWU tests. These systems possess a large fraction of young SCs, comparable with galaxies in mid-merger stages. The origin of enhanced SFRs in isolated galaxies (IC 0) and pre-first contact (IC 1) galaxy pairs remains unclear. Some other mechanism than the merger process (e.g., bars) is responsible for triggering the observed high SFRs and AGN activity.

Analysis performed in the "Results and Analysis" section aimed at elucidating the details of the merger-induces star formation processes based on SC properties as function of merger stage and a comparison with numerical merger simulations. However, this proved to be rather difficult since most trends along the merger sequence were not confirmed by the KS and MWU tests which did not support statistically significant differences between merger stages. Several possible effects are responsible for that: *(i)* The distance and extinction of the host galaxy affect the specific frequency, specific luminosity and the fraction of young SCs. *(ii)* The classification of LIRGs into different merger stages is ambiguous and misclassifications are possible. *(iii)* The present merger stage classification is too crude to follow SBs predicted by merger simulations. For example, the merger stage classification does not have a specific class for systems during the 1st pericenter, when a sharp peak in SF occurs. IC 2 is too broad, according to Barnes (2004) there is a broad peak and a decline in SF during this phase, thus IC 2 could encompass galaxies with high as well as low SFRs. *(iv)* The timing and strength of SB episodes during the merger process are strongly dependent on the properties of progenitor galaxies (mass ratio, amount of gas, bulge/disk ratio (Mihos & Hernquist, 1996)) and the

geometry of the encounter (inclination, prograde vrs retrograde collisions). For example, according to Figure 1 in Chien (2010), only a direct encounter produces a strong SB during the time between the 1st pericenter and 1st apocenter. The initial conditions of the encounter are unique for each system and the SF history has to be modeled for each system individually. It is possible that LIRGs in the same interaction class have quite different SF histories, and SFR trends are not uniform in all LIRGs in an interaction class.

### 4.3.4 Trends with Nuclear Activity Type

Variations of SC properties between galaxies belonging to different nuclear activity types are more prominent than the ones that could be uncovered in different merger stages; the statistical significance of these variation is also confirmed by the KS and MWU tests. The specific frequency $T_N$ and specific luminosity $T_L$ are enhanced in galaxies with "HII region-like" nuclei compared to galaxies with "AGN-like" nuclei. "HII region-like" galaxies have a higher median magnitude of the brightest cluster and follow more closely the $M^{max}_{F435W}$ – SFR relation. It appears that galaxies with SF dominated nucleus, on average, produce a larger number and more luminous SCs, and a larger fraction of galaxy's optical luminosity originates from SCs than galaxies that possess an AGN. The higher degree of SF activity in "HII region-like" galaxies is also translated in enhanced SC population properties. However, no difference in the fraction of age-dated SCs younger than 10 Myr was found, galaxies of both nuclear activity types are forming young star clusters, the AGN and SF appear to co-exist.

## 4.4 Conclusions

The SC populations in the complete sample of 87 GOALS LIRGs with $L_{\rm IR} \geq 10^{11.4}$ $L_\odot$ imaged with HST/ACS were investigated. The main results are summarized as follows:

- The specific frequency $T_N$ values range from 0.02 to 1.67 with a median of $0.32 \pm 0.40$ and $T_N$ shows a dependence on the distance of the galaxy. The KS and MWU tests do not support a significant change of specific frequency $T_N$ values along the merger sequence. Galaxies with "HII region-like" nuclei have a higher median specific frequency $T_N$ value (0.4) than galaxies with "AGN-like" nuclei (0.30) and the "unknown" nuclear activity sample (0.24); this finding is confirmed by the KS and MWU tests.

- The specific luminosity $T_L$ in F435W images varies between 0.1% and 10.8%, with a median of $1.8 \pm 2.3$%, in F814W images $T_L$ values range from 0.03% to 5.3%, with a median of $1.2 \pm 1.2$%. The KS and MWU tests do not support a significant change of $T_L$ values along the merger sequence. Galaxies with "HII region-like" nuclei have a higher median specific luminosity $T_L$ values (2.63 in F435W and 1.85 in F814W) than galaxies with "AGN-like" nuclei (1.40 in F435W and 0.77 in F814W) and the unknown nuclear activity sample (1.60 in F435W and 1.18 in F814W); this finding is confirmed by the KS and MWU tests.

- Luminosity function indices range from $-1.4$ to $-2.7$ with a median of $-1.86 \pm 0.27$ in F435W and $-1.77 \pm 0.24$ in F814W. KS and MWU tests do not support a significant trend with the merger stage or nuclear activity type.

- The population fraction of age-dated clusters younger than 7.6 Myr in each galaxy ranges between 0% and 70% with a median of 17%. KS and MWU tests do not support a significant trend with the merger stage or nuclear activity type.

- The absolute magnitudes of the brightest clusters cover the range of $-11.8$ mag $> \mathrm{M}^{max}_{F435W} > -18.0$ mag with the median of $-15.18 \pm 1.44$ mag. In 8 galaxies SCs with $\mathrm{M}^{max}_{F435W} < -17.0$ mag are found. KS and MWU tests do not support a significant trend with the merger stage. Galaxies with "HII region-like" nuclei have a higher median $\mathrm{M}^{max}_{F435W}$ value ($-15.7$ mag) than galaxies with "AGN-like" nuclei ($-14.9$ mag) and the unknown" nuclear activity sample ($-14.8$ mag); this finding is confirmed by the KS and MWU tests.

- The specific luminosity $T_L$(F435W) – SFR(FIR + FUV) relation found by Larsen & Richtler (2000) in a sample of nearby spiral galaxies is not applicable to Luminous IR Galaxies. However, a weak trend (Spearman rank correlation coefficient $\mathrm{r}_s = 0.41$, with significance $6.5 \times 10^{-4}$) of specific luminosity $T_L$(F435W) – SFR(FUV) is observed.

- The HST-GOALS LIRGs follow the $\mathrm{M}^{max}_{F435W}$ – SFR relation quite well, although a large degree of scatter is observed. The significant number of brightest cluster members observed below the relation may be due to extinction and over-estimation of SFRs in AGN-dominated galaxies.

- No clear trend of SC properties with merger stage is observed. The only conclusion that can be established is that in late merger stages the degree of the extended star formation diminishes and the centrally concentrated nuclear starburst or an AGN dominate the energy output of the LIRG.

- Galaxies with "HII region-like" (i.e., starburst-like) nuclear spectra exhibit higher specific frequency $T_N$, specific luminosity $T_L$ and $\mathrm{M}^{max}_{F435W}$ values compared to galaxies were an active galactic nucleus is clearly present.

Table 4.1. HST-GOALS Sample

| Visit Number (1) | Name IRAS (2) | Name Optical ID (3) | R.A. (J2000) (4) | Dec. (J2000) (5) | $V_{Helio}$ ($kms^{-1}$) (6) | $D_L$ (Mpc) (7) | scale (kpc/ ") (8) | log $L_{IR}$ ($L_\odot$) (9) |
|---|---|---|---|---|---|---|---|---|
| 1 | F00085-1223 | NGC 0034 | 00h11m06.55s | -12d06m26.3s | 5881 | 84.1 | 0.392 | 11.49 |
| 2 | F00163-1039 | Arp 256 | 00h18m50.51s | -10d22m09.2s | 8159 | 117.5 | 0.538 | 11.48 |
| | | Arp 256 NED02 | 00h18m50.10s | -10d21m42.0s | 8193 | 118.0 | 0.540 | |
| | | Arp 256 NED01 | 00h18m50.90s | -10d22m37.0s | 8125 | 117.0 | 0.536 | |
| 3 | F00506+7248 | MCG+12-02-001 | 00h54m03.61s | +73d05m11.8s | 4706 | 69.8 | 0.328 | 11.50 |
| 4 | F01053-1746 | IC 1623 | 01h07m47.18s | -17d30m25.3s | 6016 | 85.5 | 0.399 | 11.71 |
| 5 | F01076-1707 | MCG-03-04-014 | 01h10m08.96s | -16d51m09.8s | 10040 | 144.0 | 0.656 | 11.65 |
| 6 | F01173+1405 | CGCG 436-030 | 01h20m02.72s | +14d21m42.9s | 9362 | 134.0 | 0.610 | 11.69 |
| 7 | F01364-1042 | IRAS F01364-1042 | 01h38m52.92s | -10d27m11.4s | 14464 | 210.0 | 0.930 | 11.85 |
| 8 | F01417+1651 | III Zw 035 | 01h44m30.45s | +17d06m05.0s | 8375 | 119.0 | 0.547 | 11.64 |
| 9 | F01484+2220 | NGC 0695 | 01h51m14.24s | +22d34m56.5s | 9735 | 139.0 | 0.634 | 11.68 |
| 10 | F02203+3158 | MRK 1034 | 02h23m20.40s | +32d11m34.0s | 10142 | 146.0 | 0.661 | 11.64 |
| | | MCG+05-06-036 | 02h23m21.99s | +32d11m49.6s | 10106 | 145.0 | 0.659 | |
| | | MCG+05-06-035 | 02h23m18.92s | +32d11m18.4s | 10083 | 144.0 | 0.653 | |
| 11 | F02512+1446 | UGC 02369 | 02h54m01.78s | +14d58m24.9s | 9558 | 136.0 | 0.622 | 11.67 |
| | | UGC 02369 NED01 | 02h54m01.80s | +14d58m14.1s | 9354 | 133.0 | 0.609 | |
| | | UGC 02369 NED02 | 02h54m01.77s | +14d58m36.9s | 9761 | 139.0 | 0.635 | |
| 12 | F03359+1523 | IRAS F03359+1523 | 03h38m46.70s | +15d32m55.0s | 10613 | 152.0 | 0.690 | 11.55 |
| 13 | F04191-1855 | ESO 550-IG 025 | 04h21m20.02s | -18d48m47.6s | 9621 | 138.5 | 0.632 | 11.51 |
| | | ESO 550-IG025 NED01 | 04h21m19.99s | -18d48m38.9s | 9652 | 139.0 | 0.634 | |
| | | ESO 550-IG025 NED02 | 04h21m20.05s | -18d48m56.4s | 9590 | 138.0 | 0.630 | |
| 14 | F04315-0840 | NGC 1614 | 04h33m59.85s | -08d34m43.9s | 4778 | 67.8 | 0.319 | 11.65 |
| 15 | F04454-4838 | ESO 203-IG001 | 04h46m49.50s | -48d33m32.9s | 15862 | 235.0 | 1.029 | 11.86 |
| 16 | F05081+7936 | VII Zw 031 | 05h16m46.44s | +79d40m12.6s | 16090 | 240.0 | 1.048 | 11.99 |
| 17 | F05189-2524 | IRAS F05189-2524 | 05h21m01.47s | -25d21m45.4s | 12760 | 187.0 | 0.834 | 12.16 |
| 18 | 05223+1908 | IRAS 05223+1908 | 05h25m16.50s | +19d10m46.0s | 8867 | 128.0 | 0.586 | 11.65 |
| 19 | 05368+4940 | MCG+08-11-002 | 05h40m43.71s | +49d41m41.5s | 5743 | 83.7 | 0.391 | 11.46 |
| 20 | F06076-2139 | IRAS F06076-2139 | 06h09m45.81s | -21d40m23.7s | 11226 | 165.0 | 0.742 | 11.65 |

Table 4.1. – Continued

| Visit Number (1) | Name IRAS (2) | Name Optical ID (3) | R.A. (J2000) (4) | Dec. (J2000) (5) | $V_{Helio}$ ($kms^{-1}$) (6) | $D_L$ (Mpc) (7) | scale (kpc/ ") (8) | log $L_{IR}$ ($L_\odot$) (9) |
|---|---|---|---|---|---|---|---|---|
| 21 | F06259-4708 | ESO 255-IG007 | 06h27m22.45s | -47d10m48.7s | 11629 | 173.0 | 0.775 | 11.90 |
| | | ESO 255-IG007 NED01 | 06h27m21.67s | -47d10m36.3s | 11813 | 175.0 | 0.786 | |
| | | ESO 255-IG007 NED02 | 06h27m22.54s | -47d10m46.5s | 11596 | 172.0 | 0.773 | |
| | | ESO 255-IG007 NED03 | 06h27m23.23s | -47d11m03.2s | 11835 | 176.0 | 0.788 | |
| 22 | F07027-6011 | AM 0702-601 | 07h03m26.37s | -60d16m03.7s | 9390 | 141.0 | 0.640 | 11.64 |
| | | AM 0702-601 NED01 | 07h03m24.12s | -60d15m23.3s | 9390 | 141.0 | 0.640 | |
| | | AM 0702-601 NED02 | 07h03m28.62s | -60d16m44.1s | 9325 | 140.0 | 0.636 | |
| 23 | 07251-0248 | IRAS 07251-0248 | 07h27m37.55s | -02d54m54.1s | 26249 | 400.0 | 1.641 | 12.39 |
| 24 | 08355-4944 | IRAS 08355-4944 | 08h37m01.82s | -49d54m30.2s | 7764 | 118.0 | 0.543 | 11.62 |
| 25 | F08354+2555 | NGC 2623 | 08h38m24.08s | +25d45m16.6s | 5549 | 84.1 | 0.393 | 11.60 |
| 26 | F08520-6850 | ESO 060-IG 016 | 08h52m31.29s | -69d01m57.0s | 13885 | 210.0 | 0.928 | 11.82 |
| 27 | F08572+3915 | IRAS F08572+3915 | 09h00m25.39s | +39d03m54.4s | 17493 | 264.0 | 1.141 | 12.16 |
| 28 | 09022-3615 | IRAS 09022-3615 | 09h04m12.70s | -36d27m01.1s | 17880 | 271.0 | 1.170 | 12.31 |
| 29 | F09111-1007 | IRAS F09111-1007 | 09h13m37.61s | -10d19m24.8s | 16231 | 246.0 | 1.071 | 12.06 |
| | | 2MASX J09133888-1019196 | 09h13m38.83s | -10d19m19.9s | 16231 | 246.0 | 1.071 | |
| | | 2MASX J09133644-1019296 | 09h13m36.46s | -10d19m29.9s | 16489 | 250.0 | 1.086 | |
| 30 | F09126+4432 | UGC 04881 | 09h15m55.11s | +44d19m54.1s | 11851 | 178.0 | 0.797 | 11.74 |
| 31 | F09320+6134 | UGC 05101 | 09h35m51.65s | +61d21m11.2s | 11802 | 177.0 | 0.793 | 12.01 |
| 32 | F10038-3338 | ESO 374-IG 032 | 10h06m04.80s | -33d53m15.0s | 10223 | 156.0 | 0.707 | 11.78 |
| 33 | F10173+0828 | IRAS F10173+0828 | 10h20m00.21s | +08d13m33.8s | 14716 | 224.0 | 0.985 | 11.86 |
| 34 | F10257-4339 | NGC 3256 | 10h27m51.27s | -43d54m13.8s | 2804 | 38.9 | 0.185 | 11.64 |
| 35 | F10565+2448 | IRAS F10565+2448 | 10h59m18.14s | +24d32m34.3s | 12921 | 197.0 | 0.876 | 12.08 |
| 36 | F11011+4107 | MCG+07-23-019 | 11h03m53.20s | +40d50m57.0s | 10350 | 158.0 | 0.712 | 11.62 |
| 37 | F11231+1456 | IRAS F11231+1456 | 11h25m47.30s | +14d40m21.1s | 10192 | 157.0 | 0.710 | 11.64 |
| | | IC 2810 | 11h25m45.05s | +14d40m35.7s | 10243 | 158.0 | 0.713 | |
| | | IC 2810B | 11h25m49.55s | +14d40m06.6s | 10140 | 156.0 | 0.707 | |
| 38 | F11257+5850 | NGC 3690 | 11h28m32.25s | +58d33m44.0s | 3093 | 50.7 | 0.240 | 11.93 |
| 39 | F12112+0305 | IRAS F12112+0305 | 12h13m46.00s | +02d48m38.0s | 21980 | 340.0 | 1.428 | 12.36 |
| 40 | 12116-5615 | IRAS 12116-5615 | 12h14m22.10s | -56d32m33.2s | 8125 | 128.0 | 0.585 | 11.65 |

Table 4.1. – Continued

| Visit Number (1) | Name IRAS (2) | Name Optical ID (3) | R.A. (J2000) (4) | Dec. (J2000) (5) | $V_{Helio}$ ($kms^{-1}$) (6) | $D_L$ (Mpc) (7) | scale (kpc/ ") (8) | log $L_{IR}$ ($L_\odot$) (9) |
|---|---|---|---|---|---|---|---|---|
| 41 | F12540+5708 | UGC 08058 | 12h56m14.23s | +56d52m25.2s | 12642 | 192.0 | 0.856 | 12.57 |
| 42 | F12592+0436 | CGCG 043-099 | 13h01m50.80s | +04d20m00.0s | 11237 | 175.0 | 0.784 | 11.68 |
| 43 | F13001-2339 | ESO 507-G070 | 13h02m52.35s | -23d55m17.7s | 6506 | 106.0 | 0.491 | 11.56 |
| 44 | F13097-1531 | NGC 5010 | 13h12m26.35s | -15d47m52.3s | 2975 | 44.8 | 0.213 | 10.84 |
| 45 | 13120-5453 | IRAS 13120-5453 | 13h15m06.35s | -55d09m22.7s | 9222 | 144.0 | 0.653 | 12.32 |
| 46 | F13136+6223 | VV 250 | 13h15m32.80s | +62d07m37.0s | 9243 | 141.0 | 0.641 | 11.81 |
| | | VV 250a | 13h15m34.98s | +62d07m28.7s | 9313 | 142.0 | 0.645 | |
| | | VV 250b | 13h15m30.59s | +62d07m45.3s | 9230 | 141.0 | 0.640 | |
| 47 | F13182+3424 | UGC 08387 | 13h20m35.34s | +34d08m22.2s | 6985 | 110.0 | 0.507 | 11.73 |
| 48 | F13362+4831 | NGC 5256 | 13h38m17.52s | +48d16m36.7s | 8341 | 129.0 | 0.590 | 11.56 |
| | | NGC 5256 NED01 | 13h38m17.31s | +48d16m32.0s | 8274 | 128.0 | 0.585 | |
| | | NGC 5256 NED02 | 13h38m17.79s | +48d16m41.0s | 8408 | 130.0 | 0.594 | |
| 49 | F13373+0105 | Arp 240 | 13h39m55.00s | +00d50m07.0s | 6778 | 108.5 | 0.502 | 11.62 |
| | | NGC 5258 | 13h39m57.70s | +00d49m51.0s | 6757 | 108.0 | 0.500 | |
| | | NGC 5257 | 13h39m52.90s | +00d50m24.0s | 6798 | 109.0 | 0.503 | |
| 50 | F13428+5608 | UGC 08696 | 13h44m42.11s | +55d53m12.6s | 11326 | 173.0 | 0.775 | 12.21 |
| 51 | F13497+0220 | NGC 5331 | 13h52m16.29s | +02d06m10.9s | 9906 | 155.0 | 0.702 | 11.66 |
| | | NGC 5331 NED01 | 13h52m16.15s | +02d06m03.3s | 9833 | 154.0 | 0.697 | |
| | | NGC 5331 NED02 | 13h52m16.42s | +02d06m31.1s | 9910 | 155.0 | 0.702 | |
| 52 | F14348-1447 | IRAS F14348-1447 | 14h37m38.36s | -15d00m22.8s | 24802 | 387.0 | 1.594 | 12.39 |
| 53 | F14378-3651 | IRAS F14378-3651 | 14h40m59.01s | -37d04m32.0s | 20277 | 315.0 | 1.334 | 12.23 |
| 54 | F14547+2449 | VV 340 | 14h57m00.40s | +24d36m44.0s | 10103 | 157.0 | 0.710 | 11.74 |
| | | VV340a | 14h54m48.26s | +24d49m03.8s | 10094 | 157.0 | 0.710 | |
| | | VV340b | 14h54m47.89s | +24d48m25.4s | 10029 | 156.0 | 0.706 | |
| 55 | F15163+4255 | VV 705 | 15h18m06.28s | +42d44m41.2s | 11944 | 183.0 | 0.819 | 11.92 |
| | | VV 705 NED02 | 15h18m06.37s | +42d44m38.4s | 11800 | 181.0 | 0.810 | |
| | | VV 705 NED01 | 15h18m06.15s | +42d44m44.9s | 12087 | 185.0 | 0.828 | |
| 56 | 15206-6256 | ESO 099-G004 | 15h24m58.19s | -63d07m34.2s | 8779 | 137.0 | 0.623 | 11.74 |
| 57 | F15250+3608 | IRAS F15250+3608 | 15h26m59.40s | +35d58m37.5s | 16535 | 254.0 | 1.103 | 12.08 |

Table 4.1. – Continued

| Visit Number (1) | Name IRAS (2) | Name Optical ID (3) | R.A. (J2000) (4) | Dec. (J2000) (5) | $V_{Helio}$ ($kms^{-1}$) (6) | $D_L$ (Mpc) (7) | scale (kpc/ ") (8) | log $L_{IR}$ ($L_\odot$) (9) |
|---|---|---|---|---|---|---|---|---|
| 58 | F15327+2340 | UGC 09913 | 15h34m57.11s | +23d30m11.4s | 5434 | 87.9 | 0.410 | 12.28 |
| 59 | F16104+5235 | NGC 6090 | 16h11m40.70s | +52d27m24.0s | 8947 | 137.0 | 0.626 | 11.58 |
| 60 | F16164-0746 | IRAS F16164-0746 | 16h19m11.79s | -07d54m02.8s | 8140 | 128.0 | 0.588 | 11.62 |
| 61 | F16330-6820 | ESO 069-IG006 | 16h38m12.65s | -68d26m42.6s | 13922 | 212.0 | 0.938 | 11.98 |
| 62 | F16399-0937 | IRAS F16399-0937 | 16h42m40.21s | -09d43m14.4s | 8098 | 128.0 | 0.584 | 11.63 |
| 63 | F16504+0228 | NGC 6240 | 16h52m58.89s | +02d24m03.4s | 7339 | 116.0 | 0.533 | 11.93 |
| 64 | F17132+5313 | IRAS F17132+5313 | 17h14m20.00s | +53d10m30.0s | 15270 | 232.0 | 1.016 | 11.96 |
| 65 | F17138-1017 | IRAS F17138-1017 | 17h16m35.79s | -10d20m39.4s | 5197 | 84.0 | 0.392 | 11.49 |
| 66 | F17207-0014 | IRAS F17207-0014 | 17h23m21.95s | -00d17m00.9s | 12834 | 198.0 | 0.878 | 12.46 |
| 67 | 18090+0130 | IRAS 18090+0130 | 18h11m35.91s | +01d31m41.3s | 8662 | 134.0 | 0.611 | 11.65 |
| 68 | F18093-5744 | KTS57 | 18h13m39.63s | -57d43m31.3s | 5200 | 81.9 | 0.383 | 11.62 |
| | | IC 4686 | 18h13m38.64s | -57d43m57.1s | 4948 | 78.0 | 0.365 | |
| | | IC 4687 | 18h13m39.63s | -57d43m31.3s | 5200 | 81.9 | 0.383 | |
| | | IC 4689 | 18h13m40.28s | -57d44m53.5s | 4949 | 78.0 | 0.365 | |
| 69 | F18293-3413 | IRAS F18293-3413 | 18h32m41.13s | -34d11m27.5s | 5449 | 86.0 | 0.401 | 11.88 |
| 70 | F18329+5950 | NGC 6670 | 18h33m35.91s | +59d53m20.2s | 8574 | 129.5 | 0.592 | 11.65 |
| 71 | F19120+7320 | VV 414 | 19h10m59.20s | +73d25m06.3s | 7528 | 113.0 | 0.521 | 11.49 |
| | | NGC 6786 | 19h10m53.90s | +73d24m37.0s | 7500 | 113.0 | 0.519 | |
| | | UGC 11415 | 19h11m04.50s | +73d25m36.0s | 7555 | 113.0 | 0.522 | |
| 72 | F19115-2124 | ESO 593-IG008 | 19h14m30.90s | -21d19m07.0s | 14608 | 222.0 | 0.976 | 11.93 |
| 73 | F19297-0406 | IRAS F19297-0406 | 19h32m21.25s | -03d59m56.3s | 25701 | 395.0 | 1.623 | 12.45 |
| 74 | 19542+1110 | IRAS 19542+1110 | 19h56m35.44s | +11d19m02.6s | 19473 | 295.0 | 1.261 | 12.12 |
| 75 | 20351+2521 | IRAS 20351+2521 | 20h37m17.72s | +25d31m37.7s | 10102 | 151.0 | 0.683 | 11.61 |
| 76 | F20550+1655 | CGCG 448-020 | 20h57m23.90s | +17d07m39.0s | 10822 | 161.0 | 0.726 | 11.94 |
| 77 | F20551-4250 | ESO 286-IG019 | 20h58m26.79s | -42d39m00.3s | 12890 | 193.0 | 0.860 | 12.06 |
| 78 | 21101+5810 | IRAS 21101+5810 | 21h11m30.40s | +58d23m03.2s | 11705 | 174.0 | 0.780 | 11.81 |
| 79 | F22467-4906 | ESO 239-IG002 | 22h49m39.87s | -48d50m58.1s | 12901 | 191.0 | 0.853 | 11.84 |

Table 4.1. – Continued

| Visit Number (1) | Name IRAS (2) | Name Optical ID (3) | R.A. (J2000) (4) | Dec. (J2000) (5) | $V_{Helio}$ ($kms^{-1}$) (6) | $D_L$ (Mpc) (7) | scale (kpc/ ") (8) | log $L_{IR}$ ($L_\odot$) (9) |
|---|---|---|---|---|---|---|---|---|
| 80 | F22491-1808 | IRAS F22491-1808 | 22h51m49.26s | -17d52m23.4s | 23312 | 351.0 | 1.467 | 12.20 |
| 81 | F23007+0836 | Arp 298 | 23h03m16.80s | +08d53m01.0s | 4892 | 70.8 | 0.332 | 11.65 |
| | | NGC 7469 | 23h03m15.60s | +08d52m26.0s | 4892 | 70.8 | 0.332 | |
| | | IC 5283 | 23h03m18.00s | +08d53m37.0s | 4804 | 69.6 | 0.327 | |
| 82 | F23128-5919 | ESO 148-IG002 | 23h15m46.78s | -59d03m15.6s | 13371 | 199.0 | 0.884 | 12.06 |
| 83 | F23135+2517 | IC 5298 | 23h16m00.70s | +25d33m24.1s | 8221 | 119.0 | 0.547 | 11.60 |
| 84 | F23180-6929 | ESO 077-IG014 | 23h21m04.53s | -69d12m54.2s | 12460 | 186.0 | 0.831 | 11.76 |
| | | ESO 077-IG014 NED01 | 23h21m03.69s | -69d13m01.2s | 11400 | 170.0 | 0.765 | |
| | | ESO 077-IG014 NED02 | 23h21m05.33s | -69d12m47.2s | 12689 | 190.0 | 0.845 | |
| 85 | F23254+0830 | Arp 182 | 23h27m57.80s | +08d46m51.0s | 8753 | 126.0 | 0.579 | 11.56 |
| | | NGC 7674 | 23h27m56.72s | +08d46m44.5s | 8671 | 125.0 | 0.574 | |
| | | NGC 7674A | 23h27m58.80s | +08d46m58.0s | 8852 | 128.0 | 0.585 | |
| 86 | F23365+3604 | IRAS F23365+3604 | 23h39m01.27s | +36d21m08.7s | 19331 | 287.0 | 1.231 | 12.20 |
| 87 | 23436+5257 | IRAS 23436+5257 | 23h46m05.57s | +53d14m00.6s | 10233 | 149.0 | 0.677 | 11.57 |
| 88 | F23488+2018 | MRK 0331 | 23h51m26.80s | +20d35m09.9s | 5541 | 79.3 | 0.371 | 11.50 |

Note. — Column 1: Number of the *HST* dataset. Column 2: Name of the IRAS source. Column 3: Name of the optical source. Multiple LIRG systems are separated into individual galaxies. Column 4 and 5: Right Ascension and Declination from NED. Column 6: Heliocentric velocity. Column 7: The luminosity distance in Megaparsecs. Column 8: The total infrared luminosity in log10 Solar units. The redshift dependent values were derived by correcting the heliocentric velocity for the 3-attractor flow model of Mould et al. (2000) and adopting cosmological parameters $H_0 = 70 kms^{-1}Mpc^{-1}, \Omega_M = 0.28$, and $\Omega_V = 0.72$ based on the five-year WMAP results (Hinshaw et al., 2009), as provided by NED. Values are consistent with Armus et al. (2009).

Table 4.2. Host Galaxy Properties in the HST-GOALS Sample

| Visit (1) | Name (2) | $m_{F435W}$ (3) | $M_{F435W}$ (4) | $m_{F814W}$ (5) | $M_{F814W}$ (6) | (F435W-F814W) (7) | IC (8) | NAT (9) | SFR (10) |
|---|---|---|---|---|---|---|---|---|---|
| 1 | NGC 0034 | 13.91 ± 0.005 | -20.83 | 12.32 ± 0.002 | -22.36 | 1.52 | 6 | S | 46.9 |
| 2 | Arp 256 | 13.99 ± 0.005 | -21.52 | 12.61 ± 0.003 | -22.81 | | 2 | | 57.1 |
| | Arp 256 NED02 | 14.73 ± 0.007 | -20.77 | 13.34 ± 0.004 | -22.08 | 1.31 | | H | 3.9 |
| | Arp 256 NED01 | 14.75 ± 0.007 | -20.75 | 13.39 ± 0.004 | -22.04 | 1.28 | | H | 48.6 |
| 3 | MCG+12-02-001 | 16.00 ± 0.012 | -20.90 | 12.97 ± 0.003 | -22.45 | | 3 | | 54.5 |
| | South | 16.42 ± 0.015 | -20.48 | 13.34 ± 0.004 | -22.09 | 1.61 | | x | |
| | North | 17.23 ± 0.021 | -19.67 | 14.33 ± 0.006 | -21.10 | 1.43 | | x | |
| 4 | IC 1623 | 13.31 ± 0.003 | -21.42 | 12.07 ± 0.002 | -22.62 | 1.20 | 3 | H | 94.1 |
| 5 | MCG-03-04-014 | 14.93 ± 0.007 | -20.96 | 13.05 ± 0.003 | -22.79 | 1.83 | 0 | H | 78.5 |
| 6 | CGCG 436-030 | 14.93 ± 0.007 | -20.87 | 13.47 ± 0.004 | -22.24 | | 2 | | 85.9 |
| | CGCG 436-030 | 15.15 ± 0.008 | -20.64 | 13.65 ± 0.005 | -22.06 | 1.41 | | H | 85.9 |
| | SDSS J012006.36+142132.5 | 16.82 ± 0.017 | -18.97 | 15.55 ± 0.011 | -20.16 | 1.19 | | x | |
| 7 | IRAS F01364-1042 | 16.99 ± 0.019 | -19.71 | 15.11 ± 0.009 | -21.54 | 1.83 | 5 | L | 122.6 |
| 8 | III Zw 035 | 15.96 ± 0.012 | -19.69 | 13.94 ± 0.005 | -21.56 | 1.87 | 3 | L | 75.9 |
| 9 | NGC 0695 | 14.32 ± 0.006 | -21.79 | 12.49 ± 0.003 | -23.40 | 1.62 | 0 | H | 84.6 |
| 10 | MRK 1034 | 14.51 ± 0.006 | -21.64 | 12.37 ± 0.003 | -23.59 | | 1 | | 77.2 |
| | MCG+05-06-036 | 15.17 ± 0.008 | -20.97 | 12.93 ± 0.003 | -23.03 | 2.06 | | S | 51.8 |
| | MCG+05-06-035 | 15.35 ± 0.009 | -20.79 | 13.35 ± 0.004 | -22.61 | 1.82 | | x | 24.8 |
| 11 | UGC 02369 | 14.72 ± 0.007 | -21.39 | 12.46 ± 0.003 | -23.40 | | 2 | | 81.3 |
| | UGC 02369 NED01 | 15.51 ± 0.010 | -20.60 | 13.66 ± 0.005 | -22.21 | 1.61 | | H | 80.6 |
| | UGC 02369 NED02 | 15.42 ± 0.009 | -20.69 | 12.90 ± 0.003 | -22.97 | 2.27 | | H | |
| 12 | IRAS F03359+1523 | 16.35 ± 0.014 | -20.69 | 14.43 ± 0.007 | -21.98 | | 2 | | 61.2 |
| | West | 18.35 ± 0.035 | -18.69 | 15.70 ± 0.012 | -20.72 | 2.03 | | H | |
| | East | 16.54 ± 0.015 | -20.50 | 14.84 ± 0.008 | -21.58 | 1.08 | | x | 61.2 |

Table 4.2. – Continued

| Visit (1) | Name (2) | $m_{F435W}$ (3) | $M_{F435W}$ (4) | $m_{F814W}$ (5) | $M_{F814W}$ (6) | (F435W-F814W) (7) | IC (8) | NAT (9) | SFR (10) |
|---|---|---|---|---|---|---|---|---|---|
| 13 | ESO 550-IG 025 | 15.01 ± 0.008 | -20.88 | 13.02 ± 0.003 | -22.76 | | 2 | | 56.5 |
| | ESO 550-IG025 NED01 | 15.26 ± 0.009 | -20.62 | 13.34 ± 0.004 | -22.44 | 1.82 | | L | 32.3 |
| | ESO 550-IG025 NED02 | 16.67 ± 0.016 | -19.22 | 14.47 ± 0.007 | -21.31 | 2.09 | | L | 23.5 |
| 14 | NGC 1614 | 13.69 ± 0.004 | -21.13 | 11.87 ± 0.002 | -22.59 | 1.46 | 5 | H | 78.7 |
| 15 | ESO 203-IG001 | 16.98 ± 0.019 | -19.92 | 15.06 ± 0.009 | -21.81 | | 2 | | 127.4 |
| | North-East | 17.29 ± 0.022 | -19.61 | 15.33 ± 0.010 | -21.55 | 1.94 | | x | |
| | Soth-West | 18.44 ± 0.037 | -18.46 | 16.66 ± 0.018 | -20.22 | 1.76 | | x | |
| 16 | VII Zw 031 | 16.27 ± 0.014 | -21.06 | 13.98 ± 0.005 | -23.11 | 2.05 | 0 | S | 170.7 |
| 17 | IRAS F05189-2524 | 15.49 ± 0.009 | -20.99 | 13.67 ± 0.005 | -22.75 | 1.75 | 6 | S | 253.5 |
| 19 | MCG+08-11-002 | 15.48 ± 0.009 | -20.44 | 12.81 ± 0.003 | -22.39 | 1.95 | 6 | x | 50.6 |
| 20 | IRAS F06076-2139 | 15.78 ± 0.011 | -20.60 | 13.65 ± 0.005 | -22.57 | 1.97 | 3 | x | 77.8 |
| 21 | ESO 255-IG007 | 14.87 ± 0.007 | -21.48 | 13.15 ± 0.004 | -23.11 | | 2 | | 140.0 |
| | ESO 255-IG007 NED01 | 16.23 ± 0.013 | -20.12 | 14.00 ± 0.005 | -22.26 | 2.14 | | x | |
| | ESO 255-IG007 NED02 | 15.59 ± 0.010 | -20.77 | 14.27 ± 0.006 | -21.99 | 1.22 | | x | |
| | ESO 255-IG007 NED03 | 16.65 ± 0.016 | -19.70 | 14.98 ± 0.008 | -21.29 | 1.58 | | x | |
| 22 | AM 0702-601 | 15.72 ± 0.011 | -20.51 | 13.74 ± 0.005 | -22.23 | | 1 | | 76.9 |
| | AM 0702-601 NED01 | 15.99 ± 0.012 | -20.24 | 14.05 ± 0.005 | -21.92 | 1.68 | | S | |
| | AM 0702-601 NED02 | 15.90 ± 0.011 | -20.34 | 13.65 ± 0.005 | -22.31 | 1.98 | | x | |
| 23 | IRAS 07251-0248 | 17.39 ± 0.023 | -21.11 | 15.32 ± 0.010 | -22.91 | 1.81 | 5 | x | 431.0 |
| 24 | IRAS 08355-4944 | 16.79 ± 0.017 | -22.16 | 14.42 ± 0.006 | -22.56 | 0.40 | 4 | x | 72.0 |
| 25 | NGC 2623 | 14.29 ± 0.005 | -20.51 | 12.61 ± 0.003 | -22.10 | 1.58 | 5 | S | 69.2 |
| 26 | ESO 060-IG 016 | 15.91 ± 0.011 | -21.17 | 14.08 ± 0.006 | -22.74 | 1.56 | 3 | S | 115.4 |
| 27 | IRAS F08572+3915 | 16.85 ± 0.018 | -20.38 | 15.37 ± 0.010 | -21.79 | | 3 | L | 254.3 |
| | North | 17.59 ± 0.025 | -19.63 | 16.06 ± 0.014 | -21.10 | 1.47 | | | |
| | South | 17.60 ± 0.025 | -19.62 | 16.19 ± 0.015 | -20.97 | 1.35 | | | |
| 28 | IRAS 09022-3615 | 16.54 ± 0.015 | -22.37 | 14.50 ± 0.007 | -23.44 | 1.07 | 5 | S | 359.1 |

Table 4.2. – Continued

| Visit (1) | Name (2) | $m_{F435W}$ (3) | $M_{F435W}$ (4) | $m_{F814W}$ (5) | $M_{F814W}$ (6) | (F435W-F814W) (7) | IC (8) | NAT (9) | SFR (10) |
|---|---|---|---|---|---|---|---|---|---|
| 29 | IRAS F09111-1007 | 15.57 ± 0.010 | -21.67 | 13.55 ± 0.004 | -23.53 | | 1 | | 198.5 |
| | 2MASX J09133644-1019296 | 15.84 ± 0.011 | -21.40 | 14.01 ± 0.005 | -23.07 | 1.67 | | S | 154.8 |
| | 2MASX J09133888-1019196 | 17.23 ± 0.021 | -20.02 | 14.71 ± 0.007 | -22.38 | 2.36 | | S | 42.9 |
| 30 | UGC 04881 | 14.80 ± 0.007 | -21.52 | 12.94 ± 0.003 | -23.34 | 1.82 | 3 | H | 97.1 |
| 31 | UGC 05101 | 15.32 ± 0.009 | -21.06 | 13.43 ± 0.004 | -22.88 | 1.82 | 5 | L | 180.2 |
| 32 | ESO 374-IG 032 | 15.03 ± 0.008 | -21.32 | 13.42 ± 0.004 | -22.72 | 1.40 | 4 | x | 106.1 |
| 33 | IRAS F10173+0828 | 17.50 ± 0.024 | -19.36 | 15.16 ± 0.009 | -21.64 | 2.28 | 0 | x | 126.3 |
| 34 | NGC 3256 | 12.23 ± 0.002 | -21.25 | 10.43 ± 0.001 | -22.76 | 1.51 | 5 | x | 76.5 |
| 35 | IRAS F10565+2448 | 15.48 ± 0.009 | -21.06 | 13.50 ± 0.004 | -23.01 | | 2 | | 209.1 |
| | West | 15.71 ± 0.010 | -20.82 | 13.79 ± 0.005 | -22.71 | 1.89 | | H | 209.1 |
| | East | 17.24 ± 0.021 | -19.30 | 15.06 ± 0.009 | -21.45 | 2.15 | | x | |
| 36 | MCG+07-23-019 | 15.08 ± 0.008 | -20.95 | 13.59 ± 0.004 | -22.42 | 1.46 | 2 | x | 75.1 |
| 37 | IRAS F11231+1456 | 14.98 ± 0.007 | -21.13 | 12.93 ± 0.003 | -23.11 | | 1 | | 76.4 |
| | IC 2810 | 15.23 ± 0.008 | -20.87 | 13.29 ± 0.004 | -22.75 | 1.87 | | x | 49.7 |
| | IC 2810B | 16.69 ± 0.016 | -19.42 | 14.29 ± 0.006 | -21.75 | 2.33 | | x | 26.2 |
| 38 | NGC 3690 | 12.31 ± 0.002 | -21.29 | 10.74 ± 0.001 | -22.82 | 1.53 | 3 | S | 150.5 |
| 39 | IRAS F12112+0305 | 16.74 ± 0.017 | -21.01 | 14.96 ± 0.008 | -22.74 | 1.73 | 4 | x | 402.9 |
| 40 | IRAS 12116-5615 | 17.02 ± 0.019 | -20.50 | 13.82 ± 0.005 | -22.61 | 2.10 | 0 | x | 78.3 |
| 41 | UGC 08058 | 14.58 ± 0.006 | -21.88 | 12.62 ± 0.003 | -23.81 | 1.93 | 5 | S | 649.4 |
| 42 | CGCG 043-099 | 15.56 ± 0.010 | -20.78 | 13.69 ± 0.005 | -22.58 | 1.80 | 5 | L | 84.7 |
| 43 | ESO 507-G070 | 14.83 ± 0.007 | -20.89 | 12.62 ± 0.003 | -22.78 | 1.89 | 6 | S | 62.8 |
| 45 | IRAS 13120-5453 | 15.75 ± 0.011 | -21.74 | 13.11 ± 0.004 | -23.44 | 1.71 | 6 | S | 365.7 |
| 46 | VV 250 | 14.61 ± 0.006 | -21.25 | 13.11 ± 0.004 | -22.70 | | 2 | | 113.8 |
| | VV 250a | 15.36 ± 0.009 | -20.50 | 13.88 ± 0.005 | -21.93 | 1.43 | | H | |
| | VV 250b | 15.36 ± 0.009 | -20.49 | 13.84 ± 0.005 | -21.96 | 1.47 | | H | |
| 47 | UGC 08387 | 14.54 ± 0.006 | -20.72 | 12.92 ± 0.003 | -22.31 | 1.59 | 4 | L | 94.2 |

Table 4.2. – Continued

| Visit (1) | Name (2) | $m_{F435W}$ (3) | $M_{F435W}$ (4) | $m_{F814W}$ (5) | $M_{F814W}$ (6) | (F435W-F814W) (7) | IC (8) | NAT (9) | SFR (10) |
|---|---|---|---|---|---|---|---|---|---|
| 48 | NGC 5256 | 14.14 ± 0.005 | -21.47 | 12.34 ± 0.002 | -23.23 | | 3 | | 65.0 |
| | NGC 5256 NED01 | 14.93 ± 0.007 | -20.68 | 13.14 ± 0.004 | -22.44 | 1.76 | | L | |
| | NGC 5256 NED02 | 14.85 ± 0.007 | -20.76 | 13.06 ± 0.003 | -22.52 | 1.76 | | S | |
| 49 | Arp 240 | 12.86 ± 0.003 | -22.44 | 11.28 ± 0.002 | -23.95 | | 2 | | 77.5 |
| | NGC 5258 | 13.64 ± 0.004 | -21.65 | 11.97 ± 0.002 | -23.27 | 1.61 | | H | 36.0 |
| | NGC 5257 | 13.58 ± 0.004 | -21.71 | 12.10 ± 0.002 | -23.13 | 1.42 | | H | 35.7 |
| 50 | UGC 08696 | 15.05 ± 0.008 | -21.18 | 13.17 ± 0.004 | -23.03 | 1.86 | 4 | S | 282.1 |
| 51 | NGC 5331 | 14.29 ± 0.005 | -21.79 | 12.35 ± 0.003 | -23.65 | | 2 | | 80.4 |
| | NGC 5331 NED01 | 15.02 ± 0.008 | -21.06 | 13.04 ± 0.003 | -22.97 | 1.91 | | x | 60.8 |
| | NGC 5331 NED02 | 15.07 ± 0.008 | -21.01 | 13.18 ± 0.004 | -22.83 | 1.82 | | x | 18.1 |
| 52 | IRAS F14348-1447 | 16.80 ± 0.017 | -21.67 | 14.78 ± 0.008 | -23.40 | 1.73 | 4 | L | 428.5 |
| 53 | IRAS F14378-3651 | 17.57 ± 0.025 | -20.23 | 15.51 ± 0.011 | -22.12 | 1.89 | 6 | L | 294.3 |
| 54 | VV 340 | 14.36 ± 0.006 | -21.81 | 12.44 ± 0.003 | -23.62 | | 1 | | 98.3 |
| | VV340a | 15.33 ± 0.009 | -20.83 | 13.09 ± 0.004 | -22.98 | 2.14 | | L | 79.0 |
| | VV340b | 14.96 ± 0.007 | -21.21 | 13.37 ± 0.004 | -22.69 | 1.49 | | H | 17.6 |
| 55 | VV 705 | 15.01 ± 0.008 | -21.42 | 13.39 ± 0.004 | -22.97 | | 3 | | 147.8 |
| | VV 705 NED02 | 15.96 ± 0.012 | -20.47 | 14.29 ± 0.006 | -22.07 | 1.60 | | H | |
| | VV 705 NED01 | 15.59 ± 0.010 | -20.83 | 14.01 ± 0.005 | -22.35 | 1.52 | | H | |
| 56 | ESO 099-G004 | 16.44 ± 0.015 | -21.74 | 13.45 ± 0.004 | -23.36 | 1.62 | 6 | x | 95.2 |
| 57 | IRAS F15250+3608 | 16.48 ± 0.015 | -20.62 | 14.93 ± 0.008 | -22.13 | 1.51 | 5 | L | 211.1 |
| 58 | UGC 09913 | 14.08 ± 0.005 | -20.86 | 12.07 ± 0.002 | -22.75 | 1.89 | 6 | S | 327.7 |
| 59 | NGC 6090 | 14.37 ± 0.006 | -21.40 | 12.89 ± 0.003 | -22.84 | 1.44 | 4 | H | 71.1 |
| 60 | IRAS F16164-0746 | 15.72 ± 0.011 | -20.97 | 13.63 ± 0.005 | -22.42 | 1.46 | 5 | L | 72.8 |
| 61 | ESO 069-IG006 | 15.31 ± 0.009 | -21.70 | 13.11 ± 0.004 | -23.69 | | 2 | x | 167.5 |
| | North | 15.97 ± 0.012 | -21.04 | 13.74 ± 0.005 | -23.07 | 2.02 | | | |
| | South | 16.41 ± 0.014 | -20.60 | 14.17 ± 0.006 | -22.63 | 2.03 | | | |

Table 4.2. – Continued

| Visit (1) | Name (2) | $m_{F435W}$ (3) | $M_{F435W}$ (4) | $m_{F814W}$ (5) | $M_{F814W}$ (6) | (F435W-F814W) (7) | IC (8) | NAT (9) | SFR (10) |
|---|---|---|---|---|---|---|---|---|---|
| 62 | IRAS F16399-0937 | 16.38 ± 0.014 | -21.03 | 13.37 ± 0.004 | -23.02 | 1.99 | 6 | x | 73.8 |
| 63 | NGC 6240 | 13.81 ± 0.004 | -21.84 | 11.65 ± 0.002 | -23.82 | 1.98 | 4 | L | 148.4 |
| 64 | IRAS F17132+5313 | 16.20 ± 0.013 | -20.72 | 14.20 ± 0.006 | -22.67 | | 2 | H | 159.7 |
| | West | 17.15 ± 0.020 | -19.77 | 15.23 ± 0.009 | -21.64 | 1.87 | | | |
| | East | 16.78 ± 0.017 | -20.14 | 14.72 ± 0.007 | -22.15 | 2.01 | | | |
| 65 | IRAS F17138-1017 | 17.13 ± 0.020 | -20.47 | 13.38 ± 0.004 | -22.58 | 2.11 | 6 | x | 53.8 |
| 66 | IRAS F17207-0014 | 16.99 ± 0.019 | -20.98 | 14.21 ± 0.006 | -22.94 | 1.96 | 5 | H | 501.2 |
| 67 | IRAS 18090+0130 | 16.31 ± 0.014 | -21.62 | 13.24 ± 0.004 | -23.43 | | 2 | | 77.2 |
| | IRAS 18090+0130 | 16.78 ± 0.017 | -21.15 | 13.73 ± 0.005 | -22.94 | 1.79 | | x | 77.2 |
| | 2MASX J18113842+0131397 | 17.56 ± 0.025 | -20.37 | 14.42 ± 0.006 | -22.25 | | | x | |
| 68 | KTS57 | 13.50 ± 0.004 | -21.50 | 11.65 ± 0.002 | -23.11 | | 2 | | 74.7 |
| | IC 4686 | 15.13 ± 0.008 | -19.87 | 13.64 ± 0.005 | -21.12 | 1.26 | | H | 19.2 |
| | IC 4687 | 14.27 ± 0.005 | -20.73 | 12.41 ± 0.003 | -22.35 | 1.62 | | H | 38.5 |
| | IC 4689 | 14.96 ± 0.007 | -20.04 | 12.90 ± 0.003 | -21.86 | 1.82 | | H | 15.5 |
| 69 | IRAS F18293-3413 | 15.09 ± 0.008 | -20.20 | 12.35 ± 0.003 | -22.59 | 2.39 | 1 | H | 131.7 |
| 70 | NGC 6670 | 14.88 ± 0.007 | -20.89 | 12.78 ± 0.003 | -22.87 | 1.98 | 2 | H | 78.3 |
| 71 | VV 414 | 13.72 ± 0.004 | -22.15 | 11.79 ± 0.002 | -23.75 | | 1 | | 143.2 |
| | NGC 6786 | 14.30 ± 0.005 | -21.57 | 12.47 ± 0.003 | -23.07 | 1.50 | | S | |
| | UGC 11415 | 14.67 ± 0.006 | -21.20 | 12.63 ± 0.003 | -22.91 | 1.71 | | x | |
| 72 | ESO 593-IG008 | 15.63 ± 0.010 | -21.66 | 13.61 ± 0.004 | -23.37 | 1.72 | 3 | L | 150.4 |
| 73 | IRAS F19297-0406 | 19.01 ± 0.048 | -21.37 | 15.53 ± 0.011 | -23.53 | 2.16 | 4 | H | 494.8 |
| 74 | IRAS 19542+1110 | 17.38 ± 0.023 | -20.94 | 15.04 ± 0.009 | -22.75 | 1.81 | 0 | S | 232.5 |
| 75 | IRAS 20351+2521 | 14.73 ± 0.007 | -22.01 | 12.95 ± 0.003 | -23.32 | 1.31 | 0 | x | 70.3 |
| 76 | CGCG 448-020 | 14.60 ± 0.006 | -21.79 | 13.26 ± 0.004 | -22.93 | 1.14 | 3 | H | 156.8 |
| 77 | ESO 286-IG019 | 15.12 ± 0.008 | -21.50 | 13.57 ± 0.004 | -22.94 | 1.45 | 5 | H | 203.6 |
| 78 | IRAS 21101+5810 | 17.83 ± 0.028 | -20.85 | 14.98 ± 0.008 | -22.34 | 1.49 | 4 | x | 112.4 |
| 79 | ESO 239-IG002 | 14.80 ± 0.007 | -21.65 | 13.00 ± 0.003 | -23.43 | 1.78 | 5 | x | 121.7 |

Table 4.2. – Continued

| Visit (1) | Name (2) | $m_{F435W}$ (3) | $M_{F435W}$ (4) | $m_{F814W}$ (5) | $M_{F814W}$ (6) | (F435W-F814W) (7) | IC (8) | NAT (9) | SFR (10) |
|---|---|---|---|---|---|---|---|---|---|
| 80 | IRAS F22491-1808 | 16.52 ± 0.015 | -21.36 | 14.99 ± 0.008 | -22.81 | 1.45 | 4 | H | 279.2 |
| 81 | Arp 298 | 13.09 ± 0.003 | -21.46 | 11.15 ± 0.001 | -23.23 | | 1 | | 80.3 |
| | NGC 7469 | 13.30 ± 0.003 | -21.24 | 11.41 ± 0.002 | -22.98 | 1.74 | | S | 66.7 |
| | IC 5283 | 14.92 ± 0.007 | -19.62 | 12.82 ± 0.003 | -21.56 | 1.94 | | x | 10.7 |
| 82 | ESO 148-IG002 | 15.08 ± 0.008 | -21.49 | 13.63 ± 0.005 | -22.90 | 1.41 | 4 | S | 204.6 |
| 83 | IC 5298 | 15.07 ± 0.008 | -20.68 | 12.89 ± 0.003 | -22.66 | 1.98 | 0 | S | 69.7 |
| 84 | ESO 077-IG014 | 15.60 ± 0.010 | -20.91 | 13.37 ± 0.004 | -23.05 | | 2 | | 100.5 |
| | ESO 077-IG014 NED01 | 16.38 ± 0.014 | -20.13 | 14.34 ± 0.006 | -22.08 | 1.95 | | x | |
| | ESO 077-IG014 NED02 | 16.32 ± 0.014 | -20.19 | 13.93 ± 0.005 | -22.49 | 2.30 | | x | |
| 85 | Arp 182 | 13.84 ± 0.004 | -21.89 | 12.03 ± 0.002 | -23.57 | | 1 | | 61.3 |
| | NGC 7674 | 14.02 ± 0.005 | -21.72 | 12.28 ± 0.002 | -23.32 | 1.60 | | S | |
| | NGC 7674A | 15.90 ± 0.011 | -19.83 | 13.76 ± 0.005 | -21.84 | 2.00 | | x | |
| 86 | IRAS F23365+3604 | 16.31 ± 0.014 | -21.45 | 14.42 ± 0.006 | -23.08 | 1.63 | 6 | L | 276.7 |
| 87 | IRAS 23436+5257 | 16.18 ± 0.013 | -20.86 | 13.71 ± 0.005 | -22.68 | 1.82 | 4 | x | 64.8 |
| 88 | MRK 0331 | 14.65 ± 0.006 | -19.93 | 12.42 ± 0.003 | -21.97 | 2.04 | 1 | H | 55.1 |

Note. — Column 1: Number of the *HST* dataset. Column 2: Name of the optical source. Column 3: Apparent F435W magnitude in mag. Column 4: Absolute F435W magnitude in mag calculated using the luminosity distance in Table 4.1. Column 5: Apparent F814W magnitude in mag. Column 6: Absolute F814W magnitude in mag calculated using the luminosity distance in Table 4.1. Columns 7: (F435W-F814W) color of the host galaxy. Column 8: Interaction class, see the text for details. Column 9: Nuclear activity type: H is "HII region-like", L is LINER, S is Seyfert, x no classification is available. Column 10: Star formation rate in units of $M_{\odot}yr^{-1}$ derived from IRAS FIR and GALEX FUV fluxes (Howell et al 2010).

Table 4.3. Star Cluster Properties in the HST-GOALS Sample

| Visit (1) | Name (2) | $N_{cl}$ (3) | $T_N$ (4) | $T_L$(F435W) (5) | $T_L$(F814W) (6) | $\alpha$(F435W) (7) | $\alpha$(F435W) (8) | (F435W-F814W) (9) | $f$ (10) |
|---|---|---|---|---|---|---|---|---|---|
| 1 | NGC 0034 | 182 | 0.720 ± 0.03 | 2.43 ± 0.04 | 1.52 ± 0.03 | -1.68 ± 0.13 | -1.72 ± 0.16 | 0.84 ± 0.48 | 9.9 |
| 2 | Arp 256 | | | | | | | | |
| | Arp 256 NED02 | 169 | 1.322 ± 0.09 | 4.69 ± 0.09 | 2.01 ± 0.05 | -1.80 ± 0.21 | -1.75 ± 0.17 | 0.43 ± 0.45 | 56.8 |
| | Arp 256 NED01 | 105 | 0.799 ± 0.05 | 2.72 ± 0.07 | 1.37 ± 0.05 | -1.77 ± 0.22 | -1.74 ± 0.12 | 0.52 ± 0.46 | 48.6 |
| 3 | MCG+12-02-001 | 83 | 1.107 ± 0.13 | 1.17 ± 0.04 | 1.25 ± 0.02 | -1.76 ± 0.39 | -2.05 ± 0.28 | 1.00 ± 0.79 | 19.3 |
| 4 | IC 1623 | 313 | 0.917 ± 0.04 | 7.02 ± 0.12 | 3.56 ± 0.07 | -1.56 ± 0.23 | -1.57 ± 0.21 | 0.57 ± 0.72 | 44.7 |
| 5 | MCG-03-04-014 | 51 | 0.281 ± 0.01 | 2.13 ± 0.05 | 1.33 ± 0.03 | -1.62 ± 0.28 | -1.74 ± 0.24 | 0.72 ± 0.53 | 15.7 |
| 6 | CGCG 436-030 | 86 | 0.811 ± 0.05 | 2.24 ± 0.06 | 1.38 ± 0.03 | -1.73 ± 0.12 | -1.74 ± 0.21 | 0.86 ± 0.54 | 18.6 |
| 7 | IRAS F01364-1042 | 12 | 0.156 ± 0.01 | 0.92 ± 0.03 | 0.55 ± 0.00 | | | 1.49 ± 0.66 | 16.7 |
| 8 | III Zw 035 | 17 | 0.698 ± 0.04 | 0.41 ± 0.02 | 0.12 ± 0.01 | | | 0.64 ± 0.68 | 41.2 |
| 9 | NGC 0695 | 200 | 0.546 ± 0.04 | 3.80 ± 0.15 | 2.18 ± 0.09 | -1.73 ± 0.30 | -1.69 ± 0.14 | 1.01 ± 0.55 | 18.0 |
| 10 | MRK 1034 | | | | | | | | |
| | MCG+05-06-036 | 46 | 0.303 ± 0.02 | 1.31 ± 0.04 | 0.60 ± 0.02 | -1.52 ± 0.42 | -1.48 ± 0.23 | 1.16 ± 0.53 | 6.5 |
| | MCG+05-06-035 | 40 | 0.247 ± 0.01 | 3.10 ± 0.08 | 1.15 ± 0.04 | -1.36 ± 0.41 | -1.40 ± 0.20 | 0.71 ± 0.66 | 30.0 |
| 11 | UGC 02369 | | | | | | | | |
| | UGC 02369 NED01 | 83 | 0.877 ± 0.07 | 8.38 ± 0.10 | 4.52 ± 0.05 | -1.49 ± 0.19 | -1.42 ± 0.10 | 0.80 ± 0.64 | 16.9 |
| | UGC 02369 NED02 | 7 | 0.037 ± 0.00 | 0.10 ± 0.00 | 0.03 ± 0.00 | | | 0.89 ± 0.73 | 14.3 |
| 12 | IRAS F03359+1523 | 7 | 0.050 ± 0.00 | 5.48 ± 0.09 | 2.73 ± 0.04 | | | 0.51 ± 0.40 | 71.4 |
| 13 | ESO 550-IG 025 | | | | | | | | |
| | ESO 550-IG025 NED01 | 79 | 0.587 ± 0.04 | 1.97 ± 0.04 | 1.05 ± 0.02 | -1.72 ± 0.07 | -1.62 ± 0.11 | 0.94 ± 0.53 | 19.0 |
| | ESO 550-IG025 NED02 | 12 | 0.246 ± 0.01 | 0.46 ± 0.03 | 0.65 ± 0.01 | | | 1.37 ± 1.04 | 8.3 |
| 14 | NGC 1614 | 374 | 1.228 ± 0.06 | 3.37 ± 0.09 | 1.82 ± 0.04 | -1.83 ± 0.17 | -1.76 ± 0.15 | 0.70 ± 0.54 | 29.7 |
| 16 | VII Zw 031 | 32 | 0.073 ± 0.00 | 4.03 ± 0.06 | 2.82 ± 0.03 | | | 1.52 ± 0.76 | 0.0 |
| 19 | MCG+08-11-002 | 39 | 0.318 ± 0.02 | 0.37 ± 0.01 | 0.22 ± 0.01 | -1.90 ± 0.46 | -1.56 ± 0.42 | 1.05 ± 0.82 | 12.8 |
| 20 | IRAS F06076-2139 | 32 | 0.174 ± 0.01 | 2.13 ± 0.02 | 0.67 ± 0.01 | | | 0.53 ± 1.13 | 50.0 |
| 21 | ESO 255-IG007 | 62 | 0.223 ± 0.01 | 2.54 ± 0.05 | 2.10 ± 0.03 | -1.51 ± 0.14 | -1.37 ± 0.10 | 1.26 ± 0.96 | 21.0 |
| 22 | AM 0702-601 | | | | | | | | |
| | AM 0702-601 NED01 | 51 | 0.681 ± 0.05 | 1.40 ± 0.05 | 0.48 ± 0.02 | -1.88 ± 0.48 | -1.45 ± 0.41 | 0.56 ± 0.52 | 45.1 |
| | AM 0702-601 NED02 | 31 | 0.297 ± 0.02 | 10.66 ± 0.14 | 5.29 ± 0.08 | | | 1.45 ± 0.70 | 0.0 |

Table 4.3. – Continued

| Visit (1) | Name (2) | $N_{cl}$ (3) | $T_N$ (4) | $T_L$(F435W) (5) | $T_L$(F814W) (6) | $\alpha$(F435W) (7) | $\alpha$(F435W) (8) | (F435W-F814W) (9) | $f$ (10) |
|---|---|---|---|---|---|---|---|---|---|
| 23 | IRAS 07251-0248 | 6 | 0.025 ± 0.00 | 7.55 ± 0.16 | 3.60 ± 0.03 | | | 0.98 ± 0.59 | 33.3 |
| 24 | IRAS 08355-4944 | 37 | 0.051 ± 0.00 | 3.86 ± 0.10 | 3.64 ± 0.06 | | | 0.91 ± 0.67 | 19.5 |
| 25 | NGC 2623 | 211 | 0.971 ± 0.04 | 1.24 ± 0.04 | 0.69 ± 0.02 | -2.13 ± 0.27 | -2.16 ± 0.24 | 0.72 ± 0.61 | 25.1 |
| 26 | ESO 060-IG 016 | 50 | 0.268 ± 0.02 | 1.68 ± 0.03 | 1.28 ± 0.02 | -1.95 ± 0.12 | -1.89 ± 0.14 | 0.88 ± 0.78 | 16.0 |
| 27 | IRAS F08572+3915 | 14 | 0.163 ± 0.01 | 0.49 ± 0.01 | 0.30 ± 0.00 | | | 0.72 ± 0.81 | 35.7 |
| 28 | IRAS 09022-3615 | 20 | 0.023 ± 0.00 | 2.93 ± 0.04 | 1.26 ± 0.01 | | | 0.53 ± 0.85 | 45.0 |
| 29 | IRAS F09111-1007 | | | | | | | | |
| | 2MASX J09133644-1019296 | 49 | 0.189 ± 0.01 | 1.07 ± 0.01 | 0.41 ± 0.00 | -2.09 ± 0.16 | -1.93 ± 0.16 | 0.62 ± 0.46 | 32.7 |
| | 2MASX J09133888-1019196 | 14 | 0.138 ± 0.01 | 1.60 ± 0.03 | 0.77 ± 0.01 | | | 1.47 ± 0.66 | 7.1 |
| 30 | UGC 04881 | 77 | 0.227 ± 0.01 | 1.72 ± 0.03 | 0.90 ± 0.02 | -1.73 ± 0.13 | -1.80 ± 0.12 | 1.29 ± 0.49 | 1.3 |
| 31 | UGC 05101 | 60 | 0.424 ± 0.03 | 0.68 ± 0.02 | 0.63 ± 0.02 | -1.94 ± 0.16 | -1.95 ± 0.12 | 1.18 ± 0.63 | 10.0 |
| 32 | ESO 374-IG 032 | 126 | 0.737 ± 0.06 | 1.54 ± 0.05 | 1.04 ± 0.03 | -2.18 ± 0.13 | -2.09 ± 0.12 | 0.83 ± 0.47 | 23.8 |
| 34 | NGC 3256 | 1729 | 1.325 ± 0.03 | 4.85 ± 0.11 | 2.82 ± 0.06 | -1.86 ± 0.17 | -1.89 ± 0.15 | 0.90 ± 0.62 | 17.1 |
| 35 | IRAS F10565+2448 | 23 | 0.108 ± 0.00 | 1.52 ± 0.02 | 1.34 ± 0.02 | | | 1.64 ± 0.69 | 0.0 |
| 36 | MCG+07-23-019 | 108 | 0.806 ± 0.06 | 3.30 ± 0.06 | 2.80 ± 0.04 | -1.99 ± 0.11 | -1.96 ± 0.28 | 0.57 ± 0.59 | 41.7 |
| 37 | IC 2810 | 29 | 0.130 ± 0.01 | 0.80 ± 0.02 | 0.52 ± 0.01 | | | 1.04 ± 0.52 | 17.2 |
| 38 | NGC 3690 | 1321 | 1.673 ± 0.05 | 5.23 ± 0.09 | 3.08 ± 0.05 | -1.81 ± 0.15 | -1.77 ± 0.15 | 0.66 ± 0.62 | 38.3 |
| 39 | IRAS F12112+0305 | 37 | 0.195 ± 0.02 | 2.31 ± 0.07 | 1.57 ± 0.04 | -1.90 ± 0.42 | -1.72 ± 0.10 | 0.91 ± 0.64 | 13.5 |
| 40 | IRAS 12116-5615 | 14 | 0.088 ± 0.01 | 1.52 ± 0.05 | 1.62 ± 0.03 | | | 1.96 ± 0.62 | 0.0 |
| 41 | UGC 08058 | 40 | 0.093 ± 0.00 | 0.94 ± 0.02 | 0.78 ± 0.03 | -1.61 ± 0.21 | -1.59 ± 0.22 | 0.93 ± 0.48 | 5.0 |
| 42 | CGCG 043-099 | 39 | 0.309 ± 0.02 | 0.83 ± 0.02 | 1.22 ± 0.01 | -2.55 ± 0.37 | -2.46 ± 0.42 | 1.02 ± 0.46 | 7.7 |
| 43 | ESO 507-G070 | 57 | 0.363 ± 0.02 | 0.31 ± 0.02 | 0.25 ± 0.01 | -2.24 ± 0.25 | -1.94 ± 0.28 | 1.03 ± 0.59 | 12.3 |
| 45 | IRAS 13120-5453 | 18 | 0.036 ± 0.00 | 0.52 ± 0.01 | 1.91 ± 0.01 | | | 2.25 ± 1.38 | 0.0 |
| 46 | VV 250 | | | | | | | | |
| | VV 250a | 47 | 0.679 ± 0.04 | 2.18 ± 0.03 | 1.20 ± 0.01 | -1.78 ± 0.16 | -2.10 ± 0.26 | 0.71 ± 0.38 | 19.1 |
| | VV 250b | 56 | 0.874 ± 0.06 | 0.66 ± 0.03 | 0.44 ± 0.02 | -2.30 ± 0.18 | -2.22 ± 0.16 | 0.68 ± 0.48 | 28.6 |
| 47 | UGC 08387 | 164 | 1.174 ± 0.07 | 3.07 ± 0.04 | 1.90 ± 0.02 | -2.18 ± 0.22 | -2.02 ± 0.11 | 0.83 ± 0.61 | 17.1 |
| 48 | NGC 5256 | 77 | 0.195 ± 0.01 | 0.54 ± 0.01 | 0.36 ± 0.01 | -2.02 ± 0.13 | -2.05 ± 0.16 | 0.88 ± 0.61 | 18.2 |

Table 4.3. – Continued

| Visit (1) | Name (2) | $N_{cl}$ (3) | $T_N$ (4) | $T_L$(F435W) (5) | $T_L$(F814W) (6) | $\alpha$(F435W) (7) | $\alpha$(F435W) (8) | (F435W-F814W) (9) | $f$ (10) |
|---|---|---|---|---|---|---|---|---|---|
| 49 | Arp 240 | | | | | | | | |
| | NGC 5258 | 385 | 1.170 ± 0.07 | 3.81 ± 0.07 | 1.95 ± 0.05 | -1.91 ± 0.10 | -1.87 ± 0.14 | 0.88 ± 0.59 | 16.6 |
| | NGC 5257 | 475 | 1.314 ± 0.08 | 3.88 ± 0.13 | 1.89 ± 0.07 | -1.92 ± 0.19 | -1.94 ± 0.14 | 0.73 ± 0.56 | 29.5 |
| 50 | UGC 08696 | 24 | 0.081 ± 0.00 | 0.51 ± 0.01 | 0.28 ± 0.01 | | | 1.34 ± 0.79 | 0.0 |
| 51 | NGC 5331 | | | | | | | | |
| | NGC 5331 NED01 | 86 | 0.384 ± 0.02 | 2.55 ± 0.06 | 1.75 ± 0.03 | -1.92 ± 0.11 | -1.63 ± 0.12 | 1.40 ± 0.92 | 7.0 |
| | NGC 5331 NED02 | 78 | 0.237 ± 0.01 | 1.65 ± 0.04 | 0.88 ± 0.02 | -1.81 ± 0.10 | -1.65 ± 0.17 | 0.89 ± 0.72 | 9.0 |
| 52 | IRAS F14348-1447 | 28 | 0.060 ± 0.00 | 1.77 ± 0.06 | 0.77 ± 0.03 | | | 0.86 ± 0.48 | 32.1 |
| 54 | VV 340 | | | | | | | | |
| | VV 340a | 14 | 0.065 ± 0.00 | 0.21 ± 0.01 | 0.15 ± 0.01 | | | 1.78 ± 0.82 | 14.3 |
| | VV 340b | 188 | 1.364 ± 0.12 | 2.53 ± 0.10 | 1.09 ± 0.06 | -1.90 ± 0.25 | -1.98 ± 0.21 | 0.56 ± 0.49 | 44.1 |
| 55 | VV 705 | 69 | 0.389 ± 0.03 | 1.67 ± 0.05 | 1.55 ± 0.03 | -2.02 ± 0.22 | -1.96 ± 0.23 | 0.86 ± 0.56 | 18.8 |
| 57 | IRAS F15250+3608 | 10 | 0.056 ± 0.00 | 4.62 ± 0.09 | 2.79 ± 0.07 | | | 1.30 ± 0.50 | 20.0 |
| 58 | UGC 09913 | 204 | 0.727 ± 0.03 | 0.50 ± 0.03 | 0.33 ± 0.01 | -2.59 ± 0.38 | -2.01 ± 0.29 | 1.13 ± 0.65 | 6.9 |
| 59 | NGC 6090 | 108 | 0.348 ± 0.02 | 10.79 ± 0.13 | 4.43 ± 0.06 | -1.37 ± 0.41 | -1.36 ± 0.18 | 0.89 ± 0.60 | 21.3 |
| 60 | IRAS F16164-0746 | 38 | 0.431 ± 0.04 | 1.72 ± 0.02 | 1.32 ± 0.01 | -1.86 ± 0.26 | -1.64 ± 0.32 | 0.97 ± 0.74 | 10.5 |
| 62 | IRAS F16399-0937 | 62 | 0.354 ± 0.04 | 1.51 ± 0.07 | 0.89 ± 0.02 | -1.93 ± 0.36 | -1.59 ± 0.21 | 1.22 ± 0.71 | 9.7 |
| 63 | NGC 6240 | 175 | 0.551 ± 0.03 | 0.86 ± 0.02 | 0.53 ± 0.01 | -2.73 ± 0.33 | -2.26 ± 0.22 | 0.91 ± 0.80 | 14.9 |
| 64 | IRAS F17132+5313 | 21 | 0.108 ± 0.01 | 2.47 ± 0.05 | 2.06 ± 0.04 | | | 1.69 ± 1.15 | 4.8 |
| 66 | IRAS F17207-0014 | 29 | 0.117 ± 0.01 | 2.29 ± 0.06 | 2.17 ± 0.03 | | | 1.54 ± 0.58 | 0.0 |
| 67 | IRAS 18090+0130 | 20 | 0.142 ± 0.01 | 0.33 ± 0.02 | 0.20 ± 0.01 | | | 0.92 ± 0.91 | 15.0 |
| 68 | KTS57 | | | | | | | | |
| | IC 4686 | 34 | 0.384 ± 0.01 | 0.21 ± 0.00 | 0.22 ± 0.00 | -2.13 ± 0.14 | -1.97 ± | 0.97 ± 0.64 | 26.5 |
| | IC 4687 | 160 | 0.685 ± 0.03 | 3.14 ± 0.02 | 1.98 ± 0.02 | -1.75 ± 0.18 | -1.53 ± 0.17 | 1.06 ± 0.75 | 20.6 |
| | IC 4689 | 49 | 0.472 ± 0.02 | 1.39 ± 0.02 | 0.89 ± 0.01 | -1.72 | -1.67 ± 0.12 | 1.19 ± 0.48 | 6.1 |
| 70 | NGC 6670 | 69 | 0.403 ± 0.02 | 1.80 ± 0.03 | 1.20 ± 0.02 | -1.73 ± 0.24 | -1.56 ± 0.24 | 1.48 ± 0.89 | 1.4 |
| 71 | VV 414 | | | | | | | | |
| | NGC 6786 | 293 | 1.306 ± 0.10 | 6.28 ± 0.12 | 2.04 ± 0.06 | -1.83 ± 0.19 | -1.80 ± 0.10 | 0.63 ± 0.55 | 37.9 |
| | UGC 11415 | 128 | 0.839 ± 0.06 | 0.89 ± 0.04 | 0.37 ± 0.02 | -2.33 ± 0.20 | -1.97 ± 0.26 | 0.73 ± 0.53 | 27.3 |
| 72 | ESO 593-IG008 | 40 | 0.087 ± 0.00 | 1.82 ± 0.04 | 1.14 ± 0.02 | | | 1.03 ± 0.85 | 17.5 |

Table 4.3. – Continued

| Visit (1) | Name (2) | $N_{cl}$ (3) | $T_N$ (4) | $T_L$(F435W) (5) | $T_L$(F814W) (6) | $\alpha$(F435W) (7) | $\alpha$(F435W) (8) | (F435W-F814W) (9) | $f$ (10) |
|---|---|---|---|---|---|---|---|---|---|
| 73 | IRAS F19297-0406 | 7 | 0.020 ± 0.00 | 2.41 ± 0.11 | 2.45 ± 0.02 | | | 1.27 ± 1.10 | 0.0 |
| 75 | IRAS 20351+2521 | 174 | 0.355 ± 0.03 | 2.43 ± 0.06 | 1.67 ± 0.03 | -2.16 ± 0.23 | -2.10 ± 0.23 | 0.74 ± 0.95 | 25.3 |
| 76 | CGCG 448-020 | 155 | 0.389 ± 0.03 | 6.08 ± 0.10 | 3.94 ± 0.06 | -1.71 ± 0.21 | -1.62 ± 0.11 | 0.66 ± 0.78 | 33.5 |
| 77 | ESO 286-IG019 | 60 | 0.249 ± 0.02 | 3.05 ± 0.06 | 1.39 ± 0.03 | -1.70 ± 1.00 | -1.86 ± 0.21 | 0.75 ± 0.46 | 13.3 |
| 78 | IRAS 21101+5810 | 17 | 0.078 ± 0.01 | 1.91 ± 0.07 | 1.20 ± 0.02 | | | 0.67 ± 0.59 | 35.3 |
| 79 | ESO 239-IG002 | 47 | 0.219 ± 0.01 | 0.22 ± 0.01 | 0.10 ± 0.00 | -2.03 ± 0.47 | -1.69 ± 0.45 | 0.96 ± 0.70 | 14.9 |
| 80 | IRAS F22491-1808 | 24 | 0.068 ± 0.00 | 6.46 ± 0.16 | 4.90 ± 0.09 | | | 0.97 ± 0.74 | 12.5 |
| 81 | Arp 298 | | | | | | | | |
| | NGC 7469 | 332 | 0.692 ± 0.02 | 7.31 ± 0.11 | 2.66 ± 0.07 | -1.96 ± 0.28 | -2.01 ± 0.10 | 0.71 ± 0.64 | 31.9 |
| | IC 5283 | 82 | 0.908 ± 0.04 | 0.96 ± 0.05 | 0.66 ± 0.03 | -2.13 ± 0.30 | -1.59 ± 0.28 | 1.12 ± 0.87 | 15.9 |
| 82 | ESO 148-IG002 | 78 | 0.329 ± 0.02 | 3.44 ± 0.06 | 3.20 ± 0.04 | -1.57 ± 0.28 | -1.64 ± 0.25 | 0.91 ± 0.55 | 10.3 |
| 83 | IC 5298 | 36 | 0.211 ± 0.01 | 0.75 ± 0.02 | 0.53 ± 0.01 | -1.82 ± 0.35 | -2.01 ± 0.11 | 0.75 ± 0.69 | 33.3 |
| 84 | ESO 077-IG014 | 17 | 0.073 ± 0.00 | 0.27 ± 0.01 | 0.15 ± 0.01 | | | 1.23 ± 0.69 | 11.8 |
| 85 | NGC 7674 | 299 | 1.215 ± 0.09 | 1.58 ± 0.05 | 0.56 ± 0.03 | -2.05 ± 0.20 | -2.20 ± 0.20 | 0.68 ± 0.50 | 37.8 |
| 86 | IRAS F23365+3604 | 19 | 0.223 ± 0.02 | 2.17 ± 0.04 | 1.14 ± 0.02 | | | 0.92 ± 0.56 | 5.3 |
| 87 | IRAS 23436+5257 | 20 | 0.090 ± 0.00 | 0.41 ± 0.02 | 0.26 ± 0.01 | | | 0.64 ± 0.78 | 45.0 |
| 88 | MRK 0331 | 42 | 0.364 ± 0.01 | 6.25 ± 0.08 | 2.90 ± 0.05 | -1.75 ± 0.41 | | 1.73 ± 0.95 | 7.1 |

Note. — Column 1: Number of the *HST* dataset. Column 2: Name of the optical source. Column 3: Number of detected star clusters. Column 4: Corrected specific frequency $T_N$, limited to $M_{F435W} < -9$ and corrected for completeness. Column 5: Specific luminosity $T_L$ in the F435W images. Column 6: Specific luminosity $T_L$ in the F814W images. Column 7: Luminosity function index $\alpha$ for the F435W images and F814W filters. Column 8: Luminosity function index $\alpha$ for the F814W images. Column 9 : Median (F435W−F814W) color of clusters in a galaxy. Column 10: Percentage of cluster population that can be reliably age-dated as younger than 7.6 Myr with no extinction correction.

Table 4.4. Most Luminous Star Clusters in the HST-GOALS Sample

| Visit (1) | Name (2) | $M_{F435W}$ (mag) (3) | (F435W-F814W) (mag) (4) | Age (Myr) (5) | Mass $\times 10^6(M_\odot)$ (6) |
|---|---|---|---|---|---|
| 1 | NGC 0034 | -15.15 | 0.78 ± 0.00 | 7.9 | 1.33 |
| 2 | Arp 256 | | | | |
| | Arp 256 NED02 | -15.75 | -0.08 ± 0.00 | 5.0 | 1.74 |
| | Arp 256 NED01 | -14.62 | 0.28 ± 0.02 | 6.6 | 0.67 |
| 3 | MCG+12-02-001 | -13.61 | 1.87 ± 0.01 | 1999.9 | 0.73 |
| 4 | IC 1623 | -16.16 | -0.17 ± 0.00 | 4.8 | 2.54 |
| 5 | MCG-03-04-014 | -15.62 | 1.62 ± 0.01 | 1016.2 | 2.61 |
| 6 | CGCG 436-030 | -15.28 | 0.44 ± 0.00 | 7.2 | 1.29 |
| 7 | IRAS F01364-1042 | -13.68 | 0.36 ± 0.05 | 6.9 | 0.30 |
| 8 | III Zw 035 | -13.02 | 0.28 ± 0.01 | 6.6 | 0.16 |
| 9 | NGC 0695 | -15.18 | 0.60 ± 0.04 | 7.6 | 1.26 |
| 10 | MRK 1034 | | | | |
| | MCG+05-06-036 | -14.95 | 0.53 ± 0.02 | 7.6 | 1.03 |
| | MCG+05-06-035 | -15.83 | 0.09 ± 0.01 | 5.5 | 1.82 |
| 11 | UGC 02369 | | | | |
| | UGC 02369 NED01 | -17.02 | 0.12 ± 0.00 | 5.5 | 5.21 |
| | UGC 02369 NED02 | -12.52 | 0.89 ± 0.02 | 8.3 | 0.15 |
| 12 | IRAS F03359+1523 | -16.91 | 0.41 ± 0.00 | 7.2 | 5.35 |
| 13 | ESO 550-IG 025 | | | | |
| | ESO 550-IG025 NED01 | -14.19 | 1.40 ± 0.04 | 905.7 | 0.94 |
| | ESO 550-IG025 NED02 | -11.97 | 2.18 ± 0.16 | 6501.3 | 0.33 |
| 14 | NGC 1614 | -15.52 | 0.66 ± 0.00 | 7.9 | 1.84 |
| 16 | VII Zw 031 | -16.25 | 1.27 ± 0.02 | 719.4 | 3.79 |
| 19 | MCG+08-11-002 | -12.37 | -0.38 ± 0.10 | 3.5 | 0.10 |
| 20 | IRAS F06076-2139 | -14.72 | 0.66 ± 0.09 | 7.9 | 0.92 |
| 21 | ESO 255-IG007 | -15.75 | 0.64 ± 0.04 | 7.9 | 2.25 |
| 22 | AM 0702-601 | | | | |
| | AM 0702-601 NED01 | -13.35 | 0.38 ± 0.04 | 7.2 | 0.24 |
| | AM 0702-601 NED02 | -17.24 | 0.79 ± 0.01 | 7.9 | 8.18 |
| 23 | IRAS 07251-0248 | -17.56 | 0.45 ± 0.03 | 7.2 | 9.42 |
| 24 | IRAS 08355-4944 | -16.53 | 0.78 ± 0.01 | 7.9 | 4.42 |
| 25 | NGC 2623 | -14.06 | 0.91 ± 0.00 | 8.3 | 0.58 |
| 26 | ESO 060-IG 016 | -15.42 | 0.92 ± 0.03 | 8.3 | 1.88 |
| 27 | IRAS F08572+3915 | -13.00 | 0.46 ± 0.04 | 7.2 | 0.18 |
| 28 | IRAS 09022-3615 | -18.03 | -0.15 ± 0.10 | 5.0 | 13.21 |
| 29 | IRAS F09111-1007 | | | | |
| | 2MASX J09133644-1019296 | -14.09 | 0.28 ± 0.06 | 6.6 | 0.42 |
| | 2MASX J09133888-1019196 | -14.31 | 1.51 ± 0.09 | 1016.2 | 1.05 |
| 30 | UGC 04881 | -15.68 | 1.03 ± 0.01 | 509.3 | 2.33 |
| 31 | UGC 05101 | -14.21 | 2.29 ± 0.03 | 9506.0 | 1.52 |
| 32 | ESO 374-IG 032 | -14.81 | 0.49 ± 0.01 | 7.6 | 0.91 |

Table 4.4. – Continued

| Visit (1) | Name (2) | $M_{F435W}$ (mag) (3) | (F435W-F814W) (mag) (4) | Age (Myr) (5) | Mass $\times 10^6(M_\odot)$ (6) |
|---|---|---|---|---|---|
| 34 | NGC 3256 | -15.85 | 0.26 ± 0.00 | 6.6 | 1.97 |
| 35 | IRAS F10565+2448 | -16.12 | 1.43 ± 0.01 | 905.7 | 3.65 |
| 36 | MCG+07-23-019 | -15.65 | 0.98 ± 0.01 | 8.3 | 2.30 |
| 37 | IC 2810 | -15.17 | 1.52 ± 0.01 | 1016.2 | 1.90 |
| 38 | NGC 3690 | -15.85 | 0.45 ± 0.00 | 7.2 | 2.12 |
| 39 | IRAS F12112+0305 | -14.52 | 1.71 ± 0.02 | 1435.5 | 1.27 |
| 40 | IRAS 12116-5615 | -14.34 | 1.85 ± 0.06 | 1901.1 | 1.20 |
| 41 | UGC 08058 | -15.31 | 0.70 ± 0.02 | 7.9 | 1.53 |
| 42 | CGCG 043-099 | -15.31 | 2.51 ± 0.00 | 0.0 | 0.07 |
| 43 | ESO 507-G070 | -12.13 | 0.35 ± 0.06 | 6.9 | 0.08 |
| 45 | IRAS 13120-5453 | -14.94 | 2.25 ± 0.03 | 8491.8 | 2.36 |
| 46 | VV 250 | | | | |
| | VV 250a | -15.46 | 0.97 ± 0.05 | 8.3 | 1.95 |
| | VV 250b | -13.69 | -0.18 ± 0.10 | 4.8 | 0.28 |
| 47 | UGC 08387 | -16.27 | 0.75 ± 0.00 | 7.9 | 3.53 |
| 48 | NGC 5256 | -14.18 | 0.24 ± 0.12 | 6.6 | 0.45 |
| 49 | Arp 240 | | | | |
| | NGC 5258 | -16.22 | 0.92 ± 0.00 | 8.3 | 3.77 |
| | NGC 5257 | -15.35 | 0.50 ± 0.00 | 7.6 | 1.46 |
| 50 | UGC 08696 | -14.10 | 0.98 ± 0.02 | 8.3 | 0.60 |
| 51 | NGC 5331 | | | | |
| | NGC 5331 NED01 | -16.01 | 0.64 ± 0.02 | 7.9 | 2.81 |
| | NGC 5331 NED02 | -14.71 | 0.70 ± 0.01 | 7.9 | 0.91 |
| 52 | IRAS F14348-1447 | -15.15 | 1.26 ± 0.02 | 719.4 | 1.75 |
| 54 | VV 340 | | | | |
| | VV 340a | -13.15 | 1.78 ± 0.04 | 1698.2 | 0.52 |
| | VV 340b | -14.78 | 0.15 ± 0.01 | 5.5 | 0.72 |
| 55 | VV 705 | -15.73 | -0.01 ± 0.02 | 5.2 | 1.67 |
| 57 | IRAS F15250+3608 | -16.43 | 0.20 ± 0.03 | 6.3 | 3.19 |
| 58 | UGC 09913 | -12.24 | 0.73 ± 0.00 | 7.9 | 0.11 |
| 59 | NGC 6090 | -17.26 | 0.17 ± 0.01 | 6.0 | 6.32 |
| 60 | IRAS F16164-0746 | -15.78 | 0.96 ± 0.00 | 8.3 | 2.57 |
| 62 | IRAS F16399-0937 | -14.08 | 0.21 ± 0.05 | 6.3 | 0.40 |
| 63 | NGC 6240 | -16.08 | 1.18 ± 0.00 | 641.2 | 3.29 |
| 64 | IRAS F17132+5313 | -15.95 | 1.02 ± 0.02 | 509.3 | 2.83 |
| 66 | IRAS F17207-0014 | -15.11 | 2.26 ± 0.03 | 8749.8 | 2.63 |
| 67 | IRAS 18090+0130 | -13.68 | 0.64 ± 0.03 | 7.9 | 0.37 |

Table 4.4. – Continued

| Visit (1) | Name (2) | $M_{F435W}$ (mag) (3) | (F435W-F814W) (mag) (4) | Age (Myr) (5) | Mass $\times 10^6(M_\odot)$ (6) |
|---|---|---|---|---|---|
| 68 | KTS57 | | | | |
| | IC 4686 | -11.82 | 0.49 ± 0.02 | 7.6 | 0.07 |
| | IC 4687 | -14.60 | 0.51 ± 0.05 | 7.6 | 0.76 |
| | IC 4689 | -13.03 | 0.61 ± 0.01 | 7.6 | 0.19 |
| 70 | NGC 6670 | -15.12 | 0.83 ± 0.01 | 8.3 | 1.45 |
| 71 | VV 414 | | | | |
| | NGC 6786 | -16.67 | -0.14 ± 0.01 | 5.0 | 3.94 |
| | UGC 11415 | -14.75 | 0.50 ± 0.00 | 7.6 | 0.86 |
| 72 | ESO 593-IG008 | -16.07 | 0.79 ± 0.00 | 7.9 | 2.97 |
| 73 | IRAS F19297-0406 | -16.94 | 1.27 ± 0.04 | 719.4 | 6.19 |
| 75 | IRAS 20351+2521 | -15.69 | 0.46 ± 0.01 | 7.2 | 1.85 |
| 76 | CGCG 448-020 | -16.78 | 0.21 ± 0.01 | 6.3 | 4.38 |
| 77 | ESO 286-IG019 | -17.03 | 0.18 ± 0.01 | 6.0 | 5.19 |
| 78 | IRAS 21101+5810 | -15.57 | 0.64 ± 0.05 | 7.9 | 1.93 |
| 79 | ESO 239-IG002 | -12.96 | 0.32 ± 0.03 | 6.9 | 0.16 |
| 80 | IRAS F22491-1808 | -17.26 | 0.56 ± 0.01 | 64.1 | 7.71 |
| 81 | Arp 298 | | | | |
| | NGC 7469 | -17.09 | 0.27 ± 0.01 | 6.6 | 5.83 |
| | IC 5283 | -12.30 | 1.36 ± 0.01 | 807.2 | 0.24 |
| 82 | ESO 148-IG002 | -16.83 | 1.33 ± 0.01 | 807.2 | 5.89 |
| 83 | IC 5298 | -13.74 | 2.23 ± 0.09 | 7744.6 | 1.06 |
| 84 | ESO 077-IG014 | -13.59 | 1.24 ± 0.06 | 719.4 | 0.58 |
| 85 | NGC 7674 | -14.41 | 0.05 ± 0.01 | 5.2 | 0.52 |
| 86 | IRAS F23365+3604 | -16.71 | 0.65 ± 0.00 | 7.9 | 5.15 |
| 87 | IRAS 23436+5257 | -13.34 | 0.39 ± 0.03 | 7.2 | 0.24 |
| 88 | MRK 0331 | -15.71 | 0.52 ± 0.02 | 7.6 | 2.00 |

Note. — Column 1: Number of the *HST* dataset. Column 2: Name of the optical source. Column 3: Absolute F435W magnitude of the most luminous cluster. Columns 4: (F435W−F814W) color of the most luminous cluster. Columns 5 and 6: Age and mass for the respective age according to Bruzual & Charlot 2003 evolutionary models.

Table 4.5. Host Galaxy and Star Cluster Properties in Interaction Classes

| Property | Statistics | Interaction Class 0 | 1 | 2 | 3 | 4 | 5 | 6 |
|---|---|---|---|---|---|---|---|---|
| **Host Galaxy** | | | | | | | | |
| Number LIRGs | | 8 | 10 | 18 | 12 | 13 | 14 | 11 |
| $D_L$ (Mpc) | Median | 148 | 133 | 147 | 163 | 173 | 192 | 128 |
| | Mean | 180 | 131 | 157 | 153 | 216 | 184 | 149 |
| | Std. Dev. | 64 | 52 | 42 | 64 | 110 | 91 | 82 |
| SFR ($M_\odot$ $yr^{-1}$) | Median | 82 | 79 | 81 | 106 | 148 | 151 | 95 |
| | Mean | 114 | 100 | 10 | 120 | 212 | 226 | 173 |
| | Std. Dev. | 59 | 45 | 43 | 56 | 151 | 186 | 129 |
| **Star Clusters** | | | | | | | | |
| Number Clusters | Median | 44 | 49 | 66 | 73 | 37 | 40 | 57 |
| | Mean | 85 | 109 | 93 | 187 | 65 | 191 | 83 |
| | Std. Dev. | 81 | 113 | 113 | 366 | 59 | 454 | 77 |
| $T_N$ | Median | 0.25 | 0.36 | 0.44 | 0.39 | 0.11 | 0.18 | 0.35 |
| | Mean | 0.26 | 0.58 | 0.53 | 0.78 | 0.29 | 0.39 | 0.39 |
| | Std. Dev. | 0.18 | 0.45 | 0.40 | 0.88 | 0.34 | 0.45 | 0.25 |
| $T_L$(F435W) | Median | 2.28 | 1.58 | 2.21 | 1.70 | 2.31 | 2.01 | 0.52 |
| | Mean | 2.44 | 3.06 | 2.41 | 2.50 | 3.03 | 2.52 | 1.11 |
| | Std. Dev. | 1.28 | 3.08 | 1.92 | 2.28 | 2.84 | 2.06 | 0.91 |
| $T_L$(F814W) | Median | 1.65 | 0.66 | 1.36 | 1.19 | 1.57 | 1.29 | 0.89 |
| | Mean | 1.69 | 1.31 | 1.45 | 1.51 | 2.01 | 1.51 | 0.89 |
| | Std. Dev. | 0.77 | 1.39 | 1.03 | 1.30 | 1.58 | 1.01 | 0.67 |
| LF index $\alpha$(F435W) | Median | -1.78 | -1.90 | -1.78 | -1.79 | -2.04 | -1.86 | -1.93 |
| | Mean | -1.83 | -1.89 | -1.82 | -1.82 | -1.99 | -1.95 | -2.07 |
| | Std. Dev. | 0.23 | 0.28 | 0.20 | 0.16 | 0.49 | 0.28 | 0.35 |
| LF index $\alpha$(F814W) | Median | -1.88 | -1.87 | -1.74 | -1.85 | -1.87 | -1.86 | -1.72 |
| | Mean | -1.89 | -1.78 | -1.75 | -1.84 | -1.85 | -1.89 | -1.76 |
| | Std. Dev. | 0.20 | 0.28 | 0.23 | 0.18 | 0.33 | 0.28 | 0.20 |
| (F435W−F814W) (mag) | Median | 0.88 | 0.73 | 0.91 | 0.79 | 0.89 | 0.97 | 1.05 |
| | Mean | 1.11 | 1.00 | 0.98 | 0.81 | 0.86 | 1.00 | 1.21 |
| | Std. Dev. | 0.51 | 0.43 | 0.36 | 0.22 | 0.29 | 0.29 | 0.48 |
| Population fraction | Median | 21.6 | 28.7 | 18.6 | 26.4 | 21.3 | 16.7 | 9.8 |
| age-dated SC | Mean | 23.1 | 25.4 | 22.3 | 27.9 | 27.9 | 19.1 | 9.5 |
| younger 7.6 Myr (%) | Std. Dev. | 8.0 | 13.8 | 17.5 | 14.6 | 20.7 | 11.4 | 3.0 |
| $M^{max}_{F435W}$ (mag) | Median | -15.40 | -14.78 | -15.20 | -15.55 | -16.08 | -15.42 | -14.08 |
| | Mean | -15.14 | -14.92 | -14.79 | -15.02 | -15.74 | -15.49 | -13.94 |
| | Std. Dev. | 0.93 | 1.43 | 1.46 | 1.28 | 1.27 | 1.46 | 1.77 |

Note. — The median, mean and the standard deviation of the host galaxy and SC properties for all merger stages.

Table 4.6. Host Galaxy and Star Cluster Properties in Nuclear Activity Types

| Property | Statistics | Nuclear Activity Type unknown | HIIregion-like | AGN-like |
|---|---|---|---|---|
| **Host Galaxy** | | | | |
| Number LIRGs | | 40 | 34 | 41 |
| $D_L$ (Mpc) | Median | 156 | 142 | 159 |
| | Mean | 166 | 159 | 175 |
| | Std. Dev. | 77 | 77 | 78 |
| SFR ($M_\odot$ $yr^{-1}$) | Median | 78 | 94 | 149 |
| | Mean | 116 | 143 | 181 |
| | Std. Dev. | 95 | 120 | 131 |
| **Star Clusters** | | | | |
| Number Clusters | Median | 40 | 69 | 46 |
| | Mean | 121 | 116 | 118 |
| | Std. Dev. | 330 | 122 | 228 |
| $T_N$ | Median | 0.24 | 0.40 | 0.30 |
| | Mean | 0.45 | 0.55 | 0.47 |
| | Std. Dev. | 0.61 | 0.43 | 0.45 |
| $T_L$(F435W) | Median | 1.60 | 2.63 | 1.40 |
| | Mean | 2.29 | 3.48 | 1.91 |
| | Std. Dev. | 2.36 | 2.47 | 1.75 |
| $T_L$(F814W) | Median | 1.18 | 1.85 | 0.77 |
| | Mean | 1.45 | 1.99 | 1.11 |
| | Std. Dev. | 1.28 | 1.24 | 0.90 |
| LF index $\alpha$(F435W) | Median | -1.93 | -1.75 | -1.94 |
| | Mean | -1.96 | -1.78 | -1.96 |
| | Std. Dev. | 0.29 | 0.20 | 0.30 |
| LF index $\alpha$(F814W) | Median | -1.71 | -1.75 | -1.93 |
| | Mean | -1.80 | -1.77 | -1.86 |
| | Std. Dev. | 0.29 | 0.21 | 0.23 |
| (F435W−F814W) (mag) | Median | 0.94 | 0.87 | 0.91 |
| | Mean | 0.96 | 0.95 | 1.00 |
| | Std. Dev. | 0.35 | 0.37 | 0.38 |
| Population fraction | Median | 17.2 | 18.3 | 16.7 |
| age-dated SC | Mean | 22.5 | 21.3 | 19.5 |
| younger 7.6 Myr (%) | Std. Dev. | 17.6 | 17.7 | 13.7 |
| $M^{max}_{F435W}$ (mag) | Median | -14.78 | -15.65 | -14.94 |
| | Mean | -14.84 | -15.47 | -14.82 |
| | Std. Dev. | 1.36 | 1.35 | 1.52 |

Note. — The median, mean and the standard deviation of the host galaxy and SC properties for nuclear activity types.

Table 4.7. KS and MWU Test Results of Star Cluster Properties for Interaction Classes

| | $T_N$ | | $T_L$(F435W) | | $T_L$(F814W) | | $\alpha$(F435W) | | $\alpha$(F814W) | | (F435W−F814W) | | $f$ | | $M^{max}_{F435W}$ | |
|---|---|---|---|---|---|---|---|---|---|---|---|---|---|---|---|---|
| IC | KS | MWU | KS | MWU | KS | MWU | KS | MWU | KS | MWU | KS | MWU | KS | MWU | KS | MWU |
| (1) | (2) | (3) | (4) | (5) | (6) | (7) | (8) | (9) | (10) | (11) | (12) | (13) | (14) | (15) | (16) | (17) |
| 0 - 1 | 0.51 | 0.07 | 0.76 | 0.42 | 0.08 | 0.09 | 0.39 | 0.37 | 0.91 | 0.27 | 0.22 | 0.15 | 0.83 | 0.15 | 0.63 | 0.37 |
| 0 - 2 | 0.19 | 0.07 | 0.88 | 0.39 | 0.73 | 0.22 | 1.00 | 0.52 | 0.61 | 0.14 | 0.88 | 0.33 | 0.56 | 0.20 | 1.00 | 0.35 |
| 0 - 3 | 0.38 | 0.11 | 0.67 | 0.28 | 0.19 | 0.17 | 0.99 | 0.53 | 0.99 | 0.40 | 0.38 | 0.09 | 0.98 | 0.38 | 0.93 | 0.52 |
| 0 - 4 | 0.08 | 0.29 | 1.00 | 0.48 | 0.79 | 0.48 | 0.44 | 0.30 | 0.99 | 0.46 | 0.61 | 0.29 | 0.73 | 0.11 | 0.25 | 0.16 |
| 0 - 5 | 0.10 | 0.48 | 0.89 | 0.42 | 0.39 | 0.25 | 0.30 | 0.25 | 0.95 | 0.47 | 0.89 | 0.42 | 0.40 | 0.30 | 0.81 | 0.36 |
| 0 - 6 | 0.62 | 0.18 | 0.16 | 0.03 | 0.19 | 0.04 | 0.36 | 0.14 | 0.88 | 0.21 | 0.28 | 0.18 | 0.03 | 0.00 | 0.23 | 0.09 |
| 1 - 2 | 0.96 | 0.34 | 0.46 | 0.48 | 0.15 | 0.17 | 0.24 | 0.12 | 0.78 | 0.37 | 0.59 | 0.42 | 0.26 | 0.18 | 0.94 | 0.48 |
| 1 - 3 | 0.96 | 0.35 | 0.66 | 0.46 | 0.58 | 0.25 | 0.47 | 0.26 | 0.83 | 0.35 | 0.22 | 0.19 | 0.64 | 0.21 | 0.73 | 0.40 |
| 1 - 4 | 0.06 | 0.02 | 0.51 | 0.33 | 0.30 | 0.10 | 0.42 | 0.36 | 0.47 | 0.28 | 0.43 | 0.44 | 0.90 | 0.48 | 0.33 | 0.06 |
| 1 - 5 | 0.09 | 0.10 | 0.92 | 0.41 | 0.20 | 0.09 | 0.98 | 0.36 | 0.75 | 0.33 | 0.36 | 0.32 | 0.32 | 0.13 | 0.40 | 0.16 |
| 1 - 6 | 0.99 | 0.31 | 0.12 | 0.05 | 0.46 | 0.29 | 0.82 | 0.30 | 1.00 | 0.52 | 0.09 | 0.13 | 0.05 | 0.00 | 0.43 | 0.11 |
| 2 - 3 | 0.83 | 0.31 | 0.43 | 0.39 | 0.83 | 0.41 | 0.97 | 0.44 | 0.28 | 0.16 | 0.27 | 0.07 | 0.31 | 0.11 | 0.97 | 0.34 |
| 2 - 4 | 0.08 | 0.02 | 0.96 | 0.32 | 0.52 | 0.21 | 0.26 | 0.24 | 0.43 | 0.26 | 0.51 | 0.22 | 0.62 | 0.17 | 0.14 | 0.03 |
| 2 - 5 | 0.03 | 0.13 | 0.91 | 0.44 | 0.96 | 0.43 | 0.18 | 0.12 | 0.52 | 0.13 | 0.76 | 0.32 | 1.00 | 0.40 | 0.76 | 0.13 |
| 2 - 6 | 0.47 | 0.21 | 0.22 | 0.05 | 0.47 | 0.12 | 0.32 | 0.09 | 1.00 | 0.50 | 0.41 | 0.15 | 0.09 | 0.01 | 0.41 | 0.12 |
| 3 - 4 | 0.10 | 0.01 | 0.60 | 0.22 | 0.60 | 0.22 | 0.25 | 0.25 | 0.75 | 0.43 | 0.60 | 0.19 | 0.65 | 0.23 | 0.26 | 0.07 |
| 3 - 5 | 0.07 | 0.09 | 0.75 | 0.41 | 0.97 | 0.38 | 0.39 | 0.19 | 0.97 | 0.48 | 0.09 | 0.04 | 0.12 | 0.04 | 0.89 | 0.29 |
| 3 - 6 | 0.75 | 0.30 | 0.36 | 0.10 | 0.87 | 0.17 | 0.51 | 0.18 | 0.75 | 0.22 | 0.04 | 0.01 | 0.01 | 0.02 | 0.27 | 0.07 |
| 4 - 5 | 0.72 | 0.23 | 0.93 | 0.33 | 0.79 | 0.30 | 0.53 | 0.39 | 0.89 | 0.48 | 0.15 | 0.09 | 0.84 | 0.14 | 0.72 | 0.30 |
| 4 - 6 | 0.19 | 0.18 | 0.17 | 0.02 | 0.38 | 0.06 | 0.99 | 0.33 | 0.37 | 0.27 | 0.03 | 0.02 | 0.01 | 0.00 | 0.08 | 0.01 |
| 5 - 6 | 0.13 | 0.27 | 0.13 | 0.04 | 0.49 | 0.11 | 0.71 | 0.26 | 0.90 | 0.22 | 0.27 | 0.14 | 0.14 | 0.14 | 0.13 | 0.03 |

Note. — Column 1: The pair of interaction classes that the statistical test were performed on. KS and MWU test p-values: Columns 2 and 3: specific frequency $T_N$; Columns 4 and 5: specific luminosity $T_L$(F435W); Columns 6 and 7: specific luminosity $T_L$(F814W); Columns 8 and 9: luminosity function indices $\alpha$ for F435W images; Columns 10 and 11: luminosity function indices $\alpha$ for F814W images; Columns 12 and 13: the median (F435W−F814W) color of clusters; Columns 14 and 15: population fraction of SCs that can be reliably age-dated as younger than 7.6 Myr with no extinction correction; Columns 16 and 17: the absolute F435W magnitude of the brightest cluster.

Table 4.8. KS and MWU Test Results of Star Cluster Properties for Nuclear Activity Types

| | $T_N$ | | $T_L$(F435W) | | $T_L$(F814W) | | $\alpha$(F435W) | | $\alpha$(F814W) | | (F435W−F814W) | | $f$ | | $M^{max}_{F435W}$ | |
|---|---|---|---|---|---|---|---|---|---|---|---|---|---|---|---|---|
| NAT | KS | MWU | KS | MWU | KS | MWU | KS | MWU | KS | MWU | KS | MWU | KS | MWU | KS | MWU |
| (1) | (2) | (3) | (4) | (5) | (6) | (7) | (8) | (9) | (10) | (11) | (12) | (13) | (14) | (15) | (16) | (17) |
| I | 0.19 | 0.15 | 0.03 | 0.01 | 0.05 | 0.02 | 0.60 | 0.30 | 0.81 | 0.23 | 0.49 | 0.29 | 0.92 | 0.46 | 0.12 | 0.03 |
| II | 0.55 | 0.38 | 0.88 | 0.30 | 0.39 | 0.19 | 0.95 | 0.42 | 0.67 | 0.38 | 0.98 | 0.49 | 0.91 | 0.28 | 0.74 | 0.49 |
| III | 0.04 | 0.05 | 0.01 | 0.00 | 0.01 | 0.00 | 0.72 | 0.47 | 0.24 | 0.45 | 0.87 | 0.26 | 0.82 | 0.34 | 0.03 | 0.03 |

Note. — Column 1: The pair of nuclear activity type classifications that the statistical test were performed on. I denotes "unknown" – "HII region-like" galaxies, II denotes "unknown" – "AGN-like" galaxies, III denotes "AGN-like" – "HII region-like" galaxies Columns 2 and 3: KS and MWU test p-values for specific frequency $T_N$. Columns 4 and 5: KS and MWU test p-values for specific luminosity $T_L$(F435W). Columns 6 and 7: KS and MWU test p-values for specific luminosity $T_L$(F814W). Column 8 and 9: KS and MWU test p-values for luminosity function indices $\alpha$ for F435W images. Column 10 and 11: KS and MWU test p-values for luminosity function indices $\alpha$ for F814W images. Column 12 and 13: KS and MWU test p-values for the median (F435W−F814W) color of clusters. Column 14 and 15: KS and MWU test p-values for population fraction of SCs that can be reliably age-dated as younger than 7.6 Myr with no extinction correction. Column 16 and 17: KS and MWU test p-values for the absolute F435W magnitude of the brightest cluster.

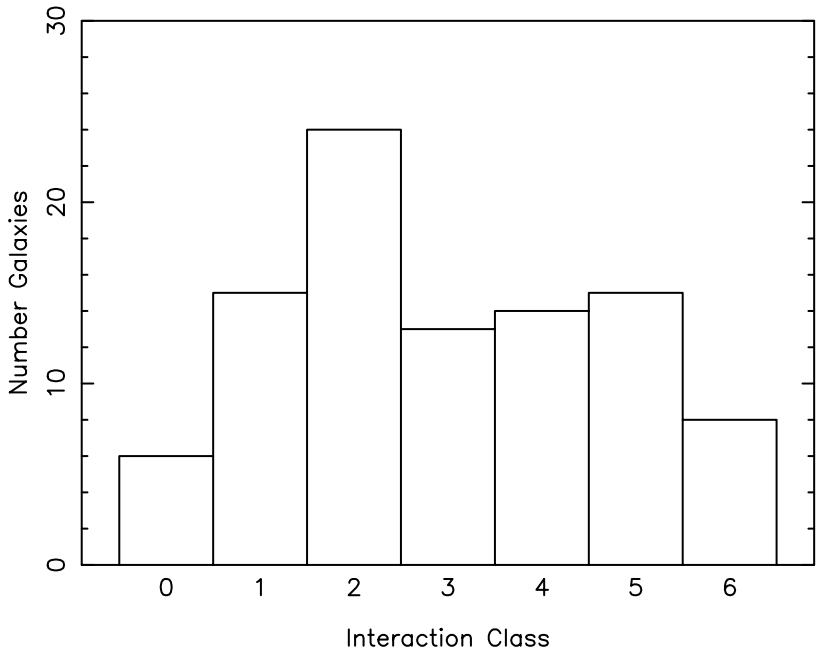


Figure 4.1: The distribution of galaxies in interaction classes.

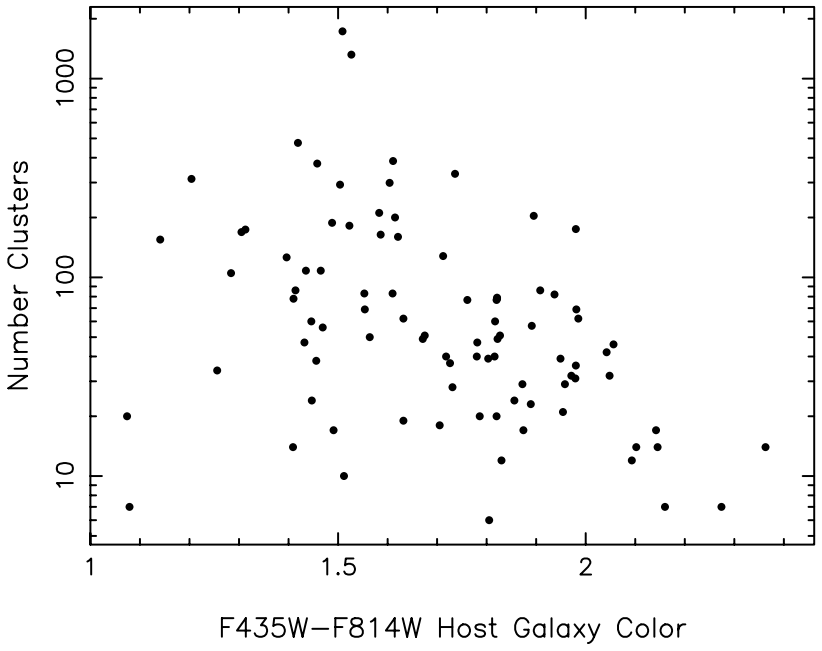


Figure 4.2: Number of detected SCs versus (F435W−F814W) host galaxy color

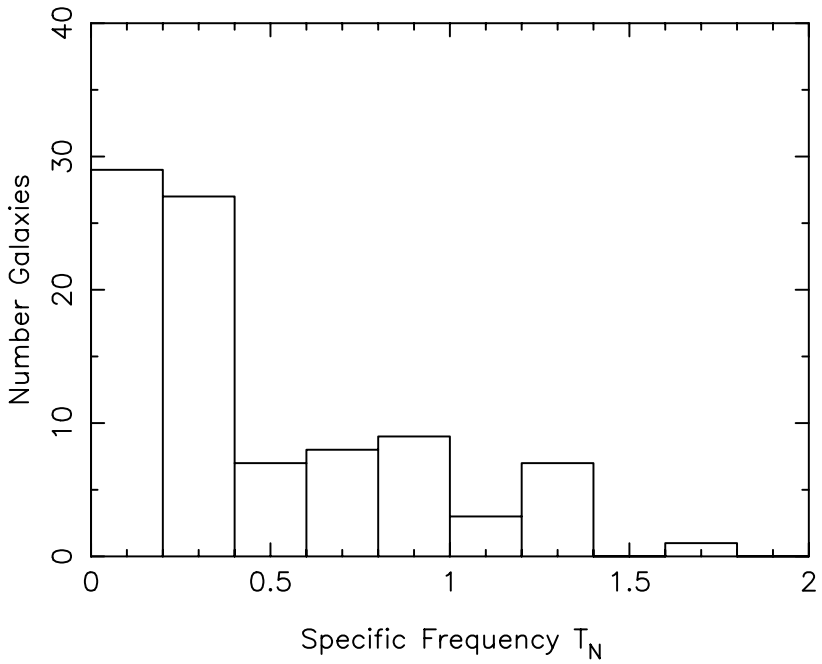


Figure 4.3: The distribution of corrected specific frequency $T_N$ values in the HST-GOALS sample.

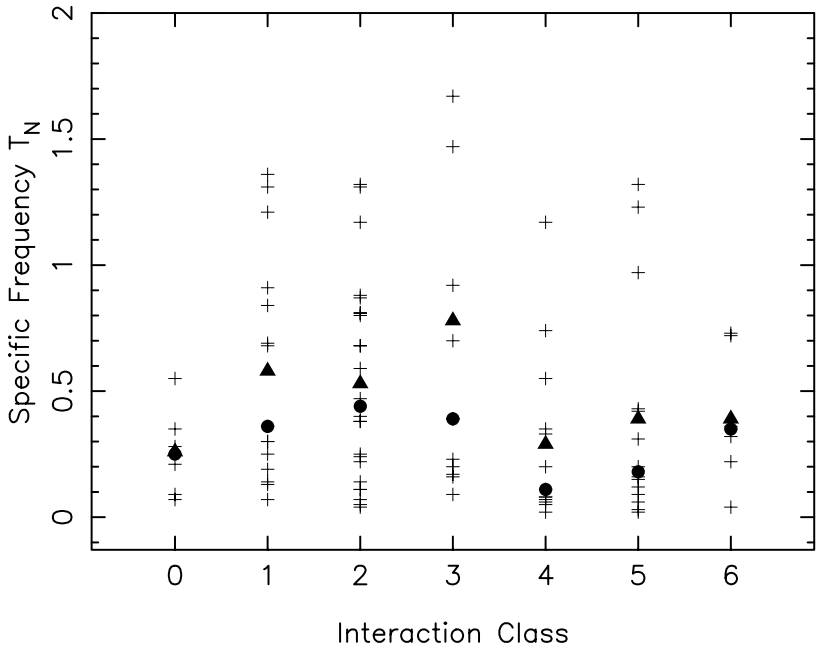


Figure 4.4: The distribution (cross marker) of the specific frequency $T_N$ values along the merger stage sequence. The median value for each bin is marked with a circle, the mean value is marked with a triangle.

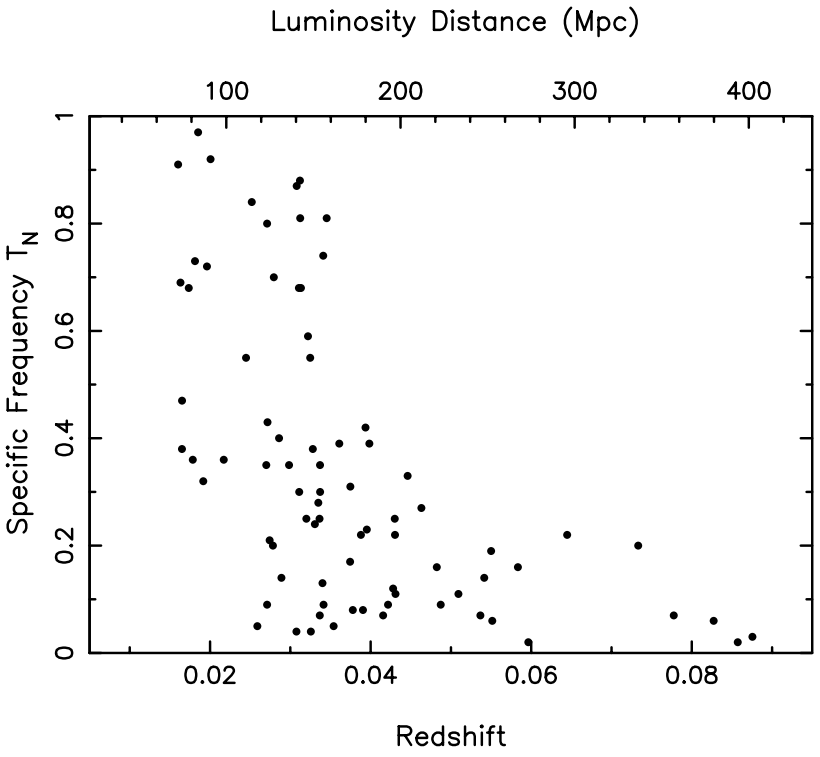


Figure 4.5: Specific frequency $T_N$ versus luminosity distance

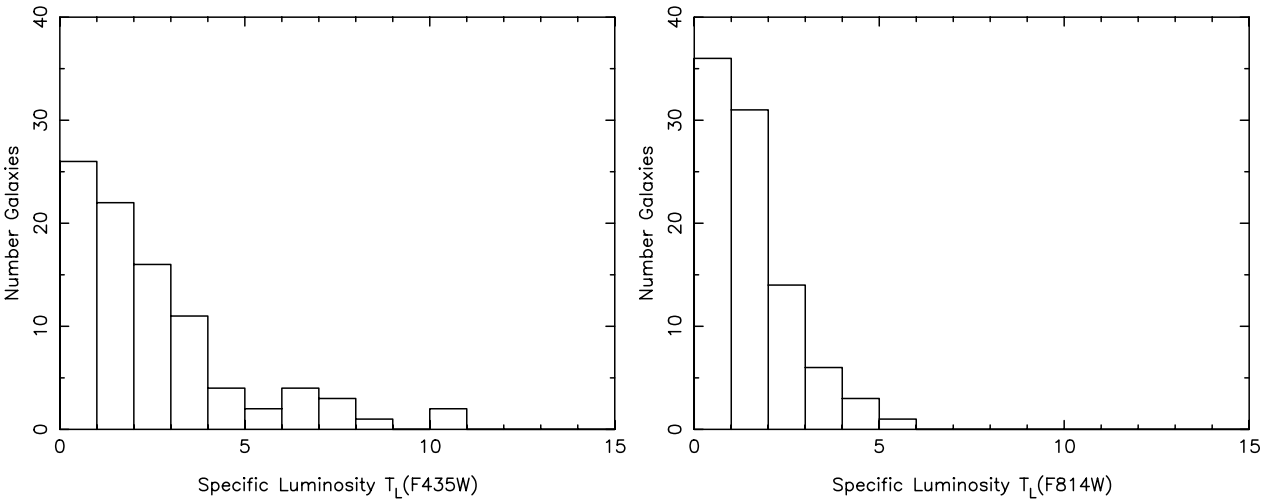


Figure 4.6: The distribution of specific luminosity $T_L$ values in the F435W (panel a)) and F814W (panel b)) images.

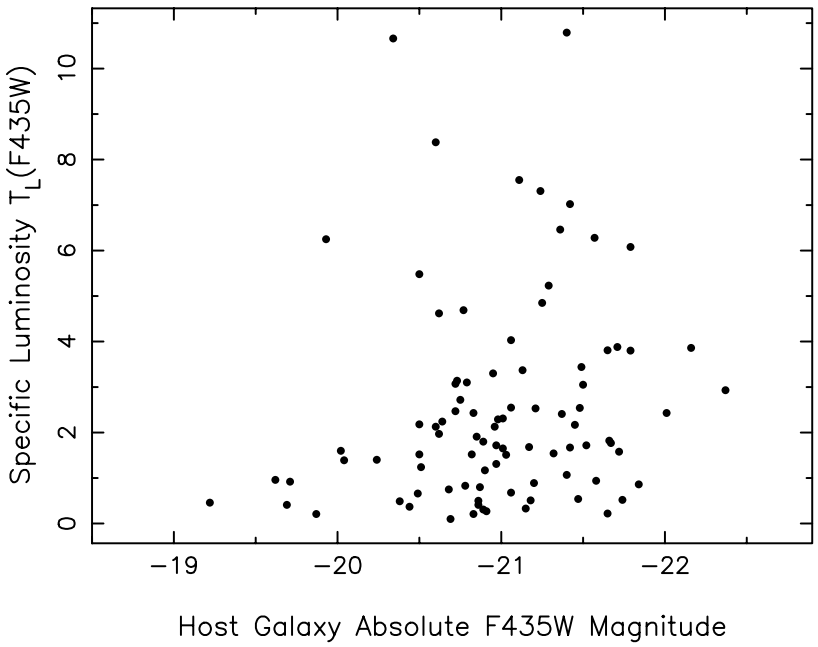


Figure 4.7: Specific luminosity $T_L$(F435W) versus $M_{F435W}$ of the host galaxy.

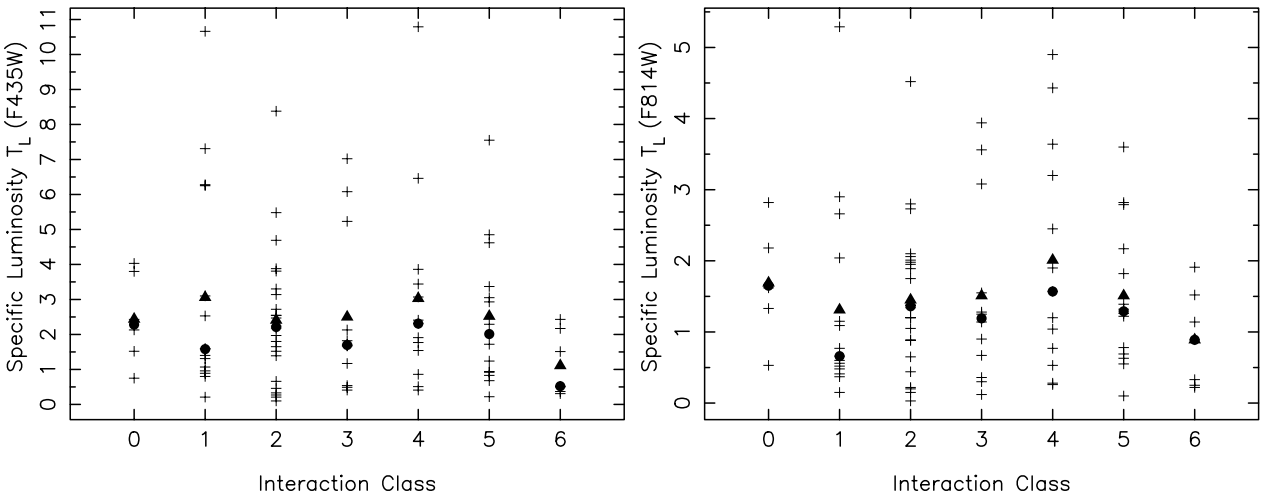


Figure 4.8: The distribution of the specific luminosity $T_L$ values along the merger stage sequence. The median value for each bin is marked with a circle, the mean value is marked with a triangle.

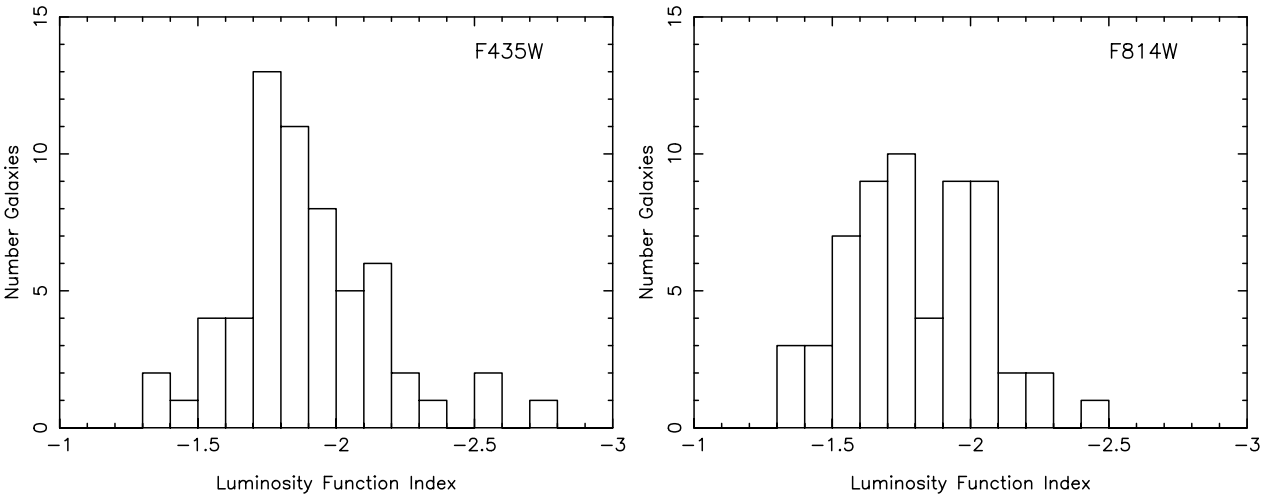


Figure 4.9: The distribution of the luminosity function indices in the F435W (panel a)) and F814W (panel b)) images.

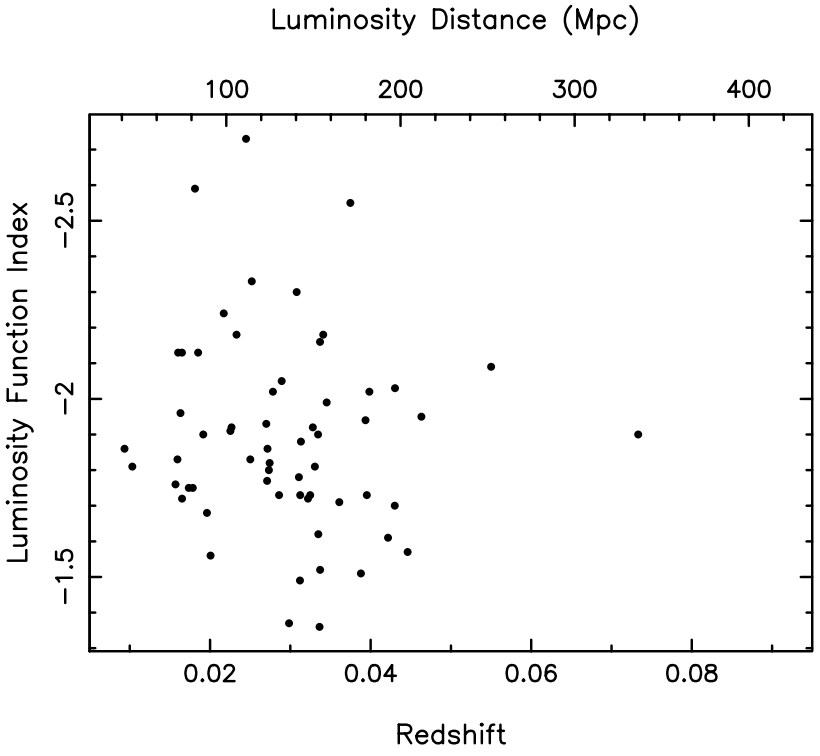


Figure 4.10: The luminosity function indices in the F435W images versus luminosity distance

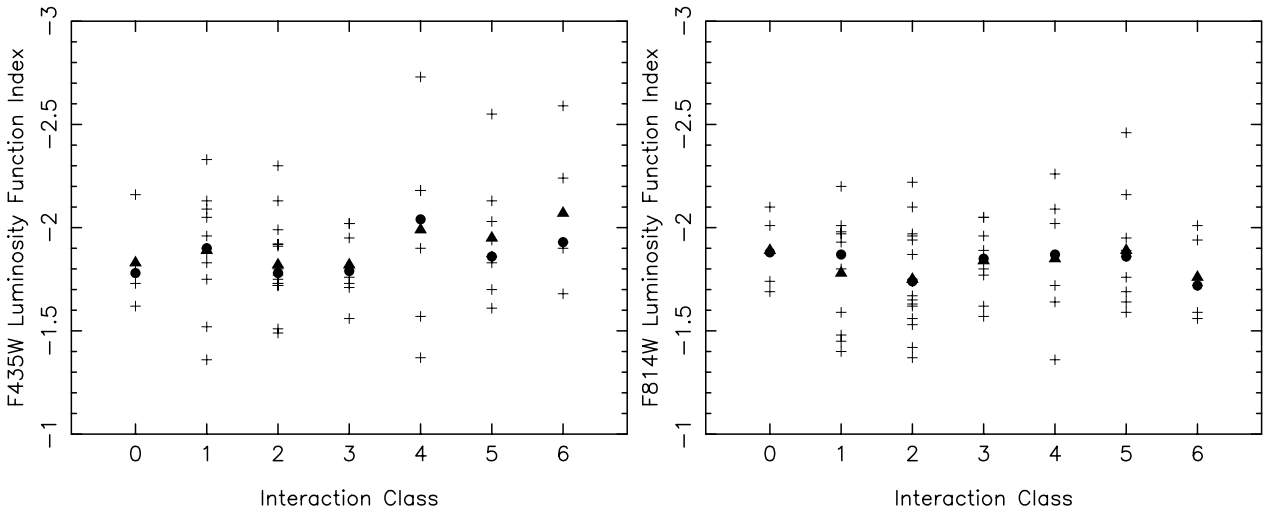


Figure 4.11: The distribution of the luminosity function indices $\alpha$ along the merger stage sequence. The median value for each bin is marked with a circle, the mean value is marked with a triangle.

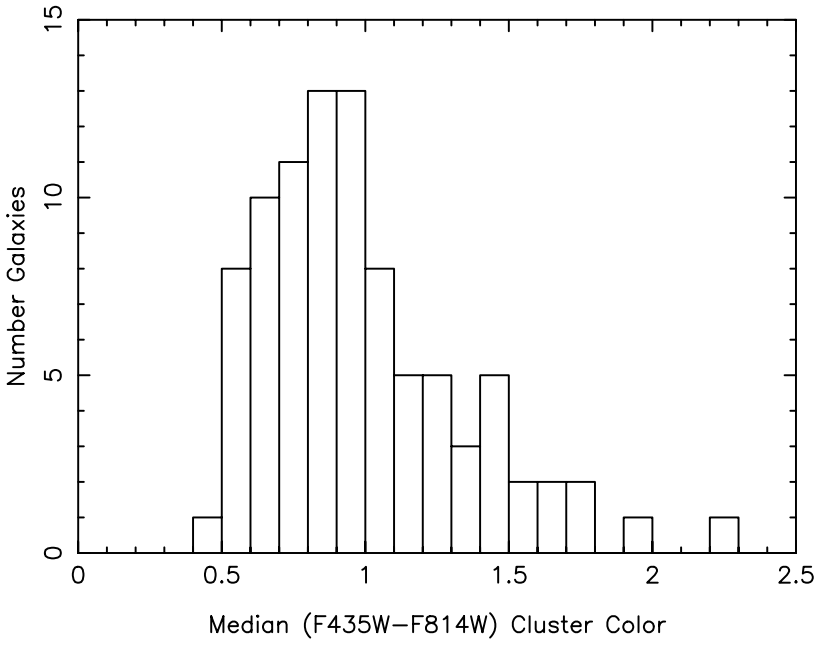


Figure 4.12: The distribution of median (F435W−F814W) cluster colors.

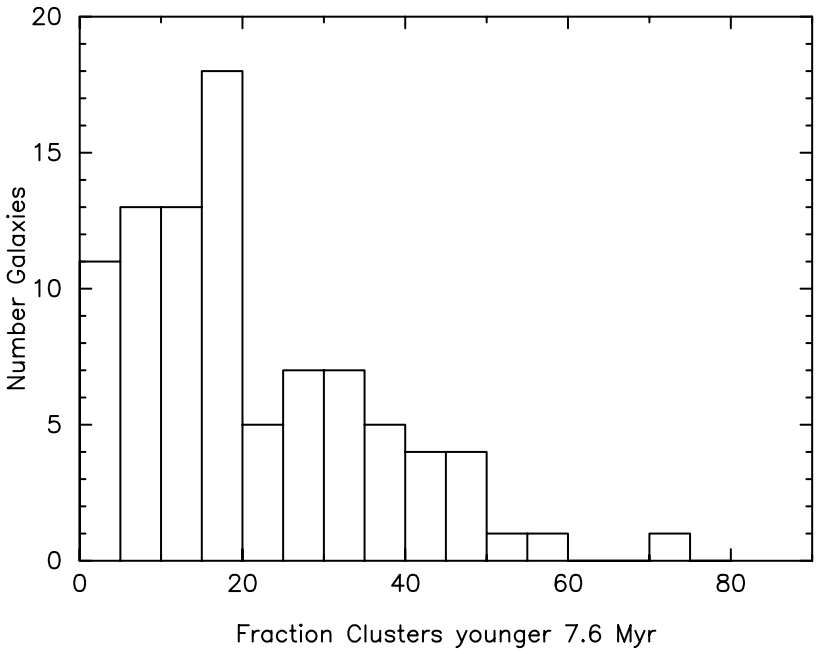


Figure 4.13: The distribution of the population fraction (in percent) of age-dated SCs younger than 7.6 Myr.

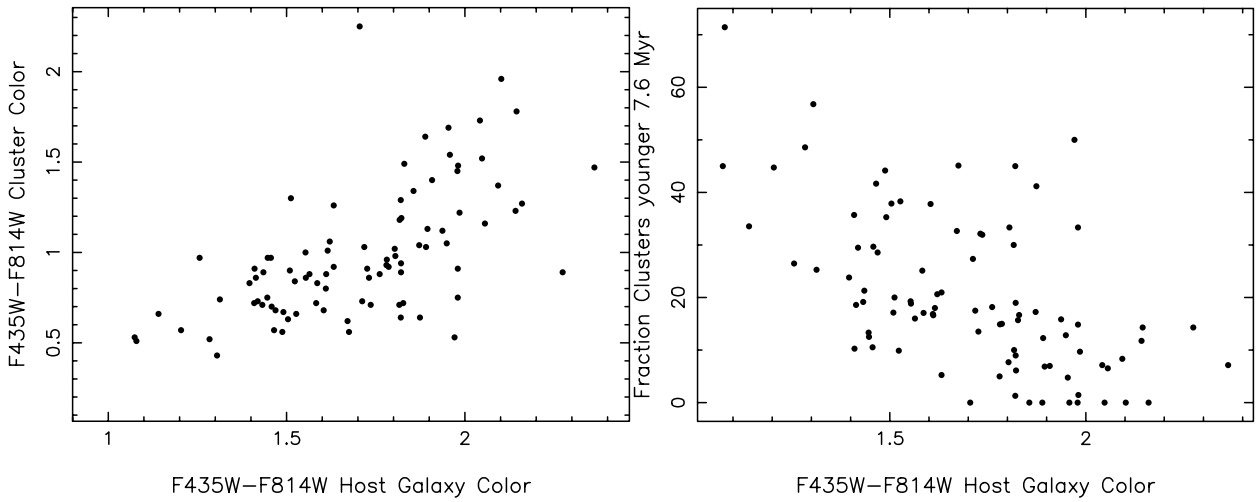


Figure 4.14: Panel a): Median (F435W−F814W) cluster color versus (F435W−F814W) host galaxy color. Panel b): Population fraction of age-dated SCs younger than 7.6 Myr versus (F435W−F814W) host galaxy color.

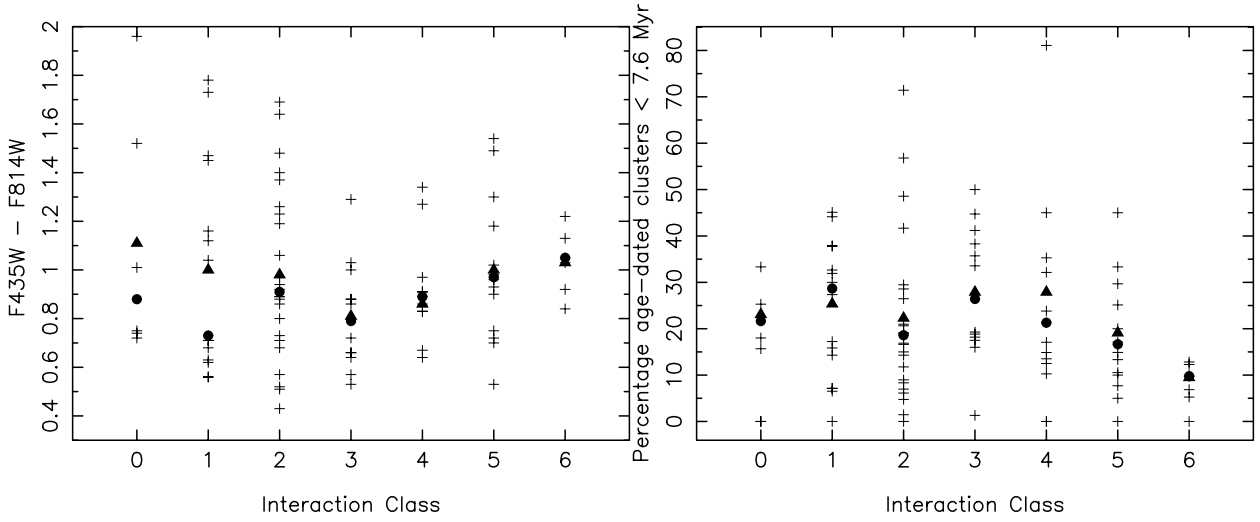


Figure 4.15: The distribution of SC colors (panel a)) and the percentage of the age-dated SCs younger than 7.6 (panel b)) along the merger stage sequence. The median value for each bin is marked with a circle, the mean value is marked with a triangle.

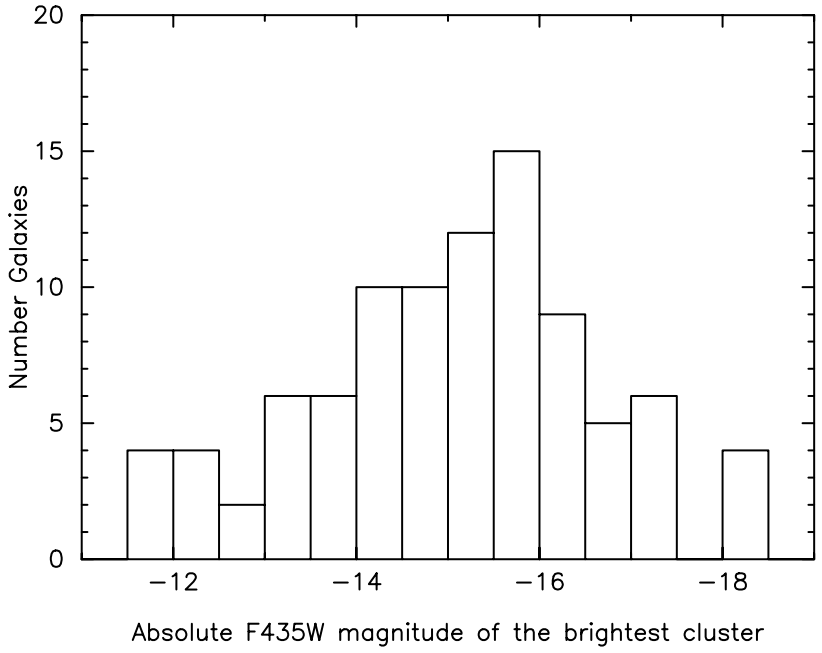


Figure 4.16: The distribution of the $M_{F435W}$ of the most luminous cluster in each galaxy.

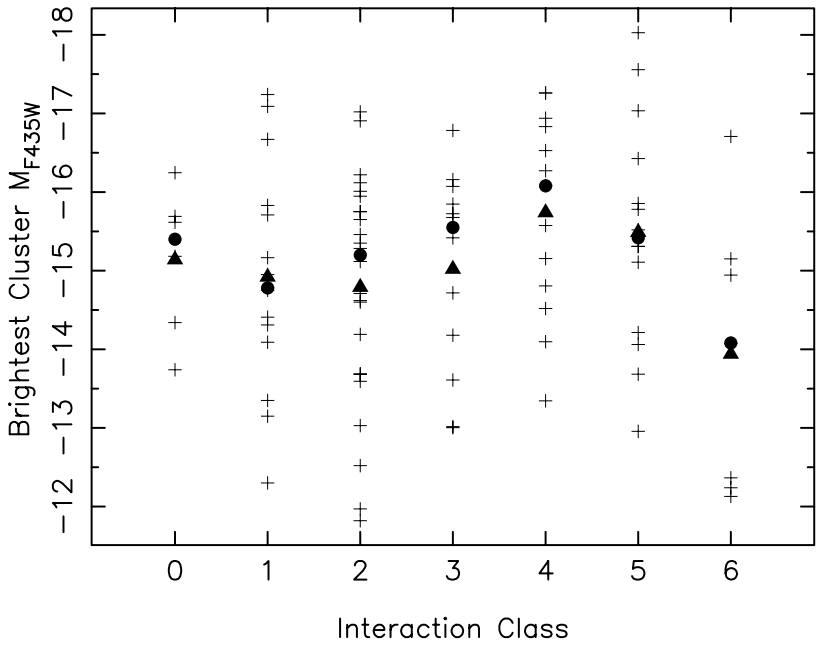


Figure 4.17: The distribution of the absolute F435W magnitudes of the brightest cluster along the merger stage sequence. The median value for each bin is marked with a circle, the mean value is marked with a triangle.

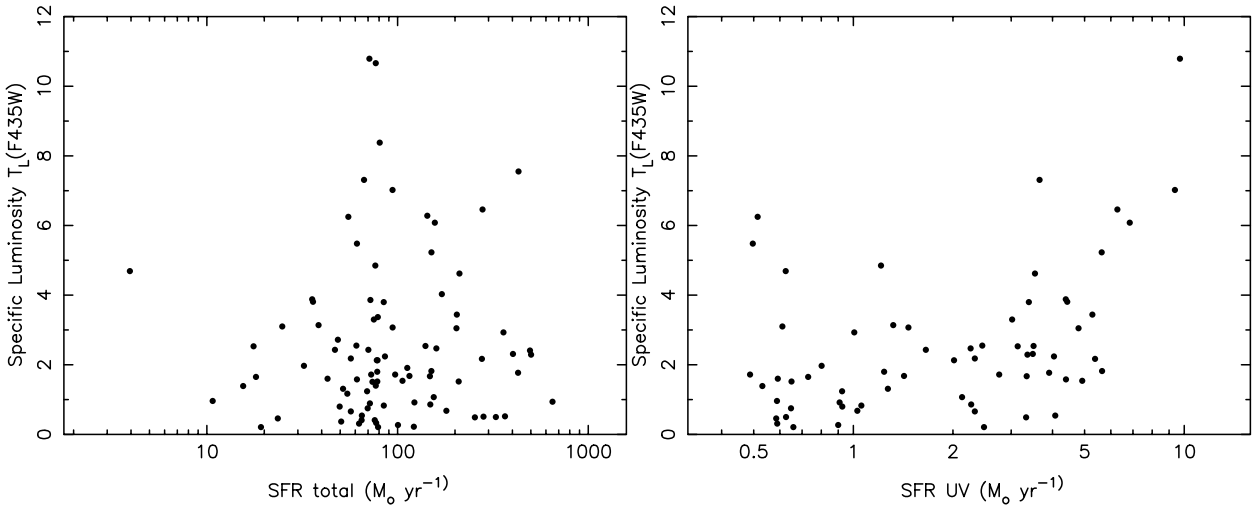


Figure 4.18: Specific luminosity $T_L$ in the F435W image versus SFR derived from FIR and FUV fluxes (panel a)) and FUV fluxes only (panel b)).

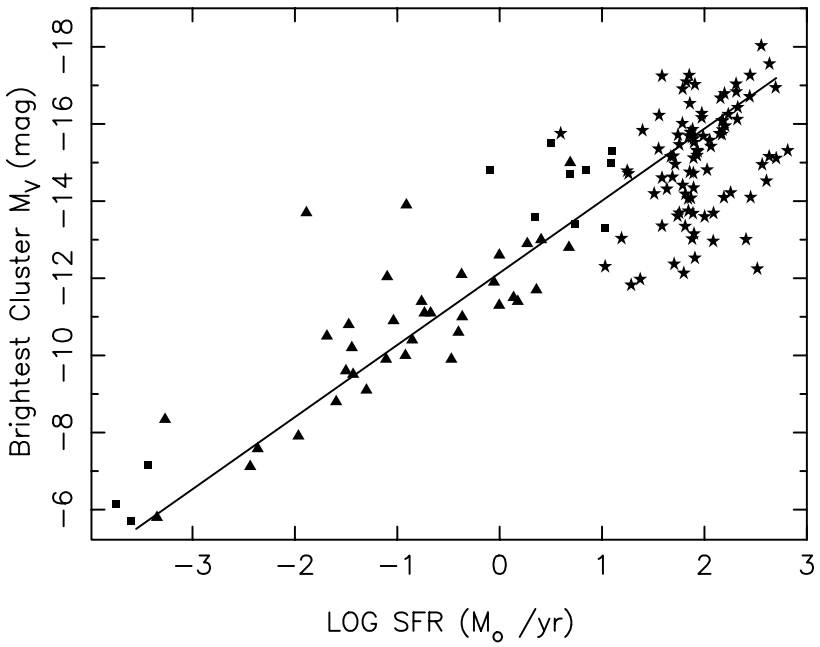


Figure 4.19: $M_V$ of the most luminous cluster within the galaxy versus SFR. The galaxies from the Larsen (2002b) sample are designated with triangles, the squares mark data from Bastian (2008) Table 1. The HST-GOALS LIRGs are indicated with star symbols. The diagonal line is the fit from Weidner et al. (2004).

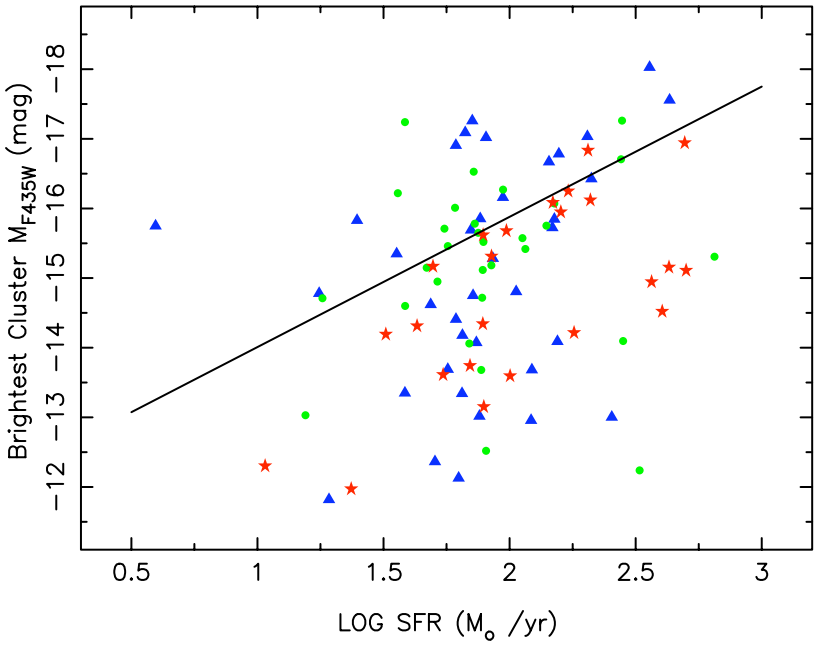


Figure 4.20: $M^{max}_{F435W}$ – SFR plot with symbols indicating (F435W−F814W) color of the cluster. Blue triangles are clusters with (F435W−F814W) $< 0.5$, green dots are clusters with $0.5 <$ (F435W- F814W) $< 1.0$ and red stars are clusters with (F435W−F814W) $> 1.0$.

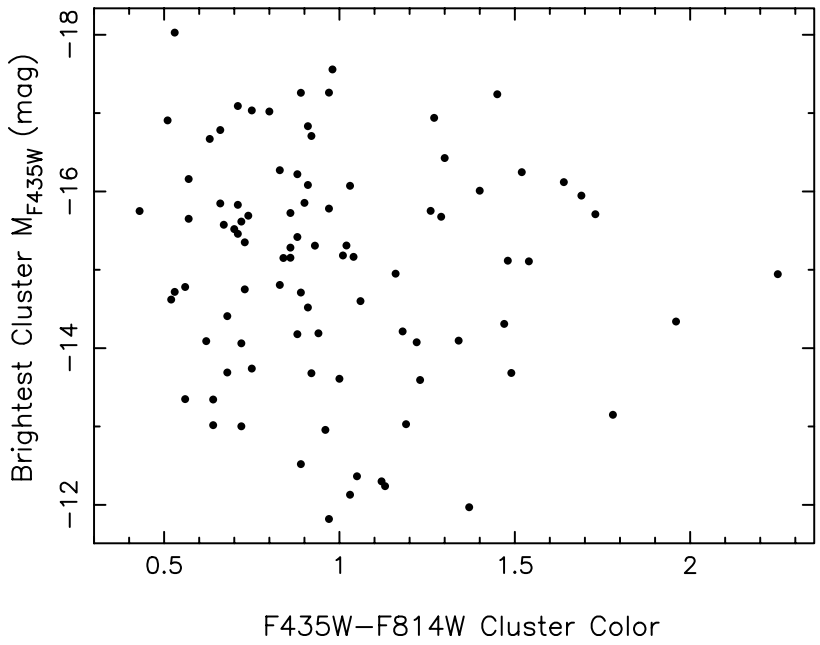


Figure 4.21: $M_{F435W}$ of the brightest cluster versus its (F435W−F814W) color.

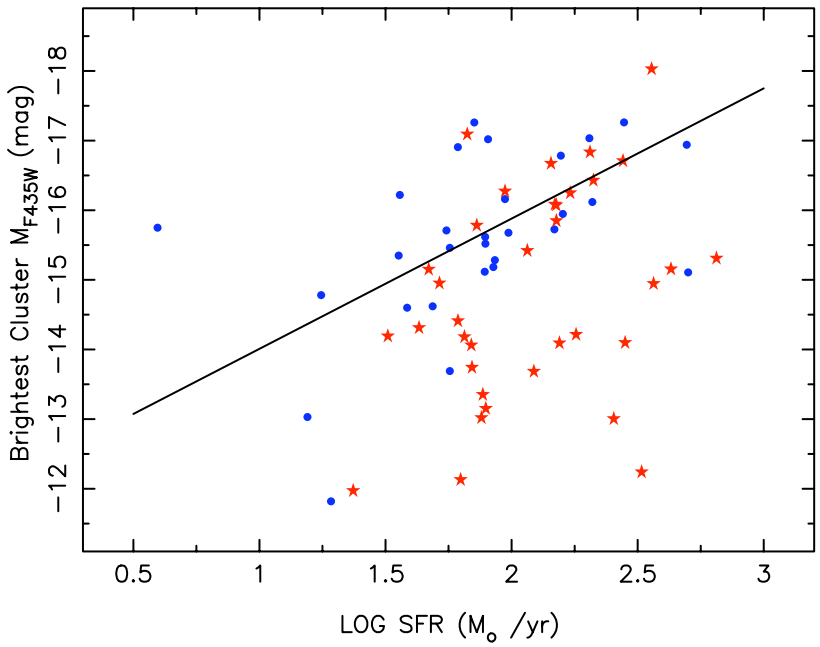


Figure 4.22: $M^{max}_{F435W}$ – SFR plot with symbols indicating the nuclear activity type of the host galaxy. The blue dots are galaxies with "HII region-like" nuclei, the red stars indicate galaxies with "AGN-like" nuclei.

# Chapter 5

# Closing Remarks

## 5.1 Summary

The purpose of this thesis project was to perform a detailed study of the basic properties of optically-luminous star clusters in a large sample of LIRGs. High-resolution *Hubble Space Telescope* ACS/WFC observations at 0.4$\mu$m (F435W) and 0.9$\mu$m (F814W) of a sample of 87 Luminous Infrared Galaxies with $L_{\rm IR} > 10^{11.4}$ L$_\odot$ from the Great Observatory All-sky LIRG Survey (GOALS) sample constitute the basis of the project. For a sub-sample of 15 most cluster-rich LIRGs, ancillary *Spitzer* IRAC and *GALEX* near-UV imaging data from the GOALS project are utilized as well.

Chapter 2 describes the data reduction and the cluster detection algorithm. The preliminary data reduction is performed by the STScI pipeline, however the presence of cosmic rays requires a re-reduction of the images, including the execution of two cosmic-ray detection algorithms and re-drizzling the images, corrections to WCS and alignment of F435W and F814W images. Next step is to execute an automated routine for SC detection and photometry. Source Extractor (Bertin & Arnouts, 1996) is used to detect SC candidates and to fit and remove the underlying galaxy. The coordinates of SC candidates are passed on to IDL routines that compute the centroids of the Source Extractor positions and the FWHM of detected sources, perform aperture photometry and apply a set of selection criteria to identify viable SCs. Finally, the efficiency of the detection algorithm and the degree of foreground star contamination are estimated.

Although not explicitly included in this dissertation, studies of individual particularly remarkable LIRGs served as a test-bed for the cluster analysis (Evans et al., 2008, Modica et al., 2011, Mazzarella et al., 2011).

A sample of the 15 most cluster-rich LIRGs with over 7000 detected luminous star clusters was chosen for a detailed analysis described in Chapter 3. A large fraction of cluster population ($\sim$ 30%) is younger than 10 Myr; the rest of the cluster population may have ages of up to few hundred Myr. The range of specific frequencies $T_N$ of SCs is $0.67 - 1.73$, with a median of $1.14 \pm 0.30$; the $T_N$ values in the cluster-rich LIRGs sample are higher than the ones observed in nearby spiral galaxies (Larsen & Richtler, 2000) and are in the merger and starburst galaxies range. These optically-visible star clusters contribute about 4% to F435W and 2% to F814W total fluxes. The cluster luminosity function exponents have median values of $\alpha = -1.91 \pm 0.22$ and $-1.88 \pm 0.20$ as measured at F435W and F814W images, respectively and are in good agreement with previously published results.

Autocorrelation functions of the spatial distribution of star clusters were calculated; they exhibit a power-law behavior on scales of 1 kpc with the median index of $-0.77 \pm 0.13$. The visual impression of early merger stage systems conveys a large degree of "clustering" of star clusters, while in late merger stages clusters are dispersed through-out the galaxy. The visual impression is also confirmed by a difference in median autocorrelation function indices: for early merger stages the median power-law index is $-0.84 \pm 0.07$ and the median power-law index for mid-merger and late merger stages is $-0.62 \pm 0.09$. Ancillary *Spitzer* IRAC and *GALEX* near-UV imaging data are also presented to examine correlations between locations of young optical stellar clusters with PAH and UV emission regions. While near-UV emission coincides closely with the distribution of optically visible clusters, no correlation is found with PAH emission (i.e., embedded star formation). Thus, optically visible clusters and UV emission trace un-obscured star formation which appears to be unassociated with the bulk of the star formation that takes place in dusty central regions of LIRGs.

In Chapter 4, the extension of the analysis to the complete sample of 87 $L_{\rm IR} > 10^{11.4}$ $L_\odot$ LIRGs in the GOALS sample is presented. The results of this analysis are consistent with the findings in the cluster-rich LIRGs sample. The distribution of ages of SCs in the HST-GOALS sample, given the constraints of the age-dating procedure using photometric measurements in just two filters, shows a spread between few Myr up to few hundred Myr, with a large fraction of cluster population ($\sim 17\%$) younger than 10 Myr. The median specific frequency $T_N$ value of the HST-GOALS sample, $0.32 \pm 0.40$, is lower than the median $T_N$ of the cluster-rich sample; this is due to the sample selection criterion of the cluster-rich sample. The median specific luminosity $T_L$ values are lower as well, $1.8 \pm 2.3\%$ in F435W and $1.2 \pm 1.2\%$ in F814W. The optically visible SCs contribute rather little to the optical luminosity of LIRGs and certainly play a minor role in the total energy output of these IR luminous systems. The cluster luminosity function exponents have median values of $\alpha = -1.86 \pm 0.27$ and $-1.77 \pm 0.24$ as measured in F435W and F814W images, respectively; they are consistent with the measurements in the cluster-rich sample and previously published results (e.g., Portegies Zwart et al., 2010). No clear trend of SC properties with the merger stage of the LIRG is observed. The only conclusion that can be established is that in late merger stages the degree of the extended star formation diminishes and the centrally concentrated nuclear SF/AGN dominates the energy output of the LIRG. Galaxies with "HII region-like" (i.e., starburst-like) nuclear spectra exhibit higher specific frequency $T_N$, specific luminosity $T_L$ and $M^{max}_{F435W}$ values compared to galaxies with AGN presence, although the fraction of SCs younger than 10 Myr remains constant. The specific luminosity $T_L$(F435W) – SFR(IR + FUV) relation found by Larsen & Richtler (2000) in a sample of nearby spiral galaxies is not applicable to Luminous IR Galaxies. However, a weak correlation of specific luminosity $T_L$(F435W) – SFR(FUV) is observed. This supports the conclusion reached for the cluster-rich sample, that optically visible SCs and UV fluxes trace un-obscured star formation, while the IR emission traces the bulk the star formation that is hidden at shorter wavelengths. LIRGs follow the brightest cluster $M^{max}_{F435W}$ – SFR relation quite closely, although a large degree of scatter is observed. The significant number of brightest cluster members observed below the relation may be due to extinction and over-estimation of SFRs in AGN-dominated galaxies. Thus, the size-of-sample effect (Whitmore, 2003; Larsen, 2002b) is responsible for high luminosity of SCs found in Luminous IR Galaxies.

## 5.2 Future directions

This study revealed a considerable amount of information about SCs in extreme star formation environments of IR luminous mergers. Despite the clear advantages, there are also several limitations connected with a study of SCs in LIRGs. LIRGs are more distant, which limits our ability to detect faint clusters and to resolve individual SCs in star cluster complexes. LIRGs are dusty and a considerable fraction of SC population might be hidden at optical wavelengths. Star clusters might suffer large and variable amount of extinction which results in uncertainties in age determination.

This study opens a door to more detailed investigations of SCs in LIRGs. Clearly, better estimates of the extinction and ages of SCs are crucial. High spatial resolution imaging with *HST* in broad-band optical U and V (possibly F336W and F555W filters on WFC3) and narrow-band H$\alpha$ imaging are needed. A knowledge of precise SC ages together with their locations would make a detailed SF history of each individual LIRG accessible. Numerical simulations of the detailed merger process of individual LIRG systems would be helpful in a comparison with SF history derived from SCs. A knowledge of SC ages would also allow a construction of SC mass functions and lead to insights into SC disruption processes.

The HST-GOALS sample, combined with the wavelength coverage available through the GOALS project, is a true treasure trove that allows to access the interplay between the SC properties and the host galaxy properties. For example, do factors such as the amount and location of dense molecular gas, the fraction of AGN versus SB contribution to LIRG's energy output, the presence of galactic-scale superwinds influence the formation and disruption of SCs and SC population properties? The HST-GOALS together with the GOALS sample will certainly be a source of a multitude of projects investigating luminous star clusters; this study marks just the beginning.

# Bibliography


Alvensleben, U. F. 2004, in Astronomical Society of the Pacific Conference Series, Vol. 322, The Formation and Evolution of Massive Young Star Clusters, ed. H. J. G. L. M. Lamers, L. J. Smith, & A. Nota, 91

Anders, P., Fritze-von Alvensleben, U., & de Grijs, R. 2003, Ap&SS, 284, 937

Armus, L., Mazzarella, J. M., Evans, A. S., Surace, J. A., Sanders, D. B., Iwasawa, K., Frayer, D. T., Howell, J. H., Chan, B., Petric, A., Vavilkin, T., Kim, D. C., Haan, S., Inami, H., Murphy, E. J., Appleton, P. N., Barnes, J. E., Bothun, G., Bridge, C. R., Charmandaris, V., Jensen, J. B., Kewley, L. J., Lord, S., Madore, B. F., Marshall, J. A., Melbourne, J. E., Rich, J., Satyapal, S., Schulz, B., Spoon, H. W. W., Sturm, E., U, V., Veilleux, S., & Xu, K. 2009, PASP, 121, 559

Arp, H. & Sandage, A. 1985, AJ, 90, 1163

Ashman, K. M. & Zepf, S. E. 1992, ApJ, 384, 50

—. 2001, AJ, 122, 1888

Barger, A. J., Cowie, L. L., & Richards, E. A. 1999, in Astronomical Society of the Pacific Conference Series, Vol. 191, Photometric Redshifts and the Detection of High Redshift Galaxies, ed. R. Weymann, L. Storrie-Lombardi, M. Sawicki, & R. Brunner, 279

Barnes, J. E. 2004, MNRAS, 350, 798

Barnes, J. E. & Hernquist, L. 1996, ApJ, 471, 115

Barth, A. J., Ho, L. C., Filippenko, A. V., & Sargent, W. L. 1995, AJ, 110, 1009

Bastian, N. 2008, MNRAS, 390, 759

Bastian, N., Adamo, A., Gieles, M., Lamers, H. J. G. L. M., Larsen, S. S., Silva-Villa, E., Smith, L. J., Kotulla, R., Konstantopoulos, I. S., Trancho, G., & Zackrisson, E. 2011, ArXiv e-prints

Bendo, G. J. 2006, in Astronomical Society of the Pacific Conference Series, Vol. 357, Astronomical Society of the Pacific Conference Series, ed. L. Armus & W. T. Reach, 192–+

Bertin, E. & Arnouts, S. 1996, A&AS, 117, 393

Bik, A., Lamers, H. J. G. L. M., Bastian, N., Panagia, N., & Romaniello, M. 2003, A&A, 397, 473

Billett, O. H., Hunter, D. A., & Elmegreen, B. G. 2002, AJ, 123, 1454

Bohlin, R. C., Cornett, R. H., Hill, J. K., & Stecher, T. P. 1990, ApJ, 363, 154

Boutloukos, S. G. & Lamers, H. J. G. L. M. 2003, MNRAS, 338, 717

Bruzual, G. 2010, Philosophical Transactions of the Royal Society A: Mathematical, 368, 783

Bruzual, G. & Charlot, S. 2003, MNRAS, 344, 1000

Buta, R., Treuthardt, P. M., Byrd, G. G., & Crocker, D. A. 2000, AJ, 120, 1289

Calzetti, D., Kennicutt, R. C., Engelbracht, C. W., Leitherer, C., Draine, B. T., Kewley, L., Moustakas, J., Sosey, M., Dale, D. A., Gordon, K. D., Helou, G. X., Hollenbach, D. J., Armus, L., Bendo, G., Bot, C., Buckalew, B., Jarrett, T., Li, A., Meyer, M., Murphy, E. J., Prescott, M., Regan, M. W., Rieke, G. H., Roussel, H., Sheth, K., Smith, J. D. T., Thornley, M. D., & Walter, F. 2007, ApJ, 666, 870

Calzetti, D., Kennicutt, Jr., R. C., Bianchi, L., Thilker, D. A., Dale, D. A., Engelbracht, C. W., Leitherer, C., Meyer, M. J., Sosey, M. L., Mutchler, M., Regan, M. W., Thornley, M. D., Armus, L., Bendo, G. J., Boissier, S., Boselli, A., Draine, B. T., Gordon, K. D., Helou, G., Hollenbach, D. J., Kewley, L., Madore, B. F., Martin, D. C., Murphy, E. J., Rieke, G. H., Rieke, M. J., Roussel, H., Sheth, K., Smith, J. D., Walter, F., White, B. A., Yi, S., Scoville, N. Z., Polletta, M., & Lindler, D. 2005, ApJ, 633, 871

Calzetti, D., Meurer, G. R., Bohlin, R. C., Garnett, D. R., Kinney, A. L., Leitherer, C., & Storchi-Bergmann, T. 1997, AJ, 114, 1834

Chabrier, G. 2003, PASP, 115, 763

Chandar, R., Bianchi, L., & Ford, H. C. 1999a, ApJS, 122, 431

—. 1999b, ApJ, 517, 668

Chandar, R., Bianchi, L., Ford, H. C., & Salasnich, B. 1999c, PASP, 111, 794

Chandar, R., Fall, S. M., & Whitmore, B. C. 2006, ApJ, 650, L111

—. 2010a, ApJ, 711, 1263

Chandar, R., Whitmore, B. C., Kim, H., Kaleida, C., Mutchler, M., Calzetti, D., Saha, A., O'Connell, R., Balick, B., Bond, H., Carollo, M., Disney, M., Dopita, M. A., Frogel, J. A., Hall, D., Holtzman, J. A., Kimble, R. A., McCarthy, P., Paresce, F., Silk, J., Trauger, J., Walker, A. R., Windhorst, R. A., & Young, E. 2010b, ApJ, 719, 966

Chien, L. 2010, in Astronomical Society of the Pacific Conference Series, Vol. 423, Galaxy Wars: Stellar Populations and Star Formation in Interacting Galaxies, ed. B. Smith, J. Higdon, S. Higdon, & N. Bastian, 197

Chien, L.-H. & Barnes, J. E. 2010, MNRAS, 407, 43

Chien, L.-H., Barnes, J. E., Kewley, L. J., & Chambers, K. C. 2007, ApJ, 660, L105

Clark, J. S., Negueruela, I., Crowther, P. A., Goodwin, S., & Hadfield, L. J. 2005, in Astrophysics and Space Science Library, Vol. 329, Starbursts: From 30 Doradus to Lyman Break Galaxies, ed. R. de Grijs & R. M. González Delgado, 13P

Clarke, C. 2010, Royal Society of London Philosophical Transactions Series A, 368, 733

de Grijs, R. 2004, in Astronomical Society of the Pacific Conference Series, Vol. 322, The Formation and Evolution of Massive Young Star Clusters, ed. H. J. G. L. M. Lamers, L. J. Smith, & A. Nota, 29

de Grijs, R. 2010, Royal Society of London Philosophical Transactions Series A, 368, 693

de Grijs, R., Bastian, N., & Lamers, H. J. G. L. M. 2003, MNRAS, 340, 197

de Grijs, R. & Parmentier, G. 2007, Chinese Journal of Astronomy and Astrophysics, 7, 155

Drinkwater, M. J., Gregg, M. D., Hilker, M., Couch, W. J., Ferguson, H. C., Jones, B., & Phillipps, S. 2003, in IAU Joint Discussion, Vol. 10, IAU Joint Discussion

Elbaz, D., Marcillac, D., & Moy, E. 2005, in Multiwavelength Mapping of Galaxy Formation and Evolution, ed. A. Renzini & R. Bender, 12

Elmegreen, B. G. 1999, Ap&SS, 269, 469

Elmegreen, B. G. 2008, in Astronomical Society of the Pacific Conference Series, Vol. 388, Mass Loss from Stars and the Evolution of Stellar Clusters, ed. A. de Koter, L. J. Smith, & L. B. F. M. Waters, 249

—. 2011, ArXiv e-prints

Elmegreen, B. G. & Elmegreen, D. M. 2001, AJ, 121, 1507

Evans, A. S., Vavilkin, T., Pizagno, J., Modica, F., Mazzarella, J. M., Iwasawa, K., Howell, J. H., Surace, J. A., Armus, L., Petric, A. O., Spoon, H. W. W., Barnes, J. E., Suer, T. A., Sanders, D. B., Chan, B., & Lord, S. 2008, ApJ, 675, L69

Fall, S. M. 2006, ApJ, 652, 1129

Fall, S. M., Chandar, R., & Whitmore, B. C. 2005, ApJ, 631, L133

—. 2009, ApJ, 704, 453

Fall, S. M. & Rees, M. J. 1985, ApJ, 298, 18

Fall, S. M. & Zhang, Q. 2001, ApJ, 561, 751

Ferrarese, L. & Merritt, D. 2000, ApJ, 539, L9

Figer, D. F., Kim, S. S., Morris, M., Serabyn, E., Rich, R. M., & McLean, I. S. 1999, ApJ, 525, 750

Figer, D. F., Najarro, F., Gilmore, D., Morris, M., Kim, S. S., Serabyn, E., McLean, I. S., Gilbert, A. M., Graham, J. R., Larkin, J. E., Levenson, N. A., & Teplitz, H. I. 2002, ApJ, 581, 258

Fruchter, A. S. & Hook, R. N. 2002, PASP, 114, 144

Gallagher, III, J. S. & Hunter, D. A. 1987, AJ, 94, 43

Gallagher, S. C., Hunsberger, S. D., Charlton, J. C., & Zaritsky, D. 2000, in Astronomical Society of the Pacific Conference Series, Vol. 211, Massive Stellar Clusters, ed. A. Lançon & C. M. Boily, 247

Gebhardt, K., Bender, R., Bower, G., Dressler, A., Faber, S. M., Filippenko, A. V., Green, R., Grillmair, C., Ho, L. C., Kormendy, J., Lauer, T. R., Magorrian, J., Pinkney, J., Richstone, D., & Tremaine, S. 2000, ApJ, 539, L13

Genzel, R., Lutz, D., & Tacconi, L. 1998, Nature, 395, 859

Gieles, M., Larsen, S. S., Bastian, N., & Stein, I. T. 2006a, A&A, 450, 129

Gieles, M., Larsen, S. S., Scheepmaker, R. A., Bastian, N., Haas, M. R., & Lamers, H. J. G. L. M. 2006b, A&A, 446, L9

Gieles, M., Portegies Zwart, S. F., Baumgardt, H., Athanassoula, E., Lamers, H. J. G. L. M., Sipior, M., & Leenaarts, J. 2006c, MNRAS, 371, 793

Goodwin, S. P. 1997, MNRAS, 284, 785

Goudfrooij, P., Puzia, T. H., Chandar, R., & Kozhurina-Platais, V. 2011a, ArXiv e-prints

Goudfrooij, P., Puzia, T. H., Kozhurina-Platais, V., & Chandar, R. 2011b, ArXiv e-prints

Harris, J., Calzetti, D., Gallagher, III, J. S., Conselice, C. J., & Smith, D. A. 2001, AJ, 122, 3046

Harris, W. E. 1991, ARA&A, 29, 543

—. 1999, Ap&SS, 267, 95

Harris, W. E. & van den Bergh, S. 1981, AJ, 86, 1627

Helou, G., Roussel, H., Appleton, P., Frayer, D., Stolovy, S., Storrie-Lombardi, L., Hurt, R., Lowrance, P., Makovoz, D., Masci, F., Surace, J., Gordon, K. D., Alonso-Herrero, A., Engelbracht, C. W., Misselt, K., Rieke, G., Rieke, M., Willner, S. P., Pahre, M., Ashby, M. L. N., Fazio, G. G., & Smith, H. A. 2004, ApJS, 154, 253

Hilker, M., Infante, L., & Richtler, T. 1999, A&AS, 138, 55

Hinshaw, G., Weiland, J. L., Hill, R. S., Odegard, N., Larson, D., Bennett, C. L., Dunkley, J., Gold, B., Greason, M. R., Jarosik, N., Komatsu, E., Nolta, M. R., Page, L., Spergel, D. N., Wollack, E., Halpern, M., Kogut, A., Limon, M., Meyer, S. S., Tucker, G. S., & Wright, E. L. 2009, ApJS, 180, 225

Howell, J. H., Armus, L., Mazzarella, J. M., Evans, A. S., Surace, J. A., Sanders, D. B., Petric, A., Appleton, P., Bothun, G., Bridge, C., Chan, B. H. P., Charmandaris, V., Frayer, D. T., Haan, S., Inami, H., Kim, D., Lord, S., Madore, B. F., Melbourne, J., Schulz, B., U, V., Vavilkin, T., Veilleux, S., & Xu, K. 2010, ApJ, 715, 572

Hunter, D. A., O'Connell, R. W., Gallagher, J. S., & Smecker-Hane, T. A. 2000, AJ, 120, 2383

Hunter, D. A., Shaya, E. J., Holtzman, J. A., Light, R. M., O'Neil, Jr., E. J., & Lynds, R. 1995, ApJ, 448, 179

Iwasawa, K., Sanders, D. B., Teng, S. H., U, V., Armus, L., Evans, A. S., Howell, J. H., Komossa, S., Mazzarella, J. M., Petric, A. O., Surace, J. A., Vavilkin, T., Veilleux, S., & Trentham, N. 2011, A&A, 529, A106

Jog, C. J. & Solomon, P. M. 1992, ApJ, 387, 152

Kennicutt, Jr., R. C. 1998, ARA&A, 36, 189

Kim, D.-C., Sanders, D. B., Veilleux, S., Mazzarella, J. M., & Soifer, B. T. 1995, ApJS, 98, 129

Kim, D.-C., Veilleux, S., & Sanders, D. B. 2002, ApJS, 143, 277

Knierman, K. A., Gallagher, S. C., Charlton, J. C., Hunsberger, S. D., Whitmore, B., Kundu, A., Hibbard, J. E., & Zaritsky, D. 2003, AJ, 126, 1227

Koekemoer, A. M., Fruchter, A. S., Hook, R. N., & Hack, W. 2002, in The 2002 HST Calibration Workshop : Hubble after the Installation of the ACS and the NICMOS Cooling System, ed. S. Arribas, A. Koekemoer, & B. Whitmore, 337

Kroupa, P., Tout, C. A., & Gilmore, G. 1993, MNRAS, 262, 545

Kruijssen, J. M. D., Pelupessy, F. I., Lamers, H. J. G. L. M., Portegies Zwart, S. F., & Icke, V. 2011, MNRAS, 414, 1339

Krumholz, M. R. & Matzner, C. D. 2009, ApJ, 703, 1352

Kundu, A. & Whitmore, B. C. 2001, AJ, 121, 2950

Lada, C. J. 2010, Philosophical Transactions of the Royal Society A: Mathematical, 368, 713

Lada, C. J. & Lada, E. A. 2003, ARA&A, 41, 57

Lamers, H. J. G. L. M. 2009, Ap&SS, 324, 183

Lamers, H. J. G. L. M., Gieles, M., Bastian, N., Baumgardt, H., Kharchenko, N. V., & Portegies Zwart, S. 2005a, A&A, 441, 117

Lamers, H. J. G. L. M., Gieles, M., & Portegies Zwart, S. F. 2005b, A&A, 429, 173

Larsen, S. S. 1999, A&AS, 139, 393

Larsen, S. S. 2002a, in IAU Symposium, Vol. 207, Extragalactic Star Clusters, ed. D. P. Geisler, E. K. Grebel, & D. Minniti, 421

—. 2002b, AJ, 124, 1393

—. 2006a, ArXiv Astrophysics e-prints

Larsen, S. S. 2006b, in Planets to Cosmology: Essential Science in the Final Years of the Hubble Space Telescope, ed. M. Livio & S. Casertano, 35

—. 2009, A&A, 494, 539

—. 2010, Royal Society of London Philosophical Transactions Series A, 368, 867

Larsen, S. S. & Richtler, T. 1999, A&A, 345, 59

—. 2000, A&A, 354, 836

Le Floc'h, E., Papovich, C., Dole, H., Bell, E. F., Lagache, G., Rieke, G. H., Egami, E., Pérez-González, P. G., Alonso-Herrero, A., Rieke, M. J., Blaylock, M., Engelbracht, C. W., Gordon, K. D., Hines, D. C., Misselt, K. A., Morrison, J. E., & Mould, J. 2005, ApJ, 632, 169

Leitherer, C., Schaerer, D., Goldader, J. D., González Delgado, R. M., Robert, C., Kune, D. F., de Mello, D. F., Devost, D., & Heckman, T. M. 1999, ApJS, 123, 3

Leitherer, C., Vacca, W. D., Conti, P. S., Filippenko, A. V., Robert, C., & Sargent, W. L. W. 1996, ApJ, 465, 717

Lutz, D. 1991, in IAU Symposium, Vol. 146, Dynamics of Galaxies and Their Molecular Cloud Distributions, ed. F. Combes & F. Casoli, 312

Magorrian, J., Tremaine, S., Richstone, D., Bender, R., Bower, G., Dressler, A., Faber, S. M., Gebhardt, K., Green, R., Grillmair, C., Kormendy, J., & Lauer, T. 1998, AJ, 115, 2285

Mandelbrot, B. B. 1983, The Fractal Geometry of Nature (New York: W. H. Freedman and Co.)

Maoz, D., Barth, A. J., Sternberg, A., Filippenko, A. V., Ho, L. C., Macchetto, F. D., Rix, H.-W., & Schneider, D. P. 1996, AJ, 111, 2248

Maraston, C. 2005, MNRAS, 362, 799

Maraston, C., Bastian, N., Saglia, R. P., Kissler-Patig, M., Schweizer, F., & Goudfrooij, P. 2004, A&A, 416, 467

Melnick, J., Moles, M., & Terlevich, R. 1985, A&A, 149, L24

Meurer, G. R., Freeman, K. C., Dopita, M. A., & Cacciari, C. 1992, AJ, 103, 60

Meurer, G. R., Heckman, T. M., Leitherer, C., Kinney, A., Robert, C., & Garnett, D. R. 1995, AJ, 110, 2665

Mihos, J. C. & Hernquist, L. 1994, ApJ, 431, L9

—. 1996, ApJ, 464, 641

Miller, B. W., Whitmore, B. C., Schweizer, F., & Fall, S. M. 1997, AJ, 114, 2381

Miller, G. E. & Scalo, J. M. 1979, ApJS, 41, 513

Mould, J. R., Huchra, J. P., Freedman, W. L., Kennicutt, Jr., R. C., Ferrarese, L., Ford, H. C., Gibson, B. K., Graham, J. A., Hughes, S. M. G., Illingworth, G. D., Kelson, D. D., Macri, L. M., Madore, B. F., Sakai, S., Sebo, K. M., Silbermann, N. A., & Stetson, P. B. 2000, ApJ, 529, 786

Mullan, B., Konstantopoulos, I. S., Kepley, A. A., Lee, K. H., Charlton, J. C., Knierman, K., Bastian, N., Chandar, R., Durrell, P. R., Elmegreen, D., English, J., Gallagher, S. C., Gronwall, C., Hibbard, J. E., Hunsberger, S., Johnson, K. E., Maybhate, A., Palma, C., Trancho, G., & Vacca, W. D. 2011, ApJ, 731, 93

Neugebauer, G., Habing, H. J., van Duinen, R., Aumann, H. H., Baud, B., Beichman, C. A., Beintema, D. A., Boggess, N., Clegg, P. E., de Jong, T., Emerson, J. P., Gautier, T. N., Gillett, F. C., Harris, S., Hauser, M. G., Houck, J. R., Jennings, R. E., Low, F. J., Marsden, P. L., Miley, G., Olnon, F. M., Pottasch, S. R., Raimond, E., Rowan-Robinson, M., Soifer, B. T., Walker, R. G., Wesselius, P. R., & Young, E. 1984, ApJ, 278, L1

O'Connell, R. W., Gallagher, III, J. S., & Hunter, D. A. 1994, ApJ, 433, 65

O'Connell, R. W., Gallagher, III, J. S., Hunter, D. A., & Colley, W. N. 1995, ApJ, 446, L1+

O'Connell, R. W. & Mangano, J. J. 1978, ApJ, 221, 62

Peebles, P. J. E. 1973, ApJ, 185, 413

Peebles, P. J. E. 1980, in Annals of the New York Academy of Sciences, Vol. 336, Ninth Texas Symposium on Relativistic Astrophysics, ed. J. Ehlers, J. J. Perry, & M. Walker, 161–171

Peebles, P. J. E. & Dicke, R. H. 1968, ApJ, 154, 891

Petric, A. O., Armus, L., Howell, J., Chan, B., Mazzarella, J. M., Evans, A. S., Surace, J. A., Sanders, D., Appleton, P., Charmandaris, V., Díaz-Santos, T., Frayer, D., Haan, S., Inami, H., Iwasawa, K., Kim, D., Madore, B., Marshall, J., Spoon, H., Stierwalt, S., Sturm, E., U, V., Vavilkin, T., & Veilleux, S. 2011, ApJ, 730, 28

Portegies Zwart, S. F., McMillan, S. L. W., & Gieles, M. 2010, ARA&A, 48, 431

Reines, A. E., Johnson, K. E., & Goss, W. M. 2008, AJ, 135, 2222

Rhoads, J. E. 2000, PASP, 112, 703

Salpeter, E. E. 1955, ApJ, 121, 161

Sanders, D. B., Ishida, C. M., Mazzarella, J. M., Veilleux, S., Surace, J. A., Guyon, O., Jensen, J. B., & Kim, D.-C. 2004, in IAU Symposium, Vol. 222, The Interplay Among Black Holes, Stars and ISM in Galactic Nuclei, ed. T. Storchi-Bergmann, L. C. Ho, & H. R. Schmitt, 477–484

Sanders, D. B., Mazzarella, J. M., Kim, D., Surace, J. A., & Soifer, B. T. 2003, AJ, 126, 1607

Scheepmaker, R. A., Lamers, H. J. G. L. M., Anders, P., & Larsen, S. S. 2009, A&A, 494, 81

Schlegel, D. J., Finkbeiner, D. P., & Davis, M. 1998, ApJ, 500, 525

Schmidt, M. 1959, ApJ, 129, 243

Schweizer, F. 1982, ApJ, 252, 455

Schweizer, F. 1987, in Nearly Normal Galaxies. From the Planck Time to the Present, ed. S. M. Faber, 18–25

Schweizer, F. & Seitzer, P. 1998, AJ, 116, 2206

—. 2007, AJ, 133, 2132

Scoville, N. Z., Sanders, D. B., & Clemens, D. P. 1986, ApJ, 310, L77

Sirianni, M., Jee, M. J., Benítez, N., Blakeslee, J. P., Martel, A. R., Meurer, G., Clampin, M., De Marchi, G., Ford, H. C., Gilliland, R., Hartig, G. F., Illingworth, G. D., Mack, J., & McCann, W. J. 2005, PASP, 117, 1049

Smail, I., Ivison, R., Blain, A., & Kneib, J.-P. 1999, in American Institute of Physics Conference Series, Vol. 470, After the Dark Ages: When Galaxies were Young (the Universe at 2 Z 5), ed. S. Holt & E. Smith, 312–321

Surace, J. A. 1998, PhD thesis, Institute for Astronomy University of Hawaii 2680 Woodlawn Dr. Honolulu, HI 96822

Surace, J. A. & Sanders, D. B. 1999, ApJ, 512, 162

Surace, J. A., Sanders, D. B., & Evans, A. S. 2000, ApJ, 529, 170

Surace, J. A., Sanders, D. B., Vacca, W. D., Veilleux, S., & Mazzarella, J. M. 1998, ApJ, 492, 116

Toomre, A. 1977, in Evolution of Galaxies and Stellar Populations, ed. B. M. Tinsley & R. B. Larson, 401

Tyson, J. A., Fischer, P., Guhathakurta, P., McIlroy, P., Wenk, R., Huchra, J., Macri, L., Neuschaefer, L., Sarajedini, V., Glazebrook, K., Ratnatunga, K., & Griffiths, R. 1998, AJ, 116, 102

van den Bergh, S. 1971, A&A, 12, 474

van Dokkum, P. G. 2001, PASP, 113, 1420

Veilleux, S., Kim, D.-C., Sanders, D. B., Mazzarella, J. M., & Soifer, B. T. 1995, ApJS, 98, 171

Watson, A. M., Gallagher, III, J. S., Holtzman, J. A., Hester, J. J., Mould, J. R., Ballester, G. E., Burrows, C. J., Casertano, S., Clarke, J. T., Crisp, D., Evans, R., Griffiths, R. E., Hoessel, J. G., Scowen, P. A., Stapelfeldt, K. R., Trauger, J. T., & Westphal, J. A. 1996, AJ, 112, 534

Weidner, C., Kroupa, P., & Larsen, S. S. 2004, MNRAS, 350, 1503

Whitmore, B., Schweizer, F., Leitherer, C., Borne, K., & Robert, C. 1993, in Bulletin of the American Astronomical Society, Vol. 25, American Astronomical Society Meeting Abstracts #182, 818

Whitmore, B. C. 2003, in A Decade of Hubble Space Telescope Science, ed. M. Livio, K. Noll, & M. Stiavelli, 153–178

Whitmore, B. C. 2004, in Astronomical Society of the Pacific Conference Series, Vol. 322, The Formation and Evolution of Massive Young Star Clusters, ed. H. J. G. L. M. Lamers, L. J. Smith, & A. Nota, 419

Whitmore, B. C. 2009, Ap&SS, 324, 163

Whitmore, B. C., Chandar, R., & Fall, S. M. 2007, AJ, 133, 1067

Whitmore, B. C., Chandar, R., Schweizer, F., Rothberg, B., Leitherer, C., Rieke, M., Rieke, G., Blair, W. P., Mengel, S., & Alonso-Herrero, A. 2010, AJ, 140, 75

Whitmore, B. C. & Schweizer, F. 1995, AJ, 109, 960

Whitmore, B. C., Schweizer, F., Kundu, A., & Miller, B. W. 2002, AJ, 124, 147

Whitmore, B. C. & Zhang, Q. 2002, AJ, 124, 1418

Whitmore, B. C., Zhang, Q., Leitherer, C., Fall, S. M., Schweizer, F., & Miller, B. W. 1999, AJ, 118, 1551

Wilson, C. D., Harris, W. E., Longden, R., & Scoville, N. Z. 2006, ApJ, 641, 763

Zepf, S. E., Ashman, K. M., English, J., Freeman, K. C., & Sharples, R. M. 1999, AJ, 118, 752

Zhang, Q. & Fall, S. M. 1999, ApJ, 527, L81

Zhang, Q., Fall, S. M., & Whitmore, B. C. 2001, ApJ, 561, 727